Ink Transfer Mechanisms in Flexographic Printing

Victoria Verona

A thesis submitted in partial fulfilment of the requirements of the Open University for the degree of Doctor of Philosophy

August 2005

Sponsoring establishment

The London College of Communication,
University of the Arts London

Acknowledgements

I wish to express my gratitude to Professor R C Thompson, my director of studies and my second supervisor Dr A N Manning, for their continuing support guidance and patience throughout the duration of this work I also would like to thank Mr J Birkenshaw for his support and advice during my time working with Pira International.

This work was undertaken with the support of Pira International in Leatherhead, Surrey, who provided the facilities for the contact angle measurement using the MAMS instrument, the OMAT wide web flexographic printing press, and donated the paper used for the press trials. I am particularly grateful for the help of Mr D Atkinson, who provided valuable support with the technical aspects of running press trials, and Mr A Diley, who provided instruction and technical support with the MAMS instrument.

I would also like to express my gratitude to the Educational Charity of the Stationers' and Newspaper Makers' Company, who provided financial support for this project.

I would like to thank the Harper Corporation of America for the donation, production and loan of three of the anilox rolls used in this study. In particular, I wish to thank Mr D Reilly for his help in establishing the working relationship with Harper and for his help in choosing the anilox specifications of the first two anilox.

The ink used in all press trails was donated by Coates Lorrelleux, now part of the Sun Chemical group. In particular, I would like to thank Mr M. W. Walkling for his help and advice on printing with UV flexo inks. I also wish to thank Sun Chemical Swale for the donation of the water-based ink used for contact angle analysis.

The image analysis of the anilox rolls was carried out with the help of Mr M Nichols at Scantron and Dr S Hamblyn at the Welsh Centre for Printing and Coating, Ink thickness analysis by optical microscopy was carried out at Coates Lorrelleux with the help of Mrs N Kessel.

The doctor blades used on the OMAT press were kindly donated by William Pinder and Sons of Manchester.

The paper used on the Pira press was converted to fit the RK press by Maidstone paper converters Ltd.

I am grateful to Dr A Milligan and Mr P Beavers for their help with the integration employed in appendix A6.

I would like to thank my family for many years of encouragement and support (emotional and financial!). I am also indebted to Pootle for keeping me company through the long days of solitude. Finally, I would like to dedicate this work to my husband Luke in recognition of his patience-, thoughtfulness and express my gratitude for the supply of tea and biscuits.

Table of Contents

List of Figures – Chapter 1

List of Figures – Chapter 2

List of Figures – Chapter 3

List of Figures – Chapter 4

List of Figures – Chapter 5

List of Figures – Chapter 6

List of Figures – Chapter 7

List of Tables – Chapter 1

List of Tables – Chapter 2

List of Tables – Chapter 3

List of Tables – Chapter 4

List of Tables – Chapter 5

List of Tables – Chapter 6

List of Tables – Chapter 7

Abstract

The work presented here describes the wetting and transfer characteristics of ceramic anilox rolls, used to meter ink flow on a flexographic printing press. The effect of the type of laser used to make engraved cells on the anilox was examined. Cells engraved by a conventional carbon dioxide (CO_2) laser, a modified CO_2 laser and a neodymium doped yttrium aluminium garnet (nd:YAG) laser were studied. Printing was carried out on a commercial OMAT wide web flexographic printing press and a laboratory scale RK press. The ink transfer from the cells was measured, along with the wettability, surface energy, geometry and interior surface roughness of the cells.

The wetting characteristics of the anilox rolls were extensively studied using contact angles measurements. Two instruments were used to make the measurements and both equilibrium and advancing contact angles were measured. The contact angle data was used in conjunction with the Wenzel, Shuttleworth and Bailey, and Cassie and Baxter theories to understand the effect of the highly structured roughness produced by the engraving process, on the wettability of the anilox rolls.

The findings of this work were that the laser type used to make the engraving changed the wettability of the anilox surface. Surface energy calculations revealed that the change was due to the polarity of the roll surface, which made the roll less receptive to wetting by polar liquids. The nd:YAG laser was found to produce cells that were less receptive to polar liquids than the CO_2 lasers.

Analysis of the contact angle data showed that the magnitude of the observed advancing contact angles was in agreement with the theory of Shuttleworth and Bailey, that the gradient of the roughness, which in this case was the slope of the cell walls, dictated the resistance to wetting by polar and non polar liquids. When the liquids were allowed to reach thermodynamic equilibrium, wetting by polar liquids was found to be consistent with the theory of Cassie and Baxter, that pockets of liquid/air interfaces were formed in the bottoms of the cells, producing a composite surface under the test liquid of solid/liquid and air/liquid areas. This produced the increase in observed contact angles with polar liquids on the engraved areas. The well-known Wenzel equation was found not to be applicable to the anilox surface wetting with any test liquid.

Printing was carried out with a standard UV curable flexographic ink. Ink transfer was observed to be affected by cell geometry. Equilibrium contact angle measurements were not directly related to ink transfer. However, it was the finding of this investigation that the relationship between advancing contact angles and ink transfer was likely and warrants further study.

Aims

The primary aim of this investigation is to assess some of the parameters that affect the amount of ink transferred from the anilox roll in a flexographic printing press. The variables identified for investigation are the surface chemistry of the anilox roll, both before and after engraving has taken place, the geometry of the engraved cells, the interior roughness of the cells and the receptiveness of the anilox to wetting, with high purity test liquids and with real flexographic inks.

A commercial OMAT wide web flexographic printing press and a laboratory RK press have been employed to produce prints from which ink transfer measurements were made. Surface chemistry and wettability information were obtained by measurement of contact angles on the anilox roll surface.

It is hoped that knowledge gained from this project will lead to improvements in the design of anilox rolls to achieve more control and consistency of ink transfer. Information on the surface chemistry of the anilox may also help ink formulators tailor the properties of the ink to further improve transfer.

1. Flexographic printing

1.1 Introduction

Modern flexography has evolved from the now obsolete process known as aniline printing, which used aniline dyes and rubber plates in a method much like an automated rubber stamp. Aniline printing produced low quality prints suitable for printing simple designs on the sides of cardboard boxes. The process was cost effective and capable of producing prints on low-grade materials, features that modern flexography has retained. There were several key factors in the transformation from aniline printing to flexography. Pigments replaced aniline dyes and the ink formulation became more sophisticated. A metering roll (anilox) was introduced to control the flow of ink to the plate, and plates made of special polymers were introduced which made the production of finer image dots possible. These changes made it possible to accurately control the amount and position of the printed ink and vastly improved the quality of the process. [1]

Nowadays flexography, or flexo, is a versatile printing technique using flexible printing plates to produce quality prints on a wide range of substrates. It is still the dominant process for printing onto rough substrates such as uncoated paper and board. The improvements in print quality have dramatically increased the use of flexo to print on high quality substrates such as coated papers and boards and self-adhesive labels, speciality substrates such as aluminium foil, copper foil, metalised films, tissue and napkins, sausage casing, and filmic materials, such as acetate, nylon, polypropylenes, polyethylenes and polyvinylchlorides (PVC). [2, 3]

The ability of flexo to print onto just about anything is one of many advantages that it has over other traditional printing processes such as offset lithography, letterpress and gravure. The other major advantages that flexo can offer are the comparatively low cost of producing high quality work, and of purchasing and setting up the presses.[1] Flexo also boasts shorter turnaround times for print orders due to reduced handling and in-line finishing capabilities, good opacity and film thickness with low viscosity fast drying inks, relatively high press speeds, excellent solid coverage and good quality halftones with digitally produced plates. [2]

Summary of the flexo market			
€ million	**1999**	**2004**	**2009**
Total	**94,863.5**	**106,443.5**	**129,733.7**
US & Canada	42,708.3	48,003.1	57,196.9
Western Europe	25,087.6	27,391.7	31,436.9
Asia & Middle East	16,267.9	19,306.7	25,577.3
Eastern Europe	2,593.8	2,836.8	3,404.0
Latin America & Mexico	5,490.6	6,443.7	9,410.0
Oceania & South Africa	2,715.3	2,461.4	2,708.6
Market sectors			
Corrugated	43,091.0	47,066.2	55,791.3
Flexible packaging	16,684.5	19,984.5	26,671.7
Labels	9,136.9	11,299.0	14,129.5
Cartons	10,486.8	11,238.4	13,722.1
Envelopes	5,174.1	5,650.4	6,329.8
Sanitary/kitchenware	3,438.0	3,776.3	4,495.2
Bags & sacks	3,452.3	3,753.2	4,392.6
Newspapers	891.6	967.0	1,040.1
Other	2,508.2	2,708.6	3,161.5

Source: Pira International Ltd

Table 1.1. The value of the flexographic printing market in 1999, 2004 and projected to 2009.[4]

Pira International valued the world flexo printing and converting market at 106.4 billion euros in 2004 and predicted that it would grow by 21.9% to 129.7 billion euros in 2009.[4] Table 1.1 shows how the value of the flexo markets have increased from 1999 to 2004 and shows the projected market values in 2009. The market values are split both geographically and by market sectors. The popularity of flexo varies significantly around the world. Flexographic printing accounts for 75% of the total US packaging industry.[5] In some American markets such as paper packaging, flexo has saturated the market leaving little room for further growth. In other areas growth is small but sustained. [6]

In the European packaging market, flexo faces stiff competition from offset lithography, gravure and from the relatively new digital printing processes. Figure 1.1 shows the division of the European packaging market in 2002. Flexo has the largest market share with 39%, but its share has not increased significantly over the last three years.[5]

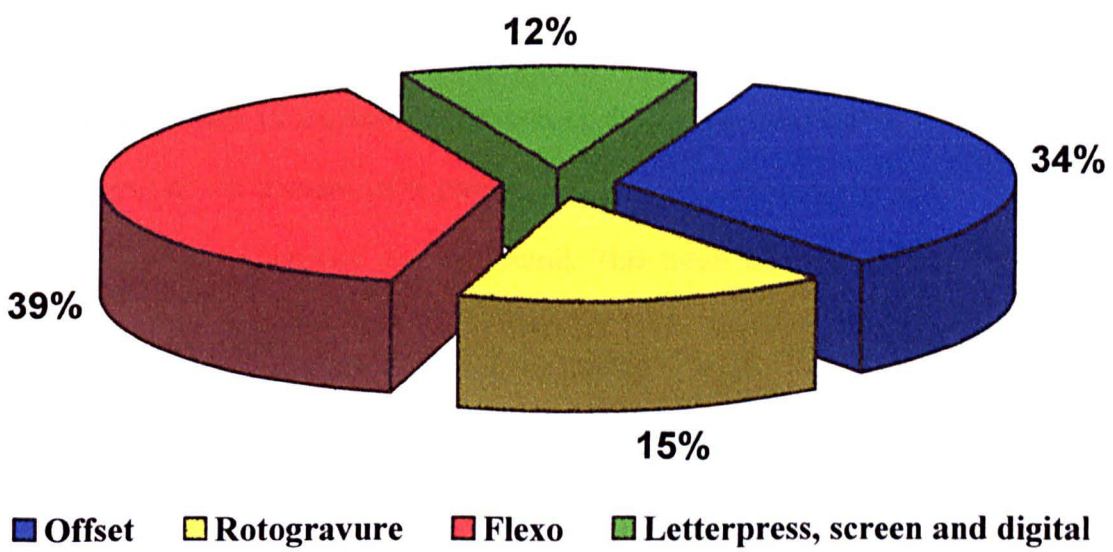

Figure 1.1 The makeup of the European packaging market in 2002.[7]

Like every sector of manufacturing and service industry, the flexo market was affected by the downturn in the US and global economies at the beginning of the new millennium. However, unlike many other areas of the printing industry the market for flexo continued to grow and indeed whilst growth was small, flexo outperformed its rivals. [8] This was attributed in part to the tendency of run lengths to become shorter as the economy slows down, giving flexo more of an advantage as it is comparatively a more economic process for shorter runs.

The improvements made in the quality of flexo have brought it into competition with the traditional quality printing techniques, gravure and offset, and also the new techniques of inline ink jet and other digital printing processes. Several years ago, flexo could offer large cost benefits over the these processes but in recent years digital processes have become more economically viable [9] and gravure cylinders in particular have become much less expensive. Therefore, flexo must work harder to maintain its growing market share. [5] Criticisms of high quality flexo printing relate to consistency, [1] and the cost and speed of producing high quality plates,[5] and it is in these areas that improvements can be made. Printing consistency is achieved by controlling the flow of ink through the process; there is therefore a need to study the mechanisms of ink transfer, as a greater understanding of the movement of ink is needed in order to optimise process control. This thesis is therefore dedicated to furthering our understanding of ink transfer.

1.2 The flexographic printing press

A simple diagram of a flexographic printing press is shown in Figure 1.2.

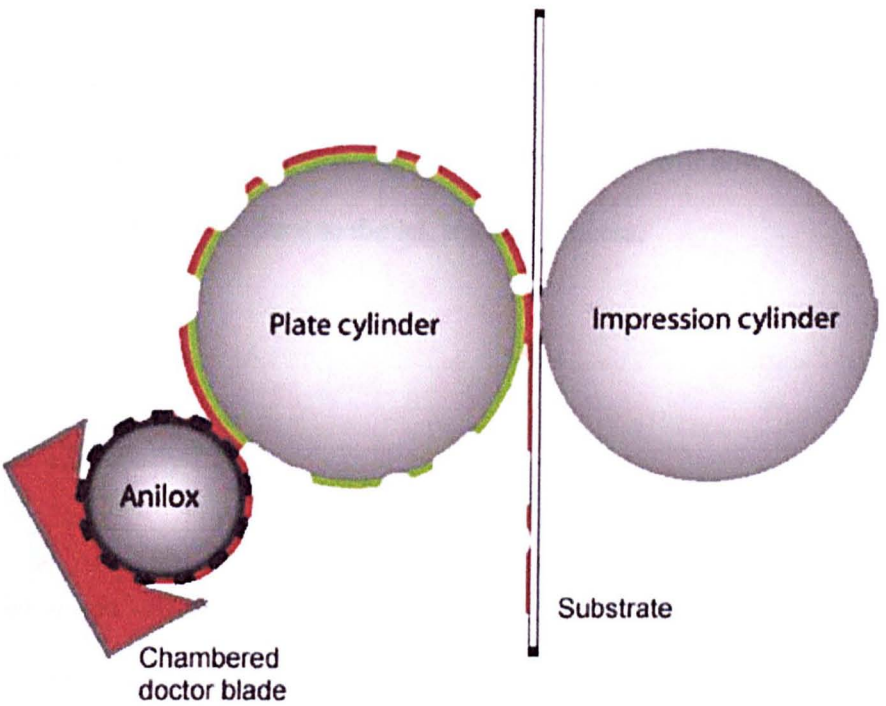

Figure 1.2. The component rolls of a flexographic press.

The ink is transferred to the anilox roll, either by a fountain roll (usually a rubber roll), or directly from an ink chamber as shown in Figure 1.1. Cells are engraved into the anilox surface and are filled with ink. Excess ink is removed from the surface of the anilox roll by a doctor blade before the anilox makes contact with the printing plate. The anilox roll therefore controls the amount of ink reaching the plate. The image is created from the raised areas of the plate (represented in the Figure 1.1 as a broken curve around the plate cylinder). Ink is applied to the plate

by a "kiss impression" by the anilox, i.e. the anilox touches the raised dots on the plate with minimal pressure to avoid compressing the dots or inking the non-image recesses. The plate transfers the ink from the image area to the substrate, which is fed through the nip between the plate cylinder and the impression cylinder.

Each component of the flexo press has an important role in controlling the amount of ink that passes through the press. These components will now be discussed in detail, along with their relevance to the ink transfer process.

1.3 The anilox roll

The anilox roll has been termed the heart of the flexographic printing process [10] as the precise metering of the ink onto the printing plate by the anilox was at the centre of the transformation from aniline printing to modern flexography. It is essential for the anilox to take up the ink easily without capturing air in the engraved cells, then to release the ink as efficiently and as completely as possible. This reduces the risk of ink drying and plugging-up of the cells, as well as improving the efficiency of the process.

Anilox rolls were traditionally manufactured by mechanically engraving a copper plated steel roll and then plating it with chromium. When in good condition, this type of roll provided good ink transfer to the plate. However, its durability was very poor and inconsistencies in the amount of ink transferred as the anilox wore down created problems.[11] The introduction of harder, more durable ceramic coatings has

revolutionised anilox production. Initially, ceramic was used to coat a mechanically engraved anilox but this process was difficult to control and ceramic build-up in the cells was a problem. Modern ceramic aniloxes have the ceramic coating applied to the roll in a plasma spray, [12] which are then engraved by a laser.[13] This type of anilox is now the industry standard for most applications. [14]

1.3.1 Ceramic coating

The stainless steel roll core is sprayed with a dense metallic bond coat to provide a key for the ceramic top layer, as well as to protect the roll core. [12, 15] The metals used are normally nickel alloys such as NiCr and NiAl. Atmospheric plasma spraying (APS) is initially carried out with a coarse powder to produce a well-adhered coating followed by spraying with a fine powder to increase the density of the coating. A chromium oxide ceramic top coat is sprayed by the APS technique to a thickness of 0.26 mm. [15] The top coat may contain small quantities of titanium oxide, added to lower the melting point of the powder, and silicon oxide, which acts as a glass former and reduces the final porosity of the ceramic.[12] The final coating has a hardness of 1200 to 1400 Vickers.[15] The Vickers is a unit relating to the indentation made by a square based diamond pyramid under a specified load. This is the usual method for describing the hardness of an anilox but does not directly convert to an SI unit. [16, 17] However, for comparison with more recognisable units, 1300 Vickers is approximately equivalent to 72-74 on the Rockwell C scale.[11] The ceramic coating has a porosity between 1% and 3%.[15] The hardness and the porosity of the ceramic coatings vary between manufacturers. In some cases, an epoxy sealer is applied to

the ceramic topcoat to decrease the porosity to a desirable level of around 1%.[18] Other manufacturers, for example APEX-Europe [19] and The Harper Corporation of America, [20] claim to have produced high quality ceramic coatings with a porosity of less than 1% where no sealer is needed. Another manufacturer, Praxair Surface Technologies, applies a hydrophobic "Rainbow" coating [21] post engraving, which lowers the surface energy of the cell interior to improve ink release. Once the ceramic coating has been applied, the roll is ground and polished until it has a mirror-like finish; then engraving with a laser can take place.

1.3.2 Laser engraving

The use of a laser to etch the cells has several advantages over traditional mechanical engraving. Firstly, since a percentage of the ceramic is vaporised by the laser instead of being pushed aside, the land areas between the cells are significantly reduced. This enables a higher cell frequency to be created on the roll, which produces a more consistent ink film as there are thinner walls between the cells. [22] Additionally, the computer controlled laser can be more accurately targeted than a mechanical engraving tool. Laser engraved cells can also be made to have a variety of shapes whereas mechanically engraved cells usually are pyramid shaped due to the shape of the standard tool. These laser engraved cell patterns result in more cells being packed into a given area. Laser engraved ceramic anilox rolls are also much more durable than mechanically engraved chrome coated copper rolls, and although they are more expensive, each roll is estimated to last from 4 to 6 times as long. [11]

Originally, carbon dioxide (CO_2) lasers were used to engrave the ceramic layer. Recently, YAG solid-state lasers were introduced to produce engravings and the two different laser types produce cells that are very different. [23, 24] Photographs showing the differences in appearance of the cells produced by the different lasers are shown in Figures 1.3 and 1.4.

Carbon dioxide lasers were originally used in pulsed mode to produce individual cells, each pulse producing a round indentation whilst vaporising a small amount of the ceramic and recasting the remainder as the cell wall. [24] As the cell profile comes from the recast ceramic being pushed aside by the laser, the cell is bowl shaped. (As shown in Figure 1.3 and Figure 1.7 right). A later development was the continuous wave or CW CO_2 laser. [25] CW CO_2 lasers produce a continuous beam of radiation that is chopped into discrete pulses by means of a shutter. This technique improves the accuracy of the engraving and allows for finer screen counts to be achieved than with pulsed CO_2 as the pulses can be focused onto a smaller area. Neither type of CO_2 laser is, however, suitable for producing very small cells. This is because the wavelength of the laser is relatively large at 10.6 μm, [26] and cannot be focused into very a small spot. The minimum cell opening that it can be produced with a CO_2 laser is about 20μm, which translates to a line count of around 400 lines/cm. [26]

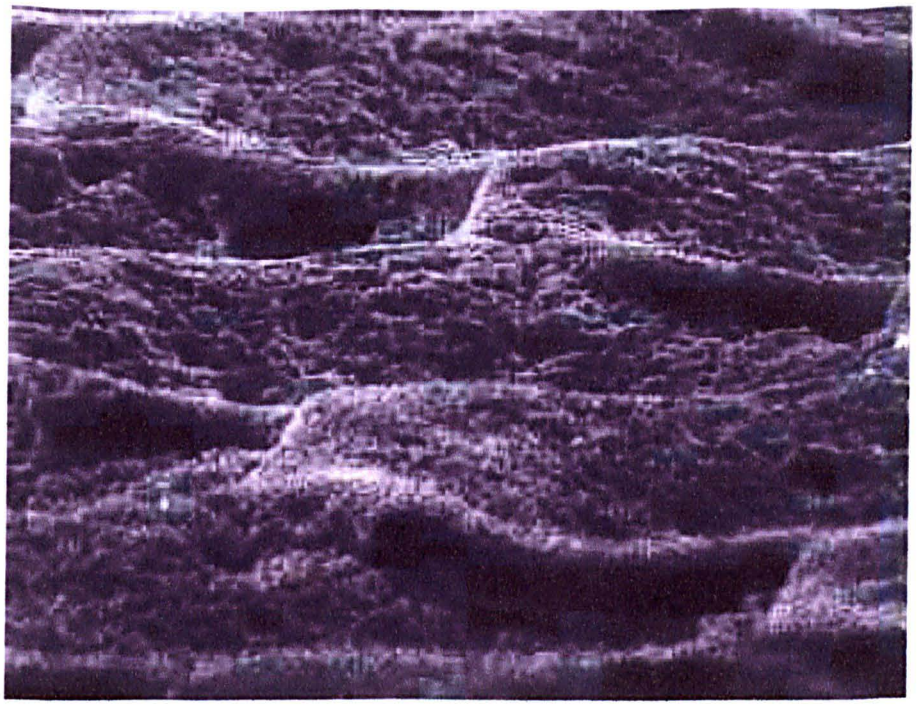

Figure 1.3. A photograph of an anilox roll engraved by a CO_2 laser at x1000 magnification. (Provided by The Harper corporation of America).

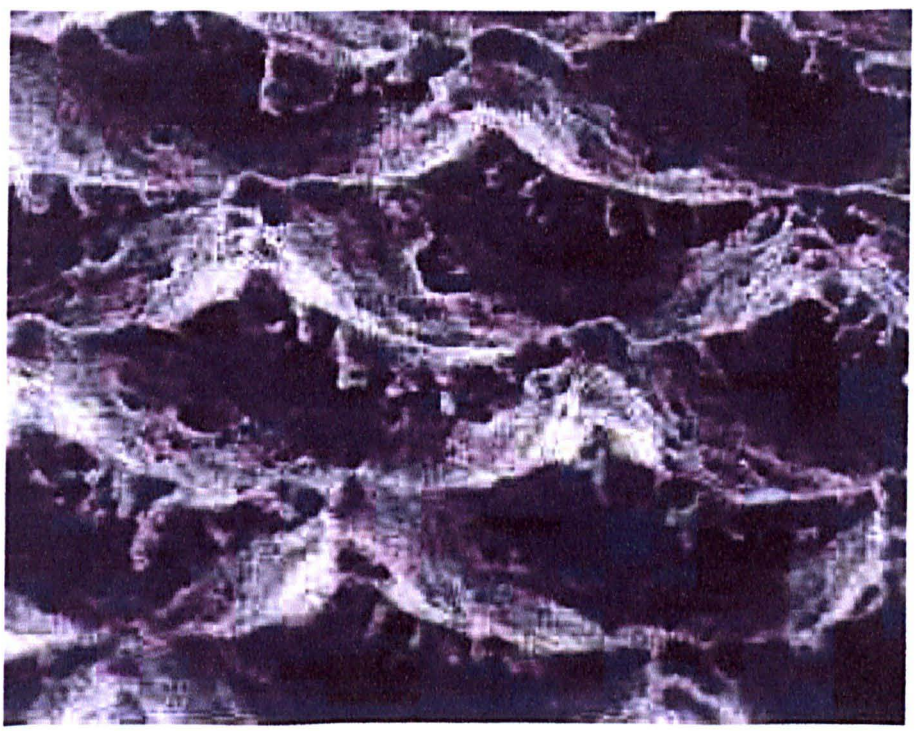

Figure 1.4. A photograph of an anilox engraved by a YAG laser at x1000 magnification. (provided by The Harper corporation of America).

In order to produce smaller cells, the wavelength of the laser had to be changed. The nd:YAG laser is a solid state laser which takes its name from the components of the solid from which the laser beam is generated. Neodymium atoms are doped into a crystal of yttrium, aluminium and the mineral composition garnet; its output wavelength is only 1.06 μm [26]. At this wavelength, more of the laser energy is absorbed into the ceramic and the cell is created by ablation rather than melting and recasting. A picture of cells produced by an nd:YAG laser (termed a YAG engraving) is shown in Figure 1.4.

The YAG laser produces little to no recast and as a result the cells formed have smoother interior surfaces with a slightly different cell profile. The smaller wavelength allows the laser to be focused onto a very small area and cells can be engraved at very high line counts. Commercially available YAG engravings can have line counts as high as 700 lines per centimetre, [27] whilst engravings of 1000 lines per centimetre are technically possible. [19] The power output of a YAG laser is much lower than that of a CO_2 laser. [28] Therefore, it is sometimes necessary to hit each cell a number of times to remove enough ceramic to achieve optimum depth and shape. Increasing the number of times each cell is hit also improves consistency between cells. [28, 29] There is a trade off between the improvement made with each hit and the cost of the additional laser use. The multi-hit technique is also used with CO_2 lasers to improve the cell shape and consistency.

Anilox rolls engraved by YAG lasers became commercially available in 1997, [24] and were initially very popular in the late 1990's. [24, 28, 30] However, problems were soon identified with poor ink transfer, susceptibility to scoring [28] and shorter lifetime

compared to anilox engraved by CO_2 lasers. [31] The problems were attributed to the lack of recast ceramic in the cell wall. [28, 31] Recast ceramic was considered undesirable as it causes inconsistencies in the shape and size of cells and creates shape peaks, which wear the doctor blades as the excess ink is scraped from the anilox surface. [26] However, the recast ceramic is harder and denser than the unablated ceramic [28] and without it YAG engraved anilox rolls were less durable. Recent advances in anilox technology have increased the length of the pulse of the YAG laser so that it melts and recasts a controlled portion of the ceramic in the same way that the CO_2 laser does. This is done as part of a multi hit system so that sufficient ceramic is removed to provide the desired cell volume and then recast is created to strengthen the cell walls. This type of YAG engraved anilox is known as 3rd generation YAG or thermal YAG. [32, 33]

Although YAG laser technology is not new, it only began to be applied to anilox technology in the late 1990's, making it a relatively new innovation to the printer. Therefore,, comparisons of the surface characteristics of the YAG and the CO_2 engraved ceramics are still of interest to the industry.

1.3.3 Cell profile and characteristics

The different methods of engraving ceramic anilox rolls produce cells with very different profiles and surface characteristics. Traditional mechanically engraved cells, were pyramid shaped due to the shape of the tool used to make them. These cells were arranged at an angle of 45° as shown in Figure 1.5. When laser engraving

was first carried out on ceramic anilox, engravings were made at 45° to mimic the familiar characteristics of the mechanically engraved cells. [28] In the early 1990's however, research into the effectiveness of the angle of engraving showed that engraving the cells in a 60° hexagonal close packing arrangement produced engravings with more cells fitted into a given area, and therefore produced anilox rolls with a greater ink carrying capacity. An example of the patterns produced by engraving at 45° and 60° is shown in Figure 1.5.

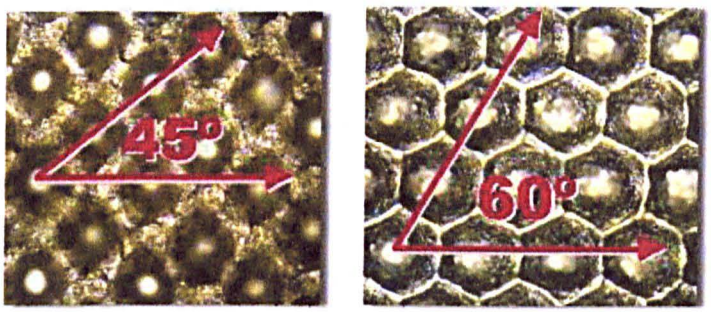

Figure 1.5. The engraving patterns of cells made at 45° and 60° angles. (Pictures provided by the Harper Corporation of America)

Unlike mechanical engraving where the shape of the cell takes the shape of the tool used to make the engraving, the shape of a laser engraved cell is produced by the number of neighbouring cells packed around it. The laser ablates a hole that forms a geometric shape dependent on the number of holes that surround it and contribute to its wall area. If the laser ablates cells at an angle of 45° each cell shares its wall area with 4 other cells. The effect of this is to make the cells diamond shaped. If on the other hand the laser ablates cells at a 60° angle, each cell has 6 cells sharing its wall area. The cells therefore take on a hexagonal shape. The profile of the cell is also

effected by the number of surrounding cells. A cell produced by a 60° engraving is approximately bowl shaped. However, cells produced by a 45° engraving are closer to the shape of a square based pyramid. An impression of the difference between the cell profiles of the 2 types of engraving is shown in Figure 1.6.

Figure 1.6. Simplified profiles of cells made with engraving at 45° and 60° angles.

The difference in the shape of the profile of the cells has consequences when the effect of wear on the cell volume is considered. The percentage of the overall volume of the cell at the very top is greater for a pyramid than a bowl. Therefore a slight decrease in cell wall height caused by wearing impacts more on the 45° degree engraving, as the cell volume decreases by a significantly greater amount. There is therefore a greater change in the transfer characteristics of a roll engraved with a 45° pattern as the anilox wears down. Anilox formed with cells having a 60° engraving pattern therefore have a longer useful life.

The profile and surface of the cell is also a characteristic of the laser used in engraving. As previously mentioned, CO_2 lasers produce recast which is pushed aside to form the cell wall which results in a bowl like shape. YAG lasers on the other hand have little to no recast and as a result the cells have a different profile.

The cells can be made deeper without any increase in opening and the cell walls are steeper, resulting in a shape which is more test tube like in appearance. Figure 1.7 shows the different cell profiles produced by the two lasers.

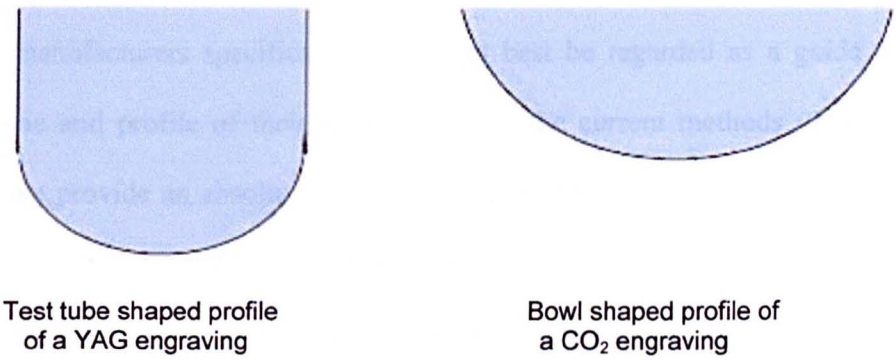

Figure 1.7. Typical cell profiles produced by YAG and CO_2 lasers.

The profile of the cell influences its ability to take up and release ink. For CO_2 engravings, the cell depth to opening relationship where the cell depth is in the order of 23% to 33% of the cell width, is generally accepted as the right balance to transfer as great a portion of the cell volume as possible. [15, 23] Shallower cells provide insufficient volume, whilst deeper cells do not empty sufficiently and plugging occurs. For YAG engravings, this relationship does not apply as the vertical walls allow the cell to empty to a greater depth. The Harper Corporation quote that comparable ink print densities can be achieved using a 1400 lines per inch (550 lines per centimetre) YAG roll and a 800 lines per inch (315 lines per centimetre) CO_2 roll. [24] As the rules of thumb applied to the ink transfer from CO_2 cells do not work for YAG, the transfer characteristics of YAG engravings are still a subject for investigation.

1.3.4 Methods of cell measurement

Measurement of the cell profiles and volumes is not easy given the microscopic dimensions of the cells. An unpublished report by SCA Packaging [34] demonstrated that manufacturers specifications could at best be regarded as a guide to the cell volume and profile of their rolls. None of the current methods of assessing cell volume provide an absolute volume. However, the best method, both of measuring the volume and profile of a cell may be by white light interferometry. [35, 36] This interferometer is a highly developed instrument which uses an interferometric microscope in conjunction with computer software to scan, record and analyse the surface of the anilox to a resolution of less than 10 nanometers. Interferometry is quoted as being up to 15 times more accurate than manual methods and over 5 times faster. [35] The main problem with determining the absolute volume of a cell is deciding where the top of the cell is, as the cell wall heights can be irregular. The interferometer calculates a mean height by looking at the variation in cell wall. Whilst this is still an approximation, it is far more accurate than any other method.

There are alternative methods of measuring cell volumes including the casting of the cells. This involves filling the cells with a liquid, which then solidifies and is removed from the cells, followed by optical assessment of the casts to determine the volume. This technique can also be used to assess damage and plugging. Another method is the drawing of a known quantity of ink across the roll surface with a blade, estimating the volume by the distance that the ink can be drawn across the surface of the roll i.e. a known volume of ink could be drawn further across the surface of a roll with shallow cells than that of a roll with deep cells. Both of these methods are

highly dependent on the skill of the human operative and are therefore less repeatable and accurate. These techniques are however popular as they are substantially cheaper to perform than interferometry.

1.3.5 Inking and doctoring of the anilox

The fountain roll is the original design used to carry ink from an ink reservoir to the anilox. These rolls are usually made of rubber and can vary from 50 to 75 durometer hardness on the Shore A scale [38] for solvent inks and can be as hard as 90 durometer for use with water-based inks. [39] A hard roll will transfer less ink than a softer roll so it is important to chose the correct fountain roll to suit the anilox to which the ink is being transferred. The hardness of the fountain roll can also be adjusted to control ink transfer and print quality. The pressure in the nip between the fountain roll and anilox is also important in aiding efficient transfer to the anilox. Insufficient pressure does not force enough ink into the cells. On the other hand, if too much pressure is applied the rubber surface of the fountain roll is damaged by the rough edges of the anilox cells. Fountain roll systems were better suited to a chrome anilox as the wiping action of the rubber against the chrome provided a self-cleaning action for the anilox. [40] In most modern flexo presses, the fountain roll and ink reservoir have been replaced by chambered doctor blade as shown in Figure 1.1.

In a chambered doctor blade system, the doctor blade is incorporated with the ink reservoir in a chamber. [41] The ink is held in contact with the anilox, contained between two doctor blades and the chamber is sealed at each end. The advantages of

a chambered doctor blade system are that the ink can be pressurised inside the chamber, which assists the filling of the anilox cells. The ink is enclosed in the chamber, reducing the evaporation of solvents, and ink splattering. However, there are problems with leakage from the ends of the chambers, [42] and the presence of two blades in contact with the anilox increases anilox wear and blade consumption.

Excess ink is scraped away from the surface of the anilox by a reverse angled doctor blade to ensure only the ink in the cell recesses reaches the printing plate. Doctor blades are usually made of carbon steel, however stainless steel is generally used for water-based inks. Where minimising blade wear is critical, a plastic material such as high-density polyethylene or a ceramic with a hardness less that of the chromium oxide coating of the anilox are used. [43] The angle of the blade is important, as it is desirable to remove the ink from the roll surface as efficiently as possible whilst minimising wear to the blade and anilox. The best angle for doctoring is accepted to be 30° to the tangent point of the roll. [23] The blade is at a reverse angle to the direction of rotation of the anilox as this minimises the extent of the lifting of the blade from the anilox surface caused by build up of ink underneath the blade.

1.3.6 Ink transfer from the anilox

In order to achieve a high quality print, it is necessary to transfer the correct amount of ink from the anilox to the plate. Too much ink would lead to dot gain, the undesirable increase in size of a printed dot, and results in a dirty looking print. However, too little ink leads to patchy solids and missing highlight dots. To improve

the fine detail in a print, the dots on flexo printing plates have decreased in size. Quality printing went from a standard of 24 lines per centimetre to 60 lines per centimetre and beyond in order to match the dot size produced by offset printing.[44] The size of the anilox cells had to also decrease to prevent dots dipping into the anilox cells. In the early days of flexographic printing, an anilox line screen count of three times that of the plate was considered acceptable, but as the push to achieve better and better quality from flexo went on it became five then seven times in order to produce a cleaner print. [44] When packing so many cells onto an area of anilox, delivering a sufficiently high volume of ink to maintain colour strength becomes an issue. Increasing the depth of the cells beyond the accepted 33% depth to opening relationship has been shown to increase solid densities. [45]

The amount of ink reaching the plate is dependent on the volume of ink delivered by the anilox. The frequency and the volume of the engraved cells determine the holding capacity of the roll, however the amount of ink transferred to the plate is approximately 40% of the cell's volume. [46] Clearly, there are other variables that affect the transfer of ink from the anilox to the plate. The surface energy and roughness of the anilox roll, the viscosity and surface tension of the ink and method of doctoring may all influence ink release from the anilox. However, to what extent each of these affects ink transfer is a question for investigation.

A study has been done by the DFTA Technology-Centre in Germany into the ink transfer of the anilox roll. [47] Factors examined included the geometry and surface of the cell, the angle at which the cells were engraved, cell aperture, and the influence of roll wear. YAG engravings were not included due to the date at which the study

was made (1995). The study reports that in order to control ink transfer from the anilox to the plate the process needs to be closely monitored with respect to the screen count, cell structure, anilox surface and ceramic coating. The study goes on to suggest points of importance when choosing an anilox. The size of the cell opening is concluded to be the most important factor in the release characteristics of the anilox. Surface roughness of the anilox, the plate and the rheology of the ink were also identified as important factors.

1.4 Flexographic printing plates

Another important development in the evolution of high quality flexography was the introduction of the photopolymer printing plate, which for most applications has replaced the traditional rubber stereo. Benefits of photopolymer plates include predictability of plate thickness and size, ease of processing and mounting, and improved reproducibility to the flexo process. [49] There are two types of photopolymer plates; liquid photopolymer plates and solid-sheet photopolymer plates. Solid-sheet plates are currently the most popular form of flexo plate, accounting for approximately 85% of the market. [48] Over the last couple of years however, rubber plates have increased in popularity due to the introduction of laser engraving techniques that can create the image on a rubber plates or rubber coated cylinders without the need for negatives.

Plates are selected for a particular job with the following properties in mind; stiffness, hardness, abrasion and tear resistance, storage stability, resistance to

chemicals such as the ink solvents and ozone and the cure rate and the moulding shrinkage of the material. [48] The merits of each type of printing plate are discussed below.

1.4.1 Solid-sheet photopolymer plates

The solid-sheet photopolymer plate consists of a number of layers, each made of a different material and playing a different part in the function of the plate. Figure 1.8 shows a simple diagram of the structure of a solid-sheet photopolymer plate.

The top layer is a protective coversheet, typically made of polyester or polystyrene with a thickness of 30 –50 microns. This layer is removed before curing of the plate takes place. Underneath this layer is a top release protective film that is washed out using a suitable solvent during the developing process. Typical materials used for this layer are vinyl acetate or polyamide copolymers and the film has a thickness of approximately 5 microns. [48]

The top layers protect the curable layer, which forms the image section of the plate. This layer consists of a photosensitive elastomeric blend of chemicals containing a thermoplastic elastomeric block copolymer, usually a styrene/butadiene copolymer, an ethylenically unsaturated acrylate compound such as ethylene glycol diacrylate, and polymerisation initiators examples of which are some aromatic ketones. The polymerisable layer typically ranges in thickness from 0.127 millimetres to a maximum of 6.35 millimetres. [48]

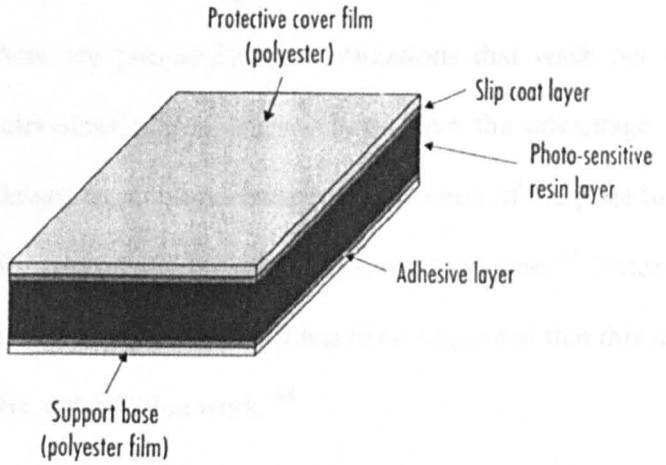

Figure 1.8. General structure of the solid-sheet photopolymer plate. [48]

The polymerisable layer is fixed to a supporting layer, termed the substrate, by a thin adhesive layer. This substrate layer could be made from a metal plate such as tin, aluminium or steel, or from polymeric material such as polyesters or polyamides. The substrate layer has a thickness in the range of 0.025 millimetres to 0.5 millimetres. [48]

There are several stages in forming the image on the plate. The first step is usually a back exposure through the substrate side of the plate. Next, the protective cover is removed and a negative of the desired image is placed over the plate. The plate is then exposed to light and heat in what is termed a relief exposure. Areas corresponding to the clear areas of the negative are exposed and become polymerised. The remaining unpolymerised areas of the plate are washed out with a suitable solvent or combination of solvents. The plate is then dried to remove absorbed solvents, which swell the plate, and allowed to stabilise. This process takes up to 10 hours. [48]

The generation of organic solvent waste in this process is an environmental concern. There are photopolymer formulations that wash out in aqueous solutions, termed water-wash plates. These plates have the advantage that they do not need to be allowed to stabilise, therefore production of the plate takes around an hour compared with around 10 hours for a solvent-wash plate. [48] Water-wash plates also have a more hydrophilic surface and it has been suggested that this improves ink transfer for some jobs, notably line work. [48]

Recently, systems have been developed for the production of the image without the need for a negative. Computer to plate (CTP) technology employs an opaque black topcoat termed the laser ablation mask system or LAMS. [50] This layer is ablated by a computer-controlled laser to produce the image. Both CO_2 and YAG lasers can be used for this purpose. This method of image production is capable of producing very small precisely controlled image dots with very steep shoulders. The quality of the images produced by LAMS CTP technology is superior to other methods, particularly for extremely small text or fine highlight work.[50] The high cost of the equipment and plate materials needed for LAMS CTP remains its principle disadvantage and restricts the use of this technology.[48, 50]

1.4.2 Liquid photopolymer plates

This type of plate material, as its name suggests, is a yellow polymeric liquid with the consistency of honey at room temperature. [48] It is not hazardous to handle and is stable unless exposed to UV light or heat. The liquid's composition includes

propylene oligomers, polyesters polyurethanes, acrylates and photoinitiators. The substrate backing for the plate is a biaxially oriented sheet, which is coated on one side to promote bonding to liquid photopolymer.

The negative is coated with a uniform film of liquid photopolymer and at the same time the substrate is applied to the surface of the liquid. The plate is then back exposed through the substrate to produce a layer of hardened polymer to adhere to the substrate. The plate is then given relief exposure to form the image areas. The uncured photopolymer is then removed and the plate is given a post exposure dose of UV radiation to further promote photopolymerisation and photocross-linking.

Liquid photopolymer plates are most commonly used with corrugated substrates or with newspaper printing as the resolutions desired for these jobs are often lower than for other applications. The development of the capped-plate technique has however substantially improved the quality of liquid photopolymer plates. The capped-plate technique uses two layers of different photopolymer. One to form the dots and one to make up the base of the photopolymer layer. The properties of these two photopolymers can be adjusted to make the dots harder, decreasing dot gain, and to create less distortion when the plate is fixed around the cylinder. [48]

1.4.3 Rubber plates

Traditionally, rubber plates known as stereos were made from natural rubber. Nowadays, a range of rubber compounds including Buna N (nitrile) rubbers, butyl

rubbers and neoprene rubbers are used. These compounds are also modified by the addition of compounds such as carbon black, zinc oxide, barites, clay or plasticising oils, the uses of which include improving the flexibility of the rubber and acting as reinforcing fillers. [48]

Traditionally, rubber plates are manufactured by a moulding method. First an engraving is made by exposing a metal plate through a negative of the image required, and processing it in an acid bath. The metal engraved plate, termed the original, is then used to make a master mould by making an impression of it using a heat setting matrix material, held under pressure against the original and heated. This master mould is filled with rubber under pressure and heated to create a rubber plate. [51] The plate must be ground on the reverse to the desired thickness. This is an expensive and time consuming process and reproducibility between plates is not good.

Rubber as a plate material has found a new use in the creation of design rolls. [52] With a design roll, the entire cylinder functions as a printing plate. A design roll is a cylinder that has been coated with rubber. The image is then engraved onto the cylinder using a computer-guided laser. After engraving, the waste material can be rinsed away with water. The design roll is then ready for immediate use if required. The obvious advantage of design rolls is that the design can be continuous making it naturally suited for printing designs on wallpaper or gift wrap, where breaks in the pattern are undesirable. Computer guided laser engraving can also be used to produce images on rubber plates.

1.4.4 Mounting tapes

The plate is fixed to the plate cylinder by means of sticky tapes known as mounting tapes. These tapes, usually made of foam, come in a large range of thickness, hardness and tackiness. The thickness is chosen in accordance with the plate thickness to fit the undercut of the printing cylinder. The hardness is selected in accordance with both the plate and the nature of the job to be printed.

Since the early 1990's, there has been a move towards the use of thinner plates (2.84mm-0.76mm) by the industry in general, [49] although label printers have been using thin plates for many years. Thin plates have many advantages. There is less polymer to be exposed, reducing exposure and washout times; less swelling occurs therefore images are sharper. Thin plates distort less under pressure therefore the quality of the final print is higher. The combination of thin plate and a compressible mounting tape is preferable to a conventional thick plate, the compressible tape takes up the excess pressure and less distortion of the plate dots takes place.

1.4.5 The influence of the plate on print quality

The compressible nature of the flexographic printing plate leads to characteristic defects in the print quality. As pressure is applied to halftone image, the raised dot is compressed downwards and spreads sideways. The resulting dot area in contact with the substrate is therefore increased. In addition, further spreading of the dot occurs due to the ink's low viscosity. To compensate for this dot gain, the size of the dot

formed on the plate is made deliberately smaller than the required image dot. There are however practical limitations to the minimum size of the dot that can be formed on the plate. If the dots are smaller than the width of the anilox cells, dipping occurs and ink is transferred from the sides of the dot as well as the top. Small dots are also fragile and tend to bend under pressure.

The compressibility of the plate also causes problems when printing solids. If excessive pressure is applied to the plate the raised image area is squashed and a halo effect is produced around the image by ink being squeezed out from between the plate and substrate. However, if insufficient pressure is applied contact between the solid image area and the substrate is not always complete and small unprinted spots appear in the printed image.

The influence of the physical and chemical properties of the printing plate on the amount of ink transferred and the print quality has been studied by the DFTA.[53] The variables studied were surface coating and composition, shore hardness, plate thickness, depth of image relief, the use of a compressible backing tape and differing methods of printing plate production. Conclusions were reached as to the effect of varying these properties on amount of ink transferred, the quality of printed solids and the amount of deformation of printed halftone dots. Increased pressure at the plate/impression cylinder nip in combination with a soft plate was found to produce good solids. When the image contained a combination of solid and line work, a compressible mounting tape was recommended. For halftone dots, the plate surface coating and composition, shore hardness, mounting material and adhesive technology were cited as the main influences on print quality. The study recommended hard

plates for fine detail work, as they are less compressible and therefore produce dots exhibiting less dot gain. The method of plate manufacture was also found to be important when considering dot deformation, as maintaining the steepness of the sides of the raised dot at as near to 90 as possible is critical in restricting the pick up of ink to just the face of the dot. If the sides or shoulders of the dot are inked, as the plate is compressed against the substrate this ink is also transferred in addition to the ink on the dot face and the printed dot gains area.

1.5 Flexographic inks

The original Aniline printing process took its name from its first ink formulations, simple solutions of aniline dyes in methylated spirits. Just like the process name, the inks used in modern flexography have changed beyond recognition. Flexographic inks are liquid inks with surface tensions ranging between 28 and 32 mJm^{-2}. [55] There are three distinct ink classifications according to the solvent system on which they are based: solvent-based, water-based and UV curable. The choice of solvent system is governed by a number of factors including the choice of plate (different plate materials have different solvent sensitivities) and roll sensitivities, resin and colorant choice, adhesion to the substrate and of a suitable toxicity level to be appropriate for the end use of the printed article.

1.5.1 Solvent-based inks

Solvent-based inks are the traditional type of flexographic ink. They are still popular despite increased pressure from environmentalists to cut the use of VOC's (Volatile Organic Compounds), as they usually have good technical properties. For example high gloss, low viscosity, good resolubility, high speed of drying, good flexibility and good adhesion properties. A typical solvent-based ink contains a binder system, a solvent system, a pigment or blend of pigments and a selection of additives. [56]

Commonly used solvents are alcohols, esters, glycols and ketones, some examples of which are ethanol, isopropanol, methoxy/ethoxy propanol, ethane-1,2-diol and ethyl ethanoate. [54] It is usual for the solvent system to contain a blend of a number of different solvents. The more aggressive solvents historically used in gravure, for example toluene and xylene, cannot be used as they attack the rubber fountain roll (if applicable) and the printing plates. [57] Controlling the evaporation of the solvents during printing is critical in maintaining constant ink properties. The viscosity of solvent-based inks must be closely monitored and additional solvent added in accordance with the ink manufacturers instructions, to maintain the recommended viscosity and solvent composition.

The most common resin used in solvent-based ink formulations is nitrocellulose. [54] It is cheap, readily available, has a very low odour, is resistant to heat and exhibits good solvent release and pigment wetting properties. It is compatible with a wide range of substrates and is often used combined with other resins and plasticisers. Nitrocellulose is sensitive to water contamination, which may lead to blushing of the

print during drying. Other resins used are shellac, ethyl cellulose, CAP (cellulose acetate propionate), polyamide, polyurethane, ketone resins and a number of acrylates and methacrylates. In solvent-based inks, the binder is dissolved in the solvent. This solution becomes the carrier for the pigment, which is not dissolved, but is dispersed by the resin. [56] The choice of binders and solvent determine the drying rate of the ink. The ink dries by evaporation of the solvent when the binder is thrown out of solution and adheres to the substrate holding the pigment and additives contained within it at the substrate surface. In the case of some plastics, the solvent also slightly dissolves the surface of the substrate, which enhances adhesion of the ink. [56]

1.5.2 Water-based inks

To cut back on the use of volatile organic compounds or VOC's, inks have been formulated with water as the primary solvent. The use of water in an ink however presents a number of problems. The choice of resins and pigments available to the formulator is restricted as few resins are miscible with water and water exhibits poor pigment wetting. The high surface tension of water, (72.8 mNm^{-1}) compared with (22.0 mNm^{-1}) for ethanol, results in slower absorption into absorbent substrates and poor wetting of non-absorbent substrates. Therefore, surfactants must be added to the ink to reduce the surface tension.

Water-based inks also contain a small amount of solvent, usually an alcohol. The addition of solvent is useful as it acts as an antifoam and a levelling agent, however

its main purpose is to speed up the drying rate of the ink. The ink must not have a solvent content above 5% in order to be classed as water-based. [58] Getting the ink to dry at a suitable rate can be difficult. Fast drying on the substrate is very desirable; however, if the ink dries too quickly it will plug the anilox or dry on the plate. There are problems associated with water-based inks, as the solvent has no recovery value so there is no incentive to process the waste ink and dumping is becoming increasingly expensive. Water-based inks have a tendency to foam on the press and the addition of an antifoaming agent is essential. There is also a less obvious problem with the production of micro-foams, tiny bubbles that are often invisible in the ink. [58] Micro-foams can be difficult to remove, and manifest as an increase in viscosity coupled with a decrease in print density.

The resins used in water-based systems are commonly carboxylated acrylics, which, whilst insoluble in water, are dissolved by the addition of alkali (ammonia or an amine). Acrylic resins are often supplied as resin-in-water emulsions that form solutions when alkali is added to produce the correct pH. The pigment is combined with the resin in one of three ways; as a dry powder with the use of milling action to form the dispersion, as a paste with mixing or as a press cake, which is combined with the resin by milling or power mixing. Pigments for use in water-based ink formulations must be stable to alkali. Acrylic copolymer emulsions can be pigmented without alkali giving ink with improved drying time and harder, more water resistant ink films, but this formulation is less stable on the press. Inks that are a mixture of dissolved resin and emulsion have been developed in an attempt to achieve the most desirable properties of the two systems. The ratio of the two systems can be adjusted dependent on the properties desired. [58]

Water-based inks have the most problems when used for printing onto filmic substrates, and foils. These substrates typically have low surface energies (discussed further in Section 1.6 and Chapter 2) and for adequate wetting of the substrate to take place the surface tension of the ink should be no higher than the surface energy of the film. [58] Even with the addition of surfactants and organic solvents the surface tensions of water-based inks are higher than those of solvent-based inks. [55] The substrates can be treated to increase their surface energy and promote wetting and adhesion, (as discussed further in section 1.6.3) as indeed they are for use with solvent-based inks. This can however result in poor water resistance of the printed ink film.

New resin systems are being developed in an attempt to overcome some of the problems experienced when printing on film and foils. [58] Alkyd-acrylic hybrids, cross-linking acrylics, epoxy acrylics and urethane acrylic hybrids are all being investigated in an attempt to produce a water-based ink with better adhesion to filmic substrates, improved hardness and water resistance. The cross-linking inks claim to outperform solvent inks once cured. The disadvantage of cross-linking inks is that they are usually two pack systems, that is, they consist of two separate components which must be stored apart and only mixed just prior to printing. New systems have been developed where curing does not take place until all the water has evaporated from the ink, leading to a press stable ink with excellent dry performance properties. [58]

1.5.3 Energy curable inks

Energy curable inks are totally different from the other classes of ink in that they are set by a chemical reaction rather than drying by solvent evaporation. As they contain no volatile components they are sometimes referred to as 100% solid inks. There are two mechanisms by which the curing can be initiated, by UV radiation in combination with photoinitiator species in the inks or by the use of an electron beam. The use of UV curable flexo inks is widespread, however electron beam curable or EB inks are relatively uncommon as the electron beam units are much more expensive than UV lamps. New systems which allow the EB inks to be printed wet on wet with a single electron beam unit at the end of the print stations may increase the popularity of EB curable inks.[59]

UV curable inks can cure by two mechanisms; free radical and cationic curing; both mechanisms are initiated by UV radiation however the photoinitiator species and reaction chemistry are very different.

Free radical curing is initiated by UV radiation splitting of photoinitiators present in the ink system to produce free radicals. There are two classes of photoinitiator, type I or cleavage and type II or abstraction initiators. [60] The cleavage initiators form radicals by cleaving in two without the need for interaction with other species. Cleavage initiators are responsible for curing the bulk of the film. A common example of a cleavage initiator is Irgacure 369, which is an aminoacetophenone. The abstraction photoinitiators, the most common of which is benzophenone, work in conjunction with a synergist, which is usually a tertiary amine, from which a

hydrogen atom is abstracted to initiate the reaction. This type of initiation is mainly responsible for curing the surface of the ink film. The abstraction initiator becomes excited by UV photons but only remains in its excited state for a short period of time. There is a danger that it will interact with atmospheric oxygen in this time. This is termed oxygen inhibition. The amine synergist helps to minimise oxygen inhibition by preferentially reacting with the excited photoinitiator. For this to be effective, the synergist needs to be present at relatively high levels, (at above 5%.) [60]

A typical free radical ink formulation contains pigment, two or more photoinitiators, additives and a mixture of acrylate oligomers and monomers, which are cured to solidify the ink film. Examples of these oligomers are epoxy acrylate, polyester acrylate and polyurethane acrylate. [61] These oligomers undergo free radical polymerisation to form a solid film. As with every free radical reaction, the radicals produced by the photoinitiator could recombine and terminate the reaction instead of reacting with the acrylates to propagate the reaction. Therefore, the UV radiation must be supplied until the film is fully cured. This is usually a very quick process, however even in a film that appears fully cured there are always small amounts of unreacted monomers and oligomers. The uncured material can be skin irritants and usually have a slight smell. The smaller components of the inks, i.e., monomers, photoinitiators and some additives such as silicones are well known for their potential to migrate through the cured ink films. [60] This makes the use of free radical UV inks less popular for some applications, for example food packaging.

As the free radical reaction involves the cross-linking of small molecules into a polymer film, the size of the film shrinks on curing. This can be a problem when

trying to achieve adhesion to filmic substrates as there is very little roughness to produce a mechanical key and ink can pull away from the film surface on curing. Typical values for the shrinkage of a free radical ink film are between 8% and 20%. [61] The amount of shrinkage can be controlled by the functionality of the monomers and oligomers used. The more reactive sites on the molecules, the higher the amount of shrinkage, using lower reactivity monomers and oligomers generally slows down the cure rate of the ink and reduces the cross link density of the cured film. The addition of a resin that does not have any acrylate functionality is another way that shrinkage is controlled.

In cationic curing, the reaction proceeds via a carbocation R_3C^+. This species goes on to promote ring-opening reactions with epoxides and oxetanes and attacks electron rich sites such as the double bonds of vinyl and propenyl ethers. [60] Once generated, the cation catalyses the reaction to completion leaving no uncured polymer. The curing reaction is slower than that of the free radical mechanism and can lead to problems if the film is not given sufficient time to cure between print stations. The curing reaction is not affected by atmospheric oxygen but is sensitive to water in any form and a humid environment can prevent the reaction curing to completion. [61] The cation is an acidic ion and as such will react with any pigments with basic functionality. The choice of pigment that can be used is greatly restricted. The cured ink film is non-toxic and without odour, making it extremely suitable for printing food packaging. As epoxide and oxetanes curing are ring opening reactions the shrinkage of a cationic ink film is much less than that of a free radical ink. Typical values for shrinkage are less than 5%. [61] Cationic UV inks are much more expensive than free radical UV inks, therefore cationic UV tends to be used where free radical

inks are not suitable.

UV inks have many advantages over traditional inks. Because UV exposure is required for curing, they will not dry on the press and therefore have a much longer press life, there is no solvent evaporation to worry about so the viscosity remains constant. UV inks can exhibit good adhesion to filmic materials and the prints display brighter colours and sharper images as they are cured immediately and do not get a chance to diffuse into the substrate. They are however more expensive than solvent or water-based inks. UV inks have taken over from water-based inks to dominate the narrow web section of the flexographic printing market, accounting for an 85% share in 2003 .[61] The cost of the larger curing systems limits the use of UV inks in medium and wide web presses.

UV inks require a UV radiation source to initiate the curing reaction. Medium pressure mercury lamps are commonly used, [60, 62, 63] and photoinitiators are selected that respond to the wavelengths peaks generated by this type of lamp. Different colours absorb different parts of the UV spectrum. Black pigments in particular present problems as they absorb UV radiation at the same wavelengths as some of the photoinitiators. Care must be taken to select a photoinitiator/oligomers combination that will cure adequately. The ability of a pigment to absorb UV radiation has a detrimental effect on the cure rate of the ink. Short wavelength UV radiation below 280nm is responsible for surface cure of the ink film with the depth of cure coming from UV radiation with a wavelength of around 365nm. [62] The shorter wavelengths of UV radiation are most susceptible to absorption by dirt on the

lamp or reflectors. As this dirt can be invisible to the eye the problem is first noticed as a loss of surface cure. The use of a spectroradiometer is recommended to measure lamp performance to avoid this and other problems. Production of ozone is a problem associated with UV curing systems. This takes place due to the interaction of the UV radiation of wavelengths below 230nm, with atmospheric oxygen. This is particularly a problem whilst lamps are warming up to operating conditions. Ozone extraction units are fitted to presses to combat this problem but when the presence of ozone is particularly undesirable, ozone-free lamps, which are lamps that cut off the emission of UV radiation with wavelengths below 230nm, can be used. [63] The use of ozone-free lamps however, has a detrimental effect on the cure time of the ink.

Radiation curing of flexographic inks can also take place by electron beam (EB) curing. [60, 63] With this method a photoinitiator within the ink is not required as the electron beam generated by the curing unit induces the reaction by ionising the molecules and generating radical cations. These species can then fall apart to produce the radicals that initiate the radical polymerisation. The curing of EB inks is not effected by the pigment choice therefore the formulation of EB curable inks allows for much more flexibility. EB curing is inhibited by oxygen for the same reasons as the free radical UV inks but in this case synergists cannot be used to reduce the problem. Therefore the printed ink film has to be covered by a blanket of nitrogen at the curing point to eliminate oxygen from the substrate surface. As press speeds increase maintaining this nitrogen blanket becomes more problematic.

1.6 Substrates

The flexo process is by its very nature versatile in terms of the number of substrates it can be used to print onto. As the printing plate is flexible it is forgiving towards rougher, lower quality substrates as the plate distorts to cover small surface irregularities, making the process suitable for printing onto lower grade papers and newspapers. Flexo is also highly suited to printing on filmic substrates, and over a thousand grades of filmic substrates are currently available to the flexo printer. [64]

Whilst there is much debate over the importance of the surface energy of the anilox or plate when considering ink transfer characteristics, (discussed further in Section 1.7) [55, 65, 67, 68] it is widely accepted that the surface energy of the substrate is very important. Surface energy is a physical property of a surface and is analogous to the surface tension of a liquid. Surface energy is measured in millijoules per metre squared (mJm^{-2}), units which are numerically equivalent to dynes per centimetre, the cgs unit predominantly used in printing industry literature.

The lower the surface energy of a surface the harder it is to wet. To spontaneously wet a surface, the wetting liquid must have a surface tension lower than the surface energy of that surface. The surface energy of the substrate therefore needs to be higher than surface tension of ink for efficient transfer to take place. [55, 68] Average values for the surface tension of flexo inks are quoted as 28-29 mNm^{-1} for solvent based systems and 30-32 mNm^{-1} for water based inks, [55] however it can vary considerably with formulation. Measuring the surface tension of an ink does not fall

within the ink manufacturers formulation or quality control checks. [69] Table 1.2 shows the critical surface energies of a number of common substrates.

Material	Critical Surface Energy (mJm^{-2})
Polytetrafluoroethylene	18.5
Polychlorotrifluoroethylene	31
Polyethylene	31
Polypropylene	31
Polystyrene	33-35
Poly(vinyl chloride) (rigid)	39
Poly(vinyl chloride) (flexible)	33-38
Poly(vinyl fluoride)	28
Poly(vinylidene chloride)	40
Poly(vinylidene fluoride)	25
Polyacrylamide	35-40
Polyacrylate (acrylic film)	35
Poly(methyl methacrylate)	33-44
Poly(ethylene terephthalate) (polyester film)	43
Poly(6-aminocoproic acid)	42
Poly(11-aminoundecarioc acid)	33
Poly(hexamethylene adipamide)	46
80:20 Poly (tetrafluoroethylene-*co*-chlorotrifluoroethylene)	20
60:40 Poly (tetrafluoroethylene-*co*-chlorotrifluoroethylene)	24
50:50 Poly (tetrafluoroethylene-*co*-ethylene)	26-27
94:6 Poly (tetrafluoroethylene-*co*-hexafluoropoprylene)	19
92:8 Poly (tetrafluoroethylene-*co*-hexafluoropoprylene)	18.3
86:14 Poly (tetrafluoroethylene-*co*-hexafluoropoprylene)	18.2
84:16 Poly (tetrafluoroethylene-*co*-hexafluoropoprylene)	18
77:23 Poly (tetrafluoroethylene-*co*-hexafluoropoprylene)	17.8
Cellulose (regenerated)	44
Poly(dimethyl siloxane)	24
Copper (dry)	44
Aluminium	45
Iron (dry)	46
Glass, soda lime (dry)	47
Silica (fused)	78
Titanium dioxide (anatase)	91
Ferric oxide	107
Tin oxide	111

Table 1.2. Surface energies of some common substrates in mJm^{-2}. [64]

As can be seen from Table 1.2, some of the substrates used in flexographic printing have surface energies lower than the inks used to print onto them. In order for wetting and adhesion of the inks to take place on these substrates it is necessary to raise the surface energy of the substrate. This can be done by a method known as corona treatment. This process makes use of corona discharge, discharge without an electrical arc, generated between electrically insulated electrodes with a high voltage passing between them. [70] This discharge ionises the surface of the substrate, raising its surface energy and making it more receptive to the ink. This effect can be extremely short-lived, dependent on the substrate treated. Therefore the corona treatment is often carried out in-line just before the ink station. Corona treatment can adversely affect the water resistance of the print, as the ionised surface is very hydrophilic. If the ionised surface is more receptive to water than the ink, water can preferentially displace the ink at the interface.

The surface energy of paper, although dependent on the type of paper and coating, is usually higher than the surface tension of standard flexo inks. Therefore modification of the surface energy is not necessary to produce wetting and ink adhesion. The surface energy of paper was however manipulated in a study to determine its influence on ink transfer. [68] The findings were that the influences of surface chemical factors on solids printed with water-based inks were small, and that the effect on a printed halftone was more significant. However the study found that press speed, surface roughness and printing pressure played a greater role in the printing properties. The study highlighted the range of chemical properties already present in different grades of paper.

1.7 Ink transfer and the significance of surface energy

Over the last ten years several attempts have been made to study the flexographic printing process and quantify the variables that affect ink transfer and print quality. Central to many of these studies is the validity of a theory that was first put forward by Frank Dick at the Flexographic Technical Association annual forum in 1978. He theorized that in a nip formed by rolls of two different materials, the higher volume of ink would follow the roll with the higher surface energy. [65] Therefore, for maximum ink transfer through the anilox/plate nip and the plate/substrate nip the surface energy of the anilox should be low, and the surface energy of the plate should be higher than that of the anilox but lower than the surface energy of the substrate. If a fountain roll is used to ink the anilox, its surface energy should be lower than that of the anilox. To allow the ink to wet each component its surface tension should be lower than the lowest surface energy of the components (i.e. the anilox or fountain roll)

Examples have been given of surface energy sequences for the ink, fountain roll, anilox, photopolymer plate and substrate with chrome and ceramic anilox. [55] It is suggested that the surface energy of ceramic anilox fall into the range of 39 - 42 mJm^{-2}, higher than the surface energy of chrome anilox, quoted at 34 mJm^{-2} and higher than the surface energy quoted as a typical value for a photopolymer plate of 37 mJm^{-2}. The high surface energy of ceramic anilox is claimed to cause inconsistent inking of the plate.

Quinn [65] quoted typical surface energy values for photopolymer plates as between 30 - 45 mJm^{-2} and varied the surface energy of his test plates from 18 mJm^{-2} to 58 mJm^{-2}. He found that the surface energy of the plate did not affect the amount of ink transferred, but his study, on a proofing machine, differed from actual printing situations in a number of ways. Firstly he separated the ink transfer stages considering firstly the anilox/plate nip and then in a separate experiment, the plate/substrate nip. The plate was not attached to a cylinder but mounted on a flat sled that passed sequentially through the two nips. The plate was therefore inked only once before the measurements were made. Significantly the anilox used was made from steel and therefore had a much higher surface energy than either chrome or ceramic anilox. The type of steel is not specified but in order to resist corrosion from the inks it is likely to have been stainless steel, which can have surface energies in the range of 700 to 1000 mJm^{-2}. The changes in the surface energy of the printing plates from 18 to 58 mJm^{-2} would therefore have little significance in relation to the overall surface energy difference between the steel anilox and the plate. The study only measured the affect of changing the surface energy of the plate on the amount of ink transferred at each nip. No assessment of the impact of changing surface energy on print quality or dot gain was attempted.

The study did however measure the ink transferred from a plate of lower surface energy than the substrate onto which it was printing. The plate was then treated to raise its surface energy leaving other variables such as hardness and roughness unchanged. No difference in the percentage of the ink transferred to the substrate was observed when the surface energy of the plate was raised above that of the substrate. The constant percentage transfer of 50% was also unaffected by printing speed and

pressure, variables that were found to be significant by the DFTA [53] where experiments took place using flexographic printing presses.

Another paper was published by the same research group, using the same flexo simulator.[66] In this investigation the anilox were ceramic coated and laser engraved with a carbon dioxide laser. The effect of cell count and engraving pattern were studied. The plate surface energy was varied from 18 mJm^{-2} to 34 mJm^{-2} and was found not to effect ink transfer or print quality. The surface energy of the ceramic anilox was not investigated, however it was likely to exceed the surface energy of the plate in all cases.

Lindholm carried out another study that looked at the effect of surface energy on ink transfer. [67] This work was done on a flexographic printing press, and used two anilox. One with a line count of 200 lines per centimetre and a cell volume of 9.09 cubic centimetres per square metre, and a banded anilox with a line count of 80 lines per centimetre with volumes of 8, 10 and 12 cubic centimetres per square metre. The paper does not make clear what material the anilox was made from nor how it was engraved. The printing was done as a continuous process, i.e. the plate was constantly re-inked and printed from. The amount of ink transferred from the anilox to the plate was assumed to be the same as the amount transferred from the plate to the substrate, the reasoning for this being that ink does not either build up or decrease on the plate. However, Quinn et al [65] found that by examining the two nips separately different percentages of ink were transferred in each case, 40% from the anilox to the plate and 50% from the plate to the substrate.

The six plates used in the study all picked up different amounts of ink from the anilox. This led Lindholm to conclude that the plate is responsible for the amount of ink transferred from the anilox. However if this were true the printer would only need one anilox and could vary the amount of ink required for different jobs by changing the plate. This is clearly not the case and the effects of varying the anilox volume in this study are not presented. Lindholm also varied the surface energy of the printing plates and saw no correlation between surface energy and volume of ink transferred. The other variables included in this study were the inks used and the speed of the press. Lindholm found that the choice of ink affected ink transfer. However the property of the ink studied, viscosity, as measured by the time the ink takes to flow through a Zahn cup, did not provide enough information to explain the influence of the ink on the percentage transfer. Lindholm observed that press speed had no affect on solid densities in full tone areas.

The specific case of UV ink transfer has been studied by the NPIRI [71] in 1996 and Fouché and Blayo [72] in 2001. The NPIRI looked at a range of UV inks of constant pigment concentration, the viscosities of which were varied by the monomer/oligomer content. They unsurprisingly found that very thick inks produced poor solid print densities, but the relationship they found between viscosity and print density was not always linear. In the case of the finest anilox line count (700 lines per inch or 27.5 lines per mm) there was a maximum print density at 2951 centipoise, the midrange in this study. The study looked at a range of anilox volumes at each line screen and concluded that the depth to opening ratio was significant. Rather than an optimum ratio the results suggest that there is a maximum depth after which no increase in print density is seen. The range of depth to opening combinations used

was from 18% to 48%, which is slightly larger than the recommended range of 23%-33%. [23] The line count and cell dimensions of the anilox used are specified but, the method of engraving, the engraving angle and the material that the anilox is made from are not specified. The study concluded that solid print density increased with decreasing ink viscosity, with decreased anilox line count and increased cell volume. The effect of ink viscosity on dot gain was also studied. In general dot gain was seen to decrease with decreased ink viscosity but the results were variable between anilox rolls, the highest line count anilox produced no change in dot gain when the ink viscosity was varied.

Fouché and Blayo looked at the printing of solids with free radical UV inks and used the Walker-Fetsko equation along with the extended splitting term proposed by Zang to model the transfer of ink from the plate to the substrate. The Walker Fetsko equation in the form used by Fouché and Blayo is shown as Equation 1.1.[72]

$$y = (1-e^{(-kx)})*\{b(1-e^{(-x/b)})(1-f)+fx\} \qquad (1.1)$$

where:

y = The amount of ink transferred to the paper. (g/m^2)

x = The amount of ink available on the plate. (g/m^2)

k = The paper smoothness parameter.(this depends on the roughness of the paper and the ability of the ink to cover the paper surface) (m^2/g)

b = The immobilization parameter (the fraction of ink immobilized within the paper mass.) (g/m^2)

f = The splitting coefficient. (A dimensionless constant, which represents the fraction of free ink transferred to the paper.)

The amount of ink on the plate and the amount transferred to the paper were measured by weighing the printing carriage before and after printing. As the paper properties and printing conditions were constant the smoothness parameter k was fixed for this study.

The study uses the Zang modification of the splitting coefficient to model a dependency of the splitting coefficient on the amount of ink available on the plate. This is shown as Equation 1.2.[72]

$$F = f_\infty + (f_0 - f_\infty) * e^{(-cf_\infty x)} \qquad (1.2)$$

Where:

F = Zang's splitting coefficient

f_∞ = the splitting coefficient at high ink amounts

c = a constant (Zang fixed this at 2, however Fouché and Blayo have varied it.)

f_0 = the splitting coefficient of the free-ink film when the amount of in on the plate tends to 0. (if the two rolls at the nip are turning at similar speeds this can be assumed equal to 0.5, i.e. a 50/50 split.)

The substrate used was paperboard. A range of UV inks with differing viscosities and surface tensions was used. They measured the surface energy of the plate, substrate, and the cured ink film. The surface energy difference at the plate paper nip was not varied and there was an increase in surface energy from the plate to the paper. The effects of ink film thickness on the final properties of the print were recorded. The Walker-Fetsko equation with the Zang modification was found to give good correlation to the ink transfer from the plate to the paper. The ink transfer from the anilox to the plate was not investigated. The prints were made on two laboratory-proofing machines, only one of which was fitted with an anilox roll, the other being inked directly from a rubber roll. The anilox rolls used were ceramic and ranged from 87 to 187 lines per centimetre. No details of engraving were given but for this range of large cells the method was most likely to have been by a CO_2 laser.

The other conclusions from this work were that two trends could be seen depending on inking levels. At high ink levels no significant change was seen in print density or gloss with changing press speed. At low ink levels print speed was observed to affect these properties. The study cited viscoelastic properties of the ink as the reason for this and highlighted the need for further work.

The studies into the affect of surface energy on ink transfer have concentrated on the plate as the main variable. The anilox has been varied to hold and in theory dispense a greater volume of ink but the surface energy of the anilox has not been varied or measured to determine the difference between the surface energies of the anilox and plate. This is probably due to the complex issues involved in making surface energy measurements on an anilox roll. As will be discussed in Chapter 2 surface energy

measurements are relatively easy to make on flat smooth samples. However, making surface energy measurements on highly textured cylindrical surfaces such as an anilox presents a challenge. If a greater understanding into the wetting and release properties of the anilox and its roll in the amount of ink transferred is to be achieved surface studies of the anilox roll are essential.

The ink transfer studies made by Quinn, Lavelle, Lindholm and the NPIRI took place before laser engraving of anilox by YAG laser became commonplace. There was in effect only one way of engraving a ceramic anilox and its properties were fixed by the depth to opening constraints of the CO_2 laser engraving process. The introduction of the YAG laser to anilox engraving has introduced new variables for the anilox in terms of increased cell depths and differing cell shapes, some information has been published on the effect of the YAG engravings on ink release but most of the information originates from the anilox or laser manufacturers. The effect of the YAG laser engraving process on the surface properties of the anilox is unknown.

The aim of the study by the author is to characterise the wetting and transfer properties of the anilox roll. This will be done by making detailed surface chemical measurements (as discussed in Chapter 2) and by measuring the ink transfer from the anilox, both on a wide web flexo press and on a lab scale press. Banded aniloxes engraved with both CO_2 and YAG bands will be studied. The effect of the type of laser used to make the engraving on the surface chemistry of the roll will be investigated along with the ink release properties.

2. Surface chemistry

As discussed in Section 1.7, the behaviour of ink in contact with an anilox, printing plate or a substrate is influenced by the physical and chemical properties of the ink and the surface with which it is in contact. In order to understand, model or predict the movement of the ink to and from the component surfaces of a flexo press, it is necessary to understand the surface interactions at a solid/liquid/vapour interface. In particular, issues that are relevant to the wetting and dewetting of the anilox roll will be reviewed.

2.1 The contact angle

Information about a surface can be obtained by observing the contact angle made by a drop of pure liquid at rest on the sample surface, or in reverse, information about a liquid can be deduced from observing the contact angle made on a solid of known properties. A contact angle is defined as "the angle between the tangent to the liquid-vapour interface and the tangent to the solid interface." [73] Two examples of contact angles are shown in Figure 2.1. When a contact angle is less than 90°, it is said to be wetting the surface. When the contact angle is greater than 90°, it is described as non-wetting.

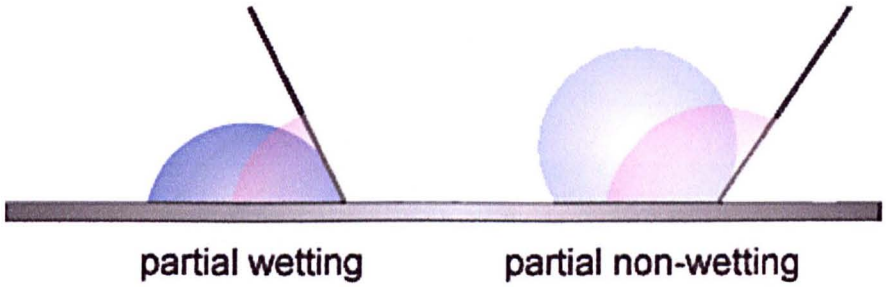

Figure 2.1. An illustration of wetting and non-wetting contact angles.

Contact angles may be static, where a known volume is applied to the surface and observed at rest, or dynamic, where liquid is first added and then removed from the drop causing the contact line to advance across the sample surface and then to recede back again. As a contact angle is advanced, the angle reaches a maximum. This angle is termed the advancing contact angle θ_a. Similarly, as a contact angle recedes, a minimum contact angle is reached which is termed a receding contact angle θ_r. The diagram showing advancing and receding contact angles is shown in Figure 2.2.

For an ideal material, the curves produced by recording advancing and receding contact angle data would overlap. However, in practice this rarely happens. Advancing contact angles are usually larger than receding angles and a hysteresis loop is usually observed. Static, advancing and receding contact angles made by a particular liquid on a specific solid surface will have different values; the advancing angle is normally larger than the static angle which in turn is larger than the receding angle. Therefore, it is important to make it clear when quoting contact angle values which type of contact angle has been measured.

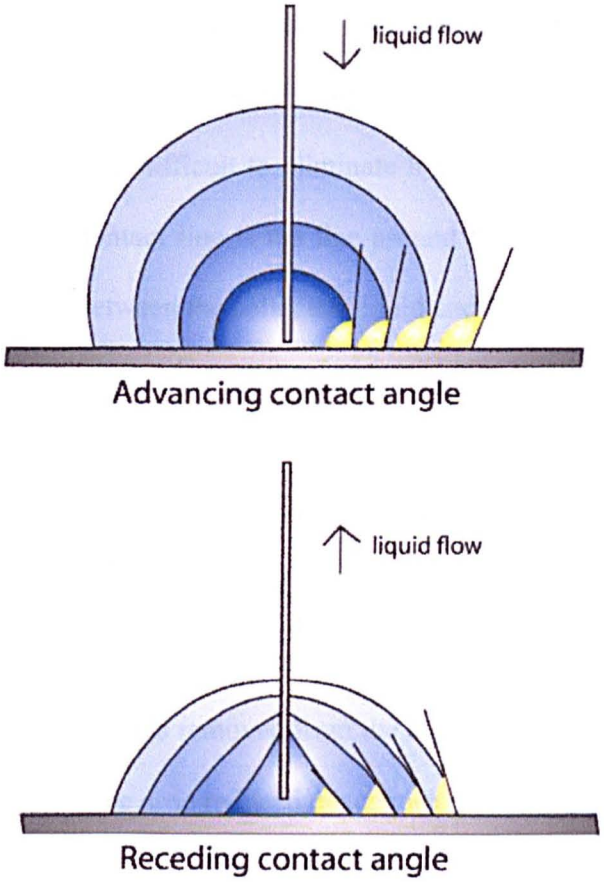

Figure 2.2. An illustration of advancing and receding contact angles.

Hysteresis can be defined as the difference between the advancing and receding angles, i.e. $\Delta\theta = \theta_a - \theta_r$.[74] As the advancing angle is normally larger than the receding angle, hysteresis is usually positive. Exceptions to this can occur in cases when the liquid interacts with the surface and is able to change the properties of the surface.[76] For example, a small amount of Ca^{++} ions present in water will affect the pH and polarity of negatively charged phospholipid surfaces. This significantly increases the hydrophobicity of the surface and therefore increases the receding contact angle, making the receding angle larger than the advancing angle

Contact angle hysteresis due to chemical interactions between the wetting liquid and the surface can be eliminated by careful selection of the wetting liquid. However, it is much more difficult to eliminate hysteresis caused by the sticking of the contact line. The contact line is the line around the edge of the liquid drop that marks the boundary between the solid, the liquid and the surrounding vapour or gas (also called the triple line). The contact line moves across the surface as the drop spreads. Irregularities in the surface such as surface heterogeneity and roughness require more energy to move the contact line across and as more liquid is added, cause its progress to slow or stick. If the contact line does not move, the expansion of the drop increases or advances the contact angle as shown in Figure 2.3. The reverse is true when the liquid is removed from the surface, as the contact line sticks the removal of liquid from the drop reduced the contact angle and a receding angle is observed.

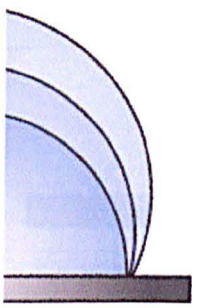

Figure 2.3. The sticking of the contact line causes the contact angle to change as the volume of the drop increases.

At a microscopic scale, the curvature of the liquid surface close to the contact line can deviate from that of the bulk drop. This can be due to molecular interactions such as van der Waals forces or polar interactions, or due to irregularities or deformations at the solid surface. [76]

2.1.1 Young's equation

Attempts to describe the interaction between a solid phase, a liquid phase and a vapour phase at an interface began as early as the 19th century. Thomas Young proposed an equation to relate the interfacial tensions at a solid/liquid/vapour interface to the contact angle made by a drop of the liquid in equilibrium with a flat, smooth, homogeneous solid surface.[77, 78]

A diagram of the triple phase system that is related to the contact angle by Young's equation is shown in Figure 2.4. and Equation Young postulated that for a flat, smooth and chemically homogeneous surface the bulk interfacial tensions of the interfaces could be related to the contact angle without any knowledge of the complex interactions taking place in the core region around the contact line.

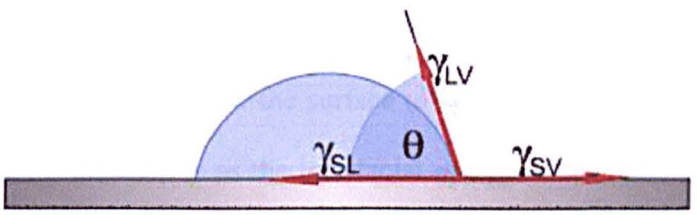

Figure 2.4. A diagram of a liquid drop with a contact angle θ and interfacial tensions γ_{SL} γ_{SV} and γ_{LV}.

Young's equation $$\gamma_{LV} \cos\theta = \gamma_{SV} - \gamma_{SL} \quad (2.1)$$

γ_{SL} is the interfacial tension at the solid/liquid interface, γ_{LV} is the interfacial tension at the liquid/vapour interface, and γ_{SV} is the interfacial tension at the solid/vapour interface. θ is the equilibrium contact angle between the liquid and solid. At the

contact line, the force due to the interfacial tension γ_{SV} is opposed by γ_{SL} and the component of γ_{LV} acting along the interface, which is $\gamma_{SL}\cos\theta$. As the contact line is in equilibrium, the net sum of the forces is zero or $\gamma_{SV} - \gamma_{SL} - \gamma_{LV}\cos\theta = 0$. This is a simple rearrangement of the more familiar form of Young's equation shown in 2.1.

The terms γ_{LV}, the interfacial tension at the solid/liquid interface, is the surface tension of the liquid in equilibrium with its saturated vapour. It is normally equal to γ_L the surface tension of the liquid. These terms are sometimes replaced by the term G^s_L, the surface free energy of the liquid. The latter term, although conceptually different to the surface tension is numerically equal. [79]

The terms γ_{SV} relates to the interfacial tension of the solid/vapour interface. It is however not the same as γ_S, the surface tension of the solid, as the freezing process does not usually allow the surface to be in equilibrium with the vapour. A way to express the term is as the interfacial energy of the solid surface in equilibrium with the vapour of the contact angle liquid, or G^s_{sv}. The term G^s_{sv} can be separated into G^s_S, the surface energy of the solid in the absence of vapour and Π, the spreading pressure of the adsorbed vapour. This spreading pressure is however generally negligible on low energy surfaces, (generally accepted to be surfaces with surface energy values of less than 100 mJm^{-2} [76]) and the term G^s_{sv} and G^s_s become equivalent. [79]

Young's equation can be expressed using these terms as

$$G^s_S = G^s_{LV} + G^s_L \cos\theta \qquad (2.2)$$

The Young equation assumes that the triple phase system is in thermodynamic equilibrium and that the solid surface is smooth, homogeneous, isotropic and non deformable. Its application therefore to real surfaces is still a cause of controversy and whilst the equation is very useful its limitations always have to be considered. [78]

One consequence of these assumptions is that the equilibrium contact angle that is related to the interfacial tensions by the Young equation is not necessarily the contact angle that is observable with standard optical techniques. The observable contact angle, which is also termed the phenomenological or macroscopic contact angle, θ_m, [78] is dependent not only on the combination of interfacial tensions at the triple phase point, but also on the physical and chemical features of the solid, i.e. roughness and chemical heterogeneity. It is θ_m rather than θ_e that gives information about properties of the solid surface such as wettability adhesion and spreading parameters.

The equilibrium contact angle θ_e, which is unique to the combinations of interfacial tensions at the triple phase line for a smooth, homogeneous surface has already been introduced. There is, however, another type of equilibrium contact angle, θ_{ES} which is the contact angle at which the system is in such a state that its free energy is minimised, irrespective of whether the system is rough or smooth, chemically homogeneous or heterogeneous. The Wenzel contact angle θ_W (Section 2.1.2) and the Cassie contact angle θ_C (Section 2.1.3) are both examples of system equilibrium contact angles. [78]

2.1.2 The Wenzel equation

In 1936, Wenzel put forward an equation to relate the macroscopic contact angle θ_m to the equilibrium contact angle θ_{ES} for a rough surface.[80, 81] His argument was essentially that if the surface of the solid is rough the liquid drop coming into contact with it will interact with a much larger area of the solid for a given drop diameter than with a smooth surface. Wenzel introduced a roughness factor r, where r is equal to the actual surface area divided by the geometric surface area. The value of r is therefore always greater than 1. He proposed the following relationship between θ_m and θ_w the Wenzel contact angle, which is the equilibrium angle θ_{ES} for a rough but homogeneous solid. The Wenzel equation was given a more rigorous mathematical derivation by Shuttleworth and Bailey in 1948 [82] and again by Good in 1952. [83]

The Wenzel equation $\cos \theta_m = r \cos\theta_w$ (2.3)

The Wenzel equation predicts that if a droplet in contact with a smooth surface has a contact angle of less than 90° roughening the surface will lower the observed macroscopic contact angle θ_m. If however a droplet in contact with a smooth surface has a contact angle of more than 90°, roughening the surface will raise the observed macroscopic contact angle θ_m.

The big problem with the Wenzel equation is that it is only seen to agree with experimental findings on very artificial roughness models. It has been shown that the Wenzel equation gives the correct results on saw tooth surfaces when the drop size is infinitely large in relation to the roughness. [84] As well as the case of a droplet

spreading radially on radial grooves with some geometric restrictions. [85] The common feature of these models is that the contact line can move reversibly, theoretically eliminating hysteresis.

2.1.3 The Cassie and Baxter equation

Cassie and Baxter considered the system of a heterogeneous solid surface made up of domains with different surface tensions. [86, 87, 88] An example of such a surface could be a polycrystalline material whose surface exposes a number of crystal planes, or a surface on which patches of a monomolecular film have been adsorbed. [78] Cassie and Baxter proposed that the contact angle on such a surface would be related to the equilibrium contact angles of each domain in proportion to their makeup of the overall surface. The Cassie and Baxter equation for two domains is shown below. The equation is not however restricted to two domains and additional terms could be added to incorporate more complex systems.

The Cassie and Baxter equation $$\cos\theta_C = a_1\cos\theta_{e1} + a_2\cos\theta_{e2} \qquad (2.4)$$

Where θ_C is the Cassie contact angle, θ_{e1} and θ_{e2} are the equilibrium contact angles for domains 1 and 2 and a_1 and a_2 are the fractional surface areas of the two domains such that $a_1+a_2 = 1$.

The Cassie contact angle is an equilibrium contact angle θ_{ES} for a heterogeneous but smooth system. As with the Wenzel equation, there are problems applying the Cassie

and Baxter equation experimentally to real surfaces, however this has been attributed to the existence of a large number of metastable contact angles on composite surfaces [78] and the Cassie and Baxter equation has been reported to agree with experimental findings.[75, 81, 89]

The Cassie and Baxter equation has been criticised for failing to consider the geometric detail of the domains.[74, 85] Models specific to certain artificial domain such as vertical and horizontal grooves,[78] concentric rings and circle segments,[90] have been studied, and the geometries have been related to the number of metastable contact angles and the amount of hysteresis.

The Cassie and Baxter equation has also been used to describe a surface such as a mesh or woven material where the surface contains gaps or pockets of air, [86] or to porous or very rough surfaces.[74] The incomplete penetration into the surface creates a composite surface of wetted and non-wetted material. The two phases become solid/liquid and solid/air interfaces and the equation reduces to

$$\cos \theta_C = f_1 \cos \theta_e - f_2 \qquad (2.5)$$

where f_1 and f_2 are the fractions of solid/liquid and solid/air interfaces, respectively

2.1.4 The Shuttleworth and Bailey equations

Shuttleworth and Bailey [82] were the first to consider the mechanisms by which a

liquid may spread across an idealised rough surface. They used a "saw tooth" or parallel groove model and considered spreading in two dimensions, parallel and perpendicular to the grooves. They showed mathematically that to exhibit minimum surface energy, a droplet must take the shape of a spherical cap. They also considered the capillary forces acting on the drop along the grooves and their effect on the shape of the contact line. Although they didn't use the terms, they drew a distinction between macroscopic and microscopic contact angles.

The two dimensional model was expanded to fit two simplified 3D systems. The systems that were considered were, a plane covered by an array of square based hills, and its opposite, a plane covered by an array of square hollows. The latter is of particular interest to this work as a flat plane with an array of hollows could be used to approximate the surface shape of an anilox roll. Shuttleworth and Bailey proposed that spreading across such a surface would follow the same mechanism as the spreading perpendicular to 2D grooves. The angle of contact would be greater or less according to whether the liquid was advancing or receding. The hysteresis would be largest when the ridges between the hollows are steep and the widths of the hollows are large compared to their depth. Shuttleworth and Bailey proposed two equations to describe the effect of the grooves on the contact angle as the contact line is advanced or receded.

The Shuttleworth and Bailey equations for advancing and receding angles are shown as Equations 2.6 and 2.7, respectively.

$$\theta_a = \theta_e + \varnothing_m \quad \text{for advancing angles} \qquad (2.6)$$

$$\theta_r = \theta_e - \varnothing'_m \quad \text{for receding angles} \qquad (2.7)$$

Where θ_a and θ_r are the observed advancing or receding contact angles on the rough surface. θ_e is theoretical equilibrium contact angle on a smooth surface. $\varnothing_m$ and $\varnothing'_m$ are equal to $\tanh^{-1}([dh/dR])$ which is the angle of maximum slope of the roughness in direction of the contact line movement.

The use of the Shuttleworth and Bailey equations to quantify the effect of roughness predicts that roughness will increase the advancing contact angle and reduce the receding contact angle. Put another way, the larger the maximum slope of the roughness the greater the contact angle hysteresis. This was supported by experimental work by Bartell and Shepherd in 1953 [91] on a paraffin substrate, engraved to produce pyramid shaped roughness where the slope of the roughness could be easily measured.

It is important to note that these equations relate the change in contact angle to the maximum slope of the roughness only. The magnitude or height of the roughness does not effect the calculations, nor does differences in surface area. This is demonstrated by Figure 2.5.

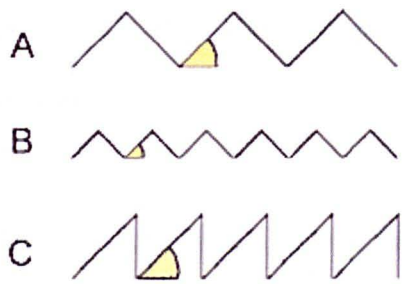

Figure 2.5. Effect of roughness profile on the Shuttleworth and Bailey calculations.

Roughness profiles A, B and C have the same slope in the horizontal direction. Profiles A and B have the same surface area however profile C has a larger surface area for the given length. According to the Shuttleworth and Bailey equation, for a drop advancing from left to right the increase in the advancing contact angle across all three bands should be the same. This contradicts the Wenzel hypothesis that the change in contact angle due to roughness is related to the contact area underneath the drop.

Bartell and Shepherd addressed this problem experimentally with their paraffin/glycerol system. [92] They created a local patch of roughness on which they measured advancing angles. They then advanced the drop to make it larger than the area of roughness so that the contact line was on the smooth surface but the contact area encompassed the roughness. They observed the contact angle to decrease to match that of a drop of the same volume on the completely smooth paraffin surface.

2.1.5 Uses of the Wenzel, Cassie and Baxter and Shuttleworth and Bailey equations

The equations of Wenzel, Shuttleworth and Bailey and Cassis and Baxter were studied from a thermodynamic perspective by Johnson and Dettre in 1964. [93] They concluded that surface roughness gives rise to a number of metastable states and that each state is separated from adjacent states by an energy barrier. It was shown for the first time that the Wenzel and Cassis equations give the state corresponding to the lowest free energy of their respective systems, and also that the energy barrier is at its highest around the phenomenological contact angle, and zero for the maximum and minimum geometrically possible combinations of contact angle and slope. It was also hypothesised that these maximum and minimum combinations, taken by Shuttleworth and Bailey to be the advancing and receding contact angles are not likely to occur due to thermodynamic constraints.

They also proposed that contact angle hysteresis on roughness could be qualitatively explained by assuming advancing and receding contact angles are a balance between the macroscopic vibrational energy of the drop and the height of the energy barrier. Hysteresis becomes greater when the vibrational energy becomes small or the energy barriers become large.

The applicability of the Wenzel, Cassie and Baxter, and Shuttleworth and Bailey's equations to specific geometries of roughness was first investigated theoretically in 1977 by Huh and Mason. [85] This work was followed up by an experimental study in 1980, [95] whereby they concluded that the Wenzel equation accurately described the

change in contact angle on spreading over rough surfaces in which the contact line could move evenly and reversibly. Examples of such surfaces were radial grooves and hexagonally packed spheres. The Shuttleworth and Bailey equation predicted the spreading on spiral grooves and bead blasted surfaces that were seen to approximate the spiral groove configuration, unless the contact angle was very low, in which case capillary action along the grooves was observed.

The paper suggested that most other surfaces would exhibit a combination of the spreading mechanisms and that the contact angle observed would fall between the values predicted by the Wenzel and Shuttleworth and Bailey equations. The exceptions being highly orientated roughness, which would distort the contact line along the angle of orientation. Therefore the contact angle would be dependent on viewing angle and defining a single θ_a would be meaningless. In addition, for deep grooves or pores, or when θ_e is very large the system would be a composite of wetted and unwetted surface, which could be described by the Cassie and Baxter equation in the form as shown in Equation 2.5.

2.1.6 Research into the effect of surface roughness on the contact angle

Research into the effects of surface roughness on the contact angle is ongoing and no universal theory on the treatment of roughness has been put forward. The debate into the usefulness of the Wenzel equation is still active with Bracke De Bisschop and Joos. [96] and Wolanski and Marmur [84] examining its mathematical basis. The Wenzel equation is still being used to describe wetting under specific experimental

conditions. [97, 98]

There are three papers that seem particularly relevant when considering the wetting of an engraved anilox. The first paper considered the effect of the introduction of small holes on wettability of stainless steel by ethylene glycol. [99] The holes were approximately 300μm in diameter which is roughly 10 times larger than an average anilox cell and tubular in shape. The presence of these holes was seen to increase the contact angle from θ_e = 60.2° +/- 1.6° to θ_a =106.7° +/- 3.6°, which was reported to be consistent with the Cassie equation for rough surfaces. (Equation 2.5)

The other papers of interest were on the wettability of surfaces modified with CO_2 YAG, excimer and high-power diode lasers. Two substrates were considered; a Al_2O_3/SiO_2 based ceramic [100] and mild steel. [101] Laser modification of the ceramic was found to lower the contact angle observed with a number of test liquids. Laser modification of the mild steel surface with a YAG laser was reported to lower the observed contact angle. However, modification with a CO_2 laser increased the observed contact angle. The study cited a measured change in surface roughness as the primary reason for the effect on the contact angle. Where a decrease in contact angle took place, the laser was seen to have produced a smoother surface. In the case of the CO_2 laser, modification of mild steel where the contact angle increased the laser treatment roughened the surface. The contact angles on the unmodified surfaces were below 90° for most of the samples, therefore the decrease in contact angle with decreasing surface roughness is in opposition with Wenzel's equation.

2.1.7 The effect of drop size and line tension on the contact angle

In 1979, Good and Koo documented a relationship between the size of a drop and the contact angle that it forms on a solid surface.[102] They concluded that the macroscopic contact angle was a function of the drop size, only when the radius of the drop is of the order of magnitude of the local contortions at the triple phase line. In other words if the drop is small in relation to local changes in the contact line around the perimeter of the drop. These changes in the contact line are attributed to surface roughness and chemical heterogeneity.

The influence of the surface roughness and heterogeneity at the contact line on the macroscopic contact angle is complex and has been studied by several groups. [103, 104, 105, 106] The influence of the interface at the contact line on the macroscopic contact angle has been quantified in the form of a line tension term, which modifies Young's equation as shown by Equation 2.8. [106]

The modified Young equation $\gamma_{LV} \cos\theta_e = \gamma_{SL} - \gamma_{SV} - \sigma \kappa_{gs}$ (2.8)

Where σ is the line tension at the triple phase line and κ_{gs} is local curvature of the three-phase line in the plane of the solid surface. If the solid surface is horizontal, flat, smooth, homogenous, and rigid and the base of the drop is perfectly circular then κ_{gs} is equal to the 1/R where R is the radius of the drop. When R becomes very large, the term σ/R tends towards zero and the original form of Young's equation is obtained. [106] Treatments of this equation to account for model roughness and heterogeneity of surfaces have been presented [105, 106] However, expansion of this

work to real surfaces is very complex and requires intimate details of the surface at the contact line.

2.2 Contact angle measurement

Two techniques can be used to measure contact angles on solid surfaces. The contact angle can be optically measured by the observation of a Sessile drop in contact with the surface under analysis, or calculated from the forces acting on a plate partly submerged in a test liquid

2.2.1 The Sessile drop method

This technique determines the contact angle of a droplet by direct observational measurement. The drop can be deposited onto the surface, suspended from the surface, injected through the surface or by means of a captive bubble held between a syringe and the surface. In the last two examples, additional liquid can be added to the drop and then removed to create advancing and receding contact angles.

Measurement of the contact angles can be done by the use of a goniometer, an instrument through which the drop can be viewed against a fixed scale (resembling a protractor). The use of the goniometer technique involves manual selection of the contact angle, therefore, it is susceptible to operator error and repeatability between different operators is poor.

For this reason, automatic measuring systems are generally used. An image of the droplet is captured and analysed by computer. A circle segment is mathematically fitted to the droplet, and its tangent at the point of intersection with the test surface is calculated. There are many methods that the computer can use to select a circle which is a close match to the droplet, each with an associated error, and it can be difficult to tell from the user interface which method is being used. Common methods include matching the droplet's height and width, using a polynomial fit and the axisymmetric drop shape analysis technique (ADSA). [107, 108]

The ADSA technique has been developed by Neumann and co-workers [108] and currently provides the most accurate method of contact angle measurement. In addition to sessile drops analysis it can be used to measure surface and interfacial tensions of pendent drops. There are two ADSA methods for the measurement of contact angles. ADSA-P is the most commonly used and analyses the profile of the drop. An image of the drop is captured and a curve is fitted using a combination of non-linear least squares fit and the Newton-Raphson method.[108] The best-fitted theoretical curve is then fitted to experimental profiles to obtain the contact angle and liquid/vapour surface tension. [108] Apart from the digital image of the drop, the only other input required is the density difference between the drop and the surrounding fluid phase.[107] In addition to the contact angle the technique can give as outputs the interfacial tension, and the base radius, volume and surface area of the drop. Contact angle measurements with ADSA-P are possible with an accuracy of +/- 0.2°. [108]

ADSA-D derives contact angle information by measuring the drop diameter. An image of the drop taken from above is analysed, this method is used to analyse drops

with very low contact angle (less that 20°) that are difficult to measure with ADSA-P or goniometry. The input parameters are the contact diameter, the surface tension of the liquid and the volume of the drop. For contact angles greater than 90° where the contact diameter cannot be observed from above an alternative method based on the maximum diameter of the drop is employed. The highest achievable accuracy obtainable with ADSA-D on a smooth homogenous surface is around +/-0.3°. [108]

The ADSA-D technique is also very useful for obtaining an average contact angle on a rough or heterogeneous surface on which an axisymmetric drop cannot be formed. By averaging the contact diameter, an average contact angle is obtained for the surface. Although anilox rolls are expected to be very rough, the roughness due to the cell structure is highly symmetrical; therefore, the formation of axisymmetric drops should not be a problem.

A schematic of the instrument setup for and ADSA-P and ADSA-D is shown in Figure 2.6.

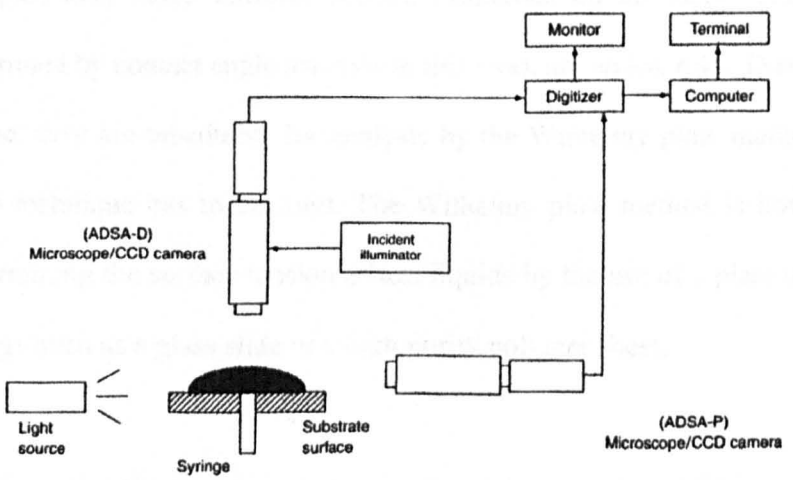

Figure 2.6. A schematic diagram of the apparatus used for the ADSA technique. [110]

When ADSA-P is employed, the liquid drop can be dispensed from above, however ADSA-D requires the camera to be mounted above the drop. The drop is injected through the sample surface from underneath. This restricts the used of ADSA-D to samples that have been constructed or modified to include a hole for the syringe.

2.2.2 The Wilhelmy plate method

The Wilhelmy plate method is a method for measuring advancing and receding contact angles only. The surface to be measured must be in the form of a thin plate. The sample is attached to a fine balance, it is dipped into, and then withdrawn, from the test liquid. The maximum size of the plate is dependent on the maximum weight that the balance can handle and the dimensions of the vessel holding the test liquid. Typically, instruments can hold samples having a maximum weight of approximately 200g.[112] Maximum diameters for the liquid vessels are around 100mm. [110] The samples must have uniform surface properties on all faces. The samples to be examined by contact angle analysis in this work are anilox rolls. Due to their size and shape, they are unsuitable for analysis by the Wilhelmy plate method so the sessile drop technique has to be used. The Wilhelmy plate method is however useful for determining the surface tension of test liquids by the use of a plate of known surface energy such as a glass slide or a high purity polymer sheet.

The force that the liquid is exerting on the plate is measured. This is the wetting force (F). The contact angle is related to the wetting force by Equation 2.9. [111]

$$\gamma = F / P \cos\theta \qquad (2.9)$$

γ is the surface tension of the liquid (mJm^{-1}) and P is the perimeter of the wetted plate. A diagram of the Wilhelmy plate instrument is shown in figure 2.7.

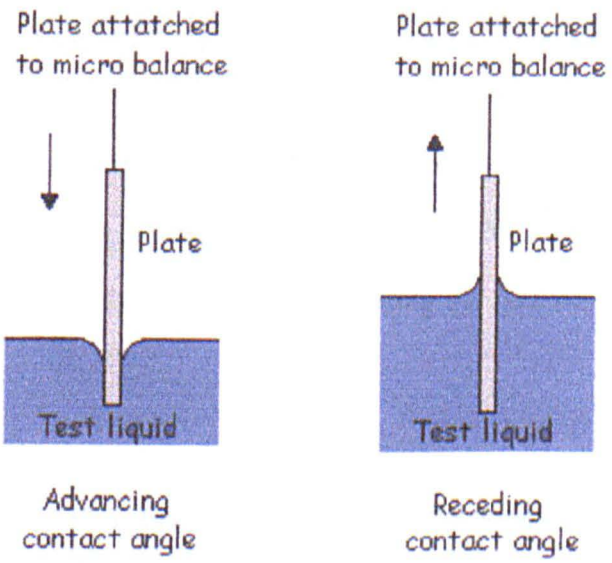

Figure 2.7. A diagram showing the basic equipment used in the Wilhelmy plate method.

The plate is fixed to a sensitive balance, which records the wetting force as a function of time. The liquid level is cycled up and down and the force recorded is used in conjunction with Equation 2.9 to produce the advancing and receding angles. Equilibrium contact angles cannot be measured with this technique.

2.2.3 Contact angle measurements on paper

Contact angle measurements on paper are particularly complex as the liquid penetrated the pores in the paper as it spreads out onto the surface. The contact angle and drop size are time dependent and the rate at which they change is very much dependent on the properties of the paper. The interactions of a test liquid on a paper surface can be separated into wetting, absorption and adsorption. If the drop volume remains constant and the contact angle is decreasing, the mechanism at work is wetting. If the drop volume and contact angle are falling but the drop diameter is constant then the drop is being absorbed whilst if the contact angle and drop volume are falling and the drop diameter is increasing the liquid is adsorbing onto the paper surface. [112]

Different types of surface treatments affect the stability of the contact angle with time. On sized papers, absorption is the likely mechanism and the rate of change of the contact angle can be expected to increase with time. On hard sized papers, little change in contact angle may occur and with laminated or polymer-coated papers, the contact angle can be stable with time. In contrast, with sorbent paper the change in contact angle with time may be very rapid. [112]

TAPPI methods T 485 [113] and T 558 pm-95 [112] deal with the surface wettability of paper. Method T 485 measures the contact angle at 5 seconds and 60 seconds after the drop is brought into contact with the paper. This method can be used with a simple goniometer and works well for some papers, but it can be too slow when adsorption into the paper sample is rapid. Method T 558 pm-95 is an automated

method that can measure the dynamic changes in the contact angle 20 to 40 microseconds after the drop is applied. This method uses an instrument of the type shown in Figure 2.6 and specifies two procedures to measure fast and slow changes in the contact angle with time. In order to determine which procedure is applicable, a drop is suspended from a delivery system and brought gently into contact with the paper surface. If the drop immediately detaches, the contact angle can be expected to change quickly and many measurements over a short time are needed. If the drop remains suspended between the paper and the delivery system, the change in contact angle (if any) will be slow and measurements can be taken at greater time intervals over a longer time frame.

2.3 Surface energy

Every solid surface has an associated energy termed the specific surface excess free energy. (Referred to from now on as surface energy for simplicity) It is a physical property of the surface and is similar to the surface tension of a liquid. It is defined as "the reversible work done in creating unit area of fresh, flat, free surface." [79] The S.I. unit of surface energy is $mJ.m^{-2}$, in older literature, and more traditional industries such as printing, $dynes.cm^{-2}$ are used. These units are fortunately numerically equivalent. Surface energy is denoted by the symbol G^s. Surface energy is a thermodynamic term, which is used as a measure of the wettability of a solid surface.

The surface tension of a liquid is a product of intermolecular forces acting at the

surface of a liquid to form something analogous to a skin. The surface tension of a liquid is defined as "The force per unit length acting to one side of an imaginary line drawn in the plane of the surface." [79] It's S.I. unit is $mN.m^{-1}$ (with $dynes.cm^{-1}$ used in older literature). Surface tension is given the symbol γ.

Although less commonly used, solids also have surface tensions and liquids have surface energies. Surface energy and surface tension are related by Equation 2.10. [114]

$$\gamma = G^s + A\,(\partial G^s/\partial A)_{T,P} \qquad (2.10)$$

where A is the area of the surface and the term $(\partial G^s/\partial A)_{T,P}$ is the rate of change of surface energy per unit area with area (at constant pressure and temperature). Therefore, if G^s does not change as area increases this term is zero and the surface energy G^s is equal to the surface tension γ. In a single component liquid, the local environment of the surface atoms does not change as the area of the surface is increased and the surface tension and surface area are equivalent. However, in a multi-component liquid changing the surface area can change the concentration of solute at the surface. Changing the surface area of a solid can involve plastic deformation of the surface, changes to the orientation of the surface molecules and changes to the local interactions at the solid surface. G^s is thus affected by surface area and does not equal γ. [114] Care should therefore be taken when using the terms surface energy and surface tension in connection with solids or multi-component liquids to avoid confusion, particularly as the terms are often used interchangeably in literature. [73, 77, 78] The surface tension of a solid is difficult to accurately measure and

is of little of use, as it cannot be used with Young's equation to calculate interfacial tensions or to predict wetting.[114]

Values for the surface energy of a solid and the surface tension of a liquid can be used as a guide to predict wetting. If the surface energy of a given surface is greater or equal to the surface tension of a low viscosity liquid, spontaneous wetting would be expected. The contribution to the surface free energy, made by the adsorption of vapour onto the solid surface, can be separated from that of the solid, and is often disregarded for low surface energy materials, as any reduction surface energy (and therefore increase in contact angle) is small, as little vapour is adsorbed. [79]

2.3.1 The work of adhesion W_{ad} and spreading coefficient S_c

The work of adhesion (W_{ad}) is a term that can be related to the surface energies at a solid/liquid/vapour interface by the Dupré equation. The work of adhesion defined as "The reversible work done in separation of a unit area of solid/liquid interface." [79] W_{ad} is related to the surface energy components by the Dupré equation [115]

Dupre equation $$W_{ad} = G^S_S + G^S_L - G^S_{SL} \qquad (2.11)$$

Where G^S_S is the surface energy of the solid, G^S_L is the surface energy of the liquid (or the surface tension) and G^S_{SL} is the interfacial energy of the solid/liquid interface. The work of adhesion is directly related to the strength of the adhesive bond at the

interface. The larger the value of the work of adhesion the more force needed to cleanly separate the two phases.

A related quantity to the work of adhesion is the spreading coefficient S_c. [115]

$$S_c = G^S_S - G^S_L - G^S_{SL} \qquad (2.12)$$

The spreading coefficient can be positive or negative and is not limited in magnitude. A stable contact angle is however only formed when S_c/G^S_L, sometimes referred to as the reduced spreading coefficient, has a value between minus two and zero. If the reduced spreading coefficient has a value greater than zero spontaneous wetting occurs. A value is below minus two would indicate complete reticulation of the liquid from the surface.

2.3.2 The Young-Dupré equation

The Dupré equation (Equation 2.10) and Young's equation (Equation 2.1) can be combined to give Equation 2.13, the Young-Dupré equation.

The Young- Dupré equation $\qquad W_{ad} = G^S_L(1+\cos\theta) \qquad (2.13)$

The contact angle is now related directly to the surface energy (or surface tension) of the liquid, and the work of adhesion. The Young-Dupré equation is true for low

energy surfaces that do not exhibit contact angle hysteresis, however, as has been previously discussed all real surfaces exhibit some degree of contact angle hysteresis.

2.3.3 Fowkes theory of fractional polarity

The surface free energy of the solid can be further separated into components corresponding to the contributions to the surface free energy from polar interactions, dispersion interactions and hydrogen bonding, using Fowkes theory of fractional polarity. [79]

$$G^S_S = G^d_S + G^p_S + G^h_S \qquad (2.14)$$

G^d_S is the surface energy contribution from dispersion interactions, G_{PS} is the surface energy contribution from polar interactions and G^h_S is the surface energy contribution from hydrogen bonding. As hydrogen bonding is technically a polar interaction, it is usual to combine the terms G^h_S and G^p_S together as G^p_S for simplicity.

Fowkes proposed a geometric mean approximation to describe the dispersive forces acting between a non-polar liquid such as a saturated hydrocarbon, and a solid surface. He proposed that the work of adhesion in a purely dispersive solid/liquid system would be given by Equation 2.15

$$W_{ad} = 2(G^d_S\, G^d_L)^{0.5} \qquad (2.15)$$

2.3.4 The Owens-Wendt geometric mean approximation

Owens and Wendt extended the geometric mean approximation to estimate the polar and dispersive force interactions at work in a system. The work of adhesion then becomes

$$W_{ad} = 2(G^d_S G^d_L)^{0.5} + 2(G^p_S G^p_L)^{0.5} \qquad (2.16)$$

This equation can be combined with Equation 2.12 to produce Equation 2.17

$$2(G^d_S G^d_L)^{0.5} + 2(G^p_S G^p_L)^{0.5} = G^S_L (1+ \cos\theta) \qquad (2.17)$$

Fowkes proposed that as a saturated hydrocarbon liquid would have no polar contributions to the surface free energy i.e. G^p_S would be zero. Therefore the term $2(G^p_S G^p_L)^{0.5}$ would also be zero and G^S_L would equal G^d_L.

$$G^S_L(1+\cos\theta) = 2(G^d_L)^{0.5} \qquad (2.18)$$

If the contact angle θ and surface tension is known for the non-polar liquid, G^d_S can be calculated. Once G^d_S is known, the contact angle obtained by a polar liquid with known values of G^S_L, G^d_L and G^p_L can be used in equation 2.18 to obtain G^d_S. The total surface energy of the surface can be found by recombining the component surface energies G^p_S and G^d_S to give G^s_S

The most common pair of liquids selected for determination of the surface energy by

the geometric mean method are water and diiodomethane. Diiodomethane is commonly used as it has a polar component small enough to be regarded as zero. [79] It has a relatively high surface tension of 50.76 mNm^{-1}, which is large enough to give finite contact angles on a wide range of surfaces. Water is again used for its high surface tension. Its highly polar nature makes it suitable for the calculation of the polar coordinate once the dispersive term has been determined. Its advantages over other polar liquids are that it is not hazardous to work with and that it is easily obtained. Pure water has a surface tension of 72.8 mNm^{-1} of which 51.0 mNm^{-1} can be regarded as due to polar interactions, with the remaining 21.8 mJm^{-2} being due to dispersive forces. [79]

The use of the geometric mean has been widely criticised, as it is believed to over overestimate the polar interactions. Other equations have been put forward, however due to its simplicity this equation is still a widely used method of extracting surface energy information from contact angle data. The geometric mean approximation does not work well for materials with extremely high or low surface energies. The Harmonic mean equation [116] proposed by Wu is a well known equation for extremely low surface energy materials such as some polymers. Schultz equation is recommended for samples with high surface energies i.e. with surface energies of over 80 mNm^{-1} [79]

2.3.5 Acid-base interactions

The Owens-Wendt geometric mean treatment of polar interactions assumed the polar interaction between two dissimilar materials could be deduced from the polar interaction acting internally within each material. However, this is not always the case. For example ethers, esters and tertiary amines, which have only a small amount of internal polarity, can produce strong interactions with dissimilar surfaces. [117] Fowkes put forward an alternative expression for the fractional polarities of the surface energy components in terms of Lewis acid theory. [118, 119] The original treatment of polar and dispersive interactions classifies dispersive interactions as due to London (dispersion) forces, forces due to the induction of temporary dipoles formed by the oscillation of electron clouds and includes the other dipole interactions, Keesom forces (dipole/dipole) and Debye forces (dipole/induced dipole) as polar interactions. Acid-base theory includes all forces due to dipoles in the dispersive component and Lewis acid-base interactions of electron donors and acceptors to explain the polar interactions.

$$G_S = G_S^{LW} + G_S^{AB} \qquad (2.19)$$

Where G_S^{LW} is the component of the surface energy made up from the Lifshitz–van der Waals interactions, i.e. the combination of all the electromagnetic interactions. G_S^{AB} is the component of the surface energy that is due to acid-base interactions. In order to obtain a value for the surface energy using acid base theory it is necessary to use three test liquids for which values for G^+, G^- and G^{LW}, the acid, base and

Lifshitz-van der Waals components, are known. The surface energy is calculated from following set of equations. [120]

$$G_{L1}(1+\cos\theta_1) = 2[(G_S^{LW}G_{L1}^{LW})^{1/2} + (G_S^{+}G_{L1}^{-})^{1/2} + (G_S^{-}G_{L1}^{+})^{1/2}] \qquad (2.20)$$

$$G_{L2}(1+\cos\theta_2) = 2[(G_S^{LW}G_{L2}^{LW})^{1/2} + (G_S^{+}G_{L2}^{-})^{1/2} + (G_S^{-}G_{L2}^{+})^{1/2}] \qquad (2.21)$$

$$G_{L3}(1+\cos\theta_3) = 2[(G_S^{LW}G_{L3}^{LW})^{1/2} + (G_S^{+}G_{L3}^{-})^{1/2} + (G_S^{-}G_{L3}^{+})^{1/2}] \qquad (2.22)$$

It is recommended that two out of the three test liquids used with these equations are polar in nature. Formamide or glycerol can be used in conjunction with water and diiodomethane, a pair that are often used with the geometric mean approximation.

The acid-base theory can also be used to separate the work of adhesion into dispersive and acid-base components. [121]

$$W_{ad} = GL(1+\cos\theta) = W_{ad}^{LW} + W_{ad}^{AB} \qquad (2.23)$$

The dispersive and acid-base contribution to the work of adhesion can be expressed in terms of the Lifshitz-van der Waals and acid –base components of the surface energy

$$W_{ad}^{LW} = 2(G^{LW}_{L}\, G^{LW}_{S})^{1/2} \qquad (2.24)$$

$$W_{ad}^{AB} = 2(G_S^+ G_L^-)^{1/2} + 2(G_S^- G_L^+)^{1/2} \qquad (2.25)$$

The Lifshitz-van der Waals and acid–base components of the surface tension of several common liquids have been determined and are shown in Table 2.1. (These can be considered numerically equivalent to the surface energy components of the liquids)

	γ_L	γ_L^W	γ_L^{AB}	γ_L^+	γ_L^-
Water (W)	72.8	21.8	51.0	25.5	25.5
Glycerol (Gl)	64	34	30	3.92	57.4
Ethylene Glycol (EG)	48	29	19	1.92	47
Formamide (Fo)	58	39	19	2.28	39.6
Dimethyl sulfoxide (DMSO)	44	36	8	0.5	32
α-Bromonaphthalene (ABN)	44.4	43.5	≡ 0		
Diiodomethane (DIM)	50.8	50.8	≡ 0		

Table 2.1. The Lifshitz-van der Waals and acid–base components of the surface tension of several commonly used liquids. (in mJ/m^2) [122]

If contact angles made by three of these liquids on a test surface are known and the three liquids are suitably dissimilar in nature, these values can be used with Equations 2.20-2.22 to calculate the acid, base and Lifshitz-van der Waals components of the surface energy of a solid surface. When the surface acid-base and Lifshitz-van der Waals components are known the surface tension component values

of a single liquid can be used with and Equations 2.24-2.25 the Lifshitz-van der Waals and acid base components of the work of adhesion.

2.4 The application of surface chemistry knowledge to the flexographic printing process

Spracha reviewed the interfacial aspects of printing in 2002. [124] He summarised the theories of surface energy calculation, the work of adhesion and acid-base interactions and gave examples of how they are relevant to printing. He cites the need to measure the surface tension of printing inks in order to produce inks with good substrate wetting and to control spreading. He also stated that the surface energy of the substrates (particularly polymer films) is critical in obtaining substrate wetting, controlling ink spreading and obtaining adequate adhesion. Although the review covers flexography and states the need to control the surface energy of the plate and substrate, the surface energy of the anilox is not considered.

As discussed in Section 1.7 of Chapter 1 several studies have been made into the importance of the surface energy of the plate and of the surface interactions between the ink and substrate, to the wetting and ink transfer. A parallel study on the wetting and transfer properties of anilox rolls is however still required. The inking and release character of the anilox roll is proposed to be a combination of its physical and surface chemical character. The macroscopic topography of the anilox is varied routinely in terms of cell size and profile but the microscopic surface topography and surface chemistry are intrinsic properties that are dependent on the ceramic from

which it is made and the laser which creates the cells. One of the reasons that the surface chemistry of the anilox has not as yet been studied is the difficulty in making and interpreting contact angle measurements on a surface which is far removed from the ideal, flat, smooth surfaces on which the theories of wetting and surface energy are developed for.

This work is dedicated to applying the theories of wetting, contact angle interpretation and surface energy to the anilox roll in order to obtain information about surface interactions between the anilox and ink. This will then be related to ink transfer. The work also encompasses the production of a method to obtain surface chemical information from an anilox roll.

3. Analysis of anilox Harper 1

The Harper Corporation of America provided an anilox, which will be referred to as Harper 1. It was made specifically for the test and comprised of three bands, the first engraved by a continuous wave CO_2 laser, the second engraved by a YAG laser and a polished unengraved band. The engraved cells were manufactured to have as near equal cell depth as the engraving processes would permit. Table 3.1 shows the specifications of the two engraved bands.

Anilox band	number of lines per cm	Cell volume (cm^3/m^2)	Cell depth (μm)	Cell opening (μm)	land width (μm)
CO_2	236	4.08	10.7	38.0	4.0
YAG	472	3.63	10.6	19.1	2.1

Table 3.1. Specifications of the banded anilox Harper 1.

3.1 Contact angles analysis on banded anilox Harper 1 with the MAMS instrument

In this investigation, contact angle analysis was carried out using a made-in-house instrument called the Micro-Absorbency Measurement System or MAMS at Pira International. The MAMS instrument consists of a CCD CCIR mono camera connected to a computer via a frame grabber card. The image was recorded as an .avi video file. The baseline of the drop was selected manually and a curve fitted to the

captured image by analysis of the height and width of the drop. Training was given in the standard method was for contact angle analysis on paper. [124]

Contact angle measurements on anilox Harper 1 were made using the MAMS instrument. Several changes had to be made to the standard method and the equipment in order to make it suitable for taking these measurements. The anilox was too large to be placed on the sample platform so the platform was removed and the apparatus rebuilt. As the anilox does not absorb the test liquid as paper does, the length of time over which the drop was photographed could be reduced. Due to the irregular nature of the surface, more measurements were required to ensure that a representative result was obtained. The drop size used also had to be reassessed. (Discussed further in Section 3.1.1.)

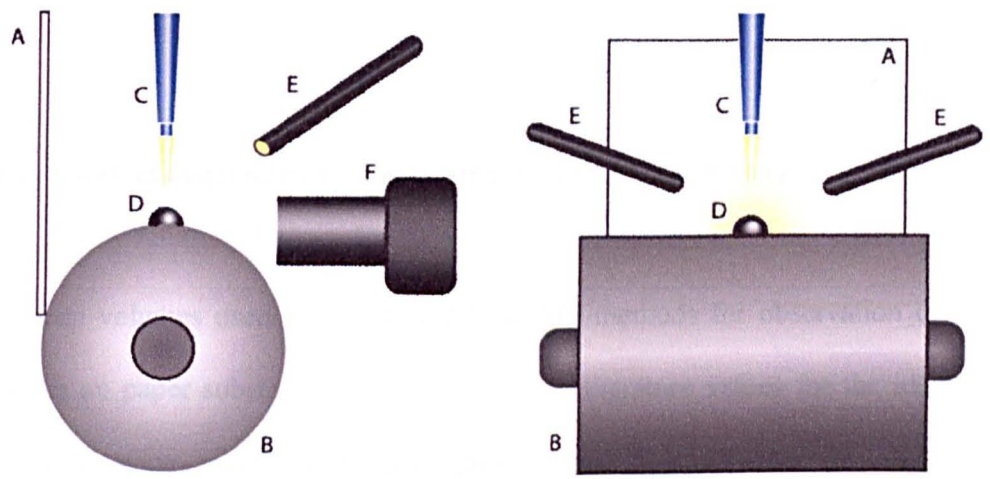

Side view

Front view

A = white screen
B = test anilox
C = pipette
D = droplet
E = flexible light
F = camera

Figure 3.1. Diagram of the MAMS instrument set up to accommodate anilox Harper 1.

The camera was removed from its mount and placed on an adjustable platform. The platform was then positioned so that the camera was at the correct height to view a drop sitting on the zenith. A spirit level was used to ensure that the anilox roll and camera were level in all directions. A pipette was clamped above the zenith of the roll with the tip at a distance of 20 mm from the roll.

Testing took place in the Pira pressroom. The pressroom has a controlled temperature of 23°C +/- 1° and a controlled humidity of 50% +/- 1%. A polar liquid and a non-polar liquid were selected to allow surface energy information to be obtained using the geometric mean approximation. The non-polar liquid selected was diiodomethane, whilst the polar liquid was water. Frames of the droplet were captured twice a second over a 10 second period and the results averaged. Unless otherwise stated, 20 measurements were taken on each band of the anilox.

3.1.1 Contact angle measurement using a polar liquid (water)

The drop volumes used in the standard MAMS methods for observation of water droplets on paper substrates is 25 µl, however, literature values for the ideal drop volume for contact angle analysis are around 1 µl. [125, 126] As the substrate in this case was very different from paper and was curved, a range of drop volumes was tested. In addition to a 20µl drop, a drop of 40µl was used to make the drop size larger in relation to the surface roughness. A drop of 5µl was used to minimise the amount of curvature at the point of contact. Attempts to use a drop with a volume of less than 5µl were unsuccessful, as the magnification of the camera was insufficient

to produce a large enough image for the software to accurately process. In addition, the dispensing force of the lower volume pipette was insufficient to produce a free falling spherical drop. Because of time constraints, only 15 measurements on each band were made with the 40μl drops, as it was harder to get a stable drop on the roll surface with this volume. Table 3.2 shows a summary of the data. The data is presented in full in Section A3-1 of the appendix.

		40μl water drop	20μl water drop	5μl water drop
Polished band	**mean**	**48°**	**53°**	**56°**
	standard deviation	3°	2°	2°
CO_2 band	**mean**	**59°**	**65°**	**64°**
	standard deviation	4°	2°	2°
YAG band	**mean**	**71°**	**78°**	**76°**
	standard deviation	3°	3°	3°

Table 3.2. The contact angles observed on three bands of anilox Harper 1 by the MAMS instrument.

There is clearly a pattern across the bands that holds true for all of the drop volumes. The contact angles on the polished unengraved band are smaller than those on the engraved bands, therefore the engraving process makes the surface harder to wet. There is a difference in wettablilty between the engraved bands, the CO_2 band being easier to wet than the YAG band. These trends are more clearly illustrated by the results from the 20μl and 5μl droplets than from the 40μl droplets.

If the data is considered by band and not by drop volume it becomes clear that whilst the results obtained with 20µl and 5µl drops are similar; the results obtained with a drop size of 40µl are lower. This is consistent with the observation that a 40µl drop observed on the surface of the roll had a flat top. The MAMS software measures the height and width of the drop and fits a circle segment. If the drop is not spherical and instead is flat at the top (on the right of Figure 3.2), the height is lower than anticipated. When the software tries to fit a segment to the measured height and width, a contact angle smaller than that of the observed drop is measured.

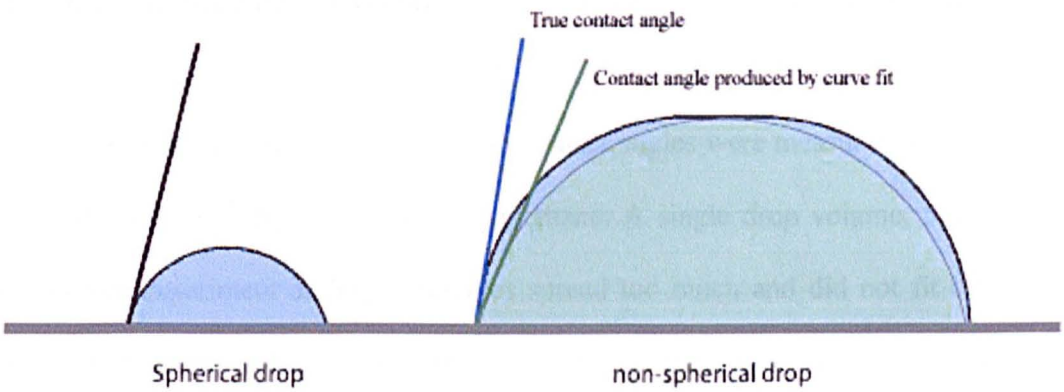

Figure 3.2. An example of a source of error in fitting a curve to a non-spherical drop.

There was also a problem with distortion of the drop around the curvature of the roll. This was more of a problem with the larger drops. The larger drops were also more difficult to centre at the zenith of the roll and had a greater tendency to run. Therefore, the 5µl drop was selected as the most appropriate drop size for future tests.

It was noted that the drop volumes calculated by the MAMS software from the measured heights and widths varied from the dispensed volume. Plots of contact angle against drop volumes were made for each band to determine if there was any relationship between large deviations in the calculated drop volume and large deviations from the mean contact angle value. No correlation could be found between deviation from dispensed drop volume and deviation from the mean contact angle for any band.

3.1.2 Contact angle measurement using a non-polar liquid (diiodomethane)

Table 3.3 shows the results obtained when contact angles were measured on each of the three bands on Harper 1 with diiodomethane. A single drop volume, 5µl, was used in this experiment as larger volumes spread too much and did not fit on the screen when photographed, whilst smaller volumes could not be used as the droplet heights became too small for the image analysis to accurately fit a curve. The complete set of data for these measurements is shown in Section A3-2 of the appendix.

		5µl diiodomethane
Polished band	**mean**	**20°**
	standard deviation	2°
CO_2 band	**mean**	**19°**
	standard deviation	2°
YAG band	**mean**	**15°**
	standard deviation	3°

Table 3.3. Results obtained on anilox Harper 1 with 5µl diiodomethane drops with the MAMS instrument.

Table 3.3 shows that the trend in wettablilty observed with water drops was not seen with diiodomethane drops. The contact angles observed on the polished and CO_2 bands are very similar with the YAG band being slightly lower. There is no statistically significant difference between the three bands. Therefore, the surface changes due to the engraving process do not measurably affect the wetting of the anilox with diiodomethane.

3.2 Contact angles analysis on banded anilox Harper 1 with the FTA instrument

Later on in this investigation, the FTA-200 instrument became available for use. As discussed in Chapter 2 it was a much newer instrument than MAMS and had an automated dispensation system for the test liquids and more advanced curve-fitting

software. The experiment was repeated on the FTA instrument. The FTA required less modification to accommodate the anilox than the MAMS instrument, as it had a removable sample stage that could be replaced by the anilox. Comparable drop volumes were achieved by pumping out 5μl of water, which remained suspended from the dispensing needle. The drop was then lightly touched off onto the roll surface by moving the pump assembly. The surface tension of diiodomethane was too low to allow a 5μl drop to be easily detached from the dispensing needle. The drop size was increased to 7μl for this experiment. Atmospheric conditions were monitored and were 25°C +/- 2° with a relative humidity of 55% +/- 2%.

A summary of the results is shown in Table 3.4. The complete set of results is included in the Section A3-3 of the appendix.

		5μl water FTA	7μl diiodomethane FTA
Polished band	**mean**	**75°**	**42°**
	standard deviation	3°	2°
CO_2 band	**mean**	**84°**	**45°**
	standard deviation	2°	2°
YAG band	**mean**	**100°**	**43°**
	standard deviation	2°	2°

Table 3.4. Results obtained on anilox Harper 1 with 5μl water drops with the FTA Instrument.

The trend in wettability of the bands remained the same as previously seen, but the contact angles produced by the FTA instrument were much larger than those observed with the MAMS instrument. The increases in contact angle are reasonably consistent for both of the liquids tested.

The difference in reported contact angles is too large to be a difference in data interpretation by the systems. Visual inspection of the drops produced by each of the dispensing systems confirmed that the test liquid spread out further when manually dispensed with a pipette as with the MAMS set up than by the FTA computer controlled pump. The test liquid, when pipetted is propelled towards the surface, causing the drop to spread out on impact, whilst when the drop was touched off or dispensed onto the surface there was no force applied to artificially boost the spreading. The difference in observed contact angle between the two instruments was therefore attributed to the different method of introducing the drop onto the sample surface.

3.3 Measurement of advancing and receding contact angles using the FTA instrument

The FTA instrument has an automated dispensing system which allows the test liquid to be pumped onto the anilox surface and then pumped back into the syringe. It was therefore theoretically possible to measure the advancing and receding contact angles. In practice, obtaining measurements was extremely difficult, as the liquid did not advance symmetrically around the dispensing needle. Once movement of the contact line occurred in a particular direction the liquid advance in that direction

only. Measurements could only be used if the contact line advanced at 90° to the direction of observation i.e. along the zenith; otherwise, a distorted result was obtained. If the contact line moved in a direction other than along the zenith, the drop had a tendency to roll down the side of the anilox and out of view.

Advancing and receding contact angle measurement was thus a lengthy and frustrating exercise. Only five results were obtained for each band. The results were however very interesting.

The advancing contact angles data for water drops is shown in Table 3.5. The values obtained for advancing angles are very similar to those obtained as static contact angles. This could mean two things, that there is no observable hysteresis or that the drop advanced as it found its equilibrium position.

	Advancing contact angles		
Run number	Polished	CO_2	YAG
1	77°	88°	96°
2	74°	92°	88°
3	72°	85°	99°
4	77°	85°	95°
5	75°	87°	100°
Mean	75°	87°	96°
Standard deviation	2°	3°	5°

Table 3.5. Advancing contact angles made by water on the bands of Harper 1.

As discussed in the previous chapter, all real surfaces exhibit a degree of hysteresis and that a major cause of hysteresis is surface roughness. It would therefore not be expected that the surface of an anilox, especially an engraved area, should exhibit no hysteresis. In addition, if the contact line could move reversibly across the surface the receding contact angle would also have the same value as the advancing angle. When attempts were made to measure the receding angle it became apparent that there was a great deal of hysteresis taking place. Figure 3.3 shows the change in contact angle as the water drop in contact with the CO_2 band was reduced in volume over a period of twelve seconds. X charts the movement of the contact line with decreasing drop volume. For ten seconds the drop width does not significantly change, indicating that the contact line is not yet receding. At eleven seconds, the contact line begins to recede and the contact angle (shown by the blue o's) drops sharply below 20°. After 12 seconds, most of the liquid had been sucked back into the syringe and the drop disconnected from the needle tip. Measurements were made until five usable results were obtained. The contact angle in all cases was less then 20°. Attempts to adjust the pump rate and drop volume to extend the period in which the contact line receded before the drop detached from the needle were unsuccessful. A value for the contact angle of less than 20° was therefore recorded.

The same problem was observed with both the polished and the YAG bands. The amount of hysteresis was not measurably less for the polished unengraved band despite its relatively smooth surface, again values for the receding contact angle of less then 20° were recorded.

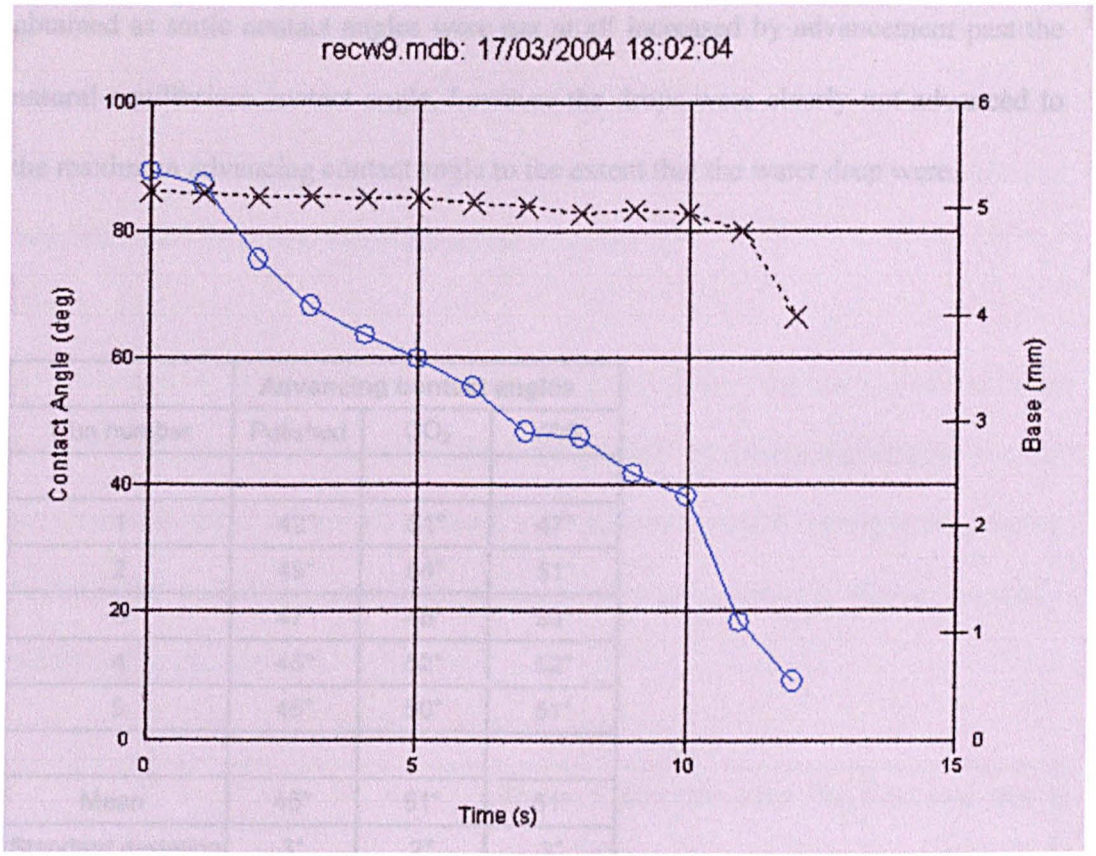

Figure 3.3. A plot of contact angle against drop base diameter with reducing drop volume.

It was concluded that the contact angles made by water on the FTA were advancing contact angles. Even though the drop had been touched off from the needle to the surface with the lightest possible pressure the drop had advanced whilst spreading into a stable position.

The advancing contact angles observed with diiodomethane were larger than the static angles. Again, it was only possible to obtain five measurements due to practical complications. It is not possible to conclude from this experiment that the values

obtained as static contact angles were not at all increased by advancement past the natural equilibrium contact angle, however the drops were clearly not advanced to the maximum advancing contact angle to the extent that the water drop were.

	Advancing contact angles		
Run number	Polished	CO_2	YAG
1	42°	51°	47°
2	49°	54°	51°
3	47°	48°	54°
4	45°	52°	52°
5	46°	50°	51°
Mean	46°	51°	51°
Standard deviation	3°	2°	3°

Table 3.6. Advancing contact angles made by diiodomethane on anilox Harper 1.

The advanced drop of diiodomethane was very unstable on the zenith of the roll and was prone to flowing down the sides. Attempts to measure receding contact angles were unsuccessful, as the drop could not be kept on the zenith long enough for liquid to be slowly sucked back into the syringe.

3.4 Calculation of surface energies from Harper 1 data

Despite the reported inaccuracies with the contact angle measurements, the contact angle data obtained on the three bands of Harper 1 were used to estimate the surface

energies of the bands. Surface energies were calculated from the average static contact angle values using the Owens-Wendt geometric mean method (Section 2.3.5) using data from the MAMS and the FTA instruments. The results are summarised in tables 3.7 and 3.8 for the two instruments respectively.

As discussed in Chapter 2, there are known inaccuracies with the geometric mean approximation, however due to its simplicity it is still extremely widely used outside the specialist field of surface science and surface energies reported in printing literature, if calculated from contact angle measurements, are almost certainly calculated by this method.

Surface energy		40µl water drop mJm^{-2}	20µl water drop mJm^{-2}	5µl water drop mJm^{-2}
Polished band	dispersive component	48	48	48
	polar component	16	13	12
	total surface energy	**64**	**61**	**60**
CO2 band	dispersive component	48	48	48
	polar component	10	8	8
	total surface energy	**58**	**56**	**56**
YAG band	dispersive component	49	49	49
	polar component	5	2	3
	total surface energy	**54**	**52**	**52**

Table 3.7. Surface energies calculated from the mean contact angle data from the MAMS instrument.

The error in each of the calculations, found by using the maximum and minimum contact angles to create the largest variation, was +/- 1 mJm^{-2}, the error associated

with the total surface energy therefore was 2 mJm^{-2}. The relatively large differences in the contact angle produced by using different drop volumes translates into differences in surface energy that are not statistically significant. This demonstrates that surface energy measurements alone are not a very sensitive indication of the wetting behaviour of the solid.

As expected, the higher contact angles reported by the FTA system translate into lower contact angles. The surface energies calculated from the FTA data are closer to the literature value of 40 dynes for engraved ceramic [55] (equal to 40 mJm^{-2}) and 50 dynes for unengraved ceramic, however these values are quoted without reference as to how they were obtained and must be regarded with suspicion.

		Average surface energy mJm^{-2}	Standard deviation mJm^{-2}
Polished band	dispersive component	39	1
	polar component	6	1
	total surface energy	**45**	**2**
CO_2 band	dispersive component	38	1
	polar component	3	1
	total surface energy	**41**	**2**
YAG band	dispersive component	37	1
	polar component	0	0
	total surface energy	**37**	**1**

Table 3.8. Surface energies calculated from the mean contact angle data from the FTA instrument.

The polar component of the surface energy of the YAG band was very small. The calculated value was $5x10^{-2}$ mJm^{-2} which when rounded off to zero decimal places resulted in a value of zero appearing in the table.

The higher the surface energy of a solid, the easier it is to wet. Therefore, the findings of this experiment were that the polished ceramic band was the easiest band to wet, followed by the CO_2 band then the YAG band. The difference in total surface energy between the bands is very small due to its domination by the dispersive component. The significant difference in the wettability of the bands is not apparent from the surface energy values of the bands. The percentage of the total surface energy made up from dispersive and polar interactions are shown in Figure 3.4.

There was a statistically significant difference between the contact angles made by water on the bands of the anilox. When the surface energy is calculated the polar component of the surface energy, which is the component that is based on the contact angle of the water, is very small in comparison to the dispersive component of surface energy. This is calculated from the contact angles made by diiodomethane, with which there was no significant difference between the bands. The significant difference in polar wetting between the bands is masked by the dispersive component.

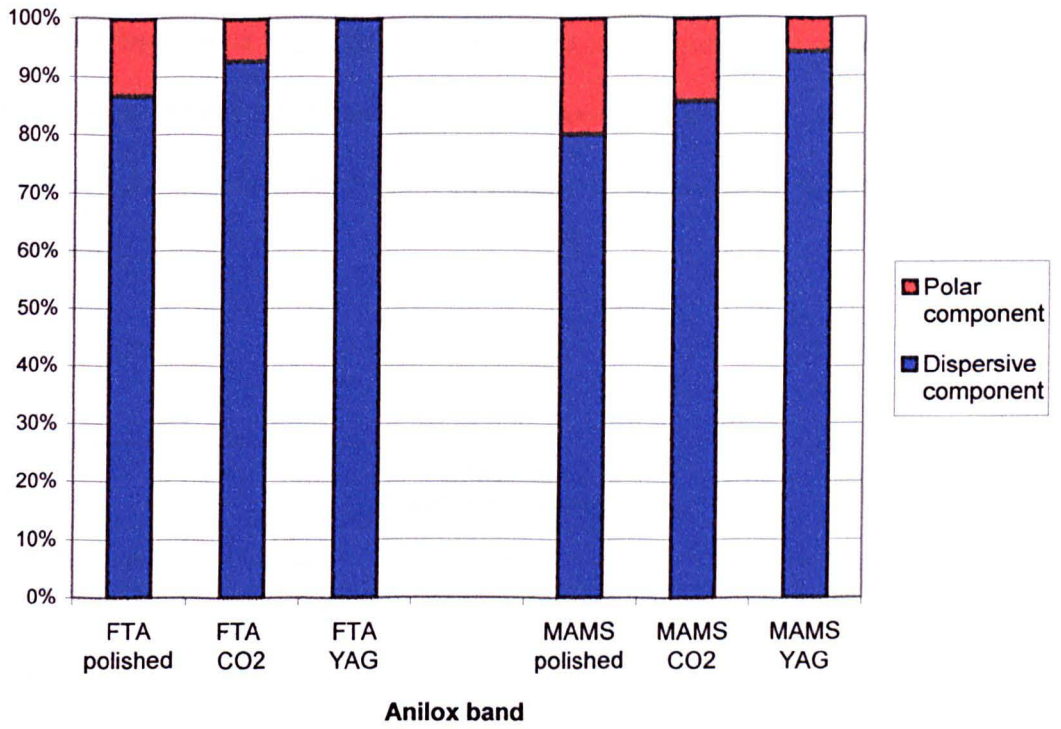

Figure 3.4. The polar and dispersive make up of the total surface energies.

The instrument used to make the measurement is again seen to affect the magnitude of the results however the trend remains constant for both instruments. The change in surface energy between the bands is because of a change in polar interactions.

3.5 Measurement of the acid-base surface interactions

The difference in wetting character is seen only in the polar component of the surface energy. As discussed in the previous chapter, the Owens-Wendt geometric mean approximation has now been superseded by the acid-base theory which classified the polar energy of the surface into Lewis acid and basic components.

By obtaining contact angle information with a third liquid, formamide, information about the acid-base interactions of the surfaces can be found. The results of the contact angle measurements made with formamide are shown in Section A3-4 of the Appendix.

		Contact angle with Formamide
Polished band	**mean**	**43°**
	standard deviation	1°
CO_2 band	**mean**	**60°**
	standard deviation	2°
YAG band	**mean**	**64°**
	standard deviation	2°

Table 3.9. Contact angles observed with formamide drops on the bands of Harper 1.

The calculation of the acid and base components is mathematically complex. The FTA software has an algorithm that calculates the dispersive, polar, and acid-base components of the surface energy when the contact angles of three suitable liquids are entered.

	Polished band	CO_2 band	YAG band
Total surface energy	43.92	38.6	37.72
Dispersive component	38.59	37.01	38.07
Polar component	5.32	1.593	-0.3456
Acid component	1.785	0.1718	0.3436
Base component	3.977	3.695	-0.089

Table 3.10. The component surface energies (in mJm^{-2}) as calculated by the FTA software using the acid-base equations.

The difference is in the basic component of the surface energy, which is relatively high for the polished band, reduces on the CO_2 band and disappears on the YAG band. This indicates a loss of basic character on the surface as a result of the engraving process. The dominant component of surface energy on the polished and CO_2 bands is the basic component. On the YAG band the acidic component becomes higher. The acidic component is also much smaller on the engraved bands

3.6 Contact angles made using standard flexo inks

The polar contribution to the surface energy is of particular significance when considering the wetting and de-wetting of a surface by water-based or UV ink. Water-based inks use surfactants to reduce the surface tension and to improve wetting. Whilst small amounts of surfactant are used in UV inks to improve substrate wetting, maintaining good overprintability is an issue. As the diluent of a UV ink is

incorporated into the film the ability to use this to control the wetting properties the ink is limited as the monomer or monomers in a formulation are chosen to control many properties of the ink.

To get an idea of how such inks would wet the anilox a standard "off the shelf" ink of each type was tested. The UV ink tested was Arena process cyan supplied by Coates Lorrelleux, the water-based ink was Gemcol process cyan supplied by Sun Chemical Swale. The inks were too viscous to be dispensed with a pipette; therefore, the contact angle measurement was carried out on the FTA alone. The measurements were made under the same atmospheric conditions as before. The UV ink tested was extremely thixotropic. The ink was worked up to reduce its viscosity and collected in a syringe, however it thickened again very quickly and some of the droplets dispensed had a lumpy appearance. These drops were not measured as the increased viscosity of the ink prevented the ink forming a sessile drop. The effect of the ink rheology on the contact angle is shown in Figure 3.5.

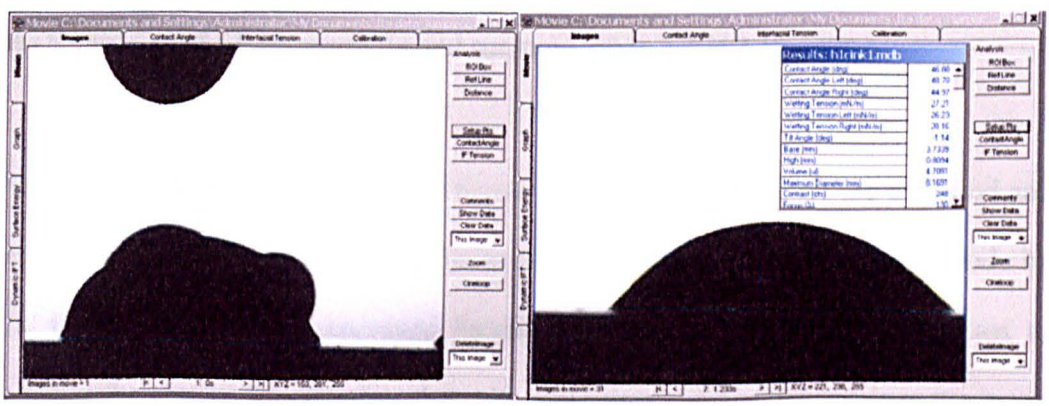

Drop formed by the UV ink
2 minutes after shear thinning

Drop formed by the UV ink
immediately after shear thinning

Figure 3.5. The affect of ink rheology on the production of a measurable contact angle.

Five measurements were made with the UV ink on each band. The results are shown in Section A3-5 of the appendix and are summarized in Table 3.11.

		UV Ink
Polished band	**mean**	**32°**
	standard deviation	3°
CO_2 band	**mean**	**45°**
	standard deviation	3°
YAG band	**mean**	**42°**
	standard deviation	3°

Table 3.11 Contact angles made by a UV ink on the bands of anilox Harper 1.

The water-based ink also provided some dispensing problems, as it was too thick for the automated system to dispense, however the syringe was compressed by hand and it was possible to obtain six results for each band. The complete results are shown in the Section A3-5 of the appendix and summarised in Table 3.12.

Although there is a clear difference between the contact angles on the engraved and unengraved bands there is no significant difference between contact angles made by the UV ink on the two engraved bands. Only five measurements were used to produce the results. It is possible that with more time a difference between the bands could be identified. It is more probable that the UV ink is predominantly basic in character. The acidic component of the surface energy remains relatively constant

between the engraved bands. The UV inks contain an amine synergist, which may give the ink an overall basic character.

		Water-based ink
Polished band	**mean**	**53°**
	standard deviation	2°
CO_2 band	**mean**	**66°**
	standard deviation	2°
YAG band	**mean**	**73°**
	standard deviation	1°

Table 3.12. Contact angles made by a water-based ink on the bands of anilox Harper 1.

By contrast, it would appear that the water-based ink has an acidic character. Although only six measurements on each band were possible, the results from the water-based ink indicated that the wettability follows the same trend as observed with water as the test liquid. The contact angle made by the water-based ink is affected by the changing basic nature of the bands. As the water-based ink wets the two engraved bands differently, the ink release from the two engraved bands could also be different.

3.7 The effect of cleaning anilox Harper 1 with a specialist product

Later in this investigation, it became apparent that contact angle measurements using inks had resulted in plugging of the anilox cells. The anilox was routinely cleaned with solvents (propanol and acetone) and rinsed with deionised water between measurements. When the plugging was identified, the anilox was cleaned with a specialist cleaner to remove the dried ink. The contact angles of the three bands were measured and a change was found to have occurred in the wetting of the YAG band. The repeated measurements are shown in full in Section A3-6 of the appendix. Table 3.13 shows the original mean contact angles and the mean contact angles recorded after cleaning has taken place

		Original water	Post-clean water	Original diiodomethane	Post-clean diiodomethane
Polished band	mean	75°	72°	42°	42°
	standard deviation	3°	3°	2°	1°
CO_2 band	mean	84°	84°	45°	43°
	standard deviation	2°	3°	2°	2°
YAG band	mean	100°	78°	43°	43°
	standard deviation	2°	2°	2°	2°

Table 3.13. The contact angles on the three bands of Harper 1 before and after cleaning.

The change to the surface of the Harper 1 was only observed with the YAG band when water was used as the test liquid. It was proposed that surfactant from the

cleaning solution had penetrated the YAG band and made the surface more hydrophilic and that the CO_2 was less porous to the solution due to the higher proportion of recast ceramic that forms the walls. It was also noted that the post-clean contact angle on the YAG band was similar to the contact angle observed on the YAG band using the MAMS instrument. It is hypothesised that the surfactant made it possible for the water to overcome the barriers to the movement of the contact line and reach thermodynamic equilibrium. This effect was not seen with diiodomethane.

3.8 Summary of results from anilox Harper 1

The conclusions drawn from the analysis of anilox Harper 1 are:

1. There is a change in the wettability of the anilox roll that is due to the presence of engraved cells.

2. There is a difference in wetting character of the CO_2 and YAG bands.

3. The values of contact angles are strongly affected by the instrument used to obtain the measurements, specifically the system for bringing the drop in contact with the test surface. The difference is due to unintentional advancement of the contact angle.

4 The Owens-Wendt geometric mean approximation indicates that the change in the wettability across the bands is due to a change in the polar nature of the roll surface. The engravings are less polar than the polished unengraved surface, and the CO_2 engraving having more surface polarity than the YAG engraving.

5 The surface energies calculated from the FTA data fall within the expected range (from the limited information obtained from the literature). However, the contact angles measured with the FTA were not equilibrium angles. The surface energies calculated from the MAMS data are a more accurate measurement of the surface energies of the bands on anilox Harper 1.

6 The acid base theory of wetting indicates that the change in surface energy is mainly due to the reduction of the basic nature of the surface. The engravings are less basic than the polished unengraved surface, and the CO_2 engraving have more basic character that the YAG engraving. The engraved bands also have less acidic character than the polished band. There was no significant difference between the acidic components of the engraved bands.

7 A standard water-based ink showed the same wetting trends as water, wetting the polished band better than the CO_2 band and the CO_2 band better than the YAG band.

8 A standard UV ink wet the polished band better than the engraved bands but produced no difference between the engraved bands. This suggests that the UV ink is basic in nature.

9 Cleaning the anilox with a specialist cleaning product improved the wettability of the YAG band with polar liquids but did not affect the wetting of the YAG band with diiodomethane. There was no change in the wettability of the CO_2 or polished unengraved bands with either liquid.

There was a clear difference in the wettability of the unengraved polished, the CO_2 laser engraved and the YAG laser engraved bands. This is believed to be due to a combination of physical and chemical differences made to the ceramic by the engraving laser. The degree of influence that the cell geometries have on the wetting of the engraved bands is at this stage still unclear. Anilox Harper 1 was designed to have cells with the same cell depth and volume. They had very different cell dimensions, the YAG band having twice as many cells per centimetre as the CO_2 band. In the next phase of work an anilox with bands having constant cell opening but variable cell depths was tested in order to remove the cell depth and size of cell opening as variables from the factors influencing wetting of the engraved bands.

4. Analysis of anilox roll Pira 1

Pira International provided an anilox for analysis that could be used on their wide web flexo press. The company that manufactured this anilox was not known therefore it was termed Pira 1. Pira 1 has engravings made by a CO_2 laser in a 45° pattern. The bands of cells have the same size cell opening but different depths and volumes. Four bands were studied: three bands engraved with a CO_2 laser having a constant line screen but varying in volume, and a polished, unengraved band. The line screen was 149 lines per cm (380 lines per inch). The measured circumference of this roll was found to be 353 mm. The diameter was calculated to be 112 mm. Anilox Pira 1 was significantly larger than anilox Harper 1, which had a circumference of 201mm and a diameter of 64mm. The specifications of the engravings on anilox Pira 1 are detailed in Table 4.1. They were provided by David Atkinson of Pira International from his records and were experimentally verified using a hand microscope and an ink drawdown tool.

Anilox band	Line screen (lines per cm)	Cell volume (cm^3/m^2)
Polished band	N/A	N/A
CO_2 band 1	149	3.3
CO_2 band 2	149	3.8
CO_2 band 3	149	4.4

Table 4.1. Specifications of the banded anilox Pira 1.

4.1 Analysis of anilox Pira 1

The anilox was too heavy to transport conveniently, so all surface analysis had to take place in the pressroom at Pira International. It was therefore only possible to perform contact angle analysis using the MAMS instrument. Atmospheric conditions in the pressroom were controlled. The temperature was maintained at 23°C with a tolerance of 2°C. The relative humidity was controlled at 50% with a tolerance of 2%.

4.1.1 Contact angle analysis of banded anilox Pira 1 using the MAMS instrument

Contact angle analysis was carried out as described for anilox Harper 1. The test liquids used were reagent grade water and diiodomethane. A drop size of 5 microlitres was used for all measurements. The data is produced in full in Section A4-1 of the appendix and is summarised in table 4.2. Twenty measurements were taken on the polished band, and bands 1 and 2. Measurements on band 3 were made at a later date with ten measurements of each liquid.

		5μl water	5μl diiodomethane
Polished band	**mean**	**50°**	**14°**
	standard deviation	3°	1°
band 1	**mean**	**52°**	**17°**
	standard deviation	3°	3°
band 2	**mean**	**52°**	**15°**
	standard deviation	3°	2°
band 3	**mean**	**52°**	**12°**
	standard deviation	2°	1°

Table 4.2. The results of contact analysis on three bands of anilox Pira 1.

There was no difference between the wettability of the two engraved bands despite the difference in cell volume and depth. Also the difference in wettability between the engraved bands and the polished band was not statistically significant. There was more variation recorded in the contact angles made by diiodomethane. This was attributed to the low angles measured being close to the limit at which the MAMS instrument could accurately measure. (Reported by Pira International as being 10° [124])

The inability of the contact angle measurement to pick up the differences between the three engraved bands was unexpected. The contact angle technique is very sensitive to changes in surface roughness. Oliver, Huh and Mason [95] reported that steps of 0.05 μm caused significant inhibition to spreading. However, Mason also

advised that the shape of the roughness affected the size at which roughness could be seen to affect the contact angle.[127] The results do however support the theory proposed by Shuttleworth and Bailey [82] (and supported by the work of Bartell and Shepherd [91, 92]) that for roughness having a pyramid shape, as 45° engravings do, that variation in the pyramid height (or in this case cell depth) does not affect the contact angle.

It is also to note that Anilox Pira 1 was not a new anilox and had been used over several years for printing research. The anilox showed signs of wear. The effect of wear on an anilox engraved at 45° is to significantly increase the size and smoothness of the land around the cells, to reduce the carrying volume of the cells and to roughen the polished unengraved areas at either end of the anilox.

As reported in Chapter 3, the MAMS and FTA instruments gave very different results, however the overall trends observed in the results remained the same regardless of the instrument used. It can therefore be concluded that although the contact angles measured on anilox Pira 1 with the MAMS instrument may be artificially low, the lack of difference in contact angle between the bands is significant. The results obtained with the MAMS instrument on Pira 1 and Harper 1 were done under the same conditions. Therefore comparisons between the two anilox rolls are valid. There were however variables between the two rolls that could not be controlled. The ceramic used, the roll circumference and the angle of engraving are all different.

4.1.2 Calculation of surface energies from contact angle data

The results were used as before to calculate surface energies for the three bands. The calculated values are shown below in table 4.3.

		average surface energy mJm^{-2}	Standard deviation mJm^{-2}
Polished band	dispersive component	49	1
	polar component	15	1
	total surface energy	**64**	2
band 1	dispersive component	49	1
	polar component	13	1
	total surface energy	**62**	2
band 2	dispersive component	49	1
	polar component	13	1
	total surface energy	**62**	2
band 3	dispersive component	50	0
	polar component	13	1
	total surface energy	**63**	1

Table 4.3. Surface energies calculated from the MAMS data for the Pira banded anilox.

The cell volume and depth were seen to have no significant effect on the contact angle, and therefore no significant effect on the surface energies of the bands. The

surface energy values are higher than those calculated from the Harper 1 MAMS data. The ceramic used to make the anilox is of unknown compositions and this is thought to account for the difference in wettability.

4.1.3 Comparison between the CO_2 engraved bands on aniloxes Harper 1 and Pira 1

The engravings on Pira 1 were made with a CO_2 laser. As the contact angle results were not significantly different for the three engraved bands the result was averaged into a single value for the engraved areas of the anilox. This was compared with the results obtained with 5 microlitre drops on the band of Harper 1 which was engraved by a CO_2 laser.

Anilox	lines per cm	Circumference of roll	Contact angle with water	Contact angle with diiodomethane	Total surface energy	Percentage of surface energy from polar interactions
Harper 1 CO_2 band	263	201mm	64° +/- 2	19° +/- 2	56 mJ/m^2	14%
Pira 1 (average of engraved bands)	149	353mm	52° +/- 2	15° +/- 2	62 mJ/m^2	21%

Table 4.4. Comparison of data obtained with the MAMS instruments on the bands of aniloxes Harper 1 and Pira 1 made by CO_2 lasers.

The contact angles obtained with diiodomethane drops on the two anilox were similar. The contact angles obtained with water were much lower on anilox Pira 1. This translates to a surface energy which is much more polar than that of anilox

Harper 1. There is no agreement in the results that could be considered a characteristic of the CO_2 laser that is independent of the anilox. There are however many unknowns which make the comparison of the engravings difficult. The engravings are made at different angles. Harper 1 was engraved at 60° whilst Pira 1 was engraved at 45°. Anilox Pira 1 is of unknown age and the type of CO_2 technology used to make it is unknown. The chemical composition of the ceramic is known to vary between manufacturers. To evaluate any differences in the ceramic, comparisons of the polished unengraved areas were made.

4.1.4 Comparison between the polished unengraved bands on aniloxes Harper 1 and Pira 1

The contact angles on the polished band of the Pira 1 were seen to be different to those observed on Harper 1. Table 4.4 shows the data for the two polished bands.

Anilox	Circumference of roll	Contact angle with water	Contact angle with diiodomethane	Total surface energy	Percentage of surface energy from polar interactions
Harper 1	201mm	56°	20°	59.6 mJ/m^2	20%
Pira 1	353mm	50°	14°	63.8 mJ/m^2	22%

Table 4.5. Comparison of data obtained with the MAMS instruments on the polished bands of aniloxes Harper 1 and Pira 1.

Since the nature of the ceramic on the Pira roll is unknown, it is impossible to rule out chemical differences between the two ceramic bands. However the percentage of the surface energy due to polar interactions (and the non-polar interactions) was comparable for the two anilox rolls. This suggests that the difference between the observed contact angles is not a chemical one but as a result differing distortions of the drops due to the difference in curvature between the rolls.

The Pira roll had a larger circumference than Harper 1. Initially it was believed that a large curvature would produce more accurate results, as the area underneath the drop would be a closer approximation to a flat surface. Unfortunately, having a shallower curvature produced some practical problems when taking the measurements. With the small curvature of anilox Harper 1, it was very easy to see when the drop was at the zenith of the roll. When measurements were made on Pira 1, it was much more difficult as the zenith was less defined. Any error in drop position resulted in the camera taking a picture with the bottom of the drop obscured by the roll. The instrument would then report a smaller contact angle.

4.2 Printing with anilox Pira 1 on a wide web flexographic Press

The anilox Pira 1 was designed for use on the research press at Pira International. The press is an Italian OMAT. A schematic drawing of the press is shown in Figure 4.1. In order to remove the influence of the transfer properties of the printing plate from the results, the web was redirected to run between the anilox and the plate cylinder. The print was made directly from the anilox in a style analogous to gravure printing. A plate was mounted onto the plate cylinder to act as a cushion between the plate cylinder (which was acting as the impression cylinder) and the web. The contact between the paper and the anilox could therefore be achieved at normal printing pressures for flexographic printing. The original web path is indicated in Figure 4.1 with a blue line; the new web path is shown as a red line.

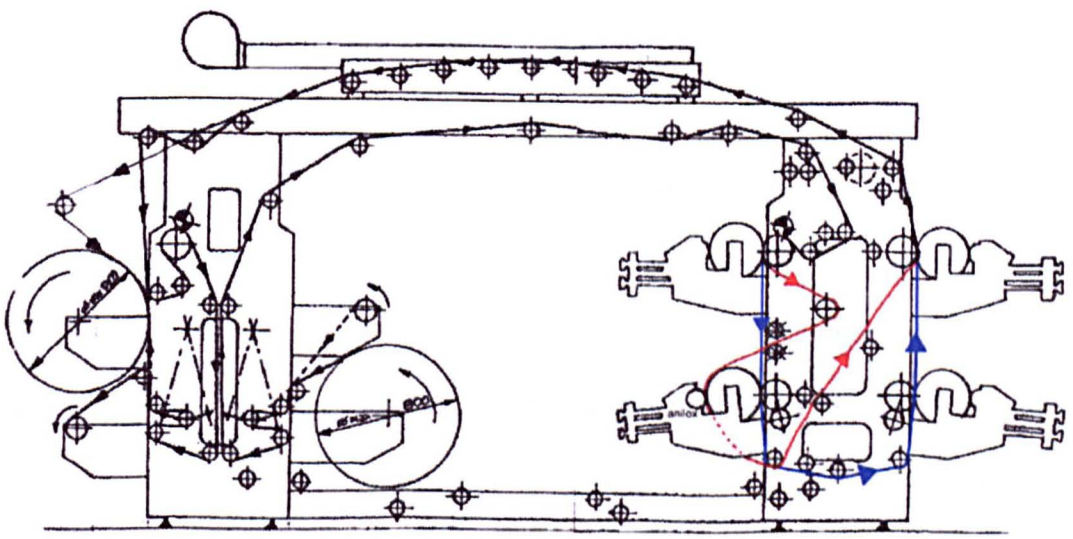

Figure 4.1. A diagram of the Pira flexo press showing the modified web path used to print from anilox Pira 1.

The substrate used for the trial was uncoated paper donated by Pira International. It was made by Stora Enso and had the brand name 4CC. Its weight was 250gsm and it had been calendared. The paper spanned two of the anilox bands and as bands 1 and 2 were at the centre of the roll they were the ones from which printing took place.

The ink used was UV ink donated by Coates Lorilleux. (Now part of the Sun Chemical group) It was a low viscosity, free radical cyan ink with the brand name Arena.[128] It was selected as the lowest viscosity UV cyan available from Coates at that time. The viscosity of the ink was 3 poise. The viscosity was also tested with a Zahn cup and it took 100 seconds for the ink to pass through Zahn cup 3. However, the thixotropic nature of the ink made its viscosity measurement in this way of little value. A high viscosity UV ink with a viscosity of 15 poise was also supplied as it had been hoped to measure the affect of ink viscosity on transfer from the anilox. This ink was extremely thixotropic and due to problems pumping the ink into the doctor blade chamber it could not be used in the trial.

The printing speed was varied between 25 and 100 metres per minute. Printing pressure was varied from the lowest possible pressure to the highest pressure obtainable at the anilox plate nip. The print densities were measured 10 times at 4 points across each band giving a total of 40 measurements per band at each pressure. An extra point was measured on the prints made at 50 m/min giving a total of 50 measurements for each band at each pressure at this speed. A repeating light line was visible across the print perpendicular to the web. The repeat length of the line was found to correspond to the circumference of the anilox and it was concluded that the line was due to anilox plugging. Optical density measurements were made but to

avoid inaccuracies no measurements were taken on areas printed by the plugged cells. The density measurements are shown in full in Section A4-2 of the appendix and summarised in table 4.6. (The data is also presented in graphical form in Figures 4.2 and 4.3.)

Speed (m/min)	Light Pressure		Medium pressure		High Pressure	
	mean OD	Standard deviation	mean OD	Standard deviation	mean OD	Standard deviation
	Band 1		**Band 1**		**Band 1**	
25	**0.62**	0.04	**0.71**	0.05	**0.68**	0.07
50	**0.64**	0.04	**0.66**	0.05	**0.65**	0.04
75	**0.47**	0.04	**0.55**	0.04	**0.65**	0.03
100	**0.44**	0.03	**0.51**	0.03	**0.54**	0.04
	Band 2		**Band 2**		**Band 2**	
25	**0.68**	0.04	**0.78**	0.03	**0.74**	0.07
50	**0.69**	0.04	**0.70**	0.03	**0.73**	0.03
75	**0.53**	0.04	**0.61**	0.04	**0.68**	0.03
100	**0.48**	0.03	**0.55**	0.03	**0.58**	0.04

Table 4.6. Density measurements taken from the prints made by anilox Pira 1 on the research press at Pira International. (Using densitometer model Gretag D 186)

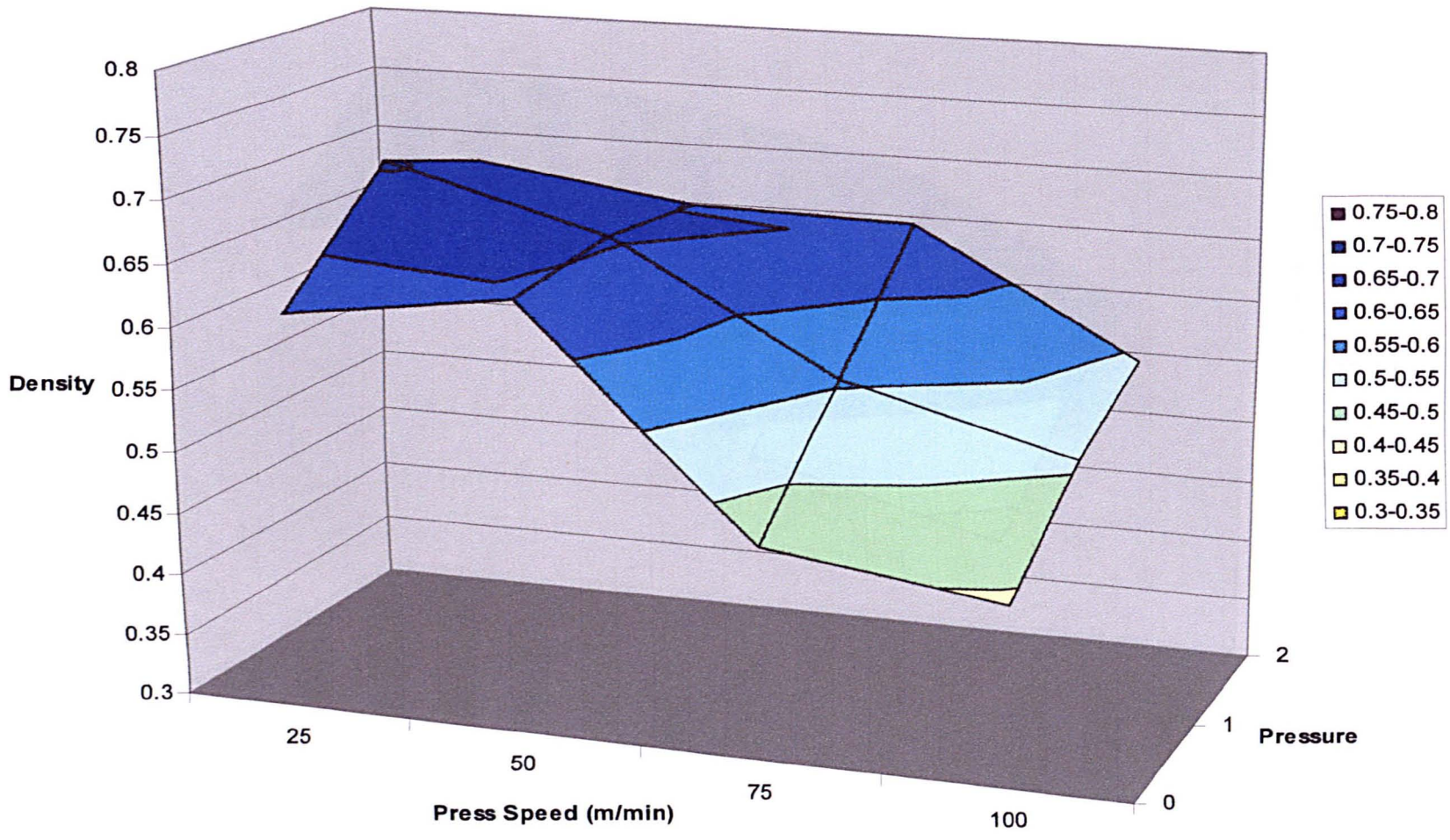

Figure 4.2. The variation in print density with printing pressure and press speed. (Band 1)

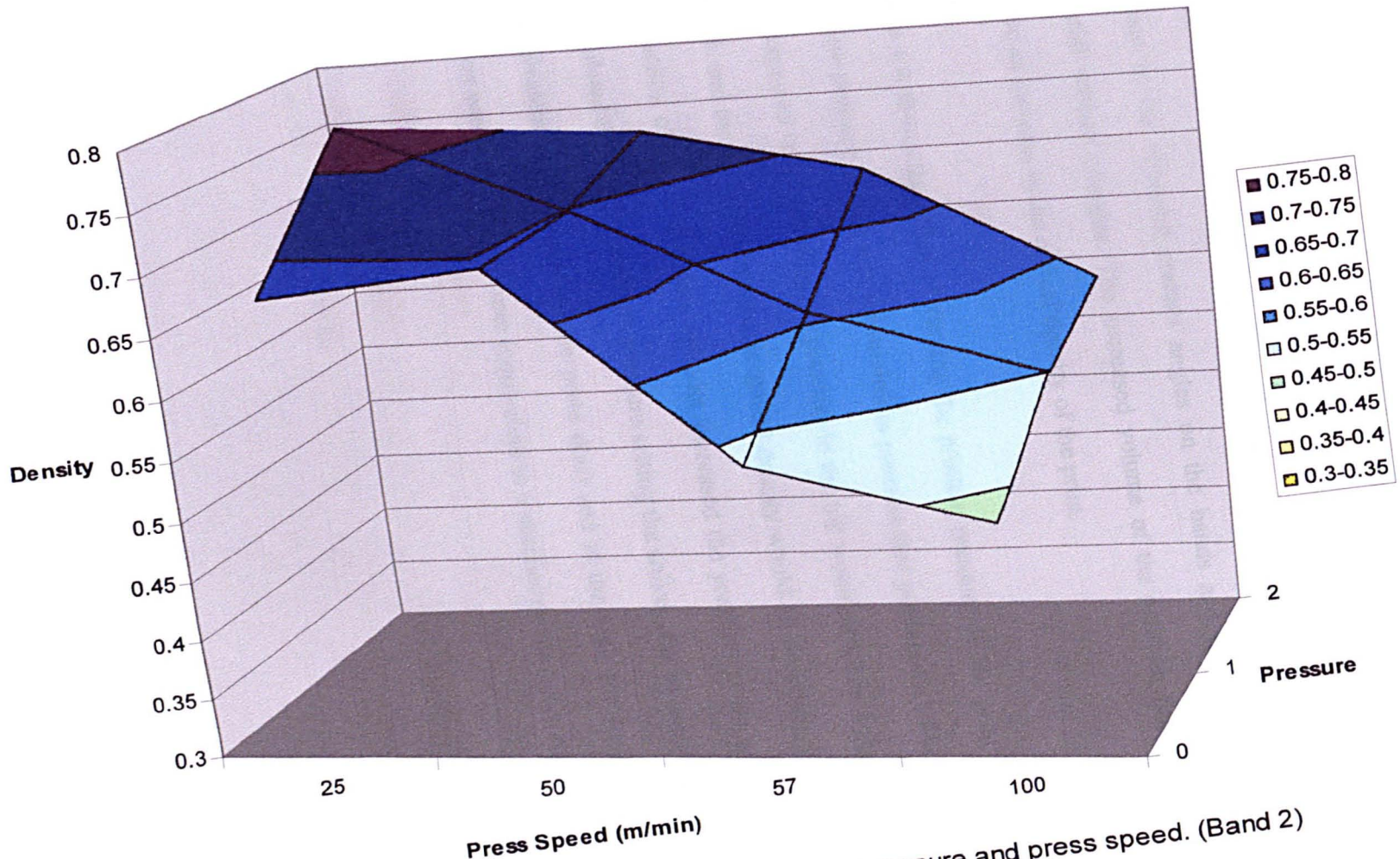

Figure 4.3. The variation in print density with printing pressure and press speed. (Band 2)

As can be seen from Figures 4.2 and 4.3, the optical densities measured on the print from band 2 are consistently higher than those measured on the print from band 1. This is true for all pressures and speeds. This was expected as band 2 was engraved to hold a greater volume of ink than band 1. As discussed in Sections 4.1.2 and 4.1.3, the difference in cell geometries was not sufficient to produce a difference in the observed contact angles on the bands and therefore in the calculated surface energies. The increased volume of the cells on band 2 did produce an increase in the optical density of the print.

Figure 4.4 shows the effect of varying the printing pressure on the print density. The low-pressure setting was the minimum pressure that produced a solid print. It was expected that increasing the pressure in the nip would result in a thicker film of ink and therefore an increase in optical density would be observed. Advancing the anilox closer to the plate cylinder increased the pressure at the nip. It was calculated than on the medium pressure setting the anilox was advanced 0.075mm (equivalent to 3 notches on the press dial) and at the high pressure setting the anilox was advanced 0.15mm (equivalent to 6 notches on the press dial)

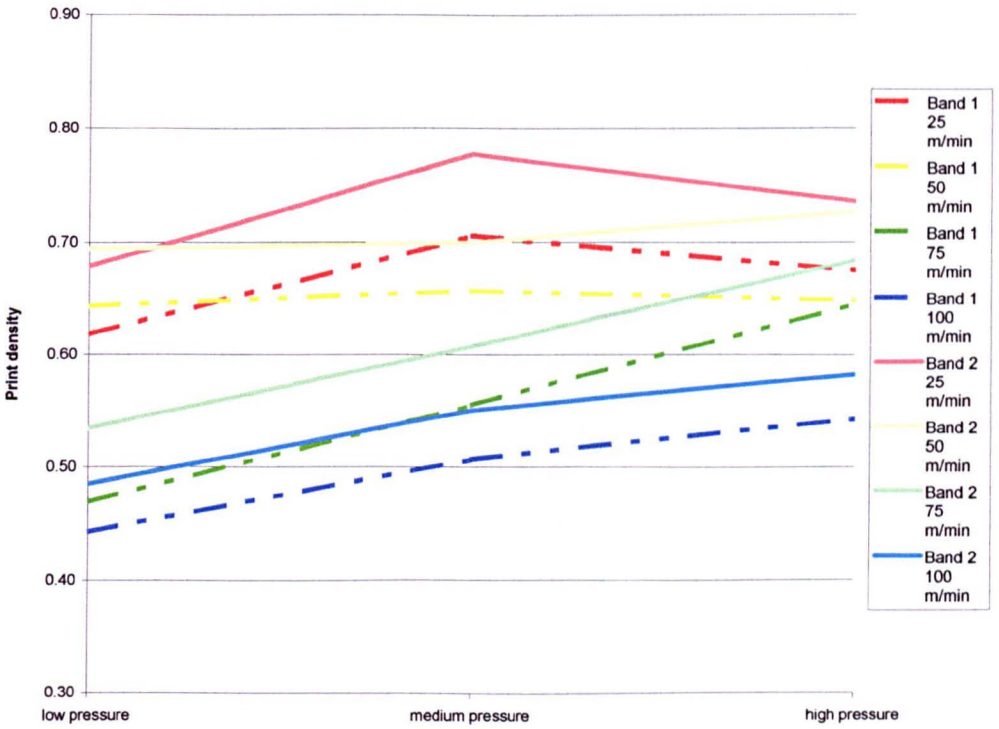

Figure 4.4. The influence of printing pressure on optical density for bands 1 & 2.

At 25 metres per minute the increased pressure from medium to high was seen to be detrimental to the print density. It was hypothesised that at this speed the ink was been driven into the paper and had time to be absorbed before it reached the curing unit. At 50 metres per minute pressure was curiously seen to have very little effect on print density. At higher speeds, the increase in pressure produced an increase in optical density.

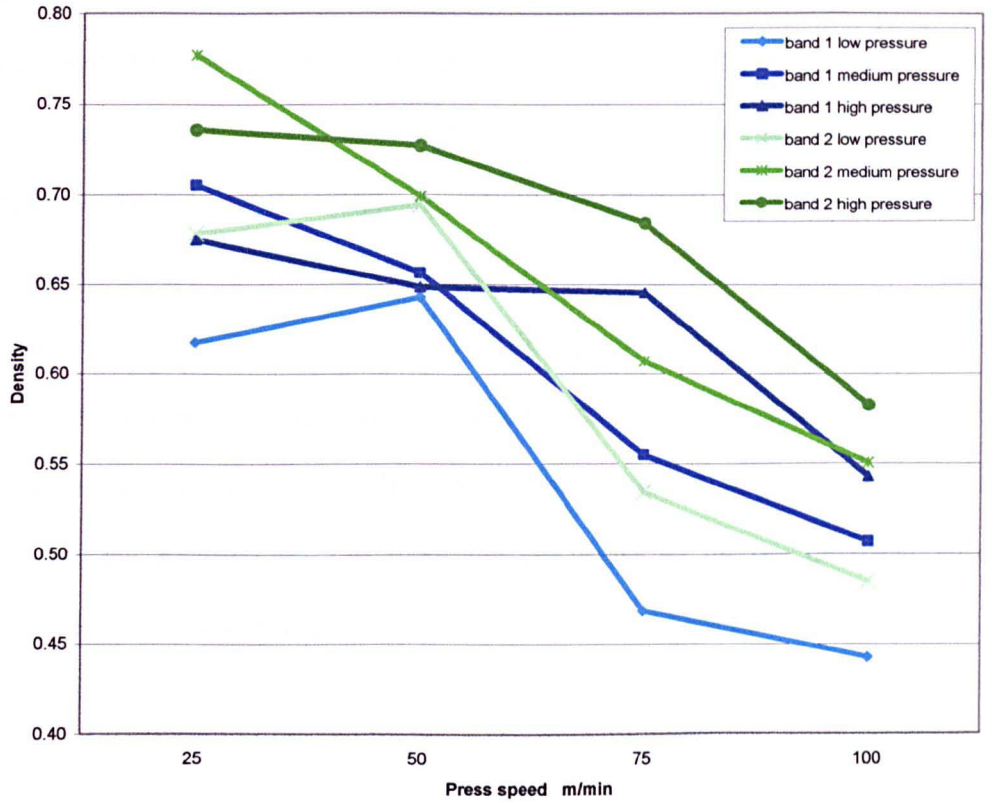

Figure 4.5. The influence of Press speed on optical density for bands 1 & 2.

In general, optical densities increase with increasing film weight. This is consistent with Fouche and Blayo's observations for an ink based around a low molecular weight oligomer at low printed film weight. [72] Again, there is an anomaly at 50 metres per minute, particularly at the low-pressure setting. It is proposed that 25 metres per minute the rotation speed of the anilox is insufficient to release the optimum amount of ink. At 50 metres per minute the rotational force becomes sufficient to sheer thin the ink and propel the ink towards the substrate.

The standard deviation of the optical density measurements was larger than expected. This was due to the low quality of the printed solid due to poor contact between the rough surfaces of the anilox and paper. A coated paper, 4CC Art, also made by Stora Enso, was originally selected for the trial and the print from both bands of the anilox onto this paper was much more uniform. The supply of the coated paper was however limited and initial problems curing the ink lead to an unforeseen amount of waste. In order to get a complete set of results an alternative paper was obtained.. Although some prints were made on coated paper at low speeds, the pressure settings were not the same as on the uncoated paper. Therefore direct comparisons between the papers could not be made.

4.3 The relation of optical density to film thickness and ink transfer

In order to assess the amount of ink transferred from the anilox cell to the substrate two attempts were made to measure the ink film thickness of the print. The first method was a direct measurement using an optical microscope in conjunction with specialist software. The second method was an indirect approach using a series of calibration prints of known density and film weight produced on a Mickle proofer.

4.3.1 Using optical microscopy to assess film thickness

In order to relate the optical densities measured to the film thicknesses laid down by the anilox, sections of the prints were examined by optical microscopy. Samples were prepared and analysed at Coates Lorrelleux. Small strips of the print were set in resin. Then cross sections of the print, held rigid by the resin were cut using a microtome. The slices of resin-encased print were placed under the microscope. Figure 4.6 shows a cross section of the print. The blue areas are the ink. The yellow to orange areas are the paper fibres. The thin slice of resin was very difficult to handle and a crease is clearly visible running diagonally across the image.

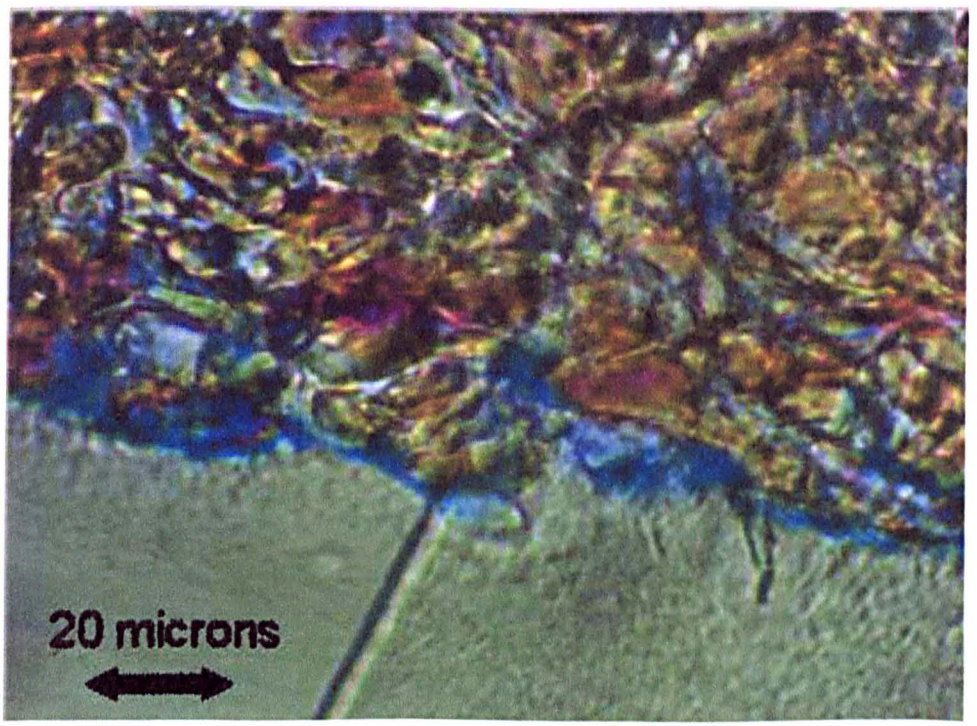

Figure 4.6. An optical micrograph of a cross-section of print.

The sample featured in Figure 4.6 is from band 1, printed at 75 metres per minute and low pressure. Six samples were analysed in all. All were from band 1 and covered all three pressure settings and speeds from 25 to 75 metres per minute. A computer program was used to provide measurements of the ink film thickness. Judgement was, however, required to identify the area of printed film at the substrate surface. Copies of the results obtained are included in the Section A4-3 of the appendix. There was obvious penetration of the blue ink into the paper. The unevenness of the print and the small amount of ink transferred also contributed to the poor accuracy of the measurements.

The values obtained for the film thickness were plotted against optical density to produce a calibration curve from which film thickness could be predicted from measured optical densities. This plot is shown in Figure 4.7.

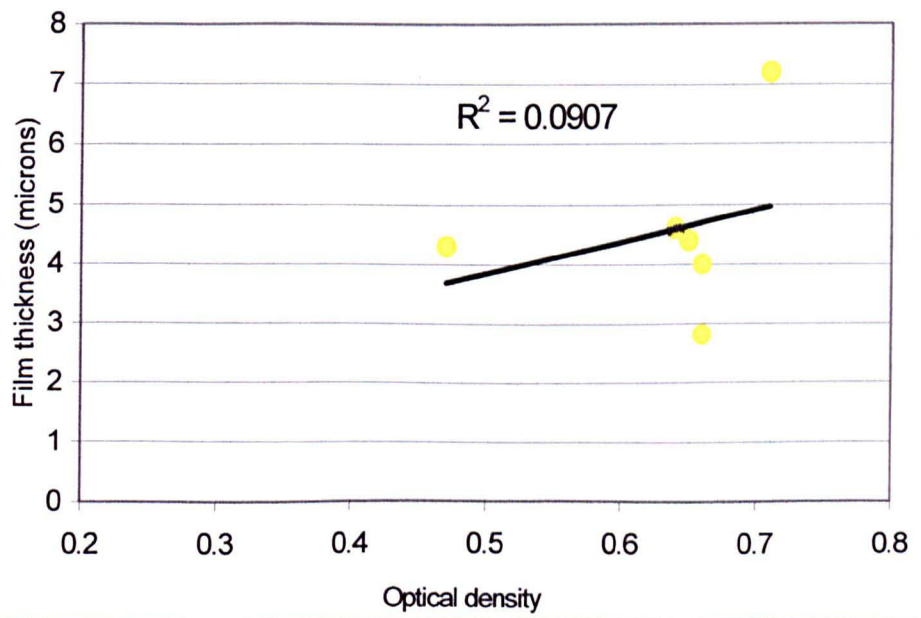

Figure 4.7. Correlation of film thickness as measured by optical microscopy to optical density.

The results did not show any relationship between film thickness and optical density. This was attributed to poor print quality, absorption of the ink and very uneven film thickness. As indicated in the results, the standard deviation of some of the film thickness results was several times that of the reported value.

The print quality of the Pira 1 prints was too low for a meaningful film thickness value to be obtained from a small cross section of print.

4.3.2 Using a proofing press to estimate film weight

An alternative method was employed to relate optical density to film thickness, by making a series of calibration prints of known film weights, using a piece of equipment called the Mickle proofer. Sample of the ink and substrate from the press trails were used for these prints to ensure consistency.

The Mickle proofer is a three-roll distribution system with a removable printing carriage. Prints are made from the carriage on a separate printing machine A diagram of the Mickle proofer is shown in Figure 4.8.

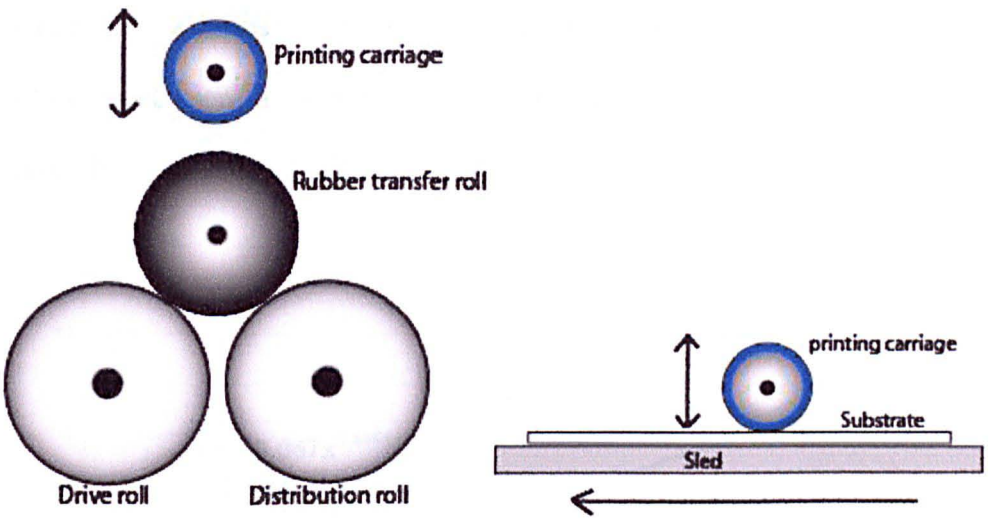

Inking system Printing system

Figure 4.8 The component rolls of the Mickle proofer.

The rubber transfer roll was inked and the drive roll activated. The friction between the drive roll and the transfer roll powered the transfer roll, which then turned the distribution roll. The distribution roll moved with a reciprocating action to evenly distribute the ink. When an even distribution of ink was judged visually to have been attained, the printing carriage was placed in contact with the transfer roll. The carriage was left to ink for at least a minute. When the carriage was evenly inked it was removed, its weight recorded, and it was placed onto the printing machine. The printing machine produced a print of 0.2m by 0.05m or $0.01m^2$, which was then immediately cured under a UV lamp. The carriage was then reweighed to determine the amount of ink that had been transferred to the substrate; the carriage was weighed to four decimal places.

A series of prints was made with a range of film weights. The optical densities of these prints were measured and plotted against the film weights as shown in

Figure 4.9. Ten density measurements were taken on each print using a Gretag D 186 densitometer. These measurements are included in the Section A4-4 of the appendix.

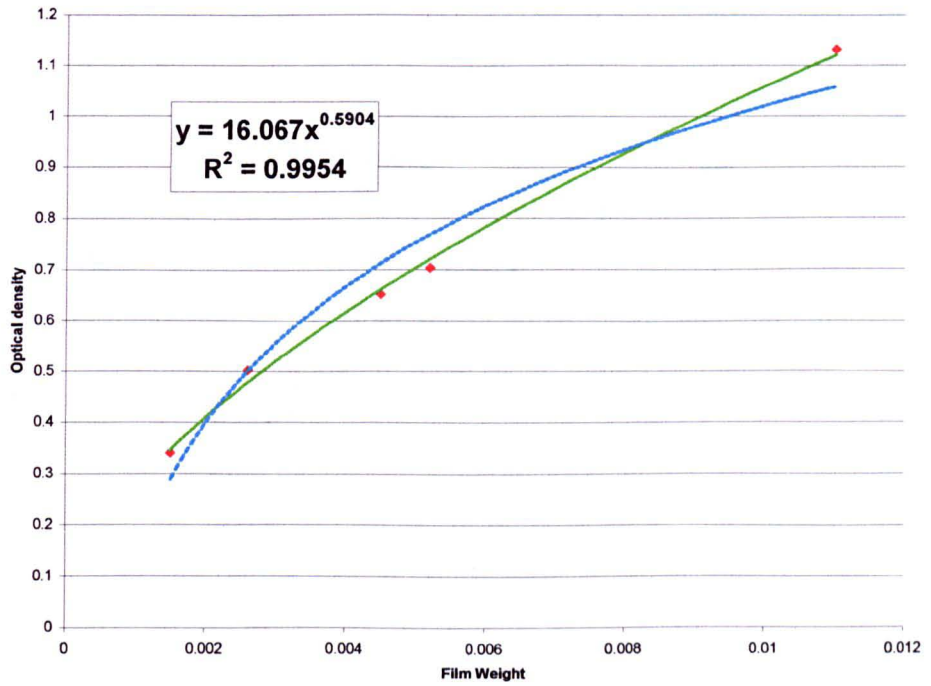

Figure 4.9. Film weight of prints made by the Mickle proofer, plotted against optical density.

As expected the relationship between optical density and film weight was not linear. A logarithmic curve fit was made and is shown in Figure 4.9 as the light blue broken line. A far better curve fit was achieved with a power relationship curve as shown by the green line. The R^2 value, which indicates the accuracy of the curve fit to the data was 0.9954.

The estimated error of the density measurements was obtained from the standard deviation of the results and found to be 0.3. The error of the film weight was

estimated at 0.0005g. When the error bars were added to the data it was noted that the logarithmic curve could be considered reasonable within the bound of the experimental error. It was however decided to use to power relationship as the calibration curve due to the accuracy of the curve fit to the data.

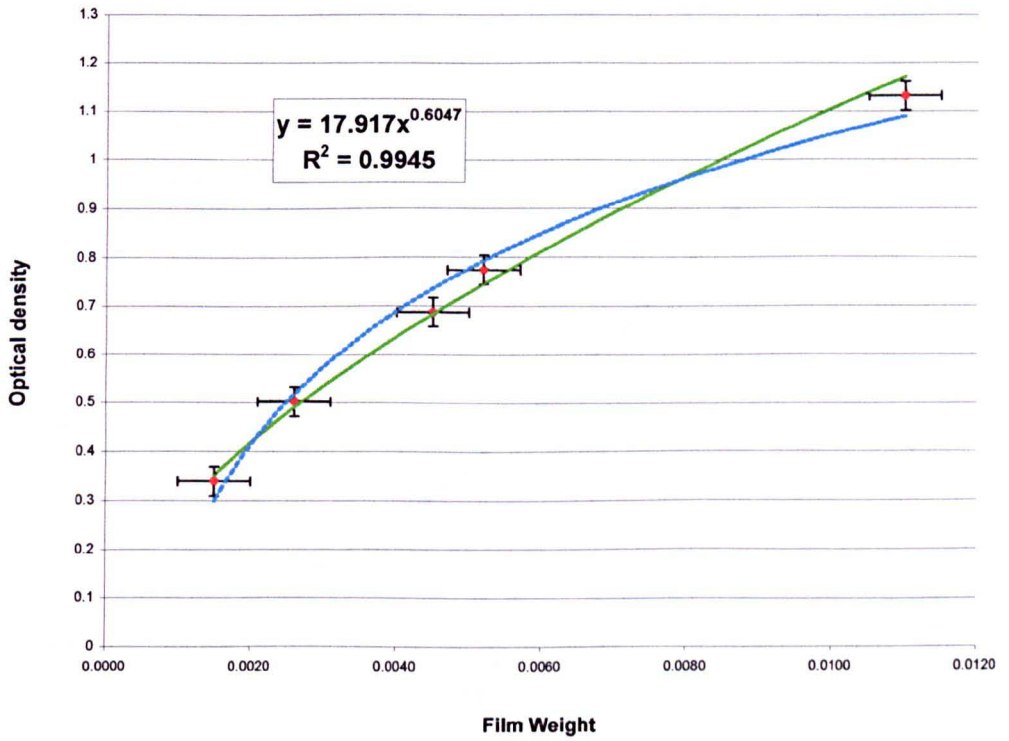

Figure 4.10. The error involved in the measurement of optical density and film weight, from the Mickle proofer data.

The data in Figures 4.9 and 4.10 were presented with optical densities on the y-axis. However in order to more easily predict the film weight of a known density series it is helpful to have the unknown, that is the film weight, as the y term. The equation of the best-fit curve could then be used to calculate the y term, (film weight) for any given value of the x term (the optical density). Figure 4.11 shows the calibration curve in its final form.

The density results from Table 4.6 were put into the equation of the calibration curve. The calculated film weights are shown in Table 4.7.

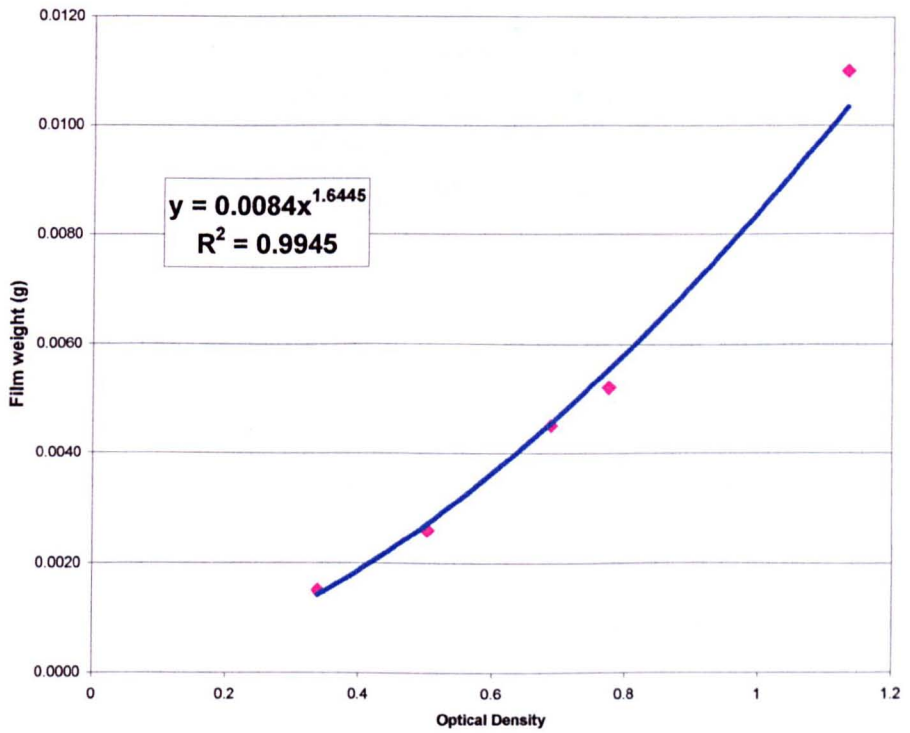

Figure 4.11. The calibration curve used to calculate the film weight of the prints from anilox Pira 1.

		Film weight in grams		
	Speed m/min	Light pressure	Medium pressure	High pressure
Band 1	25	0.0038	0.0047	0.0044
	50	0.0041	0.0042	0.0041
	75	0.0024	0.0032	0.0041
	100	0.0022	0.0027	0.0031
Band 2	25	0.0044	0.0055	0.0051
	50	0.0046	0.0047	0.0050
	75	0.0030	0.0037	0.0045
	100	0.0026	0.0031	0.0035

Table 4.7. The calculated film weight in grams of a $0.1m^2$ area of print.

The volume of ink put down on the substrate could then be calculated from the film weight. A value for the density of the ink was not available so the weight of $1cm^2$ of ink was measured. Ten repeat measurements were made. The average weight was found to be 1.194g. Measurements were made at 23°C. The anilox ink carrying capacity was specified in cubic centimetres per square metre. The weight of ink on 0.01g as calculated above was converted to a volume of ink by multiplication by 0.8375, the volume of 1 gram of ink.

		Volume transferred in cm^3/m^2		
	Speed	Light pressure	Medium pressure	High pressure
Band 1	25	0.3184	0.3962	0.3686
	50	0.3401	0.3520	0.3450
	75	0.2022	0.2670	0.3423
	100	0.1841	0.2300	0.2575
Band 2	25	0.3717	0.4646	0.4247
	50	0.3860	0.3904	0.4164
	75	0.2507	0.3095	0.3769
	100	0.2138	0.2634	0.2893

Table 4.8. The amount of ink transferred to the substrate in cm^3/m^2.

The measured holding capacity of the bands were 3.3 and 3.8 cm^3/m^2 for bands 1 and 2 respectively Table 4.9 shows the amount of ink transferred as a percentage of the amount of ink held by the anilox.

Percentage of cell volume transferred				
	Speed	Light pressure	Medium pressure	High pressure
Band 1	25	9.6	12.0	11.2
	50	10.3	10.7	10.5
	75	6.1	8.1	10.4
	100	5.6	7.0	7.8
Band 2	25	9.8	12.2	11.2
	50	10.2	10.3	11.0
	75	6.6	8.1	9.9
	100	5.6	6.9	7.6

Table 4.9. Ink transfer from the anilox as a percentage of the carrying capacity of the anilox cells.

When the percentage transfer is considered the two bands of the anilox transfer a similar percentage of their holding capacity at any given pressure and speed. Overall the amount of ink transferred is much less than would be expected from conventional flexo printing via a printing plate.

4.4 Summary of results from anilox Pira 1

The findings from the work on anilox Pira 1 were

1. Varying the depth of a cell when all other variables are fixed does not affect the wettability of the engraving.

2. Differences in cell geometry that produce different amounts of ink transfer are not detectable by contact angle analysis.

3. Optical microscopy is only a useful tool for measuring film thickness if the film weight is sufficiently high and the ink coverage is even.

A third anilox was commissioned to have CO_2 and YAG engravings with the same size and number of cells. This anilox was designed to fit on a laboratory scale press in order for contact angle measurement and ink transfer to be studied in tandem. Harper also made this anilox so that direct comparisons with the work done on Harper 1 could be made.

5. Analysis of anilox roll Harper 2

5.1 Contact angle analysis of anilox Harper 2

The original anilox studied, anilox Harper 1, was designed to have comparable cell depths, as when the study began this seemed an appropriate starting point from which the two methods of laser engraving the cells could be compared. The analysis of Pira 1 discussed in Chapter 4 revealed that varying the cell depth with respect to the cell opening had no effect on the wetting of the cells. A new anilox was therefore needed in order to determine if the wetting trend observed on Harper 1 was effected by differing numbers of cells in contact with the applied liquid drop.

A new anilox was produced for testing. As The Harper Corporation of America again provided this anilox it was termed Harper 2. Anilox Harper 2 was designed to have both CO_2 and YAG engravings with the same line screen so that any roughness effect caused by the number of cells in the area under the drop could be discounted. The cell volume was again kept constant. The specifications of the engravings as provided by the Harper Corporation are detailed in table 5.1.

Anilox band	Line screen (lines per cm)	Cell volume (cm^3/m^2)	Cell depth (microns)	Cell opening (microns)	Cell wall (microns)
CO_2	393	2.53	7.8	22.0	3.0
YAG	393	2.53	7.5	19.4	2.1

Table 5.1. Specifications of the banded anilox Harper 2.

Harper 2 was designed to fit on the RK mini web press to allow prints to be made, and consequently its diameter was slightly larger than that of Harper 1.

As with the Harper 1 anilox, contact angle measurements were initially measured using the MAMS instrument in the pressroom at Pira International. When the FTA instrument became available, the measurements were repeated in the laboratory at the London College of Communication.

5.1.1 Contact angle analysis using the MAMS instrument

The contact angle measurements on Harper 2 were carried out using the same MAMS equipment and grade of test liquid at the same conditions. A drop volume of 5μl was used for all measurements. As the experiment was done a year after the first tests on Harper 1, the measurements on Harper 1 were first repeated and found to agree well with the initial data as shown in Table 5.2. This demonstrates that the MAMS data for anilox Harper 1 was extremely reproducible. It is also interesting to note that in most cases the inclusion of a further twenty measurements had no effect on the standard deviation of the results. This demonstrates that the large standard deviations are produced by the lack of uniformity of the roll, rather than variations the measurement or drop dispensing technique. The data for the repeated measurements is in Section A5-1 of the appendix.

		5µl water original	5µl water repeat	new average 5µl water	5µl diiodomethane original	5µl diiodomethane repeat	new average 5µl diiodomethane
Polished band	**mean**	56°	56°	**56°**	20°	18°	**19°**
	standard deviation	2°	3	**2°**	3°	3°	**3°**
CO_2 band	**mean**	64°	64°	**64°**	19°	18°	**18°**
	standard deviation	2°	2°	**2°**	2°	4°	**3°**
YAG band	**mean**	76°	76°	**76°**	15°	14°	**15°**
	standard deviation	3°	4°	**3°**	4°	3°	**3°**

Table 5.2. A summary the results obtained by repeating the MAMS test on anilox. Harper 1.

Tests on anilox Harper 2 were carried out using the same test liquids under the same conditions. The results are summarised below in table 5.3 and are included in full in the Section A5-2 of the appendix.

		5µl water	5µl diiodomethane
Polished band	**mean**	**60°**	**21°**
	standard deviation	2°	2°
CO_2 band	**mean**	**75°**	**19°**
	standard deviation	3°	3°
YAG band	**mean**	**86°**	**26°**
	standard deviation	4°	3°

Table 5.3. Results for the contact angle analysis of anilox Harper 2 using the MAMS instrument.

The results showed the same trend in wetting with the polished band easiest to wet, followed by the CO2 band, with the YAG band again hardest to wet. There was more variation between the contact angle results on the three bands than with previous experiments. Table 5.4 shows the results on the two Harper rolls together for ease of comparison.

		Harper 1 Water	Harper 2 Water	Harper 1 Diiodomethane	Harper 2 Diiodomethane
Polished band	**mean**	**56°**	**60°**	**20°**	**21°**
	standard deviation	2°	2°	3°	2°
CO_2 band	**mean**	**64°**	**75°**	**19°**	**20°**
	standard deviation	2°	3°	2°	3°
YAG band	**mean**	**76°**	**86°**	**15°**	**26°**
	standard deviation	3°	4°	4°	3°

Table 5.4. Comparison between contact angle data for anilox rolls Harper 1 and 2 obtained using the MAMS instrument.

The mean contact angles observed with water on the polished ceramic bands of aniloxes Harper 1 and Harper 2 varied by 4°. This is equal to the sum of the standard deviations of the two results. These values are close enough to verify Harper's assurance that same type of ceramic was used to make both rolls.

There was a large difference between the contact angles observed on the YAG band using diiodomethane drops. This could indicate that the YAG band on Harper 2 is physically or chemically different to the YAG band on Harper 1. Harper had indicated that laser and ceramic were the same for both rolls.

The mean contact angle values from the test using water on the engraved bands of Harper 2 were much higher than those on Harper 1. It was hypothesised that this difference could be related to the difference in the line screen values. Considering the CO_2 bands, the line screen increased from 236 lines per centimetre on Harper 1 to 393 lines per centimetre on Harper 2. The contact angle was observed to increase by 11°. But in the case of the YAG band the line screen decreased from 472 lines per centimetre on Harper 1 to 393 lines per centimetre on Harper 2. The contact angle was also observed to rise by 10° ruling out any relation between the line screen and the observed contact angle.

The increase in roll circumference of anilox Pira 1 in relation to Harper 1 was believed to have produced a systematic error that reduced the observed contact angle. Harper 2 has a circumference of 254.5 mm and is therefore larger than Harper 1, which has a circumference 201.1 mm, but smaller than Pira 1 which has a diameter of 353 mm. The observed contact angle on the polished area of Harper 2 was very slightly larger than that observed on Harper 1. Although this does not support the above hypothesis, some of the difficulties experienced in centering the drop on the zenith were overcome when measurements on Harper 2 were made. Harper 2 is a much shorter in length than Pira 1. Markers were made which were attached to each end of Harper 2 and marked the zenith. The anilox could then be viewed from one end to ensure that the drop lined up with the markers. This technique could not be employed with Pira 1 as the length of the roll was such that accurate positioning in this way was not possible.

5.1.2 Contact angle measurements using the FTA instrument

The contact angles were also measured using the FTA instrument. As these measurements were taken at the same time as those on Harper 1 there was no need to reconfirm the Harper 1 results for consistency. The results are summarised in Table 5.5 and shown in full in the appendix in Section A5-3.

		Water FTA	Diiodomethane FTA
Polished band	**mean**	**74°**	**44°**
	standard deviation	3°	2°
CO_2 band	**mean**	**91°**	**43°**
	standard deviation	2°	2°
YAG band	**mean**	**105°**	**43°**
	standard deviation	2°	2°

Table 5.5. The results of contact angle analysis on anilox Harper 2 using the FTA instrument.

Again the contact angles reported by the FTA were seen to be significantly higher than those obtained using the MAMS instrument. This was again attributed to differences in the dispensing mechanisms between the two instruments. The results are compared with the contact angle data for Harper 1 (measured with the FTA instrument) and are shown in Table 5.6.

		Harper 1 water	Harper 2 Water	Harper 1 diiodomethane	Harper 2 Diiodomethane
Polished band	**mean**	**75°**	**74°**	**42°**	**44°**
	standard deviation	3°	3°	2°	2°
CO_2 band	**mean**	**84°**	**91°**	**43°**	**43°**
	standard deviation	2°	2°	2°	2°
YAG band	**mean**	**100°**	**105°**	**45°**	**43°**
	standard deviation	2°	2°	2°	2°

Table 5.6. Comparison between contact angle data for anilox Harper 1 and 2 obtained using the FTA instrument.

The results on the polished unengraved bands are very similar. This again indicates that the ceramic is comparable between the two anilox rolls and that the difference in curvature has no effect on the results. Increased water contact angles were again seen on the CO_2 and YAG bands, although the increase seen on the YAG band was only just outside the sum of the standard deviation of measurements. The results with diiodomethane drops showed no significant difference between the rolls. The change in dispersive wetting on the YAG band shown by the MAMS instrument is not reflected in the FTA results. The results on each instrument were repeatable indicating that a systematic difference is present in the results. It should be noted that the contact angles made by the diiodomethane were small and were at the limit at which the MAMS instrument could accurately measure.

5.1.3 Advancing and receding contact angles

Advancing and receding contact angle measurement was attempted in the same way as for Harper 1. Measurements were however more difficult to make on Harper 2 because its increased size made positioning under the FTA dispensing platform more difficult. The contact line moved entirely in one direction. Figure 5.1 shows a screen shot of a water drop being advanced over the CO_2 band. So long as the drop did not begin to preferentially spread down the sides of the roll, advancing contact angles could still be measured.

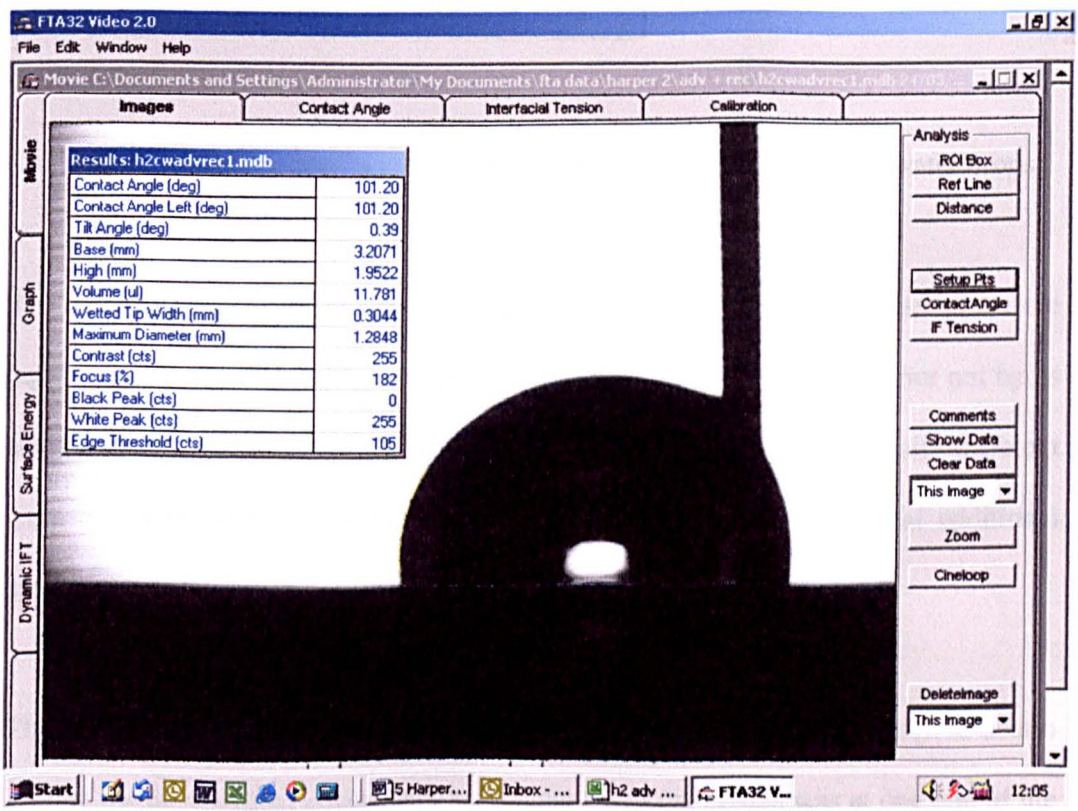

Figure 5.1. A screen shot of a water drop being advanced across the CO_2 band of Harper 2.

The contact angle was measured on the advancing side of the drop only and plotted against the diameter of the drop base to select the data for which the drop was advancing. The advancing angles were then averaged into a single result. A very small number of results were obtained. Four good measurements were recorded on the CO_2 band but only two on the polished and YAG bands. These measurements are shown in the Section A5-4 of the appendix. The average values are shown in Table 5.7.

	Polished band	CO_2 band	YAG band
Mean	93°	100°	107°
Standard deviation	1	1	4

Table 5.7. Advancing angles measured on the bands of Harper 2 using water drops.

The angle on the polished band is much higher than the value measured as the equilibrium angle. The angle measured on the CO_2 band is also higher but not by as large an amount. The angle measured on the YAG band is not statistically different from the angle measured using a static drop touched off with minimal additional spreading force.

The liquid was then pumped back into the dispensing syringe in an attempt to obtain a value for the receding contact angle. As the tip of the needle was at one end of the drop the drop detached from the needle tip before enough liquid was removed to make the contact line recede. This is illustrated in Figure 5.2. A change to the method was employed for anilox Harper 1. Advancing and receding measurements

were made separately with the tip repositioned to be at the centre of the drop before the drop was receded. This method could not be employed on Harper 2 as cleaning with surfactant accidentally changed the surface wettablity of the YAG band. This change to the surface of the anilox will be discussed in detail in Section 5.1.6.

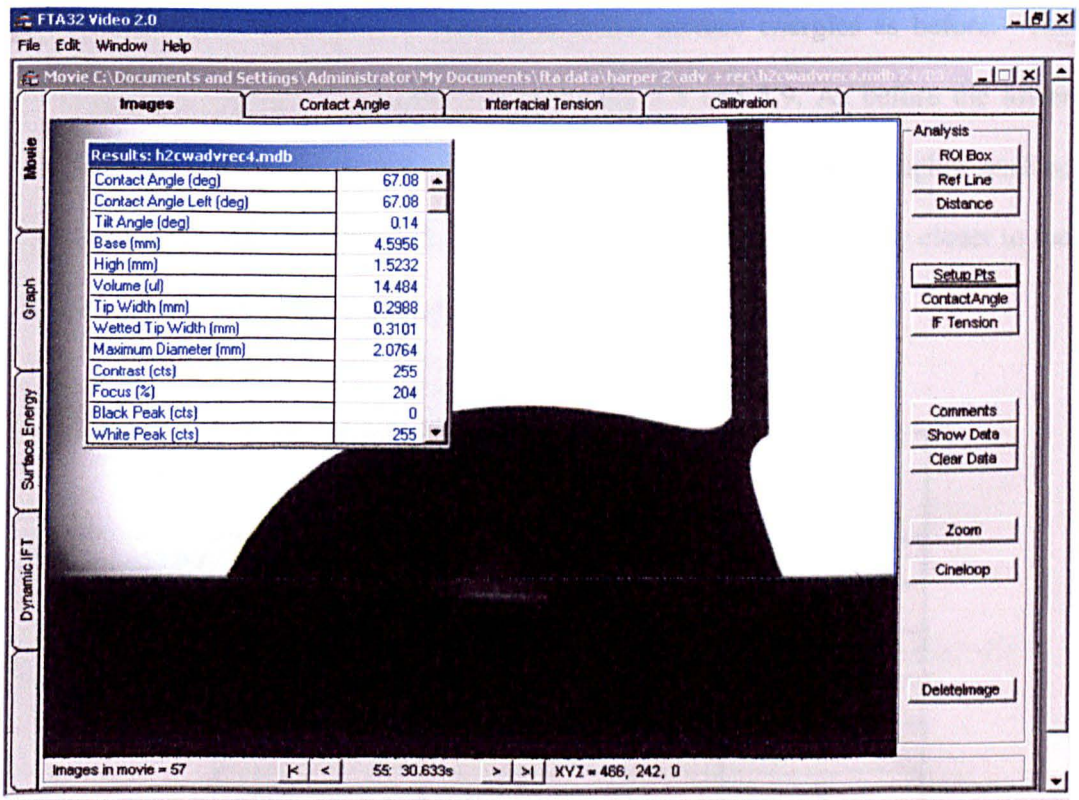

Figure 5.2 A screenshot showing the problem encountered when trying to obtain receding angles on anilox Harper 2.

It was not possible to measure advancing or receding contact angles using diiodomethane as the test liquid. When the liquid was advanced onto the roll surface it preferentially advanced down one side of the roll immediately due to its low

surface tension. There was no stable advanced drop to measure, nor to remove liquid from to observe the receding angle.

5.1.4 Surface energy calculations from the contact angle data

The contact angle results were used to calculate surface energies as before. The surface energy values are summarized in Tables 5.8 and 5.9. As before the lower contact angles reported by the MAMS instrument translated into higher surface energies. The result for the polished band with the FTA is again slightly closer to the literature value of 50 mJm^{-2} than the MAMS result.

		Mean surface energy mJm^{-2}	Standard deviation mJm^{-2}
Polished band	dispersive component	48	1
	polar component	10	1
	total surface energy	**58**	**2**
CO_2 band	dispersive component	48	1
	polar component	4	1
	total surface energy	**52**	**2**
YAG band	dispersive component	46	1
	polar component	1	1
	total surface energy	**47**	**2**

Table 5.8. Surface energies of the bands on anilox Harper 2 obtained from the MAMS data.

The surface energies calculated from the contact angles on all bands are within one standard deviation of the values calculated using the Harper 1 data. The large differences in observed contact angles made with water are again not reflected in the surface energy results. This again demonstrates the lack of sensitivity of surface energy as calculated by the geometric mean method.

		Mean surface energy mJm^{-2}	Standard deviation mJm^{-2}
Polished band	dispersive component	38	1
	polar component	6	1
	total surface energy	**44**	**2**
CO_2 band	dispersive component	38	1
	polar component	1	1
	total surface energy	**39**	**2**
YAG band	dispersive component	38	1
	polar component	0	0
	total surface energy	**38**	**1**

Table 5.9. Surface energies of the bands on anilox Harper 2 obtained from the FTA data.

The differences in the contact angles made by water on the engraved bands of Harper 2 were significantly higher than those observed on the engraved bands on Harper 1. This difference became small when the surface energies were calculated, however it can be seen when the percentage polar make-up of the total surface energy is considered. Figure 5.3 shows the polar and dispersive components of each band of the Harper aniloxes as percentages of the overall surface energy.

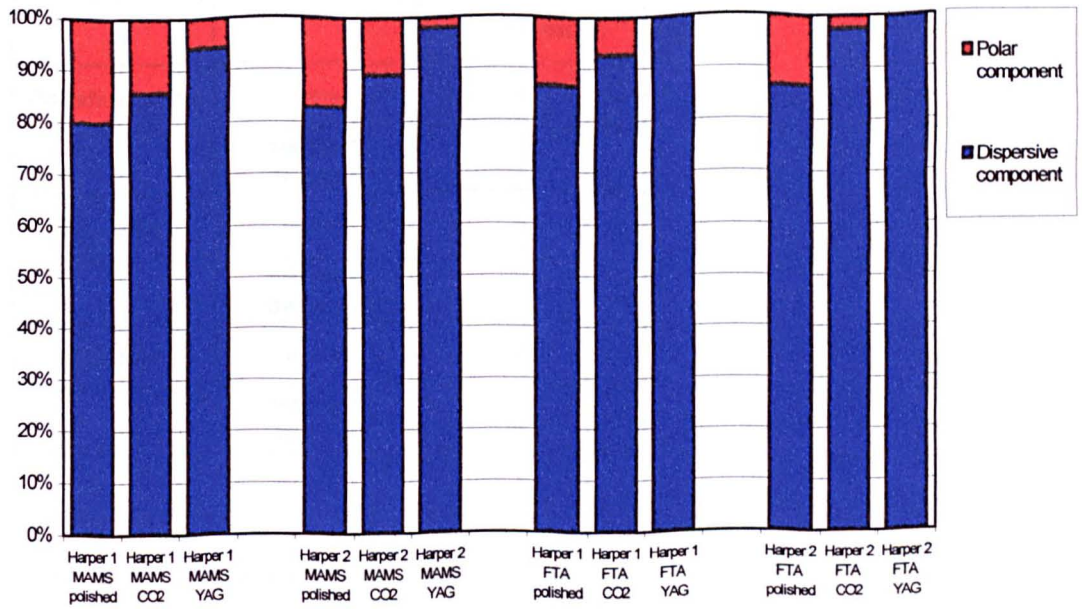

Figure 5.3.The polar component as a percentage of the overall surface energy on the Bands of aniloxes Harper 1 and Harper 2.

There is a visible reduction in the polar make up of the CO_2 bands that are shown by both instruments. The FTA instrument does not show the difference in polar wetting on the YAG band, as the polar component is so small it is reported as zero in all cases.

5.1.5 The acid-base theory of surface energy

In order to calculate the acid-base components of the surface energy, contact angle measurements with formamide were again made. These measurements were only made on the FTA instrument, as the MAMS instrument was no longer available for use. The results are tabulated in table 5.10 and are included in full in Section A5-5 of the appendix.

		Formamide
Polished band	**mean**	**43°**
	standard deviation	3°
CO_2 band	**mean**	**61°**
	standard deviation	1°
YAG band	**mean**	**65°**
	standard deviation	2°

Table 5.10. Contact angles made by formamide drops on the bands of anilox Harper 2.

The measurements are within one standard deviation of the formamide results obtained on Harper 1 in all cases. The contact angles made by water, diiodomethane and formamide on each band were entered into the FTA software, which performed the acid-base calculations. The values returned are shown in Table 5.11 along with an estimate of the error associated with the measurement, which is based on a repeat of the calculation using the mean contact angle data plus or minus the standard deviation in a way such as to produce the largest difference in the result.

	Polished band		CO_2 band		YAG band	
	mean	standard deviation	mean	standard deviation	mean	standard deviation
Total surface energy	43.5	1.9	39.0	1.2	37.2	1.2
Dispersive component	37.5	1.1	38.1	1.1	38.1	1.1
Polar component	5.94	0.08	0.89	0.18	-0.83	0.07
Acid component	1.92	0.05	0.26	0.11	0.16	0.09
Base component	4.61	1.20	0.75	0.50	-1.10	0.03

Table 5.11. Components of the total surface energy (in mJm^{-2}) calculated from contact angle data by the FTA software.

Again there is a change in acid-base nature of the surface caused by the presence of engraved cells. The dominant polar component of polished ceramic is the basic component. Engraving anilox Harper 2 with the CO_2 laser reduces the level of basic character significantly. The acidic character is also reduced. Engraving with the YAG laser again produces a small negative value for the basic component. The small amount of polarity left on the YAG band is acidic. The errors quoted are the result of repeating the acid and base calculations using the mean contact angle plus and minus one standard deviation. In the case of the acid and base component the estimate of error produced is very large in comparison to the small values of the components. The polar component quoted should be the sum of the acid and base components. However as with the data presented in Section 3.5, the numbers in Table 5.11 do not add up. That is because there is no exact solution to the three simultaneous equations from which the acid and base components are calculated. Again the lack an exact solution and the large calculated errors are due to inaccuracies in the contact angle data. These inaccuracies are in part random

measurement errors and in part due to the changing value of the contact angle with the variable surface of the roll. The values for the acidic components on the engraved bands are not statistically significant. They are however lower than the value calculated for the polished band. The basic component is statistically different on all three bands.

5.2 Ink transfer from anilox Harper 2

Anilox Harper 2 was designed to fit on the gravure station of a RK mini-web press. Using this set-up prints could be made directly from the anilox as made from anilox Pira 1 on the Pira press. Samples of the ink and paper were retained from the Pira press trial. The paper was cut down and rewound onto smaller cores in order to fit the RK press. The original ink had gelled, a fresh sample was obtained from Coates; it was made to as close to the original recipe as possible. However some of the raw materials had to be substituted, as the originals were no longer available. Coates did not make details of the substitutions available. The pressure at the anilox/paper nip was 40 PSI. (40 pound-force/square inch (PSI) = 0.276 Newton/square millimetre) Prints were made at two speeds; five metres per minute and 10 metres per minute, which was the top speed attainable. The UV lamp was set at a nominal power of 50 watts per centimetre for the lower speed and 83 watts per centimetre for the higher speed. Ten samples of print were cut from the web. Each sample was 50mm in length. Density measurements were made on these prints. The results are summarised in table 5.12 and shown in full in the appendix in Section A5-6.

		Optical density 5 m/min CO_2	Optical density 10 m/min CO_2	Optical density 5 m/min YAG	Optical density 10 m/min YAG
edge	**mean**	**0.52**	**0.47**	**0.57**	**0.49**
	standard deviation	0.04	0.02	0.05	0.02
mid 1	**mean**	**0.44**	**0.43**	**0.50**	**0.44**
	standard deviation	0.04	0.02	0.06	0.03
centre	**mean**	**0.36**	**0.35**	**0.44**	**0.40**
	standard deviation	0.05	0.02	0.05	0.02
mid 2	**mean**	**0.36**	**0.34**	**0.42**	**0.39**
	standard deviation	0.05	0.02	0.05	0.03
join	**mean**	**0.37**	**0.33**	**0.40**	**0.36**
	standard deviation	0.06	0.03	0.06	0.02

Table 5.12. Optical densities measured at 5 places across prints made from the YAG and CO_2 bands of Harper 2.

The ink density across the prints was not uniform. In order to quantify the variation of ink transfer across each band measurements were made of the edge of the print, at mid points 1 and 2, at the centre of each band and at either side of the join. These points are illustrated in Figure 5.4. Five measurements were made at each point on each sample. There were ten print samples. Fifty measurements were therefore made at each point and a total of two hundred and fifty measurements were made on each band.

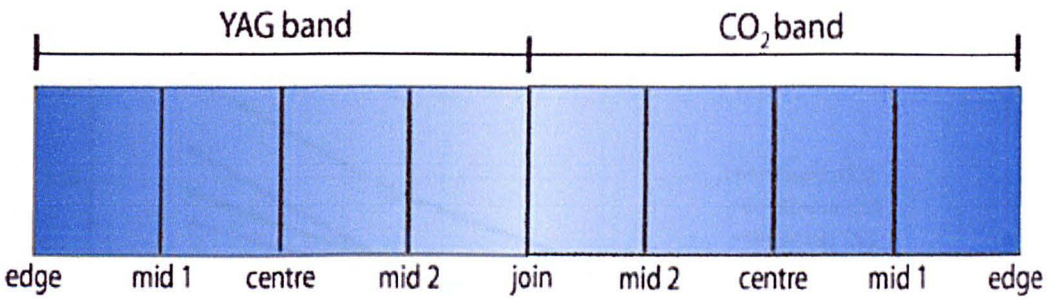

Figure 5.4. The points across the printed sample at which measurements were made.

The data from Table 5.12 is represented graphically in Figure 5.5. There is a large difference in optical density across the print area of both bands. In all cases the optical density of the prints from the YAG engraving are larger than those from the CO_2 band. This supports the literature claims that YAG cells transfer a greater percentage of the ink that they hold. [24] The difference between the optical densities of the prints from the two bands was smaller than expected. The standard deviations of the measurements are shown in table 5.12. These were large and were in most cases as large as the differences between the bands. The variation in optical density was due to the unevenness of the print produced. Printing directly from the anilox does not produce an even lay of ink as the anilox and paper surfaces are both rough and contact between them is uneven. As all the optical densities on the print from the YAG band were higher than those from the CO_2 band it is reasonable to conclude that more ink was transferred from the YAG band than from the CO_2 band despite the statistical uncertainty. Visual assessment also confirmed that the overall optical density was higher on the YAG band.

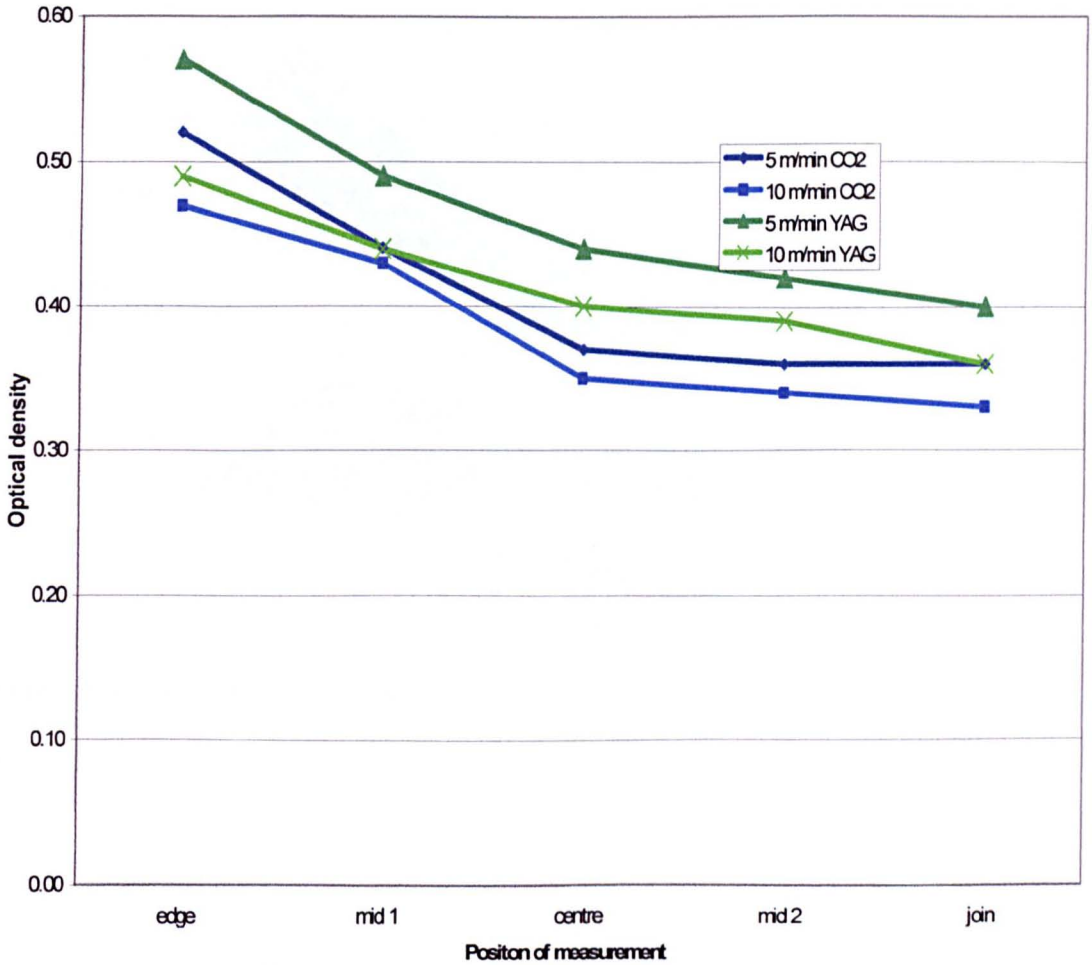

Figure 5.5. The variation of optical density across the prints made by anilox Harper 2.

The variations in print density across the bands of Harper 2 with changing speed are shown as 3D surfaces in Figures 5.6 and 5.7. In all cases less ink was transferred as the speed increased.

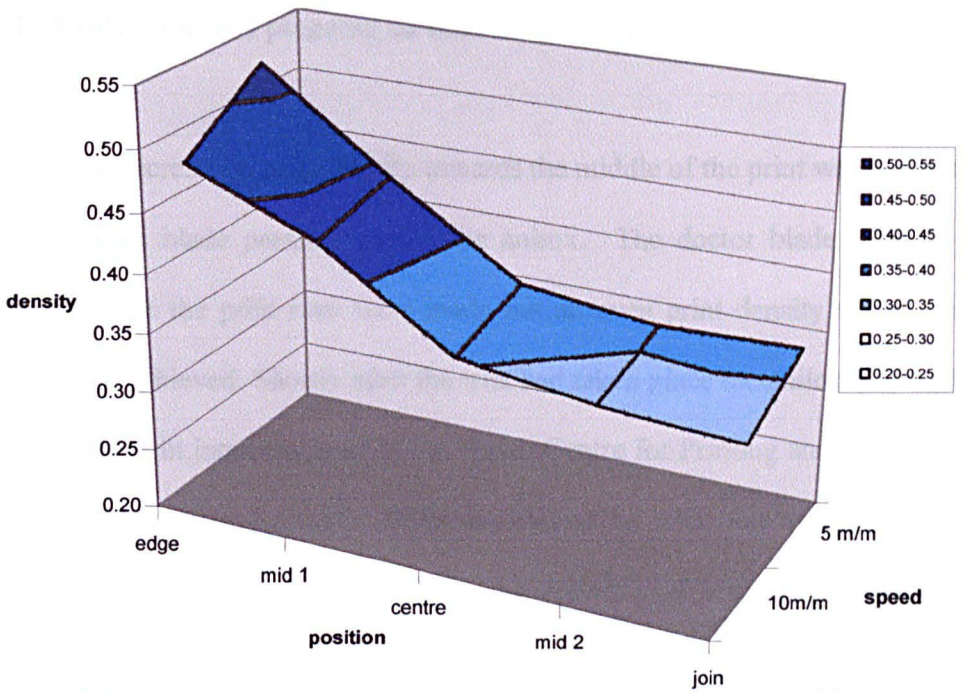

Figure 5.6. The variation of optical density across the print from the CO_2 band at two speeds.

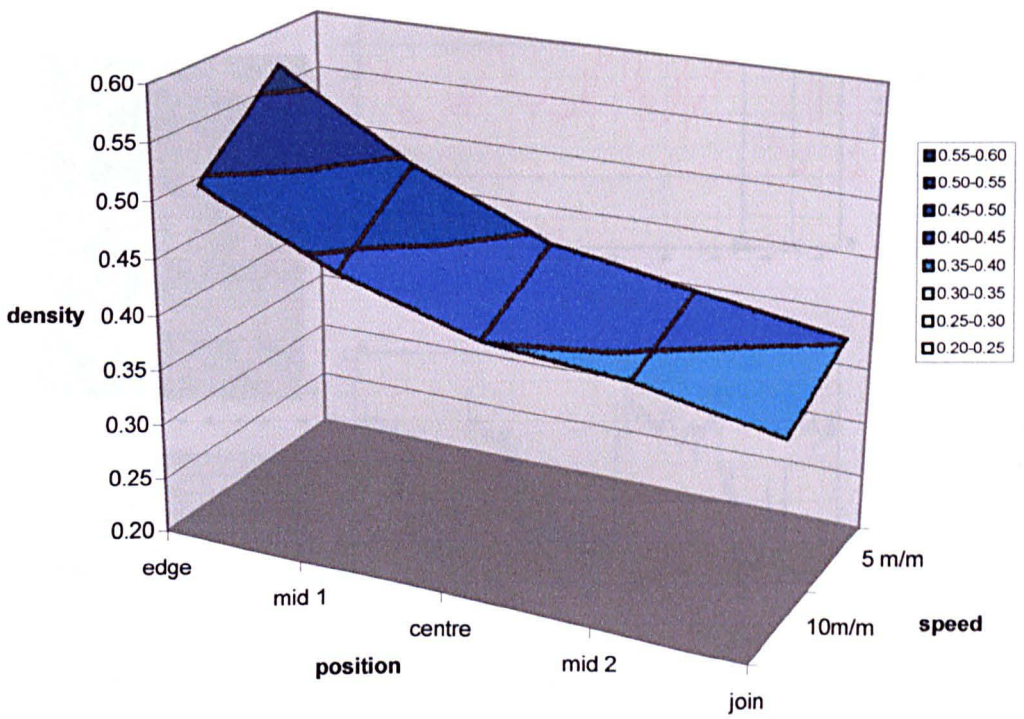

Figure 5.7. The variation of optical density across the print from the YAG band at two speeds.

5.2.1. Evidence of cell plugging on both bands of Harper 2.

Initially the decrease in print density towards the middle of the print was attributed to uneven doctor blade pressure across the anilox. The doctor blade settings were adjusted before the print runs were made but an even print density across the roll could not be achieved. Shortly after the trial had taken place the anilox was analysed with a white light interferometer at the Welsh Centre for Printing and Coating at the University of Wales in Swansea. When profiles of the cells were measured evidence of plugging of the cells was observed. An example of a screen shot showing a number of plugged cells is shown in Figure 5.8. All the cells in the shot are plugged apart from one. The unplugged cell is on the far right of the x profile line.

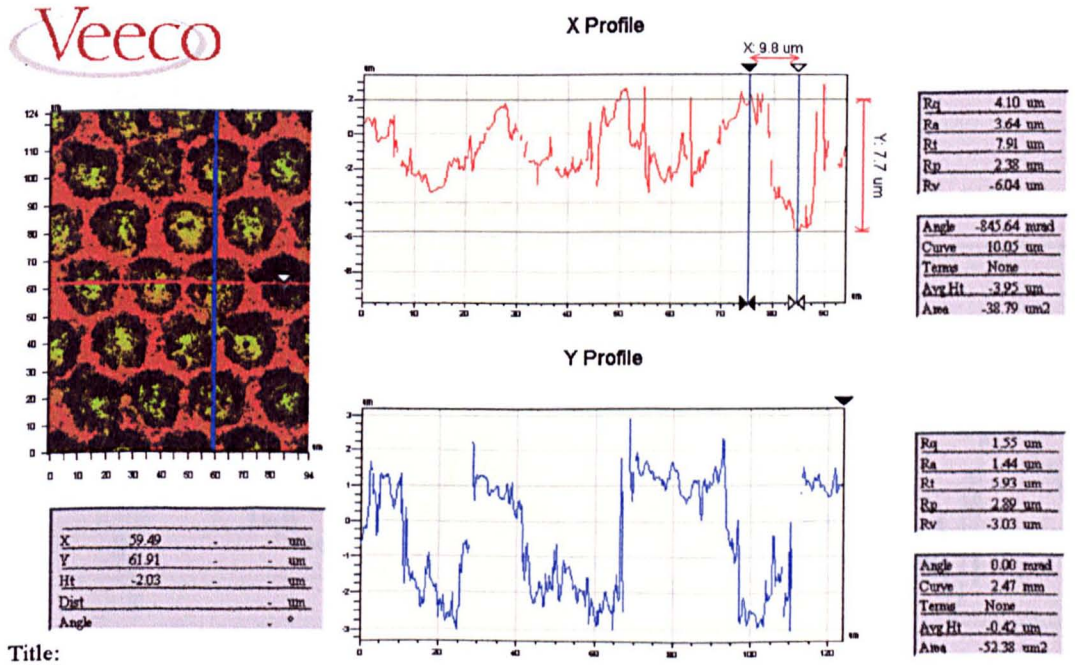

Figure 5.8. A screen shot from the Veeco roll scope showing plugged cells on the YAG band on Harper 2.

The colour-coded image on the left of the figure shows the unplugged cell as having a light blue base whilst the rest are coded yellow. The scale on the side of the x profile shows the unplugged cell to have a depth of 7.7 microns. This is close enough to the manufacturers value of 7.5 microns to support the theory that the cell is unplugged. The other cells in the shot have depths of approximately 4 microns. The plugging was very obvious on the YAG band and appeared to cover most of the roll. The plugging was not observed at the edge of the YAG band. The unplugged area was observed to extend approximately 50mm from the edge of the band. The plugging on the CO_2 band was less obvious and was initially missed when the roll was analysed. Two-dimensional profiles of area on the CO_2 band were made and when these were analysed two out of the three areas selected showed cell depths that were lower than the other measurement area and lower than the manufacturers value for the cell depth of 7.8 microns. This is illustrated in Figures 5.9 and 5.10. These profiles are used in Chapter 6.and are shown in Section A6-11 of appendix.

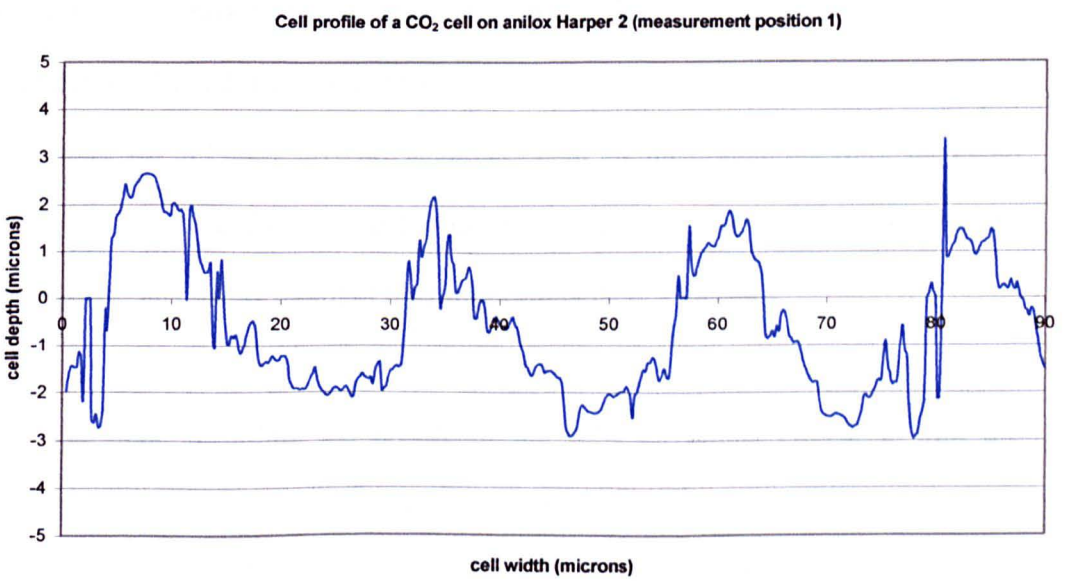

Figure 5.9. A two-dimensional profile of the CO_2 band showing plugged cells.

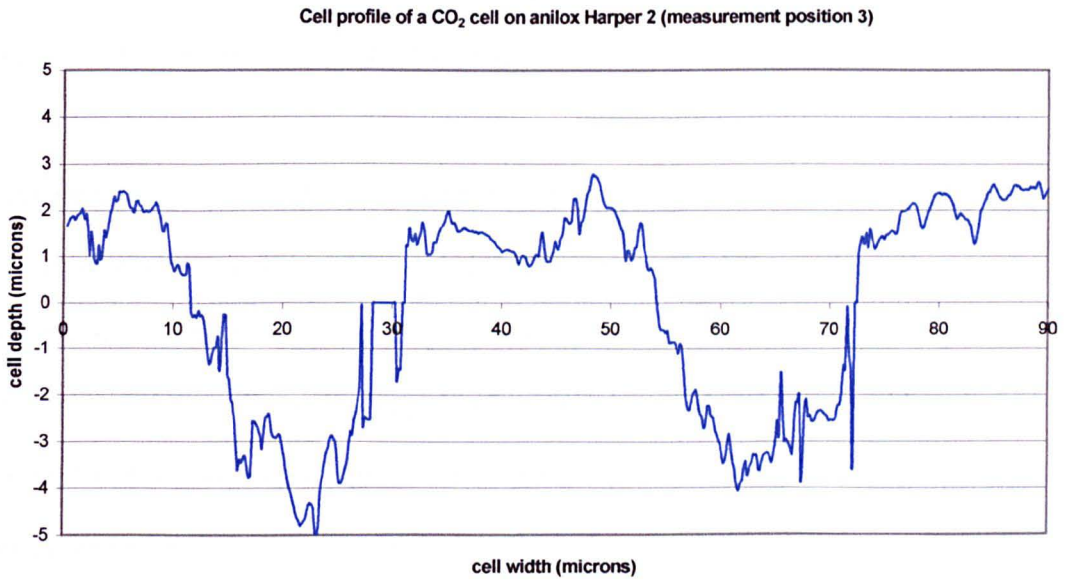

Figure 5.10. A two-dimensional profile of the CO_2 band showing unplugged cells.

The depth of the cells measured in measurement position 1 are between 4 and 5 microns. An example is shown in Figure 5.9. Measurements were made at two other positions. The cell depths measured in the other measurement positions were approximately 7 microns. An example is shown in Figure 5.10. The value supplied by Harper for the cell depth of the CO_2 band was 7.8 microns. Although the depth of the cells shown in Figure 5.10 are shallower than the manufacturers value the depth of the cells is accepted to vary and a 0.8 micron distance does not suggest plugging (although the possibility of slight plugging cannot be discounted).

The work done recording the profile of the cells on anilox Harper 2 with the interferometer concentrated on the measurement of the slope of the cell wall and the interior roughness of the cells. These measurements were made on unplugged cells. (This work is shown in detail in Chapter 6.) It was not possible to map the entire roll and quantify the extent of the plugging. It is interesting to note that although contact

angles of the engraved bands were being regularly measured before the press trial, plugging did not show up in the contact angle measurements on either band.

At the time of measurement it was assumed that the plugged ink was a result of poor wash-up after printing. It was later noted that the positions of the unplugged areas at each end of the roll are approximately the same size as the dense areas on the prints. This shows that the cells were plugged before the press trial took place. Although no printing had been done on Harper 2 before the trial, it had been used to measure the contact angles made by inks on its surface, both for this project and for another. It was noted that the ends of Harper 2 were difficult to position under the FTA instrument as the roll became unbalanced. Although the influence of doctor blade pressure cannot be ruled out, it is likely that the plugging of the cells is the cause for the uneven print across the bands of Harper 2.

There was a further problem with the results of the press trial. The optical density was observed to vary not only across the anilox, but at a press speed of five meters per minute it also varied as the run progressed. When an acceptable print was obtained at each speed (by adjustment of the doctor blade settings) the web was marked and the reel of paper was allowed to run to completion. Samples were cut from the reel at random intervals. The reel had been rewound to isolate the prints taken over the time period in which the press was stable. Samples 1 to 7 were taken in order, as the reel was unwound. Therefore sample 1 was from near the beginning of the run and 7 from near the end. Samples 8, 9 and 10 were taken at random intervals from the unwound printed web. The print density varied more than expected on the five metres per minute run. The density was observed to decrease as

the run progressed. This is illustrated in Figure 5.11. The decrease in optical density was attributed to a press problem, as it was consistent on both bands. The most obvious cause is insufficient ink in the inking tray leading to ink shortage in the anilox cells.

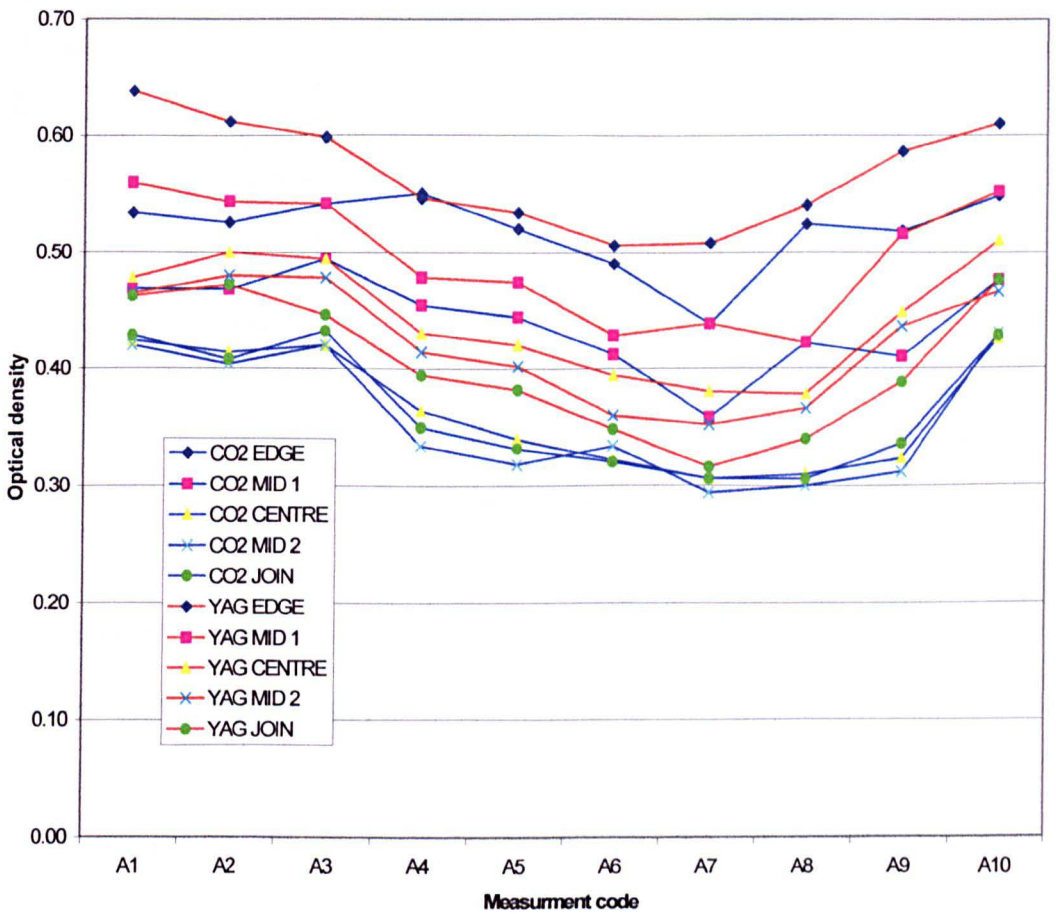

Figure 5.11. Variation in optical density of the samples printed at five metres per minute using the RK mini-web press.

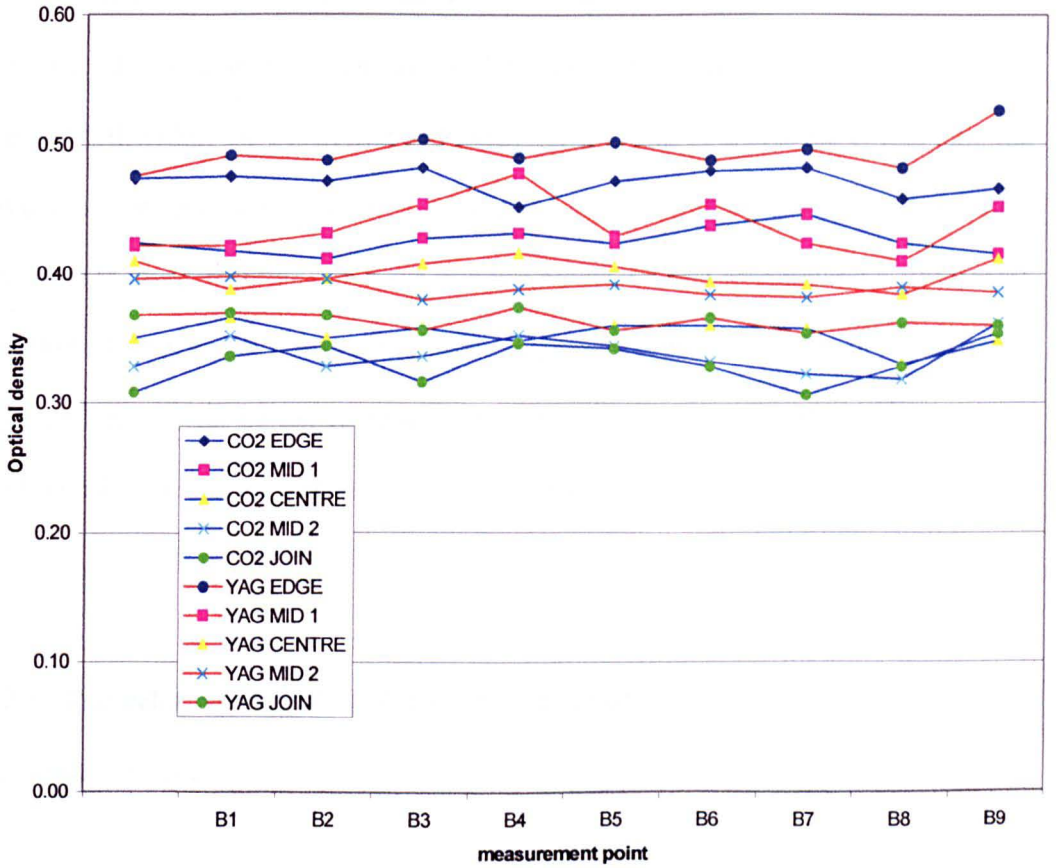

Figure 5.12. Variation in optical density of the samples printed at ten metres per minute using the RK mini-web press.

The optical density data for the ten samples is shown in Figure 5.12. There was still a small amount of variance between the optical densities on the prints taken from the run at ten metres per minute. The variation was however more random and the trend observed on the earlier run at five metres per minute was not repeated.

The optical densities of all the prints were very low. This is in part due to poor contact between the substrate and the anilox, and in part due to the plugging of the anilox with dried ink. The specification of the anilox was selected by Harper to have

a cell count and transfer volume that were typical of those used for high quality flexo printing. The line screen count of 393 lines per centimetre and the volume of 2.53 cm^3/m^2 fell within the recommended range for printing of a process colour (the ink used was Arena process cyan) as provided by Coates.[128] However they fell well outside the range recommended for printing solids. Coates recommend a line screen of 100 to 160 lines per centimetre and an engraved volume of 7 to 9 cm^3/m^2. Anilox Harper 2 would not be expected to transfer a sufficient volume of ink to produce a high-density solid print under standard printing conditions.

5.2.2 The relation of optical density to film thickness and ink transfer using a calibration curve

As discussed in Section 4.3 the relationship between optical density and the volume of ink transferred is not linear. To estimate the amount of ink transferred to the substrate in this trial a series of calibration prints were made in the same manner as was described in Section 4.3, again using the Mickle proofer. Prints were made using the leftover materials from the press trial.

As the printing pressure at the anilox/paper nip was known, the pressure setting of the Mickle proofer could be adjusted in order to replicate printing conditions as closely as possible. The movement of an adjustable weight controlled the force acting on the printing carriage. The contact area between the carriage and the substrate was determined by inking the carriage and pressing it against the substrate. The contact area was measured and found to be 400 square millimetres. It was

calculated that to replicate the printing pressure on the RK lab press 0.276 Newton/square millimetre that a force of 110N would be needed on the Mickle. The Mickle proofer produces prints of 0.05m by 0.2m or $0.01m^2$. The printing carriage was reweighed after the printing to find the weight of ink covering the $0.01m^2$ area. This process was repeated until a range of prints of differing film weights were obtained. The optical densities of these prints were measured. Figure 5.13 shows a plot of optical density versus film weight for the prints. The error in optical density measurements was taken to be the average of the standard deviations, which was 0.02. The error in the film weight was estimated to be 0.0005g as before.

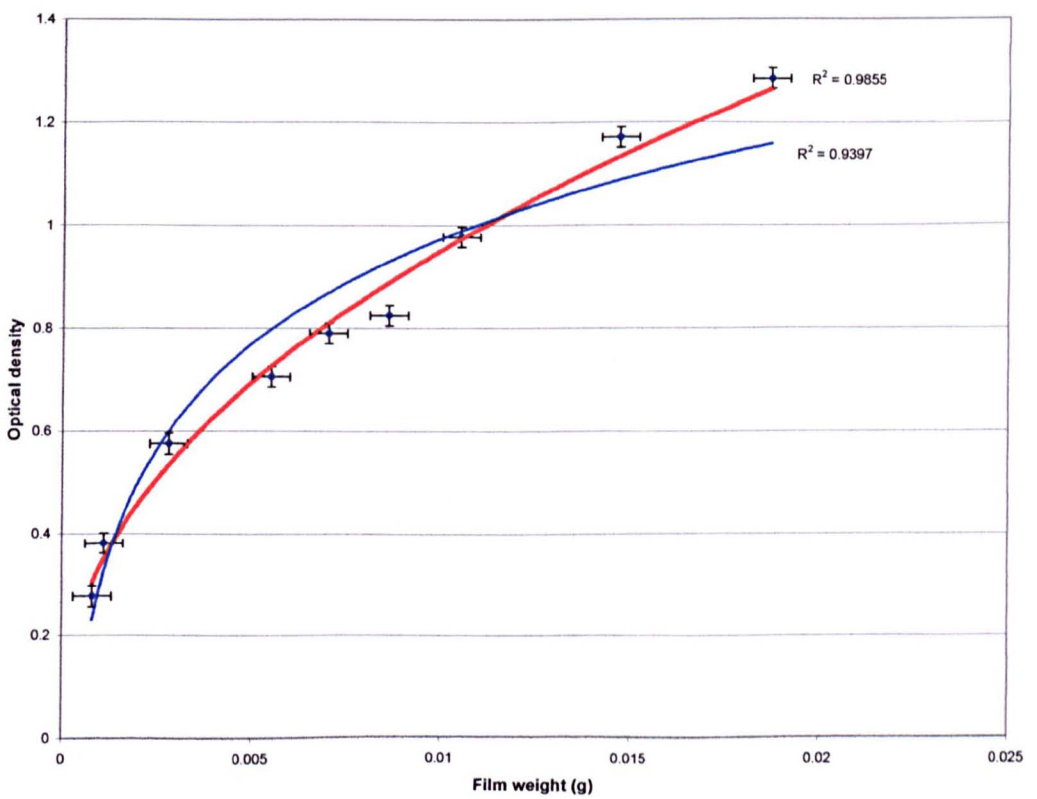

Figure 5.13. The relationship between optical density and film weight of prints produced on the Mickle proofer.

Curves were fitted to the data in an attempt to establish a suitable calibration equation. The red curve is a power relation. The blue curve is a logarithmic relation. The power relationship between film weight and optical density gives the best fit and was accepted as the calibration curve. The calibration curve is shown in Figure 5.14. For convenience the axis were again swapped around to allow the film weight to be calculated easily from the equation of the fitted curve. The equation of the curve was $y = 0.011x^{2.1707}$ where y is the film thickness and x is the optical density. The R^2 value was 0.9855 indicating that the curve is a good fit to the data.

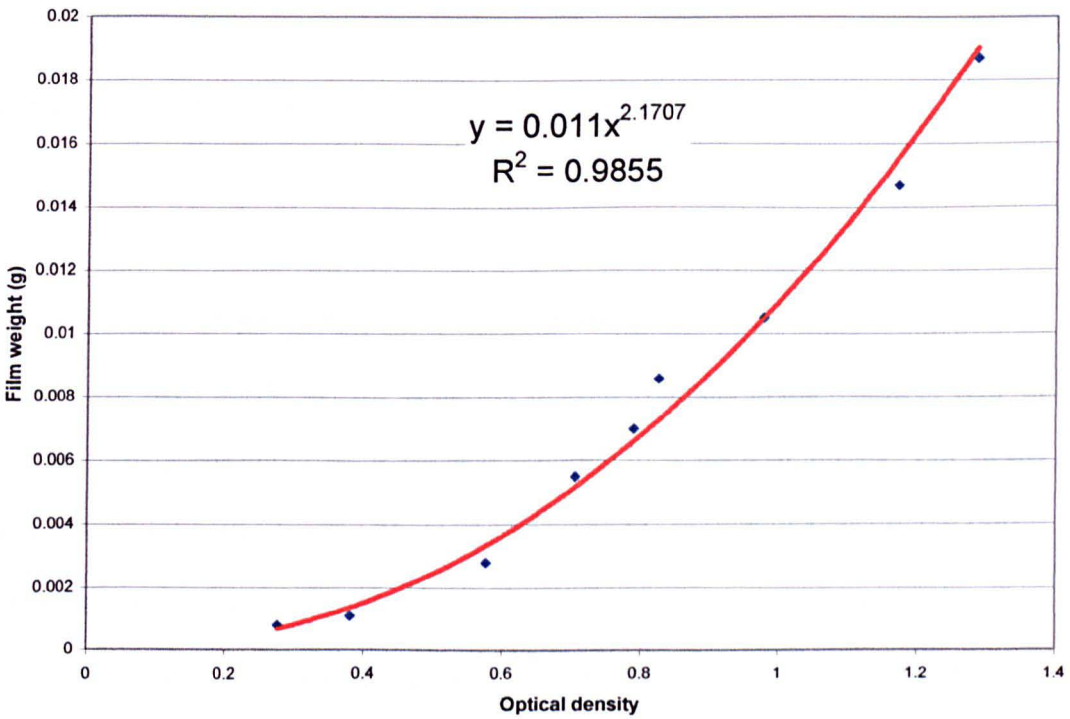

Figure 5.14. The calibration curve relating optical density to film weight for a series of prints made with the Harper 2 trail materials on the Mickle proofer.

The film thickness relating to the optical densities of the prints from Harper 2 were calculated from the values in table 5.12 using the above equation and tabulated in Table 5.13.

	Film weight in grams			
	5 m/min CO_2	10 m/min CO_2	5 m/min YAG	10 m/min YAG
edge	0.00266	0.00214	0.00325	0.00234
mid 1	0.00185	0.00176	0.00244	0.00185
centre	0.00120	0.00113	0.00185	0.00151
mid 2	0.00120	0.00106	0.00167	0.00142
join	0.00120	0.00099	0.00151	0.00120

Table 5.13. The calculated film weight in grams of a $0.1m^2$ area of print.

The volume of ink put down on the substrate could then be calculated from the film weight. A value for the density of the ink was not available so the weight of $1cm^2$ of ink was again measured on a balance accurate to 4 decimal places. Ten repeat measurements were made. The average weight was found to be 1.1385g. Measurements were made at 23°C +/- 1°. The weight of ink covering $0.01m^2$ as calculated above, was converted to a volume of ink in cubic centimetres by multiplication by 0.8793, the volume of 1 gram of ink in cm^3. This was then converted to cubic centimetres per square metre by multiplication by 100. The calculated volumes transferred in cubic centimetres per metre squared are shown in Table 5.14.

	Volume of transferred ink in cm^2/m^2			
	5 m/min CO_2	10 m/min CO_2	5 m/min YAG	10 m/min YAG
edge	0.234	0.188	0.285	0.205
mid 1	0.163	0.155	0.215	0.163
centre	0.105	0.099	0.163	0.132
mid 2	0.105	0.093	0.147	0.125
join	0.105	0.087	0.132	0.105

Table 5.14. The calculated volume of ink transferred to the substrate in cubic centimetres per square metre.

The carrying capacity for the cells on both bands of Harper 2 was specified by Harper as 2.53 cm^3/m^2. The amount of ink transferred is expressed as a percentage of the capacity of the cells in Table 5.15.

	Percentage of cell volume transferred			
	5 m/min CO_2	10 m/min CO_2	5 m/min YAG	10 m/min YAG
edge	9.2	7.4	11.3	8.1
mid 1	6.4	6.1	8.5	6.4
centre	4.2	3.9	6.4	5.2
mid 2	4.2	3.7	5.8	4.9
join	4.2	3.4	5.2	4.2

Table 5.15. The amount of ink transferred from the cells on each band as a percentage of the transfer capacity of the bands as specified by Harper.

As the carrying capacity of the cells was the same on each band translating the results to the percentage of the potential volume that was transferred does not change

the trends observed in the data. The YAG band is seen to transfer slightly more ink to the substrate in all cases. There is small difference between the bands at 5 metres per minute. The difference becomes smaller still at 10 metres per minute. The effect of press speed on release from the anilox is masked by the variance in the data from the 5 metres per minute run. In all cases the amount of ink transferred to the substrate is smaller than expected with conventional flexo printing. This can again be attributed to the poor contact between the rough surfaces of the anilox and paper at the nip. There is a marked difference in the percentage of ink transferred between the edge of each band and the join area. The percentage of ink held in the cell that is transferred, halves at the join of the roll where the cells are known to be plugged. This is reasonably consistent for both bands at both speeds. There was no difference seen in the extent of plugging or its effect on ink transfer between the bands.

5.3 Contact angle analysis of the paper substrate in order to determine the surface energy difference at the anilox/paper nip

Contact angle analysis of the paper substrate was carried out in an attempt to determine the wettability of the paper and the surface energy difference at the anilox/paper nip. Analysis was carried out on the FTA only. Drops were touched off against the substrate surface to minimise spreading due to application force. The drop volume applied to the surface was dictated by the size of drop that could be held on the needle tip. The results are summarised in Table 5.16 and are shown in full in Section A5-7 of the appendix.

	Water		Diiodomethane		Formamide	
	Contact angle	drop volume	Contact angle	drop volume	Contact angle	drop volume
mean	106°	9°	49°	3°	96°	8°
standard deviation	3°	0.4°	3°	0.2°	3°	0.2°

Table 5.16. Contact angles made on samples of the paper used in the Harper and Pira press trials using the FTA instrument.

The difficulties experienced making contact angle measurement on paper samples were different to those experienced on anilox rolls. The paper was attached onto a carriage plate in order to hold it flat. However, absorption into the substrate was a problem, particularly with diiodomethane. Drops of water and formamide were completely stable for 6 seconds. All contact angle measurements were made over the first 6 seconds after contact occurred. Diiodomethane drops started to sink into the paper as soon as contact occurred. Twenty one measurements were made over 2.1 seconds and these contact angles were averaged to produce the final reported value. Examples of the change of contact angle over time are shown for each test liquid in Figures 5.15, 5.16 and 5.17.

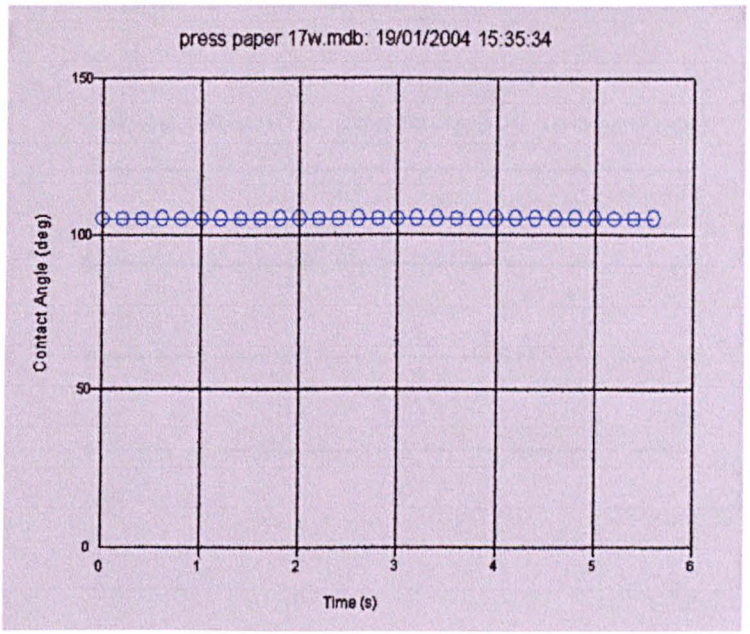

Figure 5.15. The stability of the contact angle made by a water drop on paper over 5.6 seconds.

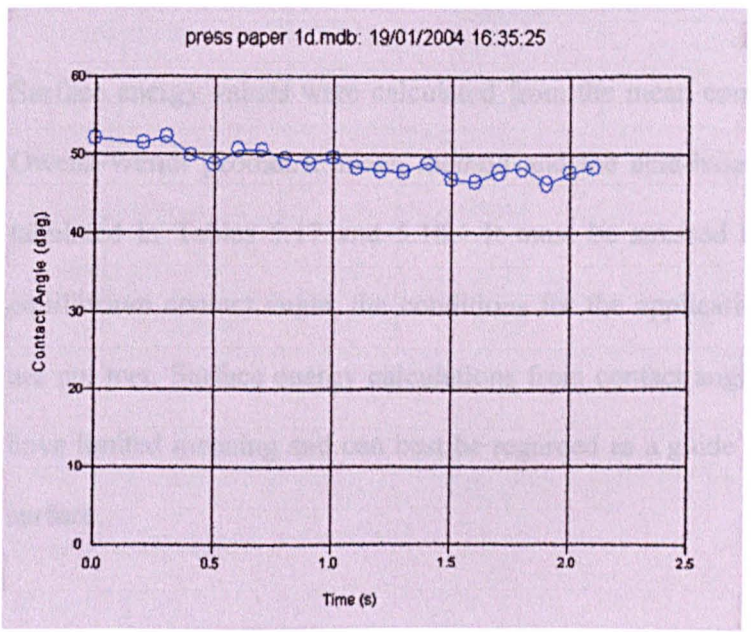

Figure 5.16. The stability of the contact angle made by a diiodomethane drop on paper over 2.1 seconds.

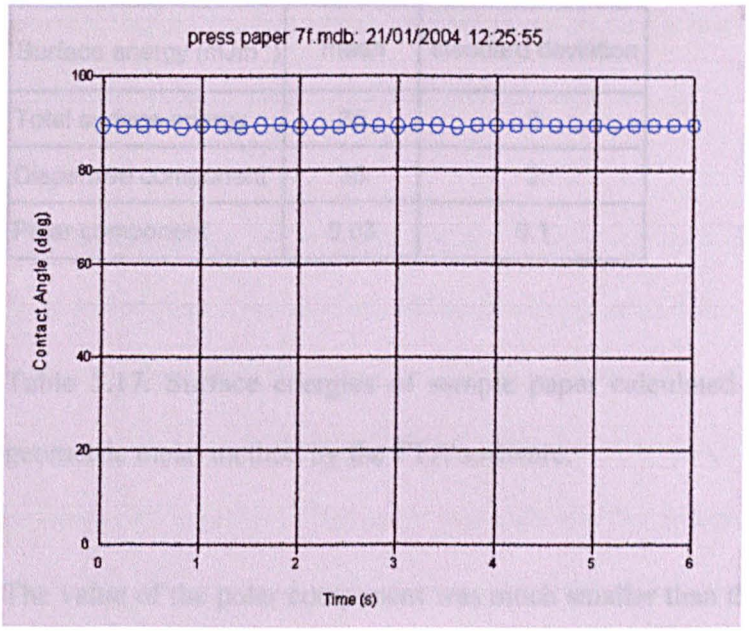

Figure 5.17. The stability of the contact angle made by a formamide drop on paper over 6 seconds.

Surface energy values were calculated from the mean contact angle data, using the Owens-Wendt geometric mean method and the acid-base method. The results are tabulated in Tables 5.17 and 5.18. It must be stressed that as there is no stable equilibrium contact angle, the conditions for the application of the young equation are not met. Surface energy calculations from contact angle data on paper therefore have limited meaning and can best be regarded as a guide to the nature of the paper surface.

Surface energy (mJm^{-2})	mean	standard deviation
Total surface energy	35	2
Dispersive component	35	2
Polar component	0.03	0.1

Table 5.17. Surface energies of sample paper calculated using the Owens-Wendt geometric mean method by the FTA software.

The value of the polar component was much smaller than the estimate of error in the calculation. This is because experimental problems in obtaining stable contact angles on paper lead to high standard deviations for all the contact angle data.

Surface energy mJm^{-2}	mean	- 1 standard deviation	+ 1 standard deviation
Total surface energy	32.0	33.6	30.4
Dispersive component	34.8	36.5	33.2
Polar component	-2.8	-2.87	-2.78
Acid component	-4.8	-0.45	-5.09
Base component	0.4	4.59	38

Table 5.18. Surface energies of sample paper calculated using the acid-base method by the FTA software.

In this calculation the acid and base values produced by entering the smallest permutations of contact angle values (based on the mean value minus the standard deviation) was very different to the values produced by entering the largest possible

contact angles (the mean plus one standard deviation). It was misleading just to quote the larger value as the error, therefore both were noted.

The surface energy of the paper calculated from the contact angle data was very low. It is lower than the value at which filmic substrates are normally corona treated. Although the wettability of paper is extremely variable and corona treatment is very occasionally needed, the hydrophobic character in these cases is usually from surface coatings or treatments. The paper was known to be uncoated. The surface energy of the paper was checked with Dyne solutions provided by Coates. All the available Dyne solutions, from 32 to 46 dynes, wet the paper. This would indicate that the surface energy is above 46 dynes. The Dyne solutions were applied by a cotton bud to the paper surface. There is an additional spreading force using this method. It has already been seen from the FTA and MAMS contact angle data on anilox Harper 1 and Harper 2 that the same liquid on the same surface can exhibit different contact angles depending on how the drop is introduced to the surface. In the case of the application of Dyne solutions to paper, the cotton bud forces the solution into pores and between fibres. Coates only recommend the Dyne solution method for the surface energy evaluation of non-porous substrates. Surface energy measurements of the same order as calculated from the contact angle data are reported in work by Huang et al [129] who quote a surface energy of 30.77 mJm^{-2} for a sized handsheet.

Contact angle measurement of the bands of anilox Harper 2 and the paper substrate were measured with the same test liquids on the same instrument using the touching off technique to dispense the drop. The total surface energies calculated from the contact angle data were 39 and 38 mJm^{-2} for the CO_2 and YAG bands respectively,

using the geometric mean approximation. (These values found not to be statistically significant when measurement of the errors were propagated.) There is a significant difference between these figures and the total value for the surface energy of the paper calculated using the geometric mean method, which was 32.Jm^{-2}. The surface energy difference at the nip is not favourable, i.e. there is no energetic incentive for the ink to transfer to the paper. This may be another factor in explaining the poor transfer of ink from the anilox to the paper.

5.4 The effect of cleaning anilox Harper 2 with a specialist product

Anilox Harper 2 was cleaned with a specialist cleaning product in order to remove the plugged ink. The effect of cleaning anilox Harper 1 with the same product has already been discussed in Section 3.7. The cleaning product was seen to change the wettability of the YAG band only on Harper 1. The contact angles were measured on Harper 2 after cleaning. The results are tabulated in Section A5-8 of the appendix and are summarised in Table 5.19. Again no change was seen on the CO_2 and polished bands but the YAG band was much more receptive to wetting by water.

		Original water	Post-clean water	Original diiodomethane	Post-clean diiodomethane
Polished band	**mean**	**74°**	**74°**	**44°**	**42°**
	standard deviation	3°	2°	2°	2°
CO_2 band	**mean**	**91°**	**93°**	**43°**	**44°**
	standard deviation	2°	2°	2°	1°
YAG band	**mean**	**105°**	**82°**	**43°**	**42°**
	standard deviation	2°	3°	2°	1°

Table 5.19. The effect of using a specialist cleaning product on the contact angles observed on Harper 2.

The contact angle observed on the YAG band using water and the MAMS instrument was 86° with a standard deviation of 4°. The contact angle observed with the FTA after cleaning is within the range of error associated with this measurement. This supports the theory that the traces of cleaning product that remained on Harper 2 helped the water reach thermodynamic equilibrium on the surface of the anilox.

The cleaning product was not easy to remove from the YAG bands of the Harper anilox.

The contact angle observed with water on the YAG band was still low after several days of cleaning the anilox rolls with water and organic solvents. The anilox were not successfully cleaned during the period of these investigations.

5.5 Summary of results from anilox Harper 2

1. The wettability trends observed on anilox Harper 1 were also observed on Harper 2.

2. The contact angle recorded on the engraved bands of Harper 2 were higher using both the FTA and MAMS instruments. This was not directly related to the size of the cell opening or the number of cells per centimetre.

3. Contact angles measured on the MAMS instrument were again lower than those measured on the FTA instrument. The trends observed in the data were the same on both instruments.

4. The contact angle obtained with a static water drop on the FTA was not statistically different to the contact angle produced by advancing the water drop. A small difference between the static and advanced water drop was seen on the CO_2 bands and a large difference was seen with the polished band. The angle measured on the YAG band with the static drop is therefore not an equilibrium angle. The angle measured on the CO_2 band is likely to be an overestimate of the equilibrium angle.

5. Measurement of advancing and receding contact angles with diiodomethane were not possible, as a stable large drop could not be obtained. Measurement

of receding contact angles with water was not obtained due to experimental difficulties.

6. The Owens-Wendt geometric mean approximation indicates that the change in the wettability across the bands is due to a change in the polar nature of the roll surface. The engravings being less polar than the polished unengraved surface, and the CO_2 engraving having more surface polarity that the YAG engraving. The YAG engraving showed a negligible amount of polar character.

7. The acid base theory of wetting indicates that the change in surface energy is mainly due to the reduction of the basic nature of the surface. The engravings being less basic than the polished unengraved surface, and the CO_2 engraving having more basic character that the YAG engraving. The engraved bands also have less acidic character than the polished band. There was no significant difference between the acidic components of the engraved bands. This trend was also seen on anilox Harper 1.

8. There was a small difference between printed ink densities from the engraved bands. The YAG band produced a print with a higher optical density. Transfer directly from the anilox to the paper was, overall, very poor.

9. Plugging of the anilox cells gave an artificially low optical density on all but the outside edges of each band. The print was uneven due to poor contact between the anilox and paper.

10. Plugging of the anilox up to an approximate height of 3 microns did not affect the contact angles made by pure liquids on the surface of Harper 2.

11. The use of a calibration curve to calculate the percentage ink transfer from the cell showed than the maximum transfer from the unplugged areas of the anilox to the paper was only 11% and 9% of the ink carried in cells on the YAG and CO_2 bands respectively at 5 metres per minute.

12. The surface energy of the paper used in the press trail was found to be lower than that of each band of the anilox.

6. Mathematical adjustment of the contact angle to compensate for surface roughness

As discussed in Section 1.3.3, the surface roughness of each engraved band is characterised by the power output of the laser used to make the engraving. The YAG laser produces cells by ablating the ceramic whilst the lower power CO_2 laser melts then recasts the ceramic to form the cells. This difference between the engraving techniques gives rise to cell interiors with different roughness. In Chapter Two, three theories for explaining the effect of roughness on the contact angle were discussed in detail. They were the Wenzel equation, the Shuttleworth and Bailey equations and the Cassie and Baxter equation. In this chapter, each theory will be applied to the contact angle data that was collected on bands on anilox Harper 1, Pira 1 and Harper 2.

6.1 Application of the Wenzel, Shuttleworth and Bailey, and Cassie and Baxter theories to anilox Harper 1

The contact angle data collected from the bands on Harper 1 was summarised and discussed in Chapter 3. The contact angle data used in this section is derived from the contact angles made with the 5µl water and diiodomethane drops measured on the MAMS instruments, and the contact angles made with formamide, diiodomethane and water measured on the FTA. For the purposes of evaluating the models, the polished band is assumed to have no roughness and the contact angles

observed on it are assumed to be a reasonable approximation of the equilibrium contact angle. The consequences of these assumptions will be discussed in Chapter 8. The curvature of the roll is constant for all measurements and its effects on the contact angle are considered constant. The profile of the cell is considered to be macroscopic roughness whilst the roughness of the cell wall and interior are considered microscopic roughness.

6.1.1 Measurement of the cells on Harper 1

Before the effects of the roughness could be calculated, the roughness itself had to be examined to determine factors such as true surface area, the maximum gradient of the roughness peaks and the fractional area corresponding to the land around the cells. In order to obtain this information detailed measurements of the anilox surface were needed. Initially, measurements were made on a Proscan 1000 optical sensor provided by Scantron. More detailed measurements were later made on a Veeco white light interferometer provided by the Welsh Centre for Printing and Coating in Swansea.

Figures 6.1 to 6.4 show images created by the Proscan optical sensor. Figure 6.1 shows an area of the CO_2 band covering multiple cells. Figure 6.2 shows the same size area on the YAG band. Figures 6.3 and 6.4 show close up images of single cells from the CO_2 and YAG bands respectively. The most obvious thing about the two images is that the YAG cells are much smaller in diameter than the CO_2 cells. As was mentioned in Chapter 3, anilox Harper 1 was designed with the cell depth as the

controlled variable, the other parameters were selected by the Harper Corporation to be typical values for the cell depth and laser type. The YAG cells are expected to release to a greater depth than the CO_2 cells, therefore the three to one ratio of cell opening to depth dimensions can be exceeded with YAG engravings and the openings can be made narrower.

In Section 1.3.3 the characteristic shapes of the cells were discussed. The cells produced by the CO_2 laser were described as bowl shaped, whilst the cells produced by the YAG laser were described as tubular. The distinction is however not apparent from the images in Figures 6.1 to 6.4. The shapes of real cells are very irregular and the images do not support the claims made in the literature. The images show that the land area on the CO_2 band is a double ridge. This is visible in Figure 6.1 in the profile in x-axis, and in figure 6.3. The YAG cells are surrounded by a single ridge. This double ridge is produced by the recast from the two adjacent cells being pushed together. As a YAG laser produces very little recast ceramic the land between two YAG cells is narrower and without the double peaks. An irregular ridge is however seen in the y-axis profile in Figure 6.2. This profile follows the length of the cell land area. The land areas between the YAG cells are very thin and it can be seen from the profile in the x-axis in the Figure 6.2 that the height of the cell wall varies more than between the CO_2 cells as there is less unablated ceramic to produce a land at a constant height. The irregularities in the long cell land area are a result of the variation between the heights of the non-adjacent cells at either end of the land.

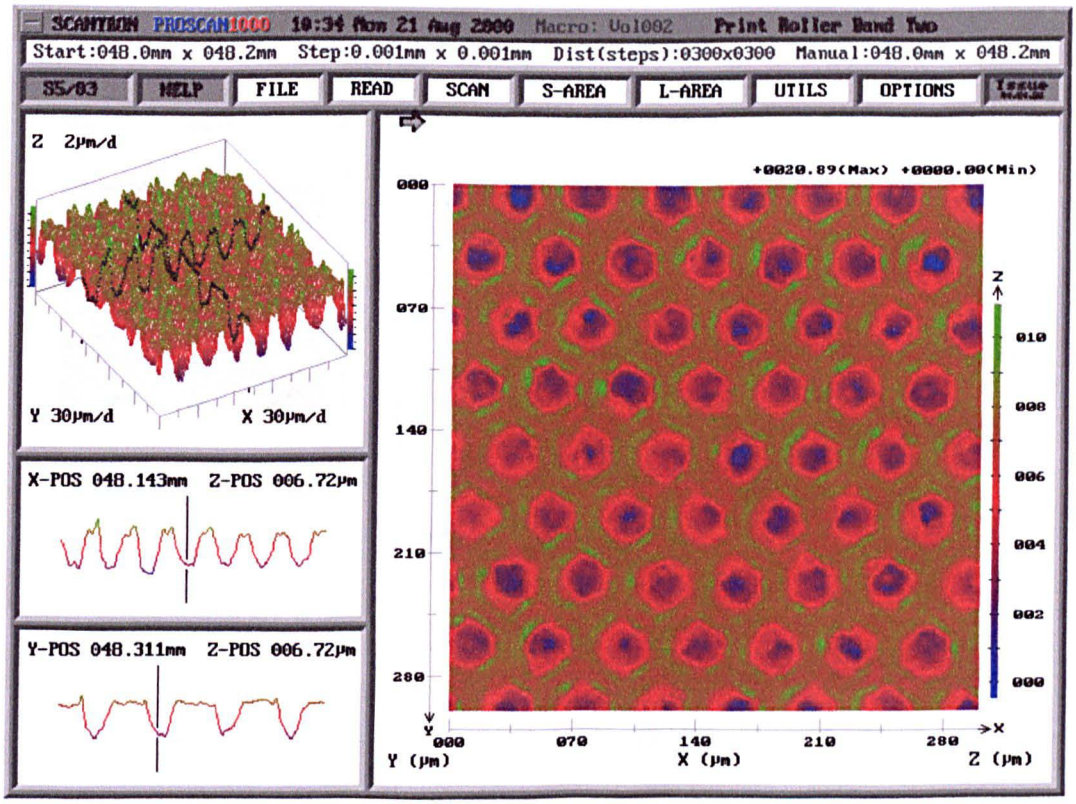

Figure 6.1. A scan showing the CO_2 band of anilox Harper 1.

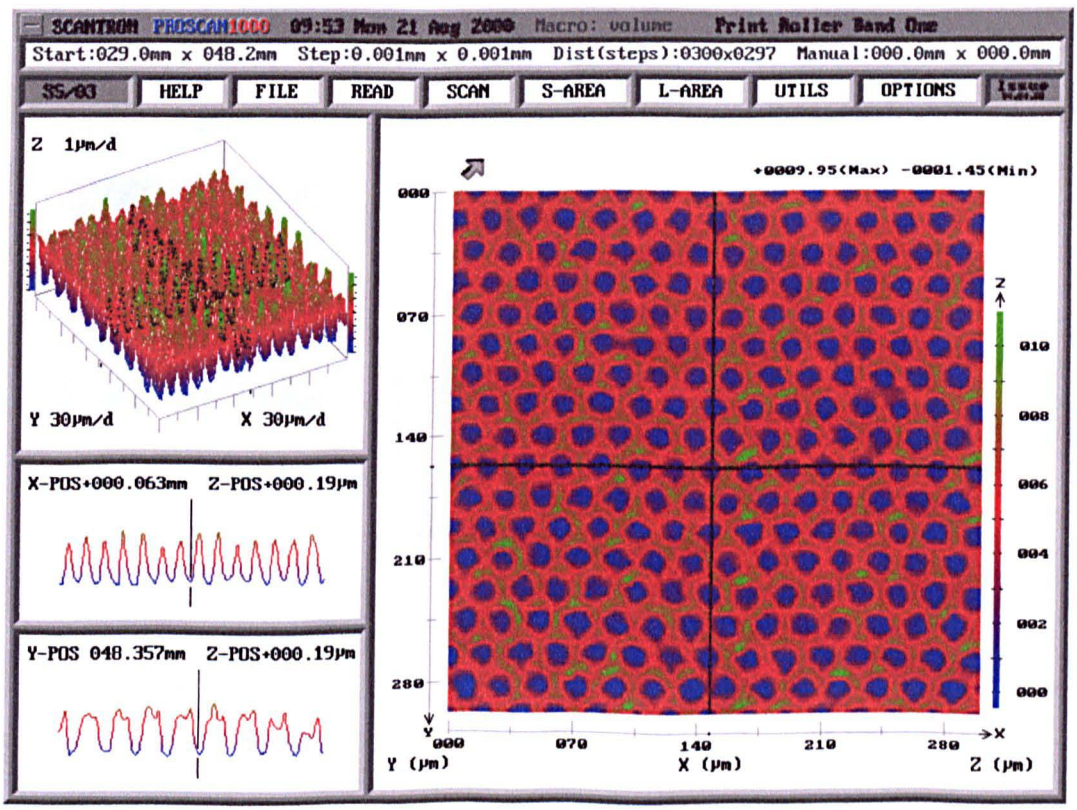

Figure 6.2. A scan showing the YAG band of anilox Harper 1.

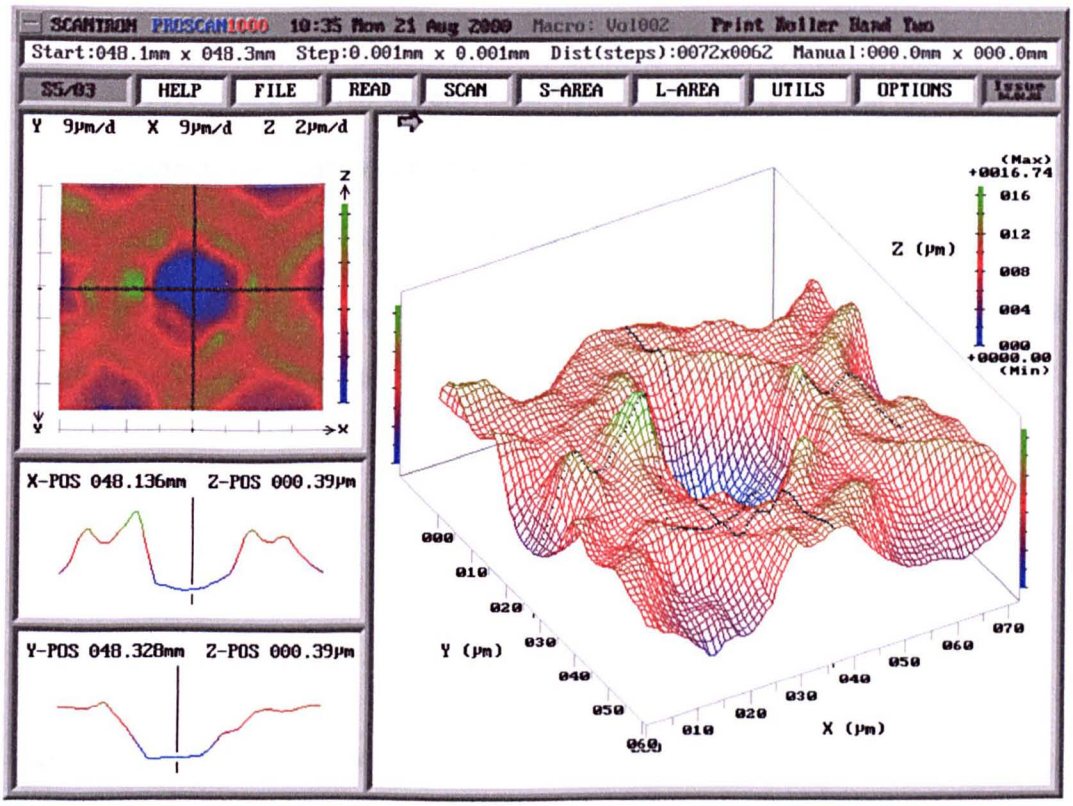

Figure 6.3. A close up scan of a single CO_2 cell on anilox Harper 1.

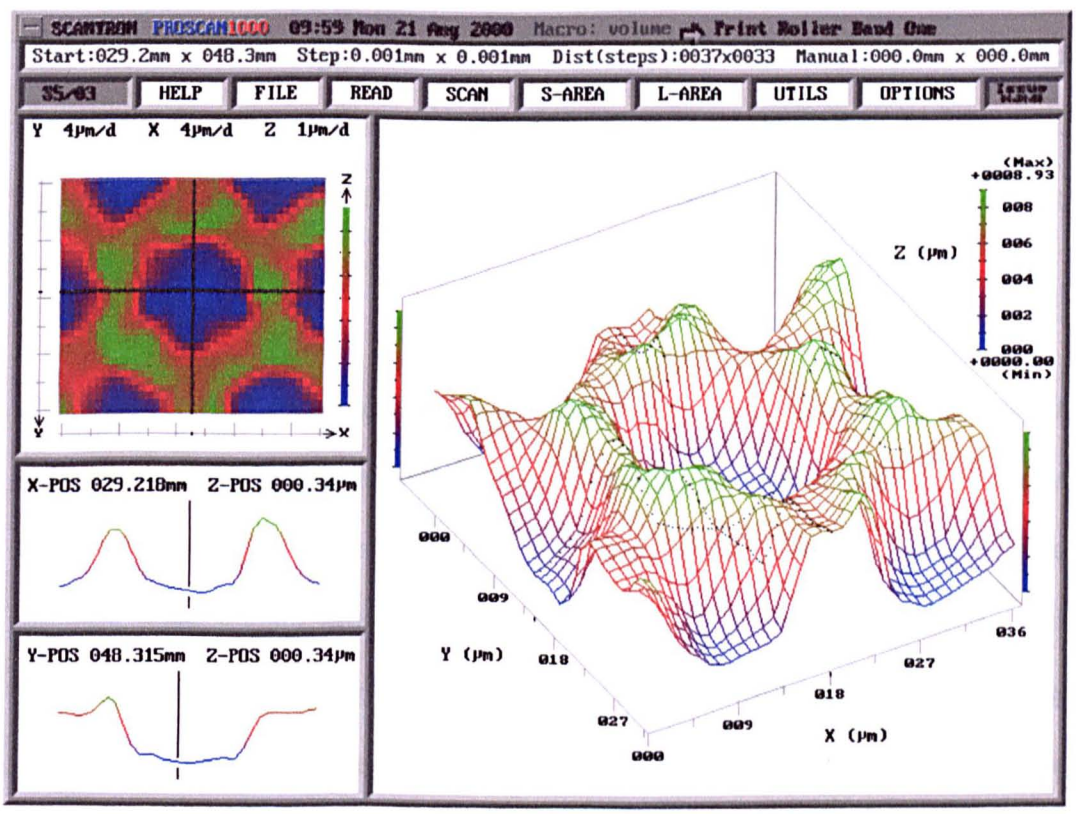

Figure 6.4. A close up scan of a singleYAG cell on anilox Harper 1.

Figure 6.5 shows images taken from the x dimension plots of Figures 6.1 and 6.2. It shows the 2D surface scan of the engraved bands made by the Proscan optical sensor placed together for comparison. Unfortunately, the original image had axes of different scales, the height of the cells being a larger scale than the width. To see the true shape of the cells the proportions of the image were carefully manipulated using Adobe Illustrator and Photoshop to make the scale of the image uniform.

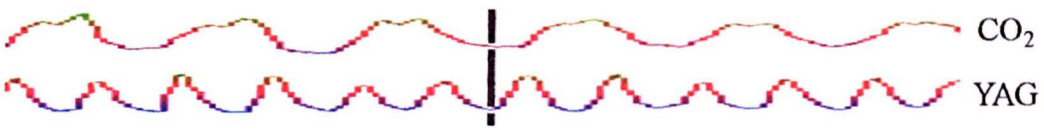

Figure 6.5. Roughness of the engraved bands as recorded by the Proscan 1000 optical sensor.

It can be seen from Figure 6.5 that when the scale of the height and width are equalised the gradient of the YAG cell walls appear steeper than the CO_2 cell walls. The land area between the CO_2 is again seen to be clearly wider than that between the YAG cells.

Whilst the Scantron instrument shows the shapes of the cells on each of the bands it is not sensitive enough to show information about the roughness of the cell interior walls. As discussed in Section 1.3.4, the Veeco white light interferometer is a specialist measurement instrument designed to obtain information about the cell dimension, volume and roughness of an anilox roll. The Welsh Centre for Printing and Coating has two interferometers. A fixed instrument with a platform on which a

small anilox can be placed for analysis and a portable roll scope for larger anilox. Harper 1 was small enough to be analysed by the fixed instrument.

Figures 6.6 and 6.7 show two-dimensional profiles of cells on the CO_2 band and the YAG band respectively. Figures 6.8 and 6.9 show three-dimensional images of an area on each band containing multiple cells.

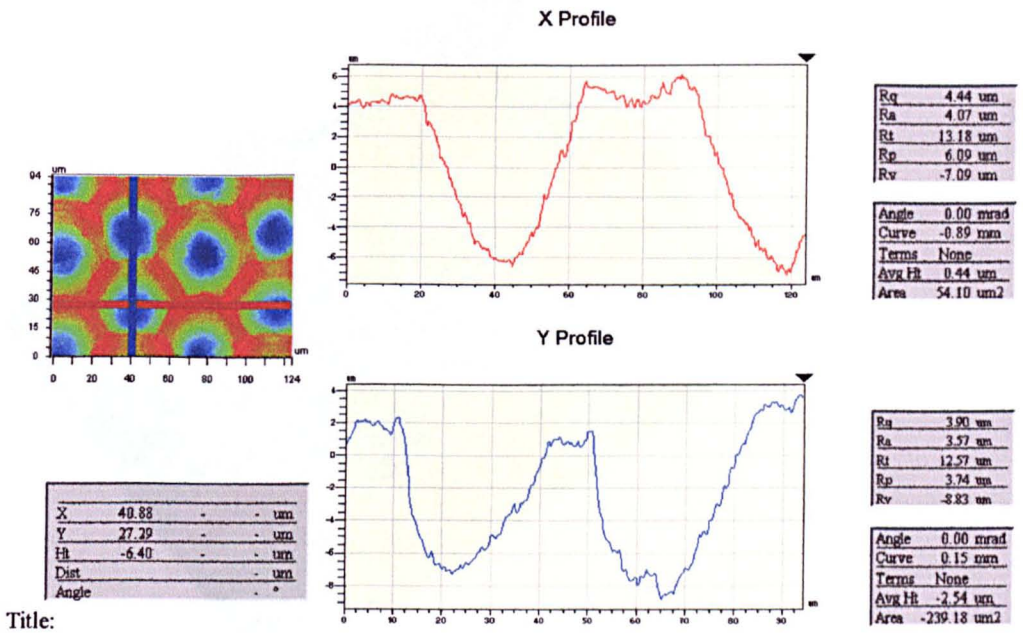

Figure 6.6. A 2D cell profile measured on the CO_2 band of Harper 1 by the Veeco interferometer.

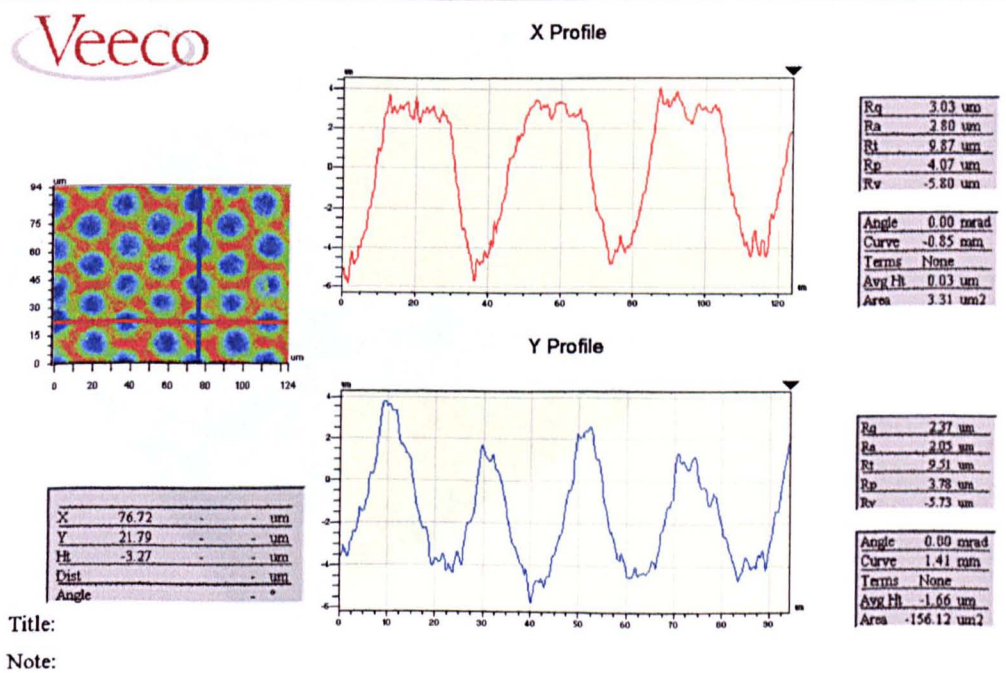

Figure 6.7. A 2D cell profile measured on the YAG band of Harper 1 by the Veeco interferometer.

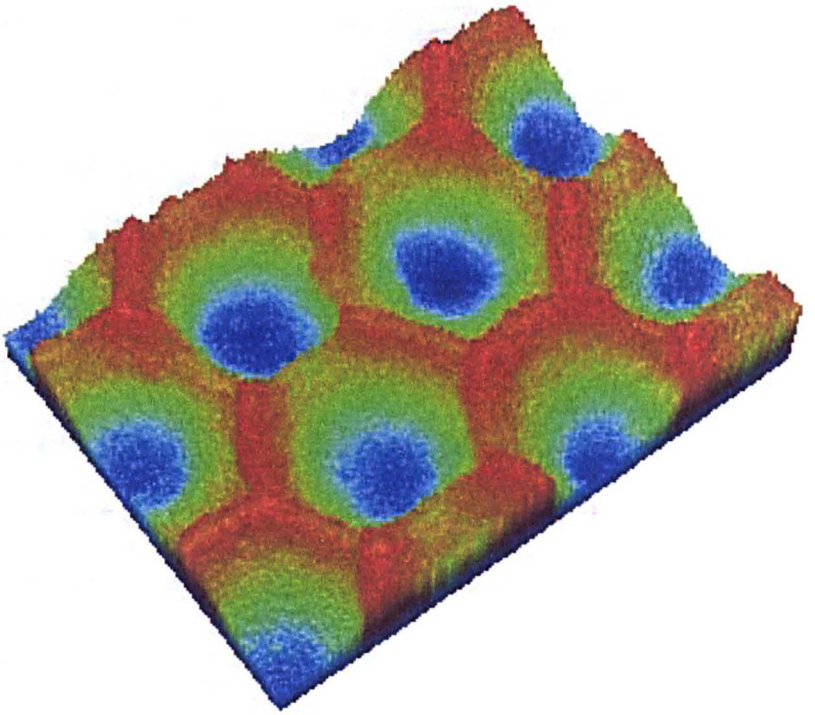

Figure 6.8. A 3D profile of cells on the CO2 band of Harper 1 measured by the Veeco Interferometer.

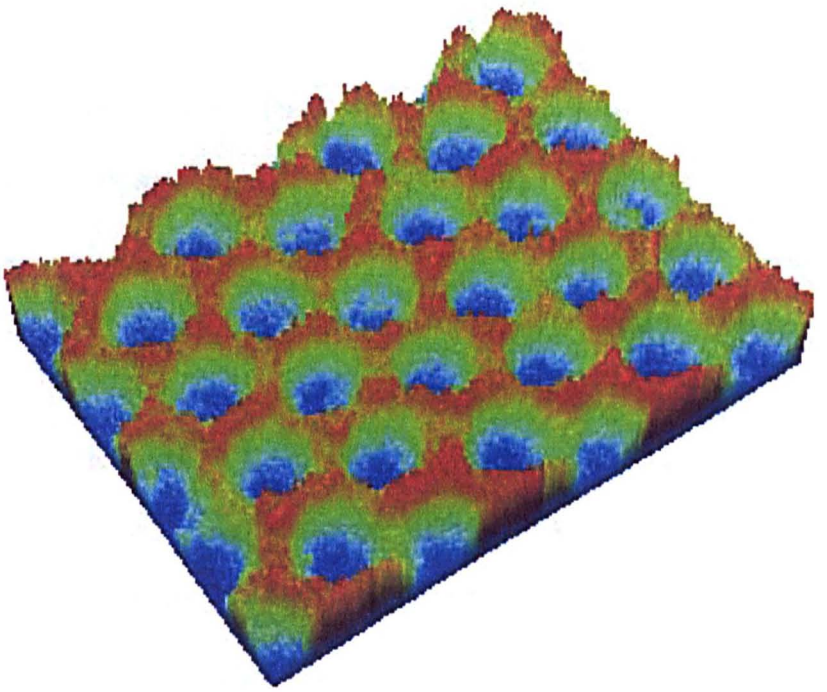

Figure 6.9. A 3D profile of cells on the YAG band of Harper 1 measured by the Veeco Interferometer.

The three-dimensional images shown in Figures 6.8 and 6.9 demonstrate the difference in roughness of the land area between the cells. Figure 6.8 shows that although some of the land between the cells is irregular it is relatively smooth when compared with the jagged land area between the YAG cells shown in Figure 6.9

The Scantron and Veeco images of the cells on the YAG band show that the cell depth appears to be less than the figure quoted by the manufacturer. However, a very small number of measurements were made and from these it is not possible to make a judgement as to how representative the results were to the anilox as a whole. It was not the remit of this work to assess the accuracy of the measurement methods or the manufacturers values. Multiple measurements to determine a statistically valid measurement for the average cell depth were not made, therefore the manufacturers value for the cell depths will be used in all calculations.

It is clear from both the Scantron and Veeco images that the real cells are not regular in size or shape. This makes the calculation of the parameters needed to modify the contact angle difficult. It was possible to obtain two-dimensional profiles of the bands on Harper 1 from which the gradient of the cell wall could be measured. Four scans were made of sections of the each band. From each scan, profiles of two cells were recorded in the x and y directions. A total of sixteen measurements were therefore made on each band. The raw data for each profile was processed by Microsoft Excel. A section of the cell wall was highlighted and a best-fit line added. The gradient of the best-fit line was recorded. The gradients of the best-fit lines were averaged to give a value for the mean slope of the cell wall for each band. The correlation coefficient, or R^2 value for each best-fit line was also noted. The R^2 value

varies between 1 and –1 and shows how well the data can be predicted from the best fit line. (1 and –1 being perfect fits whilst 0 indicates no fit). The R^2 value gives an indication of the deviation of the cell wall from its average slope, and provides a way of comparing the roughness of the cell walls. The plotted cell profiles and fitted slopes are shown in Sections A6-1 and A6-2 of the appendix respectively. The obtained values for the gradient of the cell walls are shown in Table 6.1.

CO_2			YAG		
Sample position	Gradient	R^2	Sample position	Gradient	R^2
1x1	0.61	0.965	1x1	0.84	0.956
1x2	0.65	0.952	1x2	1.04	0.972
1y1	0.56	0.978	1y1	0.88	0.945
1y2	0.56	0.988	1y2	1.06	0.952
2x1	0.49	0.963	2x1	0.97	0.964
2x2	0.67	0.979	2x2	1.13	0.967
2y1	0.65	0.996	2y1	1.27	0.963
2y2	0.52	0.991	2y2	0.15	0.945
3x1	0.66	0.980	3x1	0.87	0.969
3x2	0.67	0.989	3x2	1.25	0.949
3y1	0.75	0.995	3y1	1.24	0.915
3y2	0.67	0.992	3y2	1.16	0.974
4x1	0.70	0.989	4x1	0.71	0.933
4x2	0.75	0.994	4x2	0.96	0.976
4y1	0.58	0.976	4y1	1.01	0.949
4y2	0.60	0.977	4y2	0.94	0.899
mean	**0.63**	**0.981**	**mean**	**0.97**	**0.952**
deviation	**0.08**	**0.013**	**deviation**	**0.27**	**0.021**

Table 6.1. The gradient of the cell walls of Harper 1, measured from data collected by the Veeco interferometer.

The CO_2 cells had a shallower sloping wall than the YAG cells. The slope of the wall of the YAG cells showed a much larger deviation from the mean value, and the fit of the gradient line to the profile was worse than that of the CO_2 data, (shown by a

lower R^2 value.) indicating that the YAG cell interior is less regular than the CO_2 cell.

The roughness of the cell interior was measured using the interferometer. A sample area of 17 microns by 11 microns was profiled by the interferometer. The software made a compensation for the curvature of the cell wall and a roughness average or R_a was reported. The R_a value is the average deviation of the height (of depth) of the roughness peaks from the baseline. The R_a values were measured 5 times on 3 cells. The results were averaged and the standard deviation noted. The results are shown in Table 6.2.

Measurement number	R_a (nm) Harper 1 CO_2 band	R_a (nm) Harper 1 YAG band
1A	488.2	514.5
2A	418.9	359.0
3A	434.8	248.1
4A	484.1	390.1
5A	353.6	381.5
1B	464.9	396.8
2B	396.4	410.1
3B	490.8	464.3
4B	518.2	385.7
5B	613.8	548.0
1C	381.6	375.8
2C	450.7	406.6
3C	409.9	438.9
4C	406.6	427.5
5C	400.5	358.6
mean	447.5	407.0
standard deviation	65.4	70.0

Table 6.2. The roughness average of the interiors of the engraved cells, measured by the Veeco interferometer.

The R_a value unfortunately cannot be mathematically related to the Wenzel r-value. The measurements are however of much interest as they demonstrate that there is not a significant difference between the roughness of the interiors of the cells produced by the different lasers. There is no measurable characteristic roughness produced by the laser but the measurement in the form of R_A only reports the average height of the roughness and gives no information about the roughness shape. The Veeco images showed that the CO_2 cells had undulating roughness whilst the YAG cell interior appeared jagged. Spreading of a liquid is more sensitive to peaks with steep gradients, which pin the contact line.

Where possible the required parameters for each of the treatments of the contact angle data, were calculated from the information obtained from the Proscan optical sensor and the interferometer. However, this was not always possible. The Wenzel r factor due to the presence of the cells could not be directly measured, as although both instruments were capable of estimating the volume of a cell, neither could give the surface area of the cell interior. Therefore, attempts were made to approximate the cells on each band by a regular, mathematically definable shape from which the necessary topographical information could be estimated.

6.1.2 Using the Wenzel equation

The Wenzel equation is the simplest method of mathematically adjusting the contact angle to compensate for the effect of surface roughness. It applies the theory that the change in contact angle on a rough surface is due to the increase in contact area

between the solid and liquid. The Wenzel equation has been discussed in detail in section 2.1.2. The object of this exercise is to determine if the increased area that is produced by the engraved cells is responsible for the changes to the contact angles measured. The Wenzel equation has been criticised as only being applicable to highly artificial roughness with patterns that allow the contact line to move evenly in all directions. [84, 85] The pattern of cells is artificially regular and therefore is, in theory, a suitable surface for the Wenzel equation to be applied. . The roughness of the cells forms a regular pattern as shown in Figure 6.10. This is compared to the concentric ring model on which the Wenzel equation is knows to be applicable.

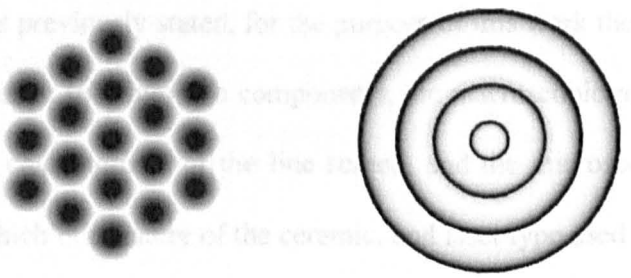

Engraved cells Concentric rings

Figure 6.10. Comparison of the regular pattern formed by cell in an engraving made at a sixty-degree angle with the concentric ring model.

The Wenzel equation uses a roughness factor, r, which is the ratio of the apparent area to the true area, this factor could not be calculated from the measured profiles as neither instrument had the capability of reporting the surface area of the cell interior wall. It was therefore necessary to estimate Wenzel's roughness ratio r. In order to do this, the cells were assumed to have the shape of hemi-ellipsoids, with two axes equal to the cell opening and the third axis equal to twice the cell depth. The equations for the surface area of an ellipsoid [130] and calculations are detailed in Section A6-3 of the appendix.

The calculations produced surface area values of 1421.42 μm^2 for the CO_2 engraving and 625.33 μm^2 for the YAG engraving. The cell wall was assumed to be circular, and the diameter of the land area of the cell was assumed equal to the cell opening plus half the width of the cell wall at each side. This gives the flat land area of the cell as 1385.44 μm^2 for a CO_2 cell and 352.99 μm^2 for a YAG cell. When the flat land area is divided by the calculated surface area for the hemi-ellipsoid model plus the wall area, Wenzel's r factor is obtained. The calculated values of r were, 1.2 for the CO_2 band and 2.0 for the YAG band

As previously stated, for the purpose of this work the surface roughness of the anilox can be split into two components, the macroscopic roughness due to the cells, which is characteristic of the line screen, and the microscopic roughness inside the cells, which is a feature of the ceramic, and laser type used to make the engraving. The size and shape of the cells are known and the ellipsoid model provides an estimate of r, Wenzel's factor of roughness, which is based on the macroscopic roughness only. Putting the calculated r-values into the Wenzel equation would, if the theory is correct, adjust the contact angle to remove the effect of the component of anilox roughness due to the line screen of the engraving. The theoretical contact angle generated by the calculation would be the theoretical contact angle produced by the interaction between the test liquid and the anilox surface, the properties of which are defined by the surface energy of the ceramic and the micro-roughness inside the cell and on the cell wall. It is not the theoretical value for a completely smooth sample. The contact angle measurement is modified to compensate for the bands having different numbers of cells over a given area and for the difference in surface area between the two cells. The Wenzel contact angles calculated from the MAMS and

the FTA data are shown in Tables 6.3 and 6.4, respectively. θ_m is the measured macroscopic contact angle and θ_w is the calculated Wenzel angle.

		CO_2 band	YAG band
θ_m	water	64°	76°
θ_w	**water**	**69°**	**83°**
θ_m	diiodomethane	19°	15°
θ_w	**diiodomethane**	**38°**	**61°**

Table 6.3. The observed and calculated contact angle values using the Wenzel equation on Harper 1 data from the MAMS instrument.

		CO_2 band	YAG band
θ_m	water	84°	100°
θ_w	**water**	**85°**	**95°**
θ_m	diiodomethane	43°	45°
θ_w	**diiodomethane**	**52°**	**69°**
θ_m	formamide	60°	64°
θ_w	**formamide**	65°	77°

Table 6.4. The observed and calculated contact angle values using the Wenzel equation on Harper 1 data from the FTA instrument.

The Wenzel equation predicts that the CO_2 band with a roughness ratio of 1:2 and a contact angle with water of 84° on the FTA instrument, would have a contact angle of 85° if the roughness was removed. However, it has been observed experimentally that the contact angle on a smooth piece of the material is 75°. This trend is repeated for the CO_2 and YAG, water contact angles measured on the MAMS instrument. The contact angles made by water on the YAG band and measured by the FTA instrument are modified towards the observed contact angle on the smooth sample. However, as the Wenzel equation modifies the cosine of the angle, the lowest obtuse contact angle can be modified to become is 90°. Therefore no matter what value of r is used the equilibrium value of 75° cannot be found.

There is a significant problem with use of the FTA instrument contact angle data in the Wenzel equation. The Wenzel equation uses equilibrium contact angle data. The contact angle data obtained using the FTA instrument, which were initially believed to be equilibrium angles, were found at a later point in the investigation to be advancing data (as discussed in Section 3.3.) the angles used are therefore already overestimates of the equilibrium contact angle.

As has been discussed in Section 2.1.2, using the Wenzel equation to predict the presence of roughness on a sample contradicts the experimental observations on all but very artificial structures with the impedance to the movement of the contact line is equal in all directions. It is clear from these results that the Wenzel equation does not describe the wetting behaviour on anilox Harper 1

It was thought that as this pattern has many lines of symmetry that the contact line would move evenly in all directions and approximate the concentric ring arrangement that the Wenzel equation has been shown to be applicable to. Contact angle analysis demonstrated that the hexagonal close packed arrangement of cells did not allow the contact line to move evenly in all directions. The Scantron and Veeco images showed that the real cell profile is far from regular and the curvature of the roll clearly promotes travel around the roll rather than along it.

The accuracy of the hemi-ellipsoid model used to approximate Wenzel's r-value was tested by making a comparison between the volume of the hemi-ellipsoid and the reported volume of the anilox cells. The volume of the hemi-ellipsoid was calculated in cm^3/m^2 and compared to the manufacturers reported volumes. The ellipsoid model overestimated the volumes for both bands, giving a volume of 5.8 cm^3/m^2 for the CO_2 band, which is high, compared to the reported figure of 4.1 cm^3/m^2, and 5.7 cm^3/m^2 for the YAG band, which is again high, compared to the reported volume of 3.6 cm^3/m^2. The calculations to obtain these figures are in Section A6-4 of the appendix.

The volume of the cells was approximated from the volumes supplied by Harper as cm^3/m^2 as 4674 μm^2 for the CO_2 band and 4160 μm^2 for the YAG band. Other regular shapes were evaluated to see if they produced an acceptable approximation to the volume of the cell. Cylinders produced twice the expected volume whilst cones and hexagonal based pyramids gave volumes of half the expected value.

Although the volumes given by the ellipsoid model are overestimates, it would not be correct to suggest that the ellipsoid model would also overestimate the surface area of the cell. The model assumes that the cell interior is smooth; the irregularity of the cell wall would increase the surface area of the cell. Contact angle measurement is sensitive to roughness of the order of 100 nm. [74] The interferometer measurements show that when the slope of the cell wall is taken into account the average height of the roughness peaks is in the order of 400nm which is therefore large enough to have an effect. The roughness of the cell interior walls was found not to differ significantly between the bands, however there are twice as many cells on the YAG band so the increased roughness would be double that for the CO_2 band.

6.1.3 Using the Shuttleworth and Bailey equation

The Shuttleworth and Bailey equations link the size of the advancing or receding contact angles to the slope of the surface roughness. These equations were discussed in Section 2.1.4. In order to adjust the contact angle data to compensate for the roughness of the cells, the maximum slope of the cell wall needed to be calculated. The hemi-ellipsoid model could not be used, as the maximum slope would be 90° for both cell shapes. Therefore to model the slope of the cell more accurately the cell shape was assumed to be a parabolic. This is shown in Figure 6.11.

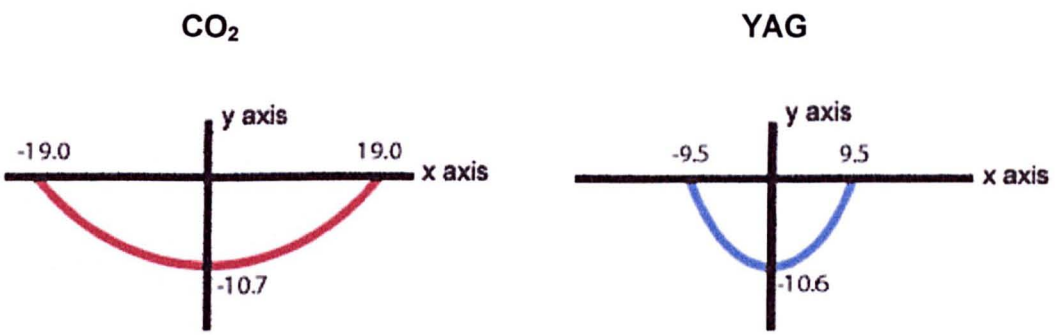

Figure 6.11. The engraved cells of Harper 1 approximated as quadratic parabola.

The term c is the y axis intercept and has the values -10.7 and -10.6 for the CO_2 and YAG parabola respectively. The term a is calculated from the value of x when y = 0 and is 0.0296 for the CO_2 curve and 0.1170 for the YAG curve. The gradient can be found by using differential of the equation of the curve, 2ax. The maximum gradient can be found by putting in the maximum value of x. The maximum gradients are 1.12 for the CO_2 curve and 2.23 for the YAG curve. Taking the inverse tangent gives the slope as an angle in degrees, giving maximum angles of 48° for the CO_2 curve and 66° for the YAG curve.

In order to verify that a parabola gave a good approximation to the cell shape data from a CO_2 cell profiled by the Veeco instrument was transformed to make fit the same mathematical space as the parabola. The data was manipulated so that it was centred about the y-axis and positioned below the x-axis. Values for the y co-ordinate were calculated for the x co-ordinates for which data was available using the above equation. The results are plotted in Figure 6.12.

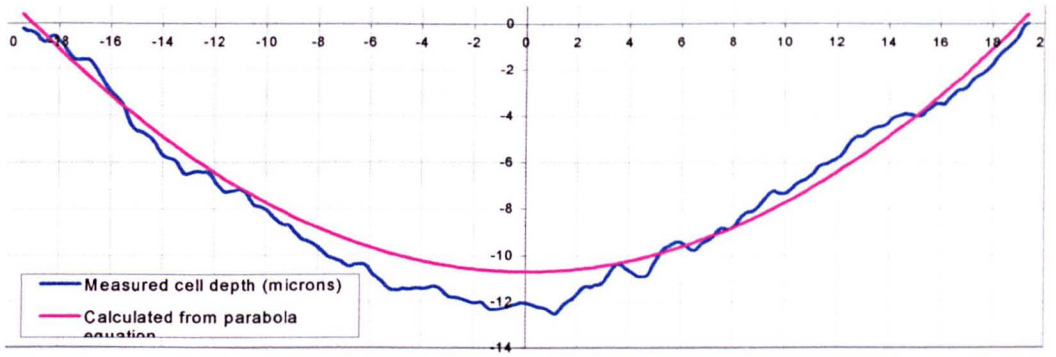

Figure 6.12. Fitting of the parabola $y = 0.0269x^2 - 10.7$ to a mapped cell from measurement Harper 1 CO_2 1x2.

The parabola appeared a good fit to the experimental data. The exercise was repeated for a YAG as shown in Figure 6.13. The fit of the parabola to the YAG cell was not as good. It was however concluded that this was due to the irregular shape of the YAG cell and that the parabola was the closest simple mathematically defined shape that could be used.

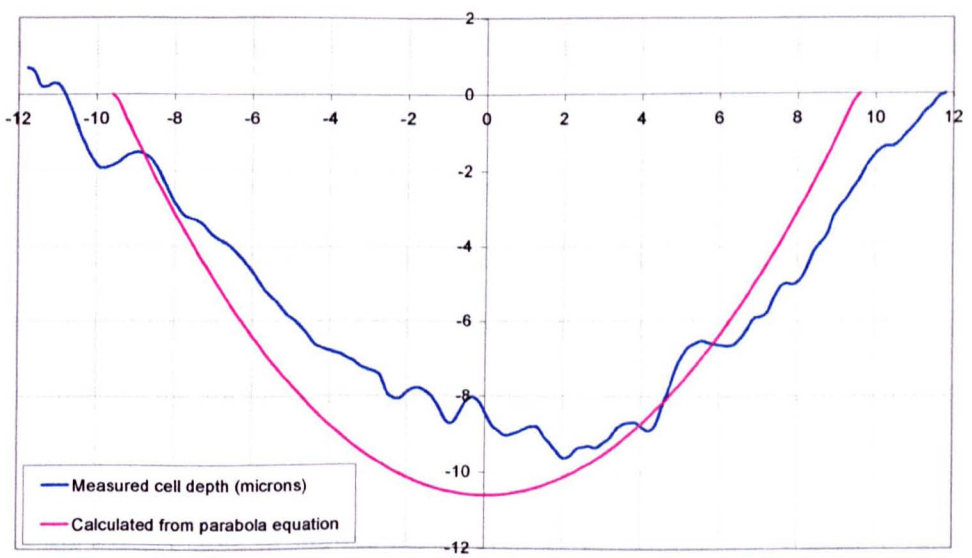

Figure 6.13. Fitting of the parabola $y = 0.1170x^2 - 10.6$ to a mapped cell from measurement Harper 1 YAG 4x2.

It was possible to generate parabola that were closer fits to the individual cells by using the trendline function in Excel. The red line in Figure 6.14 shows the best-fit 2nd order quadratic parabola along side the measured data and simple parabola.

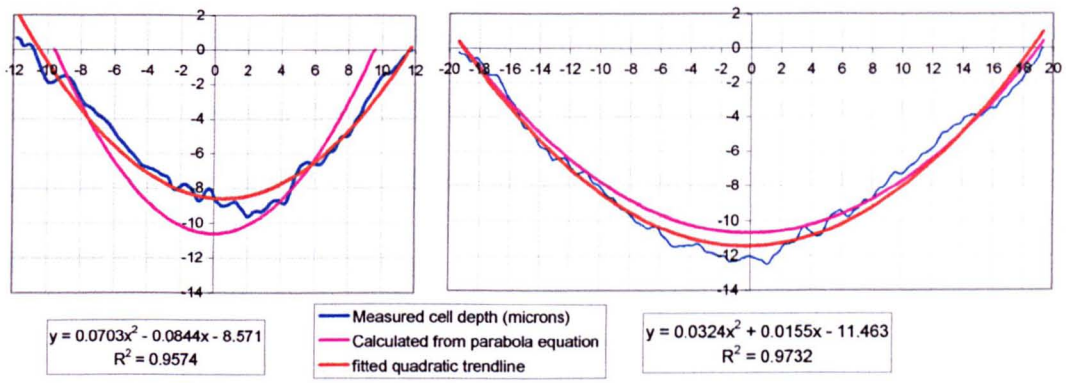

Figure 6.14. Fitted parabola to data from single cells on anilox Harper 1.

There are two advantages of using the simple parabola model. The fitted parabolas are specific to the selected cells. There is considerable variation between the measured cells and the quadratic equations generated for each cell cannot easily be averaged to give a general equation. The simple parabola is based on general measurements believed to be representative of the cells as a whole. The simple parabola can also be used to estimate the surface area. The calculations for this are shown in the Section A6-5 of the appendix. It is theoretically possible to make these calculations for the fitted equations but the mathematics becomes more complicated.

As the surface area of the parabola could be calculated, the Wenzel r-values were recalculated using this model. The calculations are shown in the Section A6-7 of the appendix. The r-value for the CO_2 cell was unchanged at 1.2. The r-value for the

YAG cell was reduced from 2.0 to 1.7 this produced a change in the Wenzel contact angle for the MAMS data from 83° to 82°. The conclusions reached in Section 6.1.2 are unchanged by the use of a more accurate model of the cell profile.

When the interferometer was used to map the anilox it became possible to measure the gradient of the cells directly from the profile data. The measurements and profiles are shown in Sections A6-1 and A6-2 of the appendix. The mean values for the gradient listed in Table 6.1 are shown in Table 6.5 along with the conversion of the gradient to an angle in degrees.

	CO_2 band			YAG band		
	tan θ	gradient	R^2 value	tan θ	gradient	R^2 value
Mean	0.63	32°	0.98	0.97	44°	0.95
Standard deviation	0.08	3°	0.01	0.27	8°	0.02

Table 6.5. The gradient of the cell wall of anilox Harper 1 calculated from data obtained with the Veeco interferometer.

The parabola approximation of the slope of the cells was seen to overestimate the angle of slope for both cells by approximately a third. Whilst the magnitudes of the slopes predicted by the model were very inaccurate the difference between the slopes of the cells was accurately predicted.

The Shuttleworth and Bailey equation for advancing angles is $\theta_a = \theta_e + \varnothing_m$. (Section 2.1.4, Equation 2.5.) The observed and theoretical equilibrium contact angles for the MAMS and FTA data are shown in Tables 6.6 and 6.7 respectively. The data from

the MAMS instrument had to be Equilibrium data as no other data was available. Advancing data was obtained on the FTA however the number of repeats was small. Advancing data was used for the diiodomethane calculations, however the advancing data using water was very similar to the equilibrium measurements (showing that the method of introducing the drop had produced advancing angles in that case). The equilibrium angles for water were used in place of the advancing data, as there were enough data points to be confident of an accurate average.

		Observed contact angle	Modified using parabola model	Modified using measured values
Polished band	**water**	**56°**	-	-
	diiodomethane	**20°**	-	-
CO_2 band	**water**	**64°**	**16°**	**32°**
	diiodomethane	**19°**	**0°**	**0°**
YAG band	**water**	**76°**	**10°**	**32°**
	diiodomethane	**15°**	**0°**	**0°**

Table 6.6. Theoretical contact angles produced by applying the Shuttleworth and Bailey equation to the MAMS data from anilox Harper 1.

		Observed contact angle	Modified using parabola model	Modified using measured values
Polished band	**water**	**75°**	-	-
	diiodomethane	**42°**	-	-
CO_2 band	**water**	**84°**	**36°**	**52°**
	diiodomethane	**51°**	**3°**	**19°**
YAG band	**water**	**100°**	**30°**	**56°**
	diiodomethane	**51°**	**0°**	**7°**

Table 6.7. The theoretical contact angles produced by applying the Shuttleworth and Bailey equation to the FTA data from anilox Harper 1.

The angle of maximum slope of the roughness is subtracted from the observed contact angle to give the theoretical angle. In some cases this is larger than the observed angles made by diiodomethane or formamide drops. This gives a modified contact angle of 0°. An angle of 0° cannot be used in surface energy calculations, as it would imply an infinitely high surface energy.

The contact angles obtained using the MAMS instrument were equilibrium contact angles. As the Shuttleworth and Bailey equations modify the advancing or receding contact angles they are not appropriate for use with the MAMS data. The FTA instrument produced advancing data. The use of the Shuttleworth and Bailey equation adjusts the contact angles made by both test liquids in the correct direction. However if the measurement on the polished unengraved area using the FTA

instrument is considered a reasonable approximation of the equilibrium angle, using this equation over adjusted the contact angles significantly for both sets of data. The FTA was used to make measurements of advancing contact angles and equilibrium contact angles. However the contact angle measurements on all bands were found to have been advanced, even when the intent was to measure equilibrium angles. The polished band was also found to be an advanced angle and therefore the estimate of the equilibrium angle is known to be too high. The equilibrium angle using diiodomethane on the polished band was not equal to the advancing angle on that band. However this does not necessarily mean that it is a good approximation of the equilibrium angle. The modification of the FTA data using the measured values for the maximum gradient give values very close to the equilibrium contact angles measured with the MAMS instrument on the polished band. This is shown in table 6.8. The errors quoted along side the angles are a sum of the uncertainties from the contact angle measurement and the gradient measurements.

The calculated angle for diiodomethane on the YAG band is the furthest away from the MAMS value. When the uncertainty in the measurement of the slope is considered the measurement could be 8° higher than the reported value. There was a 3° uncertainty in the measurement of the angle. This gives a total uncertainty of 11° and indicates that the true value for this angle could be as high as 18°, which is within the bounds of the uncertainty of the contact angle measurement on the polished band. The agreement between all the other calculations and the measured values are very good.

Water	Contact angle on the polished band measured using the MAMS instrument	56° +/- 2°
	Shuttleworth and Bailey angle calculated from advancing angle data measured using the FTA instrument and on the CO_2 band	52° +/- 5°
	Shuttleworth and Bailey angle calculated from advancing angle data measured using the FTA instrument and on the YAG band	56° +/- 10°
Diiodomethane	Contact angle on the polished band measured using the MAMS instrument	20° +/- 2°
	Shuttleworth and Bailey angle calculated from advancing angle data measured using the FTA instrument and on the CO_2 band	19° +/- 5°
	Shuttleworth and Bailey angle calculated from advancing angle data measured using the FTA instrument and on the YAG band	7° +/- 11°

Table 6.8. A comparison of the angles produced the MAMS instrument on the polished band to those calculated using the Shuttleworth and Bailey equation and the advancing data obtained using the FTA.

The use of the Shuttleworth and Bailey equation, like the Wenzel equation predicts that the diiodomethane drops should be affected by the roughness of the bands in the same way as the water drops. However, the advancing contact angles of the diiodomethane drops on the rough bands were only slightly higher than those on the smooth bands, other factors such as the curvature of the roll, micro roughness of the polished band and surface contamination clearly have produce contact angle hysteresis on the unengraved polished areas of Harper 1.

Johnson and Dettre [93] hypothesised that the maximum and minimum combinations, taken by Shuttleworth and Bailey to be the advancing and receding contact angles are not likely to occur in real conditions due to thermodynamic constraints. They

suggested that the true equilibrium contact angle was somewhere between the predictions made by Shuttleworth and Bailey, and the prediction made by Wenzel. This would give a range from 52° to 69° for the CO_2 band and 56° to 83° for the YAG band. The corresponding observed value on the polished band is 56° using the MAMS instrument. These results support the hypothesis that the contact angle on the polished band as measured with the MAMS instrument approximates the equilibrium contact angle. The error involved in these calculations is however large. The surface of the anilox was not rigorously designed to be uniform and easily modelled or measured as was the case for surfaces in which these equations have been developed on. There is significant error involved in estimating Wenzel's r-value and measuring gradients of the cells. The Shuttleworth and Bailey equations have been successfully used to explain the size of the advancing contact angle on structured paper samples by Wagberg & Westlind [97]

6.1.4 Using the Cassie and Baxter equation

When the contact angle on a surface approaches or exceeds 90°, it may not be favourable for the test liquid, in this case water, to wet the bottoms of the cells. This would result in a composite surface of solid/liquid and solid/vapour interfaces, which can be described using the Cassie and Baxter equation (Equation 2.4), $\cos \theta_C = f_1 \cos \theta_e - f_2$, where f_1 and f_2 are the fractions of solid/liquid and solid/air interfaces respectively and θ_C and θ_e are the Cassie and equilibrium contact angles.

The contact angles made by water on the engraved bands of the anilox were considered in order to determine if the Cassie and Baxter equation could be applied. A three-dimensional scan of a small section of each anilox band had been made with a Proscan 100 optical sensor. Changes in height were indicated by colour, with blue showing the low areas at the bottom of the cells and green the raised cell wall.

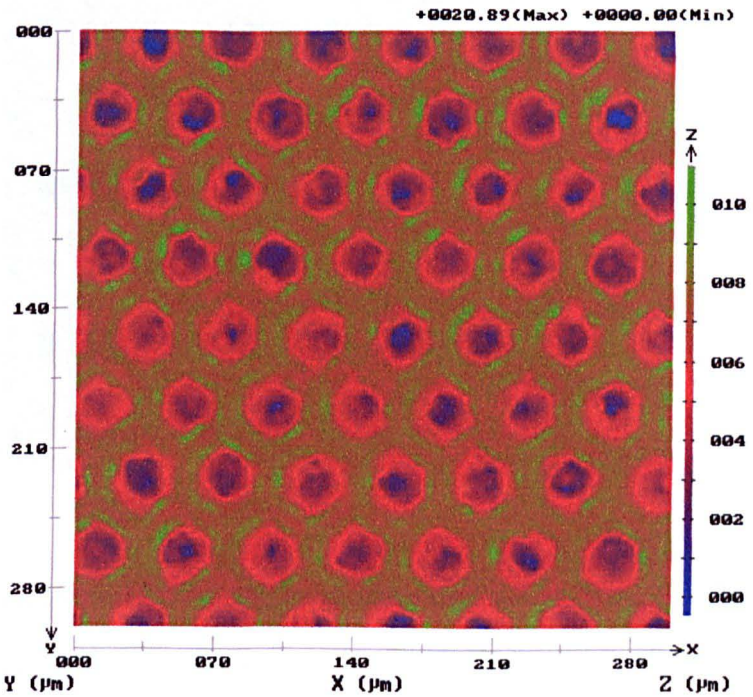

Figure 6.15. A Scan of cells on the CO_2 band made by the Scantron Proscan 100 instrument.

Graphical tools were used to determine whether the changes to the contact angle made by water on the engraved bands could be explained by the bottoms of the cells being unwet. An area of the image covering 42 cells was selected. The image size was measured and found to be 18878 pixels squared. A circle shape was selected which best covered up the blue and purple areas of the cell (up to an approximate

depth of 3μm on the scale). The image with the circles overlaid is shown in Figure 6.13. Each circle had a diameter of 9.5 pixels and therefore covered an area of 71 pixels squared. The cells in total thus take up an area of 2977 pixels squared. This translated to 16% of the overall area or a fractional area of 0.16.

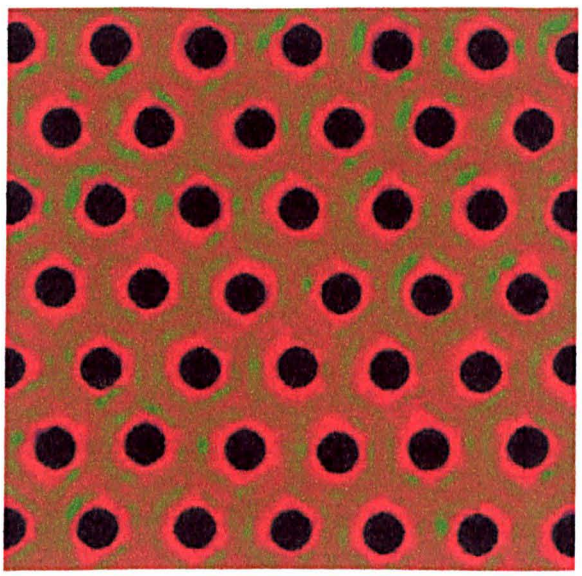

Figure 6.16. A section of the Scantron image on the CO_2 band with the bottom 3μm of each cell blacked out

The Cassie equation can be rearranged to solve for f_1, the fractional area corresponding to the solid/liquid interface, using the relationship $f_2 = 1 - f_1$.

$$f_1 = (\cos\theta_c + 1) / (\cos\theta_e + 1) \qquad \text{Equation 2.5}$$

The observed angles on the engraved bands are assumed to be Cassie contact angles. The observed angle on the unengraved, polished band is assumed to be the equilibrium contact angle.

Using the MAMS data, the value f_1 is equal to the cosine of 64, plus 1, divided by the cosine of 56 plus 1. This gives a value of 0.92 for f_1, the fraction of water/ceramic interface. The fraction of the surface that is unwet, f_2 is therefore 0.08 or 8%.

Using the FTA data, the value f_1 is equal to the cosine of 84, plus 1, divided by the cosine of 75 plus 1. This gives a value of 0.88 for f_1, the fraction of water/ceramic interface. The fraction of the surface that is unwet, f_2 is therefore 0.12 or 12%.

The values using the FTA data are closest to the value estimated by the graphical analysis of 16%. However the FTA data is advancing data and therefore should not be used either as a Cassie angle or an equilibrium angle. The value of 8% produced by the MAMS data must be the correct value if a composite air/ceramic surface is formed when the bands are wet with water and this is half that predicted by the graphical estimate.

The calculations were repeated using a Scantron image of the YAG cells, this is shown in Figure 6.17. The blue and purple areas of the scan were again overlaid with circles of known diameter. This time an area corresponding to the bottom 4 μm of the cell was covered. This is shown in Figure 6.18. The Isolated area contained 40 cells of radius 13 pixels and had an area of 13867 pixels squared. The overlaid area was found to cover 38% of the overall area.

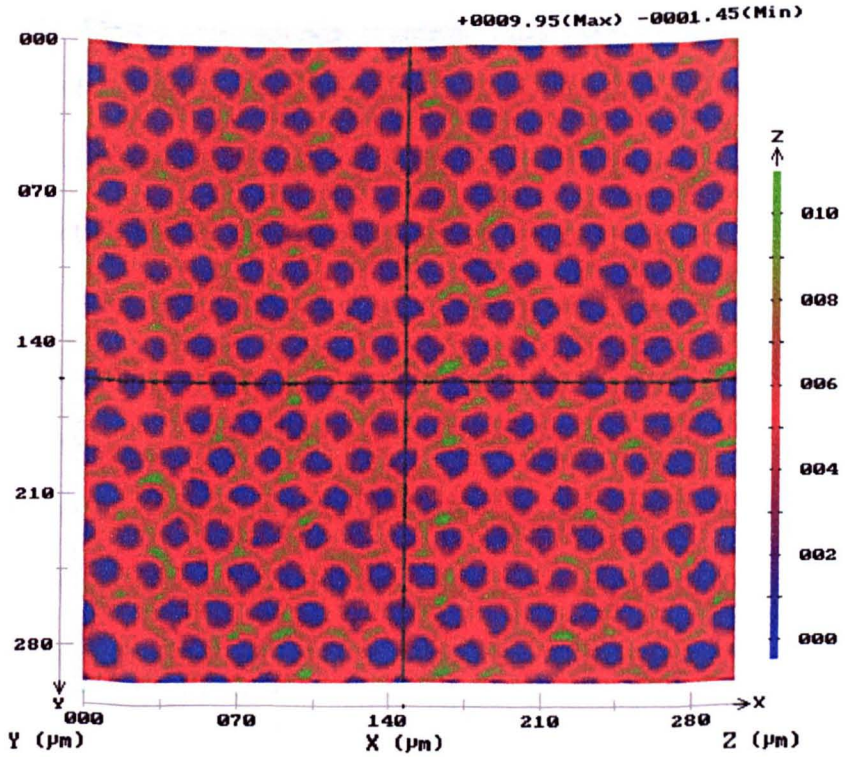

Figure 6.17. An image of cells on the YAG band, made by the Scantron Proscan 100 instrument.

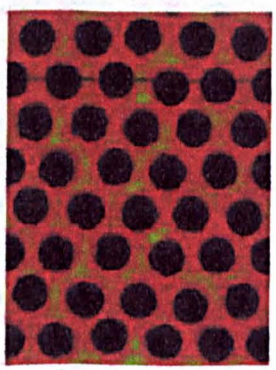

Figure 6.18. A section of the Scantron image on the YAG band with the bottom 4 μm of each cell blacked out.

Again using Equation 2.5, f_l using the MAMS data is found by the cosine of 76, plus 1 divided by the cosine of 56 plus 1. This returns an answer of 0.80 which gives the amount of unwet surface as 20%

When the FTA contact angle data was substituted into the equation f_1 was calculated to be 0.66, Giving the unwet fraction f_2 as 0.34 or 34%, This value is of the same order as the estimate of the base of the YAG cell of 38% but is again based on advancing data which is unsuitable for use in this way.

The graphic estimation of the unwet was based on the height that could easily be selected as the base of the cell from the Scantron images. The height that could be chosen was determined by the colour variation of the scale. A circle with area 36 pixels squared (which is the area of air/water interface at the base of each cell if 8% of the surface remained unwet) was added to the image of the cells in Figure 6.19. The cells however proved too irregular and the scale too large to give a definite value for the amount of unwet cell this would correspond to.

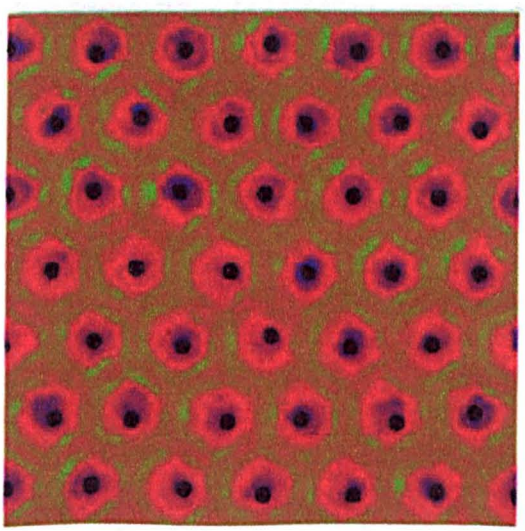

Figure 6.19. A section of the Scantron image on the CO_2 band with an area corresponding to 8% of each cell blacked out.

In order to model the depth to which an average cell would be wet to, if the prediction made by the Cassie and Baxter equation and MAMS data is correct, the parabola model detailed in Section 6.1.3 was used. The surface area of one cell with its share of land was calculated as for use with the Wenzel equation (shown in Section A6-6 of the appendix.) The surface area of a new small parabola at the bottom of the large parabola was calculated. This is illustrated in Figure 6.20. The height of the parabola from its minimum was varied by changing the y value at the top of the parabola until the ratio of the area of the circle formed at a height termed y = n. to the surface area of the large parabola minus the surface area of the small parabola, reached the desired relationship of 0.92.

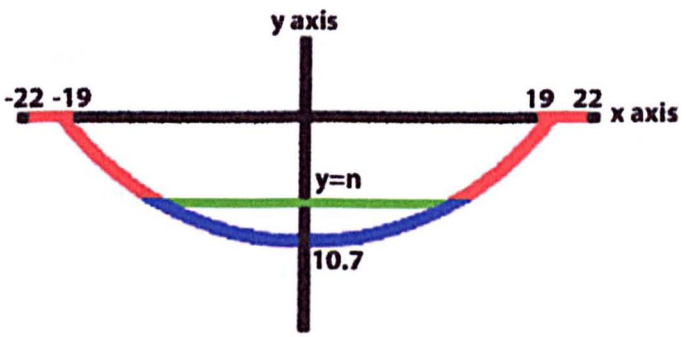

Figure 6.20. Using the parabola model to calculate the depth to which a CO_2 cell is unwet according to the Cassie and Baxter model.

The area of the circle at y=n (the diameter of which is shown by the green line in Figure 6.20.) is the area of air/water interface. The area of the cell and land in contact with the water is shown in red. The calculation is shown in detail in Section A6-7 of the appendix. When the relative areas were varied, the value of n that produced an

area of air/water interface of 8% was -9.43. This indicates that the bottom 1.27 microns of the cell remain unwet.

This calculation was repeated for a YAG cell modelled by a parabola as described in Section 6.1.3. The value of n that produced an air/water interface of 20% was –5.93. This indicates that the bottom 4.67 microns of the cell remains unwet.

The Cassie and Baxter theory can be used to explain the differences in wetting behaviour between water and diiodomethane. The surface energy of the anilox is largely non-polar and the diiodomethane wets by dispersive or non-polar interactions. Therefore the diiodomethane drops have no problems in wetting the cells completely, no composite surface is formed and therefore no change in the contact angle due to the presence of an additional solid/air interface.

If the water penetrates the cells, the volume of the drop that is observed on the surface should be less than the dispensed volume. In theory, it should be possible to check to see if there is a volume "loss" observed due to the liquid sitting in the cells and therefore being invisible to the camera. The largest drops observed during these experiments had a diameter in the order of 6 mm and therefore took up an area on the roll of approximately 2.8 $x10^{-5}$ m^2. From the volumes supplied by Harper, this equates to 0.12 µl for the CO_2 band and 0.10 µl for the YAG band. Even if the cells were completely filling this would still be too small a difference to detect with either the MAMS or the FTA instruments.

There is support for the applicability of the Cassie and Baxter equation to the wetting of the anilox cells from a paper by Oliver and Mason. [99] They examined a metal surface that contained an orthogonal array of holes (the same pattern as a 45° engraving) having an approximate line count of 28 lines per cm. Their findings on wetting this surface with ethylene glycol were that for large drops the results were consistent with the Cassie and Baxter equation, and that the liquid did not penetrate into the holes. The equilibrium contact angle reported for ethylene glycol on polished stainless steel was 60.2° +/- 1.6° indicating the liquid wet the surface more easily than the water wet the anilox. The sides of the holes in the steel were at 90° to the surface rather than the gentler slope of the cells on the anilox, making penetration of the holes less favourable. The anilox cells are however an order of magnitude smaller than the holes present in the stainless steel. Therefore smaller pockets of the air/liquid interface would have to be created in order for the cell bottoms to remain unwet.

A recent paper by Abdelsalsm et al [131] has studied the contact angles formed on a close packed array of cells formed on a gold surface, which resemble a 60° engraving on a smaller scale. The size of the pore opening is controlled by depositing varying thicknesses of gold through an array of polystyrene spheres. The size of the openings are not listed in the paper, however three pores cover a 2μm length making them about two orders of magnitude smaller than anilox cells. The findings of this work were that by increasing thickness of the gold, and therefore changing the shape of the pores from shallow bowls to almost enclosed spheres the contact angle was seen to change in accordance with the Cassie and Baxter relation. This is particularly significant to this work as the smooth gold gave a contact angle with water of less

than 90° (as does the unengraved ceramic) It was shown that roughness can make a hydrophilic surface hydrophobic.

It is the hypothesis of this author that spreading on a microscopic scale occurs by the contact line travelling over peaks and troughs due to the presence of the engraved cells, the effect of the roughness on the contact line is very localised and becomes the determining factor when the contact line is advanced or receded. The advancing angles are therefore dictated by cell geometry and uniformity. The changes to the contact angles that are observable when polar liquids are able to reach equilibrium contact angles on the engraved bands are due to incomplete penetration into the cells by liquids with highly polar nature, as is consistent with the theory of Cassie and Baxter and with the experimental observations of Oliver and Mason, [97] and Abdelsalsm et al.

6.2 Using the Wenzel, Shuttleworth and Bailey and the Cassie and Baxter equations on the contact angle data from Pira 1

6.2.1 Estimation of the dimensions of the cells on the anilox Pira 1

Anilox Pira 1 was too large to move from the Pira pressroom. As none of the measurement devices could be taken to Pira it was not possible to obtain any data on the topography of the engraved cells. The mathematical modelling strategy was used, as with anilox Harper 1 in Section 6.1, to produce estimates of the geometry of the roughness due to the cells. The theories of the modification of the contact angle were

then applied to the roughness geometries in order to assess the applicability of these theories to the contact angle data.

The shape of the cells on anilox Pira 1 was modelled mathematically. As the cells on Pira 1 were engraved in a 45° pattern the best approximation of the cell shape is a square based pyramid (see section 1.3.3) the height of the pyramid i.e. the depth of the cell, was not known and had to be calculated from the cell volume and the width of the cell opening. The calculations are shown in full in the Section A6-8 of the appendix. The width of the cell was calculated from the line screen with the cell wall estimated from literature values. The cell opening was calculated as 4.9×10^{-5}m or 49 microns. The volume of an individual cell was calculated by multiplying the reported volume in cm^3/m^2 by the area that the cell occupies and were found to be 1.5×10^{-14} m^3 for band one, 1.7×10^{-14} m^3 for band two and 1.9×10^{-14} m^3 for band three. The calculated cell depths were 1.9×10^{-5}m or 19 microns for band one, 2.1×10^{-5}m or 21 microns for band two and 2.4×10^{-5}m or 24 microns for band three. From this information the parameters needed for the Wenzel, Shuttleworth and Bailey, and Cassie and Baxter equations were calculated. These calculations form Sections A6-9 and A6-10 of the appendix.

6.2.2 Application of the Wenzel, Shuttleworth and Bailey and Cassie and Baxter equations to the Pira 1 data

In the absence of any chemical change to the anilox surface brought about by the engraving process, it would be expected that the roughness created by the presence

of the cells would change the observed contact angle. The Wenzel and Shuttleworth and Bailey and Cassie and Baxter equations were used as before in an attempt to estimate the magnitude of predicted change in contact angle.

The Wenzel equation was applied to the contact angles observed on anilox Pira 1 in the same way as with Harper 1. The r term was calculated by assuming that the increased volume was equal to the surface area of the triangular faces of the pyramid plus the cell wall. The calculations are shown in full in Section A6-9 of the appendix. The r values were: for band one, r = 1.13 and for band two r = 1.15, for band three r = 1.20. The r-values were then used along with the contact angle data obtained using the MAMS instrument, to calculate the Wenzel contact angle for each band. The results of the calculation are shown in Table 6.9.

The theoretical contact angles predicted by the Wenzel equation again shifted the contact angles in the opposite direction to the experimental observations. However the estimated cell dimensions for the bands were very similar and gave r values for bands one and two that were only 0.02 apart. These r values were not rounded to one decimal place, as has been the case in other calculations, as the difference would have been exaggerated to 0.1. The r values used in the calculations were correct to two decimal places.

		Observed contact angle	Wenzel contact angle	Shuttleworth & Bailey contact angle
Water	Polished band	50°	-	-
	CO_2 band 1	52°	57°	14°
	CO_2 band 2	52°	58°	11°
	CO_2 band 3	52°	59°	8°
Diiodomethane	Polished band	14°	-	-
	CO_2 band 1	17°	32°	0°
	CO_2 band 2	15°	33°	0°
	CO_2 band 3	12°	35°	0°

Table 6.9. The effect of applying the Shuttleworth and Bailey, and Wenzel equations to the Pira 1 data.

The use of the Wenzel equation not only moved the contact angles in the opposite direction to the observations but also created a small difference between the bands. It is clear that the Wenzel equation does not describe the wetting interactions at the surface of Pira 1.

The slope of the cell wall was calculated for each band and found to be 38°, 41° and 44° for bands 1, 2 and 3, respectively. When these angles were subtracted from the MAMS contact angles in accordance with the Shuttleworth and Bailey equation for advancing angles the resulting calculated contact angles were much lower than the equilibrium value observed on the unengraved band. The modification of the diiodomethane contact angles took them below 0°. As discussed in Section 6.1.2, the Shuttleworth and Bailey method used is for advancing contact angles. The contact angles that have been observed on the bands of anilox Pira 1 have been allowed to find an equilibrium shape and have not been further advanced by the addition of

more liquid. The observed angles are therefore lower than true advancing angles would be. It was not possible to measure advancing angles with the MAMS instrument therefore the Shuttleworth and Bailey modifications have no relevance to the Pira 1 data.

As the contact angles observed on the polished and unengraved areas are within the deviation of measurement there is no evidence to suggest that there is incomplete wetting of the cells, leading to a composite air/ceramic surface which could be described by the Cassie and Baxter equation. It is apparent that none of the methods of modifying the contact angle to compensate for the deviation of the anilox surface from the ideal are appropriate. It is unfortunate that advancing and receding contact angles could not be measured on anilox Pira 1, as the Shuttleworth and Bailey model, is in theory, the best suited to apply to the system. The engraved pyramids are of a smaller order of magnitude than those used in the work of Bartell and Shepherd [91, 92] however the surfaces are topographically similar and the Shuttleworth and Bailey equations were shown to be applicable in that case.

6.3 Application of the Wenzel, Shuttleworth and Bailey, and Cassie and Baxter theories to anilox Harper 2

6.3.1 Measurements of the cells on Harper 2

Measurements of the cell profiles of Harper 2 were made using a Veeco interferometer at the Welsh centre for Printing and Coating in Swansea. Harper 2

was too large to fit on the sample platform of the instrument used to measure Harper 1. The Veeco roll scope, a portable interferometer therefore had to be used. The roll scope was less sensitive than the instrument used to measure Harper 1 and the amount of noise in the measurements was much greater. Two-dimensional measurements of the cells were made in the same way as for anilox Harper 1. The data was exported into Excel. Measurements were made at three sites on the CO_2 band and two sites on the YAG band. Four profiles of the cell were made at each site. The data was graphed in Excel and gradients were fitted to the slope of the cell wall as done with the Harper 1 data. The graphical profiles and fitted gradients are shown in Section A6-11 and A6-12 of the appendix. The results of this work are tabulated in Table 6.10.

CO_2			YAG		
Sample	**Gradient**	**R^2**	**Sample**	**Gradient**	**R^2**
1x1	1.57	0.947	1x1	0.71	0.916
1x2	0.38	0.915	1x2	0.97	0.882
1y1	0.39	0.952	1y1	0.70	0.895
1y2	0.87	0.782	1y2	0.94	0.891
2x1	0.35	0.941	2x1	0.59	0.952
2x2	0.57	0.865	2x2	0.74	0.788
2y1	0.37	0.943	2y1	0.47	0.965
2y2	0.47	0.956	2y2	0.52	0.924
3x1	0.42	0.970			
3x2	0.45	0.969			
3y1	0.59	0.956			
3y2	0.51	0.973			
mean	0.58	0.931	**mean**	0.71	0.901
deviation	0.34	0.055	**deviation**	0.18	0.054

Table 6.10. The gradient of the cell walls of Harper 2, measured from data collected by the Veeco roll scope interferometer.

There was a problem with dried ink plugging the cells of the anilox. Some plugging damage to the cells was visible with the naked eye. This had been visible since before the press trial and was believed to be from attempts to measure contact angles using UV curable and water-based inks. Surface measurements were not made in these areas. Further plugging of the anilox that was not visually discernable was obvious from the image produced by the interferometer. Scans which showed obvious plugging were discarded. Unfortunately some plugged cells on the CO_2 band were overlooked when the measurements were taken and identified only when the data was studied at a later date. The sites coded 1 and 2 on the CO_2 band were seen to have significant plugging. Figures 6.21 6.22 and 6.23 show examples of cell profiles from sites 1, 2 and 3 respectively. Graphs showing all measurements made are included in Section A6-11 of the appendix. The cells from sites 1 and 2 are shallow and have flatter bases showing that they are plugged with ink. The cells measured at site 3 are deeper and have a more pointed bottom on the graphs. It is useful to note here that the scales of the x and y axis are unequal and exaggerate the depths of the cells.

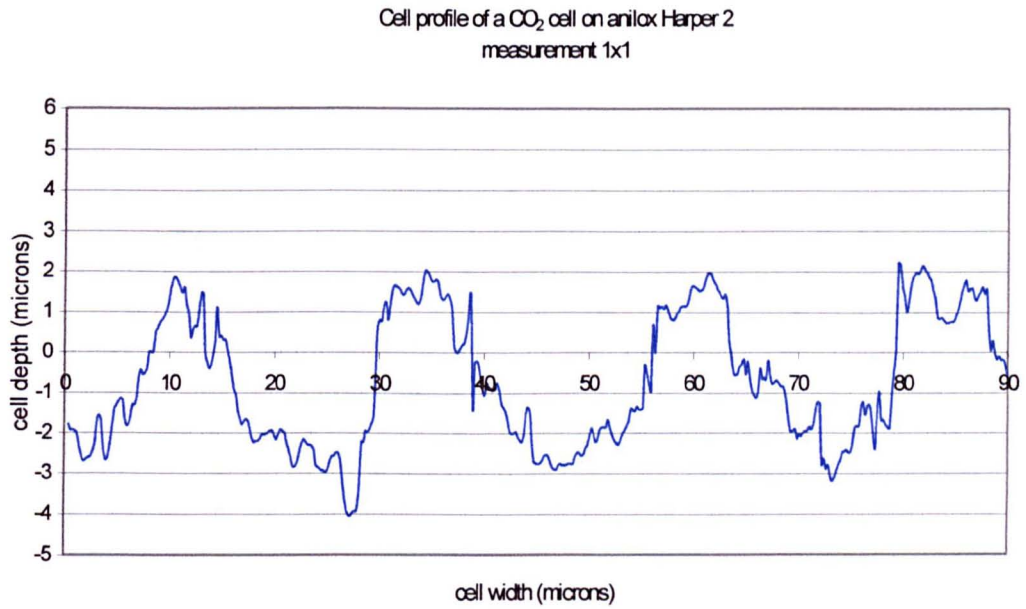

Figure 6.21. A profile of cells at measurement site 1 on the CO_2 band showing plugged cells.

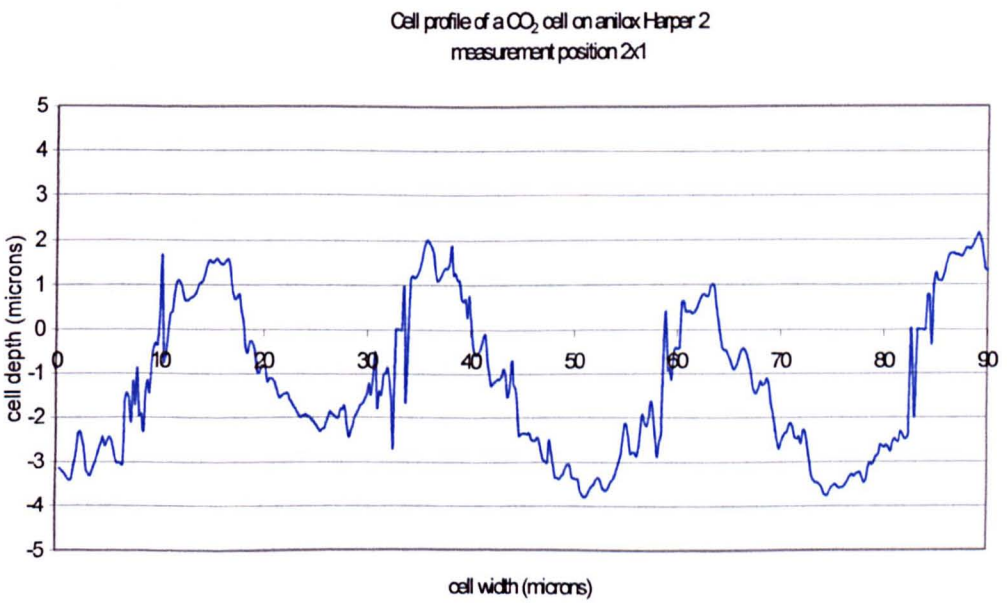

Figure 6.22. A profile of cells at measurement site 2 on the CO_2 band showing plugged cells.

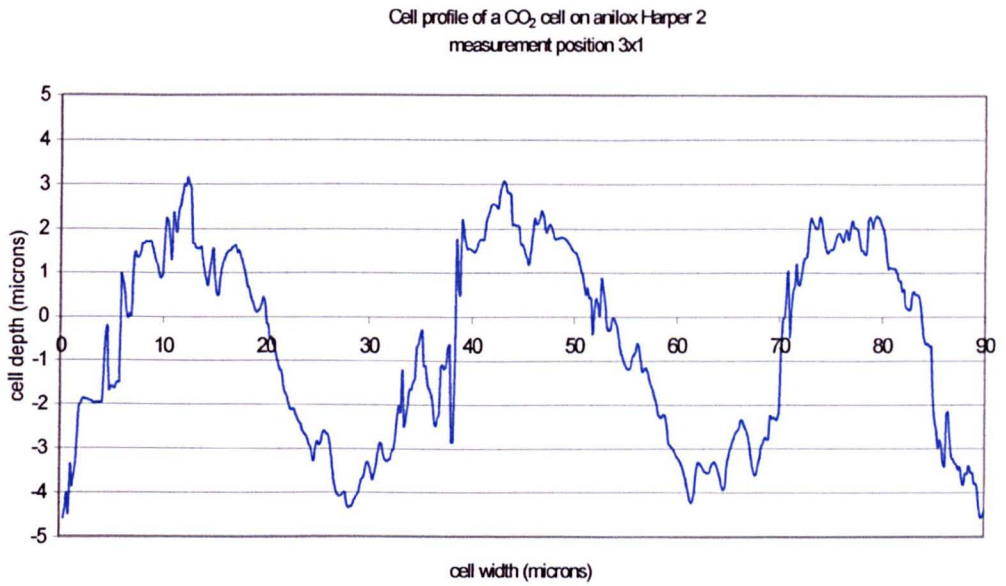

Figure 6.23. A profile of cells at measurement site 3 on the CO_2 band showing unplugged cells.

The cell depth reported by the Harper Corporation was 7.8 microns. Although the cells shown in Figure 6.23 are deeper than in those in Figures 6.22 and 6.21 they are of the order of 7 microns, 0.8 microns less than stated. As previously discussed in Section 5.2.1 and Section 6.1.1, the manufacturers values for the cell depth are an average value and as multiple measurements were not taken the accuracy of these values is not known. The values of the cell depths on Harper 1 were also lower than the values reported by Harper. It is therefore reasonable to assume that the cells measured at site 3 on the CO_2 band are unplugged and that the small variation from the manufacturers value is as a result of different measurement techniques to establish the value for the cell depth and normal manufacturing variations in the cell dimensions.

The gradients measured from the cells at site three, when averaged, gave a result that was smaller than the average gradient on all CO_2 sites. The results for site three are shown in Table 6.11. Four measurements are however too few to be confident that the result is representative. The data was reconsidered and two more gradient measurements were made at each position on site 3. The results are shown in Table 6.12. The average gradient of these measurements is of the same order as the initial calculation from all sites showing that cell plugging has no affect on the gradient of the cells.

CO_2		
Sample position	**Gradient**	R^2
3x1	0.42	0.970
3x2	0.45	0.969
3y1	0.59	0.956
3y2	0.51	0.973
mean	0.49	0.967
deviation	0.08	0.008

Table 6.11. The gradient of the cell walls measured using initial measurements on cells at site 3 only.

CO_2		
Sample position	**Gradient**	**R^2**
3x1a	0.42	0.970
3x1b	1.05	0.940
3x1c	0.52	0.960
3x2a	0.45	0.969
3x2b	0.38	0.942
3x2c	0.83	0.938
3y1a	0.59	0.956
3y1b	0.70	0.933
3y1c	0.53	0.963
3y2a	0.51	0.973
3y2b	0.47	0.902
3y2c	0.54	0.748
mean	**0.58**	**0.933**
standard deviation	**0.19**	**0.062**

Table 6.12. The gradient of the cells on site 3 of the CO_2 band calculated from 3 measurements in each position.

The exercise of making multiple measurements on the cell profile data demonstrated a possible systematic error in the results. When measurements were made, in order to select a best-fit line with a high R^2 value, a cell wall that was relatively smooth was normally selected. As the selection of the walls measured was therefore not random the results could not be assumed to be representative of the sample set as a whole. Figure 6.24 shows an example of how the profile of the cell influenced the measurement of the gradient. Figure 6.24 shows a graphical representation of the profile of two cells that has been converted into a picture in order to add multiple gradient lines. The gradient lines are an illustration of the lines fitted by Excel. The

original best-fit graphs can be found in Section A6-12 of the appendix. The first two lines fitted to the profile, 3y2a and 3y2b, are shown in Figure 6.24 in red. Both best-fit lines are a good fit to the data. They are both measurements of slope in the same direction, the positive direction (\ ). When the third measurement was taken the best-fit line (shown in yellow) is not a good fit to the data. If this measurement is ignored then only measurements in one direction are made. However the slope calculated is not an accurate measure of the steepness of the cells (as in the case of the gradient indicated by the yellow line). Measurements were therefore taken wherever possible on both positive and negative slopes

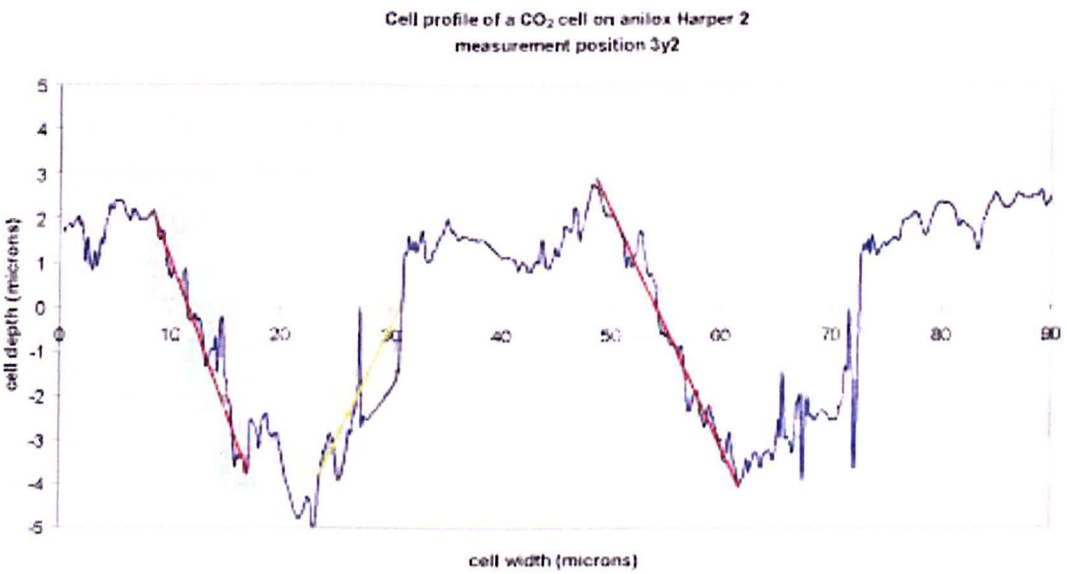

Figure 6.24. An example of how the quality of the profile can influence the gradient measurement.

The data obtained on the YAG bands was re-examined and further measurements were made to increase the number of measurements. Care was taken to include

measurements from each side of the cell wall. Two measurements were made on each profile. The complete set of measurements is shown in Table 6.11. The extra measurements made did not significantly alter the average gradient reported, the average R^2 value (used as an indication of the roughness) or the standard deviation of the results. The gradient values used with the Shuttleworth and Bailey equations will be the mean values for Tables 6.12 and 6.13.

YAG		
Sample position	**Gradient**	**R^2**
1x1	0.71	0.916
1x2	0.97	0.882
1y1	0.70	0.895
1y2	0.94	0.891
2x1	0.59	0.952
2x2	0.74	0.788
2y1	0.47	0.965
2y2	0.52	0.924
1x1b	1.05	0.958
1x2b	0.48	0.935
1y1b	0.78	0.829
1y2b	0.64	0.916
2x1b	0.72	0.912
2x2b	0.74	0.851
2y1b	0.97	0.834
2y2b	0.78	0.887
mean	**0.74**	**0.896**
standard deviation	**0.18**	**0.050**

Table 6.13. The gradient of the cells on site 3 of the YAG band calculated from 2 measurements made on each profile measured.

The roughness was again measured using the roll scope interferometer. The reading again included more noise and although the difference in roughness between the two bands was larger than on Harper 1 the amount of noise in the reading made it impossible to determine if this difference is real.

Measurement number	R_a (nm) Harper 2 CO_2 band	R_a (nm) Harper 2 YAG band
1A	396.97	437.59
2A	380.02	756.95
3A	498.98	401.51
4A	574.41	510.95
5A	407.48	593.67
1B	340.73	556.00
2B	361.55	670.64
3B	326.04	500.04
4B	502.82	404.10
5B	318.33	716.36
1C	323.89	581.43
2C	404.53	348.27
3C	485.23	508.61
4C	418.42	459.97
5C	457.91	717.06
mean	413.15	544.21
standard deviation	76.79	127.03

Table 6.14. Measurements of interior surface roughness of the two engraved bands on Harper 2.

In order to calculate the parameters needed for analysis the cells on each band were modelled by a parabola in the same way detailed for Harper 1 in Section 6.1.3. The parabolas with their equations are shown in Figure 6.2.4. The parabolas are mapped onto measured data from a CO_2 and YAG cell in Figure 6.25 and 6.26 respectively.

The fit of the parabolas to measured cell data is not as good as was seen with the Harper 1 data. This is for three reasons. The CO_2 engraving was made close to the size limit of the laser and the cells are likely to be less regular. The roll scope used to make the measurement is a much less accurate interferometer than the one used to map Harper 1 and the measurement included much more noise due to vibration, as the roll was not measured on a sample stage due to its larger size.

$y = 0.0645x^2-7.8$ $y = 0.0797x^2-7.5$

Figure 6.25. Parabola derived from the cell specifications of Harper 2.

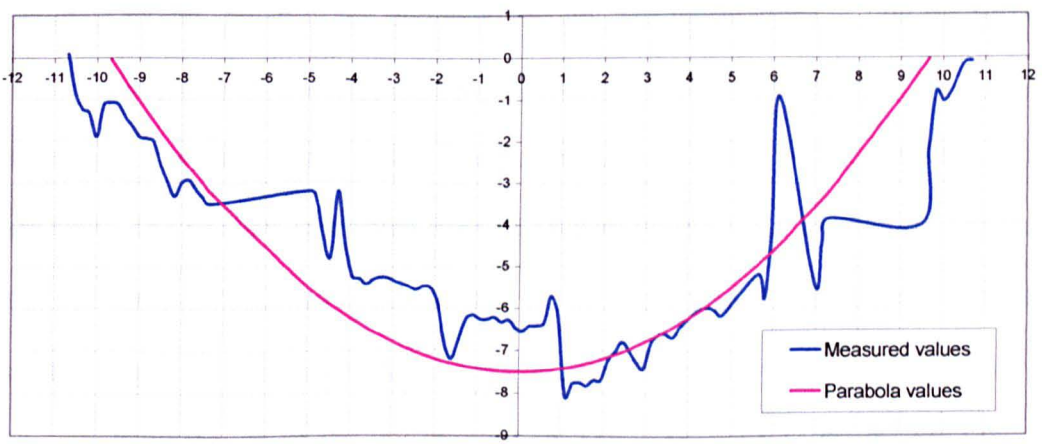

Figure 6.26. Fitting of the parabola $y = 0.0645x^2-7.8$ to a mapped cell from measurement Harper 2 CO_2 3x1.

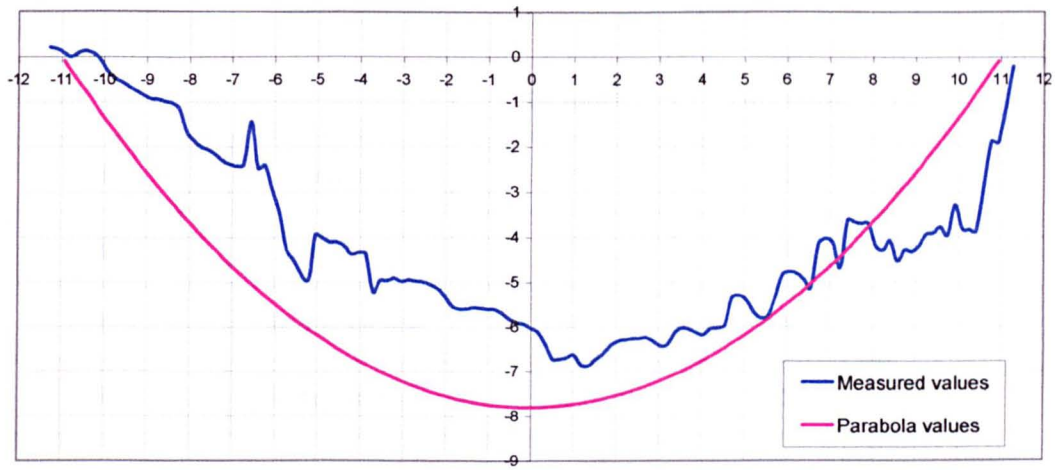

Figure 6.27. Fitting of the parabola $y = 0.0797x^2 - 7.5$ to a mapped cell from measurement Harper 2 YAG 2y2.

6.3.2 Applying the Wenzel equation to the Harper 2 data

As with the work on anilox Harper 1, the r-value needed in order to calculate Wenzel angles from the Harper 2 data could not be measured and was estimated by the parabola model shown in the previous Section. The calculations to find the surface area of the parabolas that approximate the cells are shown in Section A6-5 of the appendix. The calculations of the Wenzel r-values are shown in Section A6-6 of the appendix The r-values calculated from this model were r = 1.3 for the CO_2 cells and r = 1.4 for the YAG cells. The above values were used to calculate the Wenzel contact angle θ_w from the MAMS and FTA data that was presented in Chapter 5. The results of the calculation are shown in Tables 6.15 and 6.16 for the MAMS and FTA data respectively.

		CO_2 band	YAG band
θ_m	water	75°	86°
θ_w	water	79°	87°
θ_m	diiodomethane	20°	26°
θ_w	diiodomethane	44°	50°

Table 6.15. The observed contact angle θ_m and calculated Wenzel contact angle θ_w values using the Wenzel equation and Harper 2 data from the MAMS instrument.

		CO_2 band	YAG band
θ_m	water	91°	105°
θ_w	water	91°	101°
θ_m	diiodomethane	43°	43°
θ_w	diiodomethane	56°	59°

Table 6.16. The observed contact angle θ_m and calculated Wenzel contact angle θ_w values using the Wenzel equation and Harper 2 data from the FTA instrument.

The use of the Wenzel equation on the FTA data is questionable, as it is known that the contact angle was advanced when measurements were made. The case of the FTA data is however interesting as the Wenzel angles modify the contact angle towards the observed angle on the unengraved band when the angle is greater than

90°. The maximum modification of these angles is to 90° therefore modification using the Wenzel equation can never produce the observed equilibrium angles. The Wenzel equation again fails to predict the effect of the engraved cells on the wettability of the band.

6.3.3 Applying the Shuttleworth and Bailey equations to the Harper 2 data

The previous sections have demonstrated that the Shuttleworth and Bailey equations can only be meaningfully applied to advancing and receding contact angle data. This data was difficult to measure on Harper 2 (see Section 5.1.3) and only advancing data for engraved bands using the FTA is available. The gradients needed for use in the equation were measured from profiles of the cells as discussed earlier in Section 6.3.1. The gradients obtained from that work were converted to degrees and are listed in Table 6.17 along with the deviation, which gives an indication of the error involved in the measurement.

	CO_2 band			YAG band		
	tan θ	gradient	R^2 value	tan θ	gradient	R^2 value
Mean	0.55	29°	0.92	0.74	36°	0.90
Standard deviation	0.13	6°	0.07	0.18	7°	0.05

Table 6.17. Measured gradients from the Veeco images converted into degrees

The slope of the cell can also be estimated from the parabola model by differentiating the equation of the curve as discussed in Section 6.1.3. The maximum

gradients are 1.419 for equation of the CO_2 parabola, which equates to an angle of 54°, and 1.546 for the equation of the YAG parabola, which equates to an angle of 57°. These angles are obviously much higher than the measured values. This is due in part to the larger error in fitting a parabola to the cells on Harper 2.

The advancing FTA data was used along with the measured and estimated slopes to calculate the equilibrium contact angles in accordance with the Shuttleworth and Bailey equation for advancing angles. The results are shown in Table 6.18.

	Observed contact angle (FTA)	Modified using parabola model	Modified using measured values
Polished band	**74°**	-	-
CO_2 band (advanced)	**100°**	**46°**	**71°**
YAG band (advanced)	**107°**	**50°**	**71°**

Table 6.18. Modification of the observed contact angles (measured using the FTA instrument) using the Shuttleworth and Bailey equation.

Water	Contact angle on the polished band measured using the MAMS instrument	60° +/- 2°
	Shuttleworth and Bailey angle calculated from advancing angle data measured using the FTA instrument and on the CO_2 band	71° +/- 8°
	Shuttleworth and Bailey angle calculated from advancing angle data measured using the FTA instrument and on the YAG band	71° +/- 9°

Table 6.19. Comparison of the advancing contact angle data on Harper 2 modified with the Shuttleworth and Bailey equation with the equilibrium contact angles obtained by the MAMS instrument.

The estimate of error in the modified contact angle calculated from the advanced data and the measured gradients, and the equilibrium data measured on the polished unengraved band using the MAMS instrument overlap. The modified angles are not however as close to the equilibrium value was seen for the Harper 1 data. There was a very small amount of advancing data measured on anilox Harper 2 due to the stability of large drops at the zenith of the larger anilox. Only two data points were available for the YAG band and four for the CO_2 band. (The data is therefore not reliable.) The data initially believed to be equilibrium data is was later shown to be advanced data. The Shuttleworth and Bailey equation was applied to this data (using the measured gradient). The data is tabulated as a comparison to the equilibrium contact angle data obtained on the polished band with the MAMS instrument.

Water	Contact angle on the polished band measured using the MAMS instrument	60° +/- 2°
	Shuttleworth and Bailey angle calculated from advancing angle data measured using the FTA instrument and on the CO_2 band	62° +/- 8°
	Shuttleworth and Bailey angle calculated from advancing angle data measured using the FTA instrument and on the YAG band	69° +/- 9°
Diiodomethane	Contact angle on the polished band measured using the MAMS instrument	21° +/- 2°
	Shuttleworth and Bailey angle calculated from advancing angle data measured using the FTA instrument and on the CO_2 band	14° +/- 7°
	Shuttleworth and Bailey angle calculated from advancing angle data measured using the FTA instrument and on the YAG band	7° +/- 9°

Table 6.20. Comparison of the FTA data for water and diiodomethane on Harper 2, modified with the Shuttleworth and Bailey equation with the equilibrium contact angles obtained by the MAMS instrument.

The result of applying the Shuttleworth and Bailey equation to the FTA data is closer to the equilibrium value measured using the MAMS instrument. The results are more varied for the diiodomethane measurements, however, it is worth noting that the equilibrium value for the diiodomethane was measured at the limit of the MAMS instrument and the inaccuracy in the reading is larger than the deviation of results suggests.

Although the Shuttleworth and Bailey equation has been shown to explain the size of the advancing angle on the engraved bands there is a large advancing angle on the polished band. The difference between the equilibrium measurement with water as the test liquid on the MAMS instrument and the advanced measurement on the FTA was from 60° to 74° The angle was advanced to 93° indicating using the Shuttleworth and Bailey equation in reverse that there is roughness with a gradient of the order of 33° on the polished band. Although the band is polished and smooth to the eye there is micro-roughness that could cause such hysteresis. The size of roughness that contact angles measurement is sensitive to has been reported as less than 100nm.[74] As stated in Section 2.1, hysteresis occurs on all but the most artificial of surfaces and impurities and irregularities certainly exist on the all bands that would increase the observed advancing angle, and alter the observed static angle from the true equilibrium value. Whilst the static value observed with the MAMS instrument is as close to the equilibrium value as it was possible to measure, it is important to remember that it is not a necessarily true equilibrium value as would fulfil the criteria for use with Young's equation. The presence of hysteresis on the polished bands indicates that this surface does not fulfil the conditions required by the young equation. The agreement of the advancing data on the engraved bands

with the angle observed on the polished band using the MAMS instrument, when combined with the Shuttleworth and Bailey equation, suggests that whilst other factors contribute to hysteresis, roughness is the dominant influence on the advancing angle and that the static contact angle measured with the MAMS instrument is a good approximation of the equilibrium contact angle.

6.3.4. Applying the Cassie and Baxter equation to the Harper 2 data

As with Anilox Harper 1 the contact angles measured on the engraved bands of Harper 2 are large when polar liquids are used, indicating that it may not be favourable for the liquid under test to wet the entirety of the cell. As anilox Harper 2 was not measured using the Scantron optical sensor there is no top view image available for analysis as there was for Harper 1. The parabola method was used to estimate the height from the bottom of the cell that would remain unwet assuming the Cassie and Baxter equation to be applicable to the data. The surface area of each parabola was calculated as discussed in Section 6.1.4. The point n on the Y axis of the parabola was adjusted until the ratio of the surface area above point n to the area of the circular disc at point was equal to the figure predicted by the Cassie and Baxter equation describing a composite solid/air interface. Taking the Cassie contact angle θ_c to be the angle observed on the engraved band and the equilibrium angle θ_e to be the angle observed on the polished band and using the Cassie and Baxter relationship $f_l = (\cos\theta_c + 1) / (\cos\theta_e + 1)$, The fraction of ceramic in contact with the liquid at the interface (f_l) is therefore 0.84 or 84% for the CO_2 band and 0.71 or 71% for the YAG band.

The calculations detailed in Section A6-7 of the appendix produced an unwet height of 2.07μm for the CO_2 cells and 3.44μm for the YAG cells. The plugged cells on the CO_2 band as shown in Figures 6.21 and 6.22 are approximately 5μm deep. The cells shown in figure 6.32 had a depth of approximately 7μm showing that the extent of the plugging was in the order of 2μm. Figure 5.8 in Chapter 5 showed that the plugged YAG cells had a depth of approximately 4μm, the bottom 3.5 μm being plugged with ink. The plugged cells on both bands had gone undetected by contact angle analysis. Contact analysis is normally very sensitive to contamination of the sample surface therefore it is reasonable to suggest that the bottoms of the cells were not wet by the test liquid. The prediction of the air/ceramic composite interface in contact with a non-wetting liquid is reasonable for water and maybe Formamide however Diiodomethane wet the surface well and would be expected to penetrate to the bottom of the cells. There was no indication of the contact angle made by Diiodomethane on either of the bands changing. However it is not known when the plugging happened and which results were made before or after plugging took place. Therefore it is impossible analyse the data to prove or disprove this theory.

6.4 Summary of results

The conclusions that can be drawn from this work are:

1. The assumption that the YAG laser produced a rougher cell interior was found not to be valid. The difference between the measured roughness average (R_A) values of the interior of the CO_2 and YAG engraved cells was smaller than the standard deviation of the results. This measurement did not however compare the shape of the roughness. When the profiles made of the two types of cells were considered the shape of the roughness was found to be different.

2. The Wenzel equation did not explain the change in contact angle on the engraved bands for any of the anilox rolls, when measured using the MAMS instrument.

3. The Wenzel equation was not appropriate for use with the FTA contact angle data as the angles measured were not equilibrium angles. The Shuttleworth and Bailey equation for advancing angles was the most suitable to apply as the parameters needed were all directly measurable.

4. The results found when the Shuttleworth and Bailey equation was applied to the advancing contact angle data for water obtained with the FTA instrument were very close to the equilibrium contact angle data obtained

with water using the MAMS instrument. This was true both for the Harper 1 and Harper 2 data.

5. The increase in contact angle due to advancement of the contact line across the engraved bands as described by the Shuttleworth and Bailey theory provides an explanation for the different contact angle values produced by the MAMS and FTA instruments.

6. The Cassie and Baxter theory that roughness produces a composite solid/air surface at the liquid interface for liquids which exhibit poor wetting was cited as applicable similar systems. The amount of cell unwet by water was consistent with the level of plugging which was undetected by contact angle analysis

As expected, the Wenzel theory did not predict the influence of the roughness caused by the process of engraving on the contact angle observed. This is consistent with results found in the literature search and is as a result of the theory's assumption that the contact line is free to move evenly in all directions.

The Shuttleworth and Bailey, and Cassie and Baxter theories were however found to be relevant to the wetting of engraved anilox bands. The Shuttleworth and Bailey equations explain quite well the increase in contact angle when the test liquid is advanced across an engraved band. The theory holds for all bands on which advancing data is available. The theory also explains the difference in reported

contact angles produced by the two instruments used in this work. The large advancing angle observed on the polished band indicates that environmental factors such as the curvature of the roll and impurities on the surface make a large contribution to hysteresis, however the consistency of the results indicates that the slope of the cell wall produces the largest barrier to the movement of the contact line and it is this which dictates the receptiveness of the engraved band to a test liquid. This theory may also explain why the YAG cells on Harper 2 transferred more ink than the CO_2 cells.

The Cassie and Baxter theory explains the difference in equilibrium contact angle on the polished and laser engraved bands with polar liquids and the lack of such a difference with non-polar liquids. It also could explain why plugging of anilox Harper 2 went unnoticed despite routine checks with polar liquids being made. It does however not explain how such plugging could have no effect on the contact angle made by diiodomethane.

This work has highlighted some of the problems encountered when attempting to measure and interpret contact angle data in practical situations. Applying the three theories to explain the behaviour of wetting of a rough surface has built up a picture about how the test liquids interact with the engraving and the polished areas. It has established that the contact line is pinned as the liquids move over the engraved surface and that the effect of this is so strong that it can be done accidentally as in the case of the measurements using the FTA. The work has also raised to possibility the hypothesis that the bottoms of the cells are not wet when the engraving is put in contact with a drop of water.

A report was written for the Harper Corporation of America describing the contact angle analysis done using the MAMS instrument on anilox Harper 1 and some of the early work looking at the use of the Wenzel equation. This report is included in Section B-1 of the appendix. The report was written at a very early stage in the investigation and cited cell interior roughness as a major factor in wettability of the anilox. After receipt of this report the Harper Corporation introduced a method of modifying the interior roughness of a cell produced by a CO_2 Laser. The new anilox was given the name "Platinum" by Harper. [132] The change appeared to be in the chemical nature of the ceramic used but Harper would not provide any details. A sample roll was obtained for testing to see if the theories developed on the initial anilox would hold for a 3rd Harper roll.

7. Analysis of anilox roll Harper 3

Anilox Harper 3 was created to demonstrate Harper's latest product, the "Platinum" engraving. Harper disclosed that the composition of the ceramic and the pulse of the CO_2 laser had been modified in order to produce cells with smoother interior walls and a reflective appearance. The name Platinum refers to the appearance of the engraving and does not necessarily indicate that the ceramic contains platinum metal. Harper cited reactions between the laser and trace elements in the ceramic for the change but gave no specific information.

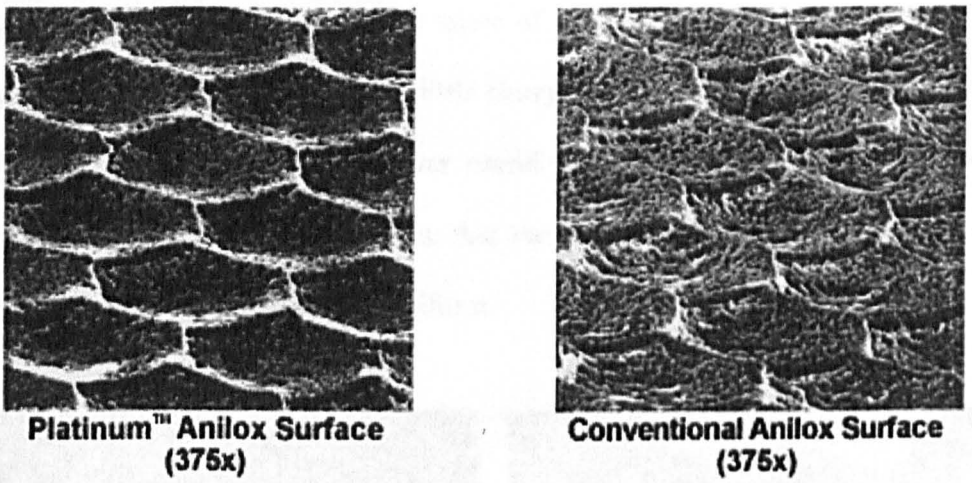

Figure 7.1. Scanning electron microscopy (SEM) images of the conventional and Platinum anilox bands taken from Harpers website. [132]

The anilox had two engraved bands. Both bands were engraved by a CO_2 laser however one was made by the conventional Echocell CO_2 laser and the other was made by a CO_2 laser with a modified pulse profile. Harper did not disclose details of how the pulse was modified. The bands were termed Normal CO_2 and Platinum CO_2.

There was also a very small polished band, which was 2mm wide. The engraved bands had line counts of 80 lines/cm. The cells were much larger than those on Harper 1 or 2. Harper gave values for the cell depth of 19 μm for the platinum band and 11 μm for the conventional CO_2 band. The cell opening was specified as 120 microns, with a wall of 7 microns for both bands. It should be noted that the band termed Normal CO_2 has the same "Platinum" ceramic composition as the Platinum engraving, because the ceramic composition could not be varied across the anilox. The difference between the engravings is in the laser used. The Normal band should, in theory, be chemically different to the CO_2 bands on aniloxes Harper 1 and 2.

Figure 7.2 shows photomicrographs taken of cells on each band of Harper 3. The images of the base of the cells are a little blurry as the microscope was focused on the cell land. The images are however useful to illustrate the difference in colour between the engravings and to show that the land area between the Platinum cells appeared better defined and more uniform.

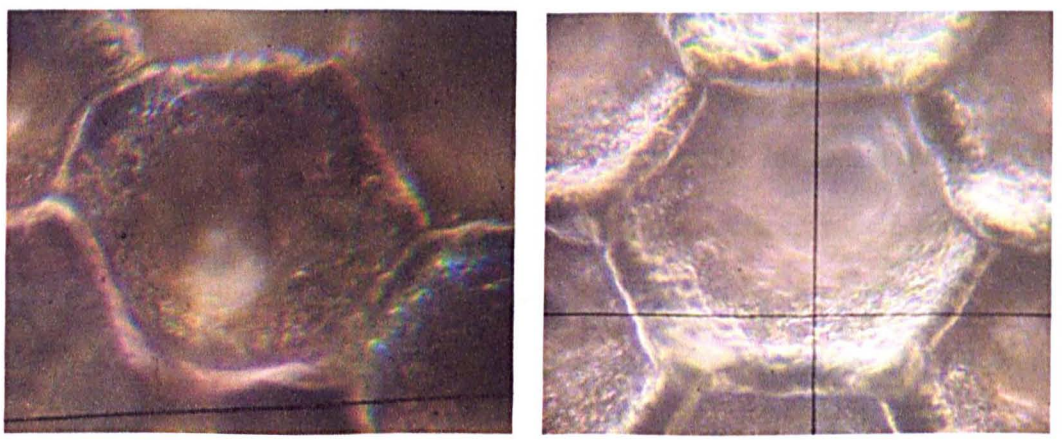

Conventional CO_2 cell (400x) **Platinum CO_2 cell (400x)**

Figure 7.2. A digital photomicrograph of a cell on each of the engraved bands of Harper 3.

7.1 Contact angle analysis of anilox Harper 3

Contact angle analysis was done with the FTA instrument. The analysis was carried out at the same time as the analysis of the other two Harper anilox rolls and under the same conditions. Water, diiodomethane and formamide were used as test liquids. The results are summarised in Table 7.1. The data is shown in full in Section A7-1 of the appendix.

		Water	Diiodomethane	Formamide
Polished band	**mean**	**82°**	**48°**	**79°**
	standard deviation	3°	2°	2°
CO_2 band	**mean**	**88°**	**46°**	**63°**
	standard deviation	2°	1°	2°
CO_2 Platinum band	**mean**	**86°**	**44°**	**64°**
	standard deviation	2°	1°	2°

Table 7.1. Contact angles observed on anilox Harper 3 using three test liquids.

As shown in Figure 7.2, the Platinum and Normal CO_2 bands appear to have a different physical or chemical composition at the surface, which changed the appearance of the engravings. The change that produced the platinum coloured surface of the Platinum band did not change the contact angle for any of the three test liquids.

Smaller drop volumes had to be used on the polished band, as it was too narrow to accommodate the standard sized drops. The largest drop size that could be

accommodated on the band was used. This was different for each liquid. The drop sizes used were approximately 1.5μl for water, 1μl for formamide and 0.4 μl for diiodomethane. In order to check that using smaller drops did not change the contact angle on the polished band contact angles using 1.5μl water drops were measured on the polished band of anilox Harper 1. The results are shown in Table 7.2.

	Anilox Harper 1				Anilox Harper 3	
Repeat number	Contact angle (degrees)	Drop volume (microlitres)	Contact angle (degrees)	Drop volume (microlitres)	Contact angle (degrees)	Drop volume (microlitres)
1	72	5.0	76	1.6	82	1.7
2	76	4.6	77	2.1	86	1.6
3	72	3.9	76	1.6	79	1.3
4	71	4.7	75	1.5	81	1.7
5	69	4.8	73	1.5	80	1.6
6	75	4.1	77	1.7	85	1.6
7	76	4.5	74	1.6	84	1.6
8	71	4.1	74	1.5	83	1.3
9	76	5.0	73	1.5	81	1.4
10	70	4.1	77	1.6	82	1.3
Mean	**73**	**4.5**	**75**	**1.6**	**82**	**1.5**
Standard deviation	3	0.4	2	0.2	2	0.2

Table 7.2. Comparison between large and small water drops on the polished band of Harper 1 and of small drops on the polished band of Harper 3.

It is clear that not only did varying the drop size make no significant difference to the contact angle on the polished band of Harper 1, but that the polished Platinum ceramic of Harper 3 is more hydrophobic than that of Harper 1.

The contact angles made by the three test liquids on the polished bands of anilox Harper 1, 2 and 3 were tabulated in Figure 7.3 so that the data obtained on all three Harper rolls could easily be compared.

	Water	Diiodomethane	Formamide
Harper 1	75° +/- 3°	42° +/- 2°	43° +/- 3°
Harper 2	74° +/- 3°	44° +/- 2°	43° +/- 3°
Harper 3	82° +/- 2°	48° +/- 2°	79° +/- 2°

Table 7.3. Comparison between contact angle data made by water, diiodomethane and formamide on the polished bands of the three Harper anilox rolls.

The ceramic on the polished bands of Harper 1 and 2 shows the same wetting character. There are small decreases of the wetting of Harper 3 with water and diiodomethane but there is a marked decrease in the wetting of the band with formamide.

The contact angle data on the CO_2 bands of all three Harper anilox were also collated and are shown in Table 7.4.

	Water	Diiodomethane	Formamide
Harper 1	84° +/- 3°	43° +/- 2°	60° +/- 2°
Harper 2	91° +/- 3°	43° +/- 2°	60° +/- 1°
Harper 3 normal CO_2	88° +/- 2°	46° +/- 2°	63° +/- 2°
Harper 3 Platinum CO_2	86° +/- 2°	44° +/- 2°	64° +/- 2°

Table 7.4. Comparison between contact angle data made by water, diiodomethane and formamide on the CO_2 bands of all three Harper anilox.

The contact angles observed using all three test liquids on the engraved bands of Harper 3 are not only not significantly different from each other, they are also not significantly different from those on Harper 1. The formamide and diiodomethane contact angles are comparable to those on Harper 2. The large difference in the wetting with formamide of the Harper 3 polished ceramic is not seen on the engraved bands.

The only anomaly is the water contact angle on Harper 2. The line screen and diameter of the three anilox are shown alongside the contact angle values in Table 7.5 in order to rule out a trend based on physical properties of the anilox.

	Water contact angle (degrees)	Line count (cells/cm)	Roll diameter (mm)
Harper 1 CO_2	84° +/- 3°	600	64
Harper 2 CO_2	91° +/- 3°	1000	81
Harper 3 Normal CO_2	88° +/- 2°	80	59
Harper 3 Platinum CO_2	86° +/- 2°	80	59

Table 7.5. Contact angles made by water on the CO_2 bands of the three Harper anilox along with line count and diameter of the rolls.

Harper 2 has a much finer line count than the other Harper rolls and shows a higher contact angle. However, the contact angle on Harper 1 is smaller than that on Harper 3 despite more than an order of magnitude difference in the line count. This does not support a relationship between line count and contact angle. The change in degree of curvature of the roll (related to roll diameter) does not reveal a trend. The CO_2 engraving on Harper 2 was however made at the limit of how small the cells could be at that time.

In Chapters 3 and 5 dealing with the contact angle measurements on anilox Harper 1 and 2 respectively, it was discovered that the contact angles measured using the FTA instrument were advancing contact angles. As the contact angles made on Harper 3 were made in the same way under the same conditions it it is reasonable to compare the measurements on Harper 3 with those for other Harper anilox (measured using the FTA) It is also reasonable to assume that these angles will also be advancing angles.

To check the validity of this assumption a drop was advanced across each of the bands. The mean advancing contact angles observed were 92° normal band and 91° on the Platinum band. These are slightly larger than the contact angles measured as equilibrium angles. It was observed that the contact line moved in a series of jumps. The contact line sticks and the contact angle increases without any movement in the line, then the line jumps and the angle falls. Two consecutive frames from the advancing drop on the Platinum band were captured and are shown together in Figure 7.3. They show an increase in the contact angle from the first frame to the second as the contact angle sticks. It was noted that the lower angle was within the observed range of the static angles measured. The advancing angle quoted was an average, which included many sticks and jumps of the contact line.

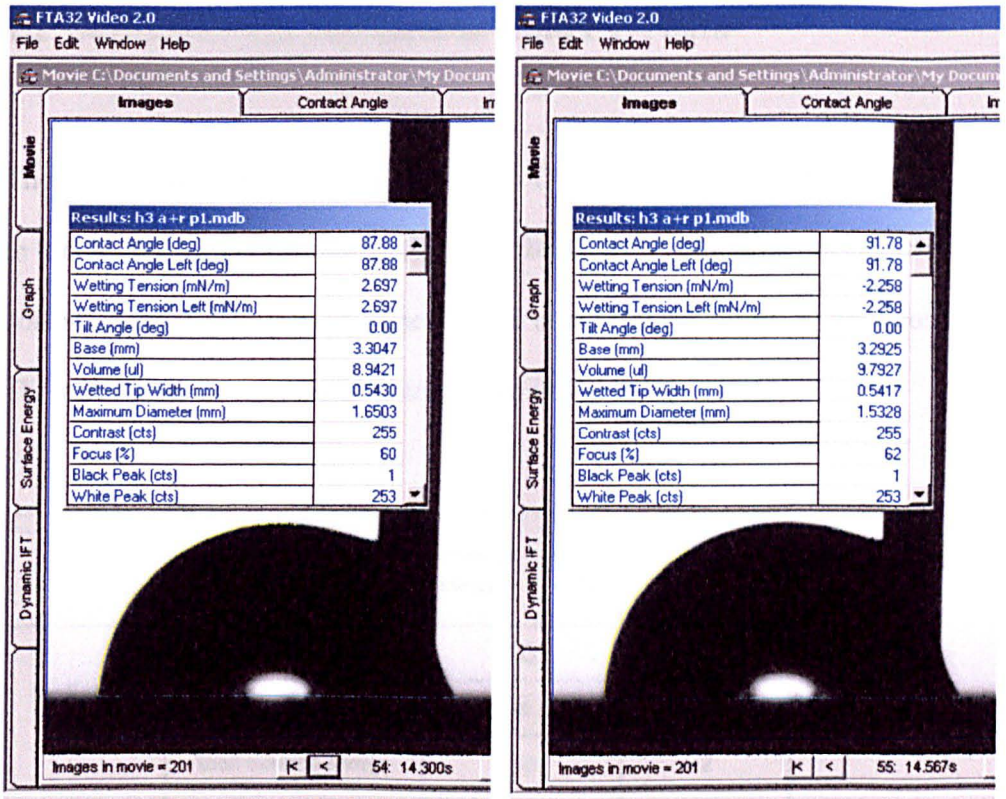

Figure 7.3 Consecutive frames showing the advancing contact angle sticking.

An attempt was made to measure receding angles on each of the bands. As with the other anilox it was only possible to quote receding angles as being less than the cut off at which the drop breaks away from the tip of the syringe. For the normal CO_2 band the value was less than 51° and for the polished band the value was less than 6°. There is a large difference between these values, however the tip of the syringe was higher when the measurement was made on the normal CO_2 band and far less of the volume of the drop was removed before the drop detached.

7.2 Surface energy calculations from FTA data

The contact angle data was used with the Owens & Wendt geometric mean equation to calculate the surface energies of each band, as a sum of the dispersive and polar contributions. (As has been done for the other Harper anilox in previous chapters.) The calculated surface energies are shown in Table 7.6.

		Average surface energy mJm^{-2}	Standard deviation mJm^{-2}
Polished band	dispersive component	35	1
	polar component	4	1
	total surface energy	**39**	**2**
CO_2 band	dispersive component	36	1
	polar component	2	1
	total surface energy	**38**	**2**
Platinum CO_2 band	dispersive component	38	1
	polar component	2	1
	total surface energy	**40**	**2**

Table 7.6. Surface energies calculated using the Owens and Wendt equation with the contact angle data for water and diiodomethane.

As has been seen for the other Harper aniloxes large changes in contact angles, particularly with the polar liquid, result in small changes in the calculated surface energies. The surface energies calculated in this way are based on the diiodomethane and water contact angles only and therefore do not reflect the large differences in the formamide contact angle between the engraved and unengraved bands.

The calculated surface energies are compared to those calculated from FTA data from anilox Harper 1 and 2, in Table 7.7. The estimates of error are not shown for clarity but are in order of +/- 1 mJm^{-2} for the dispersive and polar components and +/- 2 mJm^{-2} for the total surface energies. The difference observed in the contact angles on the polished bands shows up as a difference in surface energies between the polished band on Harper 3 and the polished bands on the other Harper aniloxes. The dispersive and polar components of the surface energy of the polished band of Harper 3 are both smaller resulting in a lower total surface energy. The total surface energies on the CO_2 engraved bands all fall within twice the standard deviation of error (Indicating a 95% confidence level that there is no difference between the bands.) The difference in surface energy of the unengraved platinum ceramic is therefore seen to disappear once engraving with a CO_2 laser has taken place.

		Harper 1	Harper 2	Harper 3 Normal	Harper 3 Platinum
Polished band	dispersive component (mJm^{-2})	39	38	35	
	polar component (mJm^{-2})	6	6	4	
	total surface energy (mJm^{-2})	**45**	**44**	**39**	
CO_2 band	dispersive component (mJm^{-2})	38	38	36	38
	polar component (mJm^{-2})	3	1	2	2
	total surface energy (mJm^{-2})	**41**	**39**	**38**	**40**

Table 7.7. Surface energies (mJm^{-2}) calculated from the FTA advancing contact angle data on the polished and CO_2 engraved bands of the three Harper anilox rolls.

The contact angles made by water, diiodomethane and formamide were used to calculate the components of surface energy in accordance with acid base theory. As the solving of the three simultaneous equations for the dispersive, acid and base components of surface energy is complicated it was again left to the FTA software to make the calculations from the average contact angles. This however gives no value of error associated with the results. The FTA does report any problems with the calculation and for the normal CO_2 band reported that there was no solution for the set of data. (Indicating that the sum of the components does not equal the total surface energy.) The other results included negative values. Both these observations indicate that the result has been affected by error in the contact angle measurements. The values returned for the dispersive, polar, acid and base components for each band are shown in Table 7.8.

		Polished band	Normal CO_2 band	Platinum CO_2 band
Average surface energy mJm^{-2}	dispersive component	35.4	36.5	37.5
	polar component	-4.5	1.0	-0.3
	acidic component	-0.3	0.1	0.0
	base component	16.9	2.4	3.9
	total surface energy	**30.9**	**37.5**	**37.3**

Table 7.8. Surface energies of the bands on Harper 3 calculated using the acid-base equations and the water, diiodomethane and formamide contact angle data.

The large contact angle made by formamide on the unengraved band translates to a large value for the base component of surface energy. This component is seen to drop significantly after engraving has taken place. The acid and base components for the

polished bands on all three Harper anilox are shown together in Table 7.9. The base component of Harper 3 again stands out as being far larger than on the other bands.

		Polished band Harper 1	Polished band Harper 2	Polished band Harper 3
Average surface energy mJm^{-2}	dispersive component	38.59	37.5	35.4
	polar component	5.32	5.9	-4.5
	acidic component	1.785	1.9	-0.3
	base component	3.977	4.6	16.9
	total surface energy	**43.92**	**43.5**	**30.9**

Table 7.9. The acid base components of surface energy on the polished bands of the three Harper anilox rolls.

When the same information is presented for the CO_2 bands in Table 7.10 it is the base component of Harper 2 that stands out as being small in comparison to the other calculated values.

		CO_2 band Harper 1	CO_2 band Harper 2	Normal CO_2 band Harper 3	Platinum CO_2 band Harper 3
Average surface energy mJm^{-2}	dispersive component	37.0	38.1	36.5	37.5
	polar component	1.6	0.9	1.0	-0.3
	acidic component	0.2	0.3	0.1	0.0
	base component	3.7	0.7	2.4	3.9
	total surface energy	38.6	39.0	**37.5**	**37.3**

Table 7.10. The acid base components of surface energy on the CO_2 bands of all three Harper anilox.

7.3. Modification of the contact angle data to estimate the equilibrium contact angle

As no measurements were taken using the MAMS instrument there is no equilibrium angle data for the polished band of Harper 3. The Shuttleworth and Bailey equation for advancing angles was used to predict the value of the equilibrium angle on unengraved ceramic.

As no topographical measurements were made on Harper 3 the slope of the cell wall is estimated from parabola with y and x intercepts set to match the dimensions of the cells. The parabola are show in Figure 7.4 and have the equations $y = 0.028x^2 - 10$ for the normal CO_2 band and $y = 0.056x^2 - 20$ for the Platinum band.

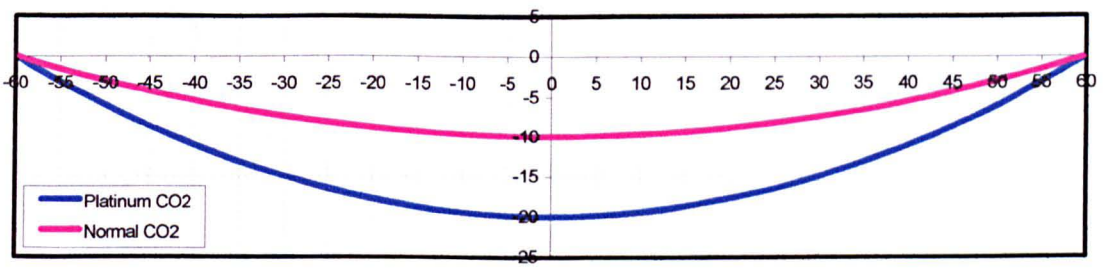

Figure 7.4. Parabolas representing the curvature of the engraved cells on anilox Harper 3.

The maximum gradients of the parabola are the inverse tangent of 2ax and are 34° for the Platinum band and 19° for the normal CO_2 band.

Using the Shuttleworth and Bailey equation for advancing angles gives two different values for the equilibrium angle as the advancing angles are almost identical but the slopes given by the model are very different. Using the measured advancing angle for each band the values calculated for the equilibrium angle are 73° using the Normal CO_2 angle and 57° using the Platinum angle.

The cells on Harper 3 are more than a factor of 10 larger than those on Harper 1 for which the parabola gave a good approximation of the shape. As no information on the shape of the curvature of the cells on Harper 3 is available it is impossible to tell if the lack of agreement between the measurements is due to the inaccuracy of the parabola method of from other factors.

7.4 Summary

The conclusions that can be drawn from the work on Harper 3 are:

1. The ceramic composition affects the wettability of the unengraved band. The change that Harper made in the ceramic of Harper 3 increased polar component of its surface energy, the polar increase was seen to be basic in nature.

2. Surface composition, cell interior surface roughness and cell depth were seen to have no affect on the contact angles observed on the engraved bands.

3. The increased basic surface energy of the Harper 3 ceramic was reduced to normal levels by the engraving process.

Anilox Harper 3 reinforces the findings on anilox Pira 1, that the cell depth does not affect the wettability of the engraving, it also indicates that the laser type controls the final wettability of the band.

8 Conclusions and further work

8.1 Conclusions

This research has demonstrated that during the process of laser engraving, a ceramic anilox changes the wettability of its surface, in particular its receptiveness to polar liquids. The type of laser used to make the engraving has been found to greatly influence the change in wettability. The CO_2 laser produced a surface that was more easily wetted by a polar liquid than the YAG laser, however, both types of laser engraving were less receptive to polar liquids than the unengraved material.

Anilox Harper 1 was designed to have cells engraved by each type of laser and to have engraved cells with similar depths. There were twice as many YAG cells as CO_2 cells per centimetre of engraving. Harper 1 also had a polished unengraved band. The engraving process changed the wettability of Harper 1 when water and formamide were used as the wetting liquids, however the engravings did not produce a change in the wettability when diiodomethane was used as the wetting liquid. When these contact angles were used with the Owens-Wendt and acid-base theories of surface energy calculation, the surface energies of all bands were found to be predominantly dispersive in nature. The laser engraving process reduced the polar character of the surface and the change between the bands was characterised by a loss of basic character from the CO_2 band to the YAG band. When commercially available inks were used, the standard water-based ink showed the same trend as was observed with water (although with lower contact angles) and a UV curable ink followed the same trend as formamide. This led to the hypothesis that UV inks

interact with surfaces having a basic character. This hypothesis seemed sensible when the formulation a generic UV ink was considered. Water interacts with a solid with acid and base character in equal amounts. The water-based ink interacted with the anilox in a similar manner despite the pH of the ink being slightly alkaline. However the acid-base theory uses the Lewis definition of acid and bases rather than the Lowry Bronstead acids and bases (as measured by pH meters).

When anilox Harper 1 was commissioned, the cell depths of the engraving were designed to be equal, there was a small difference between the cell volumes but this was not practically significant. These variables were fixed as in the early stages of this work it was believed that it was important to control the volume of test liquid which entered the cells in order to obtain comparable results between the engraved bands. The cell opening and land sizes were very different.

Pira 1 was a commercially obtained banded anilox with cells engraved by a CO_2 laser. There were three bands with constant cell opening and land sizes but variable cell depths (and therefore volumes) across the different bands. Varying the cell depth was seen to have no affect on the observed contact angle. As expected increasing the cell volume increased the amount of ink transferred when the anilox was used. Contact angle analysis cannot therefore be used to directly predict ink transfer. There was less difference between the wetting of the engraved and unengraved bands than was seen with the other anilox rolls studied. This is believed to be as a result of wear, resulting in a smoother and larger land area around the cells, smoother cell interiors and a roughening of the unengraved area. Pira 1 was the only anilox studied that had been extensively used for printing before testing.

Anilox Harper 2 was designed to have engravings made by CO_2 and YAG lasers with the same number of cells per centimetre and the same cell volumes. The cell depths were comparable. The cell geometries were different and were characteristic of the laser used. Anilox Harper 2 also had unengraved polished areas at both ends. The engraved and polished bands were wetted more or less equally by diiodomethane. The decrease in receptivity to wetting by polar liquids was again seen on the engraved bands. The YAG band was the least receptive to wetting by the polar liquids used, namely water and formamide. The difference between the engravings was again a reduction of basic character from the CO_2 engraving to the YAG engraving. The YAG engraving had a negligible amount of polar character. Both engraved bands on anilox Harper 2 were harder to wet with water than their corresponding bands on Harper 1. The receptiveness to formamide and diiodomethane were unchanged. This decreased receptiveness to water was barely significant for the YAG band but was larger for the CO_2 band. It was believed to be related an increase in roughness of the land area around the cells of Harper 2.

When anilox Harper 2 was used to print a UV ink, there was a small difference in print density produced by the two bands. The YAG band put down very slightly more ink than the CO_2 band. Overall transfer amounts were low due to poor contact between the anilox and paper, both of which being rough surfaces, and the high surface energy of the paper, which made transfer less favourable.

After receiving a report from this author into the wettability of anilox Harper 1 citing cell interior roughness as a major factor in wettability, (see Section B-1 of the

appendix) Harper developed a new type of engraving, which they named Platinum due to its silvery appearance. The ceramic of the Platinum anilox was a modified composition, as was the pulse of the CO_2 laser used to produce it. Harper claimed that the Platinum engraving had smoother cell interior walls, and that this produced better ink release. A sample roll was provided to this author for analysis; this roll was named Harper 3. Contact angle analysis on the unengraved, polished areas of Harper 3 confirmed that the wettability of the ceramic had been modified chemically and that the unengraved material was far less receptive to wetting by formamide and water. The polished unengraved ceramic was also slightly less receptive to diiodomethane than the ceramic of the previous two Harper anilox rolls. Calculations of surface energy using acid-base theory showed that the basic component surface energy had been significantly increased. Anilox Harper 3 was engraved by conventional CO_2 laser and by a modified "Platinum" CO_2 laser. The process of laser engraving was observed to destroy the increased basic character seen in the unengraved polished areas of the roll. Harper claimed that the cell interior roughness of the Platinum cells was reduced. Contact angle analysis with water, diiodomethane and formamide did not reveal differences in wettability between the cells on the normal CO_2 and Platinum bands.

The main differences cited in the literature between the CO_2 and YAG laser engraved cells are the amount of recast ceramic that the lasers produce, this makes up the walls of the engraved cells, and determines the shape of the cells. The CO_2 laser melts the ceramic, which is recast into the walls of a bowl shaped cell. On the other hand, the YAG laser ablates a high percentage of the ceramic and is said to produce "test tube" shaped cells. It is an observation of this research that, whilst

profiles of the CO_2 cells fitted the approximation of a bowl or quadratic parabola reasonably well, the YAG engraving was found to have a very irregular shape which was not described well by the "test tube" analogy or any simple mathematical form. The work also found no difference between the average heights of the interior roughness (R_a values) of the cells created by the different lasers. It is however important to note that the R_a values measure do not give any information on the topography of the cell interior walls and that the profiles of the cells showed a difference between the engravings, the YAG engraving having a more jagged appearance. Also, the observed change in wettability of the YAG band after exposure to a specialist cleaning product suggests that there the YAG band is more porous then the CO_2 band.

This work has also demonstrated the problems of measuring an equilibrium contact angle on a rough surface. The instrument used, or more specifically the method of introducing the drop to the solid surface, was shown to influence the observed contact angle. This was found to be as a result of pinning of the contact line. When the drop was introduced with minimum force it lacked the energy to overcome local barriers, for example the roughness of the cell land areas, and the observed angle, intended to be an equilibrium angle was found to be close or equal to the advancing angle. This is a problem associated with all equilibrium contact angle measurements on rough surfaces and is consistent with the observations of Good. [120] The angles measured using the FTA instrument were found either to be advancing angles or to be very close to the advancing angles. In this method the test liquid was dispensed via a syringe with a computer controlled pump, The contact angles measured with the MAMS instrument, which were manually pipetted on to the roll surface, were

found to be much lower and were found to be closer approximations of the equilibrium angle.

Advancing angles are a much more reliable measurements to make in comparison to equilibrium angles, as it is obvious to the operator when the advancing angle has been reached. However, they are difficult to measure on anilox rolls due to the curvature of the surface. As the contact angle is advanced, the drop increases in size. Large drops are unstable on the zenith and are prone to rolling down the curved surface of the anilox. The disadvantage with measuring advancing angles is that they should not be used with Young's equation, which relates the contact angle to the interfacial forces at the solid/liquid/vapour interface. This in turn means that they should not be used to calculate the surface energy of the anilox. It is however common practice to calculate surface energies from advancing data. This calculation has no theoretical basis as the conditions for Young's equation are not met, but advancing contact angles and the surface energies calculated from them provide a guide to the nature of the surface and are in some ways more relevant to processes such as printing where equilibrium wetting rarely takes place.

This work identified the primary reason for the deviation of the observed macroscopic contact angle θ_m from the equilibrium contact angle θ_e as the extreme roughness of the surface. Three well-known theories, put forward by Wenzel, Shuttleworth and Bailey, and Cassie and Baxter, which attempt to describe the effect of roughness on the macroscopic contact angle, were discussed and applied to the experimental data for each anilox.

The Wenzel equation modified the equilibrium contact angle observed on a rough surface to compensate for the extra contact area produced by surface roughness. Calculations of the roughness were made using a mathematical model to approximate the shape of the cell. This model was much more accurate for the CO_2 cells than the YAG cells and only accounted for the macroscopic roughness, i.e. the overall shape of the cell, and did not take into account increased contact due to interior cell roughness. As the Wenzel equation uses equilibrium contact angles the experimental data obtained using the MAMS instrument was expected to be most suitable for use. The Wenzel equation modified the contact angle value to make it further away from the equilibrium value (taken as the contact angle measured on the unengraved ceramic). This is a common observation when the Wenzel equation is applied to real surfaces and is one reason that the Wenzel equation receives much criticism. It was the conclusion of this work that the Wenzel equation does not describe the influence of the roughness on the wetting of the anilox and cannot be reasonably applied to the experimental data.

The Shuttleworth and Bailey equations modify the advancing and receding contact angles to remove gradient of the roughness. The FTA data was used along with measurements of the gradient of the interior cell walls obtained from profiles recorded with a Veeco interferometer. It was noted that when the measured slopes were taken away from the advancing contact angles obtained using the FTA instrument, the value obtained was in all cases within the range of experimental error of the value for the same test liquid measured on the polished unengraved band of the anilox using the MAMS instrument. This confirmed that the contact angles observed using the MAMS instrument were close to the true equilibrium angles. The

slope of the cell walls was shown to be influential in the receptiveness to the test fluids when they were advanced across the engraved bands. The large advancing angle seen on the polished unengraved bands shows that this band is not an ideal surface and that there is resistance to the movement of the contact line due to micro roughness, the curvature of the roll and impurities on the surface. The correlation of the data with the Shuttleworth an Bailey equation indicates that whilst these factors are important on the polished band, the influence of the cell gradient on the progress of the contact line across the engraved bands is so large that it becomes the dominant factor in pinning the contact line and controlling the advancing angle.

The Cassie and Baxter theory states that the contact angle of a heterogeneous surface is related to the equilibrium contact angles of each domain present on that surface in proportion to their makeup of the overall surface. A rough surface can be treated in this way if some of the surface remains unwet and the surface underneath the liquid phase is a composite of air and solid interfaces. The equilibrium angles observed using the MAMS instruments on the engraved bands were used to calculate the amount of air/liquid interface that would be present if this accounted for the change in the observed contact angle on the engraved bands with water, a test liquid that did not easily wet the engraved bands. This theory was selected to describe the wetting on the Harper anilox rolls as it explained the different wetting behaviour when polar and non-polar liquids were used. It can also be used to explain why the Pira anilox did not show the same trends as the Harper anilox. On the Pira anilox factors the smoothness of the anilox due to wear, the increased land area around the cells and the increased wettability of the ceramic could reasonably result in water wetting the cells completely.

It is the conclusion of this study that the Cassie and Baxter theory of the creation of a composite solid/air interface describes the wetting when a polar liquid is applied with enough momentum to overcome boundaries due to local roughness and find thermodynamic equilibrium. The creation of the composite surface results in an increase in the observed equilibrium contact angle, which is proportional to the amount of the surface that is unwet. When a non-polar liquid is applied in the manner it is thermodynamically favourable to wet the entire cell and no composite interface is formed. The contact angle is therefore similar when non-polar liquid is allowed to reach equilibrium on the engraved and unengraved areas of the anilox. When the test liquid is forced across the surface of the anilox the gradient of the cell interior walls becomes the important factor in the wettability of the anilox. The steeper the cell walls the harder it is to wet.

There was a small difference in printing from the bands of Harper 2 and Pira 1. In both cases, the band with the steeper slope transferred more ink. In the case of Pira 1 this band held more ink in the cells but in the case of Harper 2 it did not. This study found that the slope of the cells is related to ink transfer and the advancing angle and it is the opinion of the author that ink transfer predictions could be made from advancing contact angle measurements.

8.2 Further work

When undertaking a piece of academic research in a commercial environment, it is expected that the technology will progress whilst the work is in progress. One of the more significant commercial advancements during the course of this investigation is with the rheology of UV curable inks. The original ink used throughout this investigation was very thixotropic and relatively thick, even when the structure of the ink had been broken down. Modification of dispersion techniques and advancements in raw material technology have improved the flow of free radical UV inks, reducing the viscosity of the ink and making the inks much more Newtonian in flow behaviour. The improvement in rheology makes the UV inks much more suitable for contact angle analysis work as there is less likelihood that the viscosity will limit the movement of the ink, preventing it from finding thermodynamic equilibrium. The new generation inks also have a longer working time before they restructure so it may now be possible to measure advancing contact angles with real inks and correlate this to ink transfer directly. New cationic UV ink systems have also been developed with even lower viscosities than the new generation free radical inks and as these are based on a different chemistry with theoretical acidic functionality, it is reasonable to believe that these inks will wet the anilox differently to the free radical inks studied, It is hypothesised that a difference in the receptiveness of the CO_2 and YAG bands to cationic UV inks will be seen.

Further work should therefore include benchmarking the new generation UV and free radical inks to determine their wetting characteristics on anilox Harper 2. Both equilibrium angles (using the MAMS dispensing method) and advancing angles

should be measured. The advancing angles could then be correlated to the amount of ink that is released from the cells using RK laboratory press and the methods detailed in this work.

Another significant finding of the study was that the different engraved bands on anilox Harper 1 showed different levels of receptiveness to wetting by a standard water based ink. Further work should include contact angle analysis using a water-based ink on Harper 2 and with modification of the RK laboratory press to include a suitable drying unit; the ink transfer of water-based inks could be evaluated. The wetting character of water-based inks is heavily influenced by the inclusion of surfactants and organic solvents in the formulation. The formulation is optimised for the end use, i.e. the wetting of the substrate. The effect of wetting additives on the equilibrium and advancing contact angles could be studied using the methods detailed in this work. This work should also be extended to take into account changes to the contact angle over time caused by movement of the surface active ingredients. Dynamic contact angle measurements using the Wilhelmy plate method discussed in Section 2.2.2 could be used for this purpose.

The amount of ink released from the cells in both press trials was lower than expected; this was attributed to the poor contact between the rough anilox and paper surfaces, and the unfavourable surface energy gradient at the nip. Further work should include the use of filmic substrates rather than paper. This would serve two purposes. The surface of a film would be smoother and increase contact with the anilox at the nip. Also with the use of surface treatment such as corona treatment,

plasma treatment or flame treatment, the surface energy of the film could be varied and the effect of the surface energy difference at the anilox nip quantified.

In this work, the FTA instrument was used to produce advancing and receding contact angles by the injection of test liquid into and then out of a static drop on the roll surface. For smaller samples the Wilhelmy plate method discussed in Section 2.2.2 is a much more reliable method of obtaining advancing and receding data. Further work could include scaling up of the apparatus used to accommodate anilox rolls. The apparatus consists of a sensitive balance which records the force exerted on the sample as it is moved up and down through a fluid. The problem in scaling up the apparatus would be designing a balance that could cope with holding anilox rolls with weights in the order of a kilogram whilst still being sensitive to the tiny increases in force as the anilox moves through the liquid and wetting and dewetting take place.

Whilst the use of current contact angle theory has helped this author to a good understanding of the effect of the roughness of the anilox on its wetting properties there are two methods in which further valuable information could be obtained. A method has been employed in which a rough surface has been coated with a very thin layer of extremely pure gold. [134] The roughness of the surface is retained but the chemical nature of the original surface is removed. By measuring the contact angles made by test liquids (pure liquids or even inks) on a section of anilox coated in this manner and an atomically smooth and pure gold surface the effect of the roughness on the observed contact angle could be directly measured.

There are a number of analytical techniques that have been developed to measure the chemistry of surfaces and interfaces. These include XPS (X-ray photoelectron spectroscopy) ToF SIMS (time of flight secondary ion mass spectroscopy), AFM (atomic force microscopy), and AES (Auger electron spectroscopy). The most appropriate technique to future the understanding of the surface of the anilox is XPS, This technique involves placing the sample in a high-vacuum chamber and irradiating it with soft X-rays. Electrons from atomic core levels are ejected, and the chemistry of the surface can be mapped from their kinetic or binding energy. Surface properties which determine wetting spreading and adhesion character can be predicted from the chemical data This would allow chemical changes to the anilox cell interior surface produced by different laser engraving methods and conditions to be characterised and related to wetting and ink transfer. The advantage of this technique over other surface analytical techniques is that it can make measurements on rough surfaces. A small slice of the anilox surface would however need to be removed for analysis in order to fit into the vacuum chamber.

References

1 Hide, L., *The versatility of flexo.* Flexotech, 54, 27-28 & 33. 2003.

2 Roy, G., *The Flexographic industry – overview, growth and potential growth. 22nd June 2003.* [online] Available from: http://www.indianprinterpublisher.com/aug/packaging/flexographic%20industry.htm [Accessed 14th August 2003]

3 White, A., *High quality flexography.* 2nd ed. Pira International, Leatherhead UK & British Printing industries federation, London UK. 49-59. 1998.

4 Smyth, D., *The future of flexographic printing, Strategic five-year forecasts.* Pira International, Leatherhead UK. 2005.

5 White, M., *The future of flexography in the western world.* Flexotech 64, 45-46. 2004

6 Pianoforte, K., *The flexo ink market* Ink world [online] March 2005 Available from: http://www.inkworldmagazine.com/March05Feature3.htm [Accessed 8th May 2005]

7 Jeschke. W., *Flexo vs. Gravure – Market situation and trends* [online] 2004 Available from: http://www.gconline.de/files/VORT_ERA2_WJ.PDF#search ='flexo% 20market%20shar [Accessed 8th May 2005]

8 Savastano, D., *The flexo report* [online] Ink World Feb 2003 Available from: http://www.inkworldmagazine.com/february031.htm [Accessed 14th January 2004]

9 Hancock, M., *Consumer technologies will spur growth.* [online] Pira - Profit through innovation 2003 Available from: http://pira.atalink.co.uk /welcome.phtml [Accessed 24th August 2003]

10 Field, S., Anilox rollers: The heart of Flexo printing. *Flexo,* December 1994, 61-63.

11 Praxair surface technologies, *UCARLOX Anilox rolls.* (date unknown). obtained in March 1999.

12 Pawlowski, L., Technology of thermal sprayed anilox rolls: State of art, problems and perspectives. *J. Thermal spray Technol.* 5 (3) 317-333. 1996

13 Pawlowski, L., Chapter 4 Post spray treatment *In:* L. pawlowski *The science and engineering of thermal spray coatings,* , Chichester. UK. Wiley. 53-67. 1995

14 Weinburg, M. L., Rolling along. *Package printing & converting,* 44(2) 50, 52, 54 & 59. 1997.

15 Gill, P., The anilox roller. *In: Flexography for carton printing,* Conference proceedings. Pira International Leatherhead 11th December 1997.

16 Efunda Engineering fundamentals. *Vickers hardness; Diamond pyramid hardness.* [online] (date unknown) Available from: http://www.efunda.com/ units/hardness/convert_hardness.cfm?HD=HV&Cat=Steel [Accessed 1st July 2003]

17 McColm I. J., *Ceramic hardness.* Plenum press NY 10-11 1990

18 Foot, M.M Transcripts of visit to Praxair Surface technologies, Manchester on the 11th March 1999.

19 Hendriks, M., Transcripts from visit to Apex-Europe, Einhoven, NL. 21st May 1999.

20 Reilly, D., Transcripts of meeting of at the London College Printing on 14th July 1999.

21 Leizert, S., *Rainbow Rolls Enhance Ink Release.* Flexo, 20 (10) 38-39, 1995

22 Carrillo, C.M., *Optimise Your Anilox Rolls* Flexo, 20 (7) 58-62. 1995,

23 White, A., *High quality flexography.* 2nd ed. Pira International, Leatherhead UK & British Printing industries federation, London UK. 25-32. 1998,

24 Reilly, D., *YAG Laser Engraving Technology.* FlexoTech, February 1999, 50-51.

25 Gunton, A., *Laser Engraving of Anilox Rolls.* FlexoTech, December 2000/January 2001, 74-75.

26 STORK, *Laser Engraving* [online] (date unknown) Available from: www.cellramic.storkgroup.com/business/anilox%flexography.html#laser [Accessed 19th July 2003]

27 Harper Corporation of America, *Echocel product information.* [online] (date unknown) Available from: http://www.harperimage.com/ echocel/Echocel-ET2000XC.htm [Accessed 9th January 2003]

28 Schoulepnikoff, L., *Anilox Engraving Technology and Future Trends.* FlexoTech, 2003, 52, 47-55.

29 Buckmann, U., *Flexibility in Laser Engraving Technology.* FlexoTech, December 2000/January 2001, 82-83.

30 DeRosa, M., *Product Trend Report: Anilox Rolls.* Flexo, 16-23, February 1998.

31 Atkinson, D., Transcript of meeting at PIRA International on 6th August 2003

32 Pollard, B., *Laser Engraved Anilox: A Global Commodity or a Customised Speciality?* FlexoTech, August 2000, 27-28.

33 Clinton, G., *Trends in Anilox Engraving.* FlexoTech, 45, 37 2002.

34 Streefland, W., Unpublished report by SCA packaging. Viewed 12th July 1999

35 Tucker, S., *Interferometric Anilox Volume Measurement* Flexo 21 (10) 2 8-39, 32, 1996.

36 Anon. *Measurement of Anilox Rolls.* FlexoTech, 45, 17 2002.

37 Atkinson, D., *Instructions for use of hand roll to measure anilox volumes.* Discussion at Pira international, Leatherhead. 15th May 2000

38 Pamarco, *Proofing / How to use your hand proofer* [online] (date unknown) Available from: http://www.pamarcoglobal.com/flexo-pages/_body-flexo-content1-07c.htm [Accessed on 29th July 2003]

39 PNEAC. *Water based inks for flexographic printing.* [online] (date unknown) Available from: http://www.pneac.org/sheets/flexo/waterbasedinks.pdf [Accessed on 9th August 2003]

40 Ralton, H., 11th June 1997. Flexochat forum [online] Available from: http://www.flexonet.co.uk/bbs/msg.asp?pagno=234&msgid=2204 [Accessed 9th August 2003]

41 Kamp, F., *Doctor Blades for Every Flexographic Printing Machine.* FlexoTech, September 2000, 24-25.

42 Aldrich, S., *Doctor Blade Systems Are Not Created Equal.* Flexotech, May/June 1999, 29-30.

43 DeRosa, M., *Product Trend Report: Doctor Blade Systems* Flexo, April 1999, 18-23.

44 Kamp, F., *Anilox Rollers, The Past, New Developments and Possibilities* FlexoTech, 38, 22-23 2001.

45 Lanska, D., 2001. Anilox Technology for Today's High Print Quality Environment *FlexoTech,* September 2001, 37-38 & 42.

46 ANON, *Flexographic printing - The anilox* [online] (date unknown) Western Michigan university web pages. Accessible from: http:// www.wmich.edu/ppse/flexo/pp9.htm [Accessed on 9th August 2003]

47 Meyer, K-H., Durholz, R. Butterich, K., *The Influence of The Anilox Roller on Ink Transfer in Flexoprinting.* DFTA-Technology-Centre Technical College of Printing, Stuttgart December 1995

48 Liu, X. & Guthrie, J.T., *A Review of Flexographic Printing Plate Development.* Surface Coatings Internationals Part B: Coatings Transactions 86(B2) 91-168 June 2003

49 White, A., *High quality flexography.* 2nd Ed. PIRA & BPIF publishing Leatherhead & London. 15-22 1998

50 Dreher, M., *The Imaging Process in Flexo Platemaking* Flexo & Gravure Intl January 2002 12-15

51 Anon., *Print Process Descriptions: Printing Industry* [online] (date unknown) Available from: http://www.pneac.org/printprocesses/flexography /moreinfo8.cfm [Accessed on 9th August 2003]

52 Anon., *Laser-Engraving Design Rolls* [online] (date unknown) Available from: http://www.iams.org/iamsorg/p2iris/pri nting/2661-s.htm Accessed on [9th August 2003]

53 Meyer, K-H. Durholz, R. & Butterich, K., *The Printing Plate as a Quality Characteristic in the Reproduction of the Printed Image in Flexographic Printing.* DFTA-Technology-Centre Technical College of Printing, Stuttgart December 1996

54 Leach, R.H. & Pierce, R.J., *The Printing Ink Manual. 5th ed.* Blueprint London 1993

55 Weiss, H., *Surface Energy Can Inhibit Ink Transfer on Anilox Rolls* Pap. Film Foil Converter v68 (1), 62, Jan 1994,

56 Olsson, N., *Innovations in Water Based Inks.* FlexoTech, 34-35, March 2002

57 Thompson, B., *Printing Materials Science & Technology.* Pira – Leatherhead UK, 1998.

58 Williams, C.H., *Water Based Flexo Inks.* FlexoTech, July/August 200321-22,

59 Sun Chemical, Press release 2004 *Wetflex EB inks* [online] (June 2004) http://www.sunchemical.com/press_2004_1_1090262196725.htm June 3005

60 Davidson, S., *Radiation curing, A short course covering the theory, chemistry and some applications of radiation curable materials for Coates Lorilleux Ltd.* Internal publication obtained through Sun Chemical, March 2004

61 Kamp, F., *Ongoing Developments in UV Curable Inks and Lacquers.* FlexoTech, May 2003 46-48,

62 Ridyard, A. & Walmsley, K., *UV Curing for Flexo.* FlexoTech, 45-46 August 2000

63 Bean, A.J., *Radiation Curing of Printing Inks.* Radiation Curing - *Sc*ience & Technology, 301-332 Ed. S. Peter Pappas, Plenum NY 1992

64 White, A., *High quality flexography.* 2nd Ed. PIRA & BPIF publishing Leatherhead & London 1998 Flexographic substrates 49-58

65 Quinn, J.A. Valenzuela, D.P. Micael, F.J. & Lavelle, J.S., *Does The Surface Energy of The Plate Affect Ink Transfer?* Converter Cartotechnica 10 (55) 135-143 Jan/Feb 1997

66 Lavelle, J.S. Quinn, J.A. Gallagher, J.E. & Micael, F.J., *Measurements of Flexographic Ink Transfer on a Modified Proufbau.* Tappi Proceedings 1996 International Printing & Graphic Arts Conference. Tappi Press, Atlanta

67 Lindholm , G., *Ink Transfer in Flexo.* Flexo, 40-41, 43-45 February 1998

68 Lagerstedt, P. & Kolseth, P., *Influence of Surface Energetics of Paper on Ink Transfer in Flexo Printing.* Reviews in Printing Science & Technology, 23rd rev. Conf. 270-299 September 1995

69 Palmer, T., Transcript of discussions with Sun Chemical staff at Flexo2003 trade show 5th March 2003.

70 Anon., 3-D Corona treatment [online] (date unknown) Available from: http://www.simoni.com/coronaing/top.htm [accessed on 9th August 2003]

71 Damroth, G. et al., *The effect of UV flexo ink viscosity, anilox cell volume and press speed on print density and dot gain.* NPIRA task force on UV Flexo ink. TAGA proceedings 1996 86-101

72 Fouché, L. Blayo, A., *Transfer characterization of UV flexo inks* TAGA Proceedings 2001 426-7443

73 Schrader, M. E. & Loeb, G. I., *Modern approaches to wettability: theory and application,* Plenum Press New York, London 1992

74 Extrand, C. W., *Hysteresis in contact angle measurement.* In: The Encyclopaedia of Surface and Colloid science, Volume 2, ed. Hubbard, A. Marcel Dekker inc. New York & Basel. 2002 2414-2429

75 Van Oss, C. J., Ch. VII. Contact angle and surface and interfacial tension determination 89-108 In: Interfacial forces in aqueous media. Van Oss, C. J. ed. Marcel Dekker inc. New York 1994.

76 De Gennes P.G., *Wetting, Statics and Dynamics,* Rev. modern Physics, 57 (3) 827-873. 1985.

77 Young, T., in miscellaneous works' vol.1 Ed. Peacock, G. J. Murry London 1855.

78 Li, D. Neumann, A.W., *Thermodynamic status of contact angles* 109-168 Neumann, A.W. & Spelt, J. K. Applied surface thermodynamics. Surfactant series volume 63, Marcel Dekker, New York, Basel, Hong Kong. 1996.

79 Sutherland, I. & Heath, R. J,. *Application of contact angle measurement to wettability, Surface energy and adhesion properties of polymers.* Progress in Rubber and Plastic Technology, 14 (3), 151-173, 1998.

80 Wenzel R. N., *Resistance of a solid surface to wetting by water.* Ind. Eng. Chem. 28 (8), 988-994, 1936.

81 Wenzel R. N., *Surface roughness and contact angle.* J. Phys. Colloid chem. 53, 1466-1467, 1949.

82 Shuttleworth, R. & Bailey, G. L. J., *The spreading of a liquid over a rough surface.* Discussions of the Faraday society, 3, 16-22, 1948.

83 Good, R. J., *A thermodynamic derivation of Wenzel's modification of Young's equation for contact angles together with a theory of hysteresis.* J. Am. Chem. Soc. 74, 211-215, 1952.

84 Wolanski, G. & Marmur, A., *Apparent Contact Angles on Rough Surfaces: the Wenzel Equation Revisited.* Col. Surfaces A: Physiochemical and Engineering Aspects 156 381-388, 1999.

85 Huh, C. & Mason, S. G., *Effects of Surface Roughness on Wetting (Theoretical)* J. Col. And Interface Sci. 60 (1) 1 June 1977.

86 Cassie, A. B. D. & Baxter, S., *Wettability of porous surfaces.* Transactions of the Faraday soc. 40, 546-551, 1944.

87 Baxter, S. & Cassie A. B. D., *The water repellency of fabrics and a new water repellency test.* J. Textile Inst. 36:T, 67, 1945.

88 Cassie, A. B. D. *Contact angles.* Discussions of the Faraday soc. 3, 16-22, 1948.

89 Adamson, A.W., *Physical chemistry of surfaces.* Wiley, New York. 1990.

90 Johnson, R. E. & Detree, R. H., *Contact hysteresis III Study of an idealised heterogeneous surface.* J. Phys. Chem. 68(7), 1744-1750, 1964.

91 Bartell, F. E. & Shepherd, J.W., *Surface roughness as related to hysteresis of contact angles 1. the system paraffin-water-air.* J. phys. Chem. 57, 211-215 1953.

92 Bartell F. E. & Shepherd, J. W., *Surface roughness as related to hysteresis of contact angles 2. the systems paraffin-3 molar calcium chloride solution-air and paraffin-glycerol-air.* J. phys. Chem. 57, 455-458, 1953.

93 Johnson, R. E. & Detree, R. H., *Contact hysteresis I Study of an idealised rough surface.* Advances in chemistry series 43 112-135, 1964.

94 Detree, R. H. & Johnson, R. E., *Contact hysteresis II. Contact angle measurement on rough surfaces.* Advances in chemistry series 43 136-144, 1964.

95 Oliver. J. F. Huh, C. & Mason, S. G., *An experimental study of some effects of solid surface roughness on wetting.* Colloids and Surfaces 1, 79-104, 1980.

96 Bracke, M. De Bisschop, F. & Joos, P., *Contact angle Hysteresis due to surface roughness.* Preg. Colloid Polym. Sci. 76, 251-259, 1988.

97 Wagberg, L. & Westlind, C., *Spreading of droplets of different liquids.* Mid Sweden University report no. R-00-3, 2000.

98 Bico, J. Tordeux, C. & Quere, D., *Rough wetting.* Europhysics letters 55 (2) 2, 14-220, 2001.

99 Oliver, J. F. & Mason, S. G., *Liquid spreading on rough metal surfaces* J. material sci. 15 431-437 1980.

100 Lawrence, J. & Li, L., *Wettability characteristics* of *an Al_2O_3/SiO_2-based ceramic modified with CO_2, nd:YAG, excimer and high powered diode lasers* J. Phys. D: appl. Phys. 32, 1075-1082, 1999.

101 Lawrence, J. & Li, L., *Wettability characteristics of a modified mild steel with CO_2, nd:YAG, excimer and high powered diode lasers* J. Phys. D: appl. Phys. 32 2311-2318, 1999.

102 Good, R. J. & Koo, M. N., *The effect of drop size on contact angle* J Colloid interface sci. 71, 283-292, 1979.

103 Drelich, J. Miller, J., *The effect of solid surface heterogeneity and roughness on the contact angle/drop (bubble) size relationship.* J. Colloid Interface Sci. 164, 252-259, 1993.

104 Drelich, J. Miller, J. Good R. J., *The effect of drop (bubble) size on advancing and receding contact angles for heterogeneous and rough solid surfaces as observed with sessile drops and captive bubble techniques.* J. Colloid Interface Sci. 179, 37-50, 1996.

105 Lin, F. Y. H. Li, D. Neumann, A. W., *Effect of surface roughness on the dependence of contact angles on drop size.* J. Colloid Interface Sci. **159** 86-95 (1993)

106 Li, D., *Drop size dependence of contact angles and line tension of solid-liquid systems.* Colloids and Surfaces A: Physiochemical and engineering aspects 116, 1-23, 1996.

107 Gu, Y., *Contact angle measurement techniques for the Determination of Wettability,* 1213-1227, In: Encyclopaedia of surface and colloid science Ed. Hubbard, A. T. volume 1 Marcel Dekker New York 2002.

108 Lam, C.N.C. Lu, J.J. & Neumann, A.W. *Measuring Contact Angles* Chapter 14 *251-280* From Handbook of applied surface and colloid chemistry, volume 2, Ed. Holmberg, K., Wiley, Chichester UK. 2002.

109 Khamsi, M. A. & Knaust, H., The Newton-Raphson method [online] (date unknown) Available from: http://www.sosmath.com/calculus/diff/der07/der07.html [Accessed on 12th September 2003]

110 Dataphysics, *Product information* [online] Available from: http://www.dataphysics.de/english/produkte_dcat-11.htm [Accessed on 2nd June 2005]

111 Mulqueen, M. Huibers, P. D. T., *Measuring equilibrium surface tension. Chapter 11.* 219-223, In: Handbook of applied surface and colloid chemistry. Volume 2. Holmberg, K ed. Wiley, Chichester UK 2002

112 TAPPI Provisional method T558 PM-95, *Surface wettability and absorbency of sheeted materials using and automated contact angle tester.* 1995.

113 TAPPI Method T 458 *Surface wettability of paper*

114 Van Oss, C. J., *Ch. IX. Other approaches for interpreting contact angel data and determining the surface tension and surface tension components of solids* 112. In: *Interfacial forces in aqueous media.* Marcel Dekker inc. New York 1994.

115 Padday, J. F., *Wetting and work of adhesion* in Handbook of adhesion Ed. Packham, D.E. Longman Scientific & Technical Harlow UK. 1992

116 Wu, S., *Surface and interfacial tensions of polymer melts, polyethylene, polyisobutene and polyvinylacetate* J. Colloid Interface Sci. 37, 686-690 1971

117 Allen, K.W.& Evans, J. R. G., *Acid-base interactions.* 5-7 In: Handbook of adhesion, ed. Packham, D.E., Longman Scientific & Technical Harlow UK. 1992.

118 Fowkes, F. M., *Determination of interfacial tensions, contact angles and dispersion forces in surfaces by assuming additivity of intermolecular interactions in surfaces* J. Phys. Chem. 66, 382, 1962.

119 Fowkes, F. M., *Quantitative characterisation of the acid-base properties of solvents, polymers and inorganic surfaces,* 93-115 in: Acid-base interactions, Relevance to Adhesion Science and Technology, Mittal, K. L. ed. Brill

academic publishers, NY 2000.

120 Good, R.J., *Contact angle, wetting and adhesion: a critical review* J adhesion sci. technol. Vol. 6 No. 12 1269-1302, 1992.

121 Morra, M., *Acid-base behaviour of polymer surfaces* 74-90 from Encyclopaedia of surface and colloid science Ed. Hubbard, A. T. volume 1 Marcel Dekker, New York. 2002.

122 Good, R.J. van Oss, C.J., *The modern theory of contact angles and the hydrogen bond components of surface energies* 1-21 from Modern approach to wettability, Theory and applications Ed. Schrader. M.E. Leob, G. I. Plennum NY. 1992.

123 Sprycha, R., *Interfacial aspects of printing* 2660-2675 from Encyclopaedia of surface and colloid science Ed. Hubbard, A. T. volume 1 Marcel Dekker New York. 2002.

124 Diley, A., Transcript of discussions at Pira international on 17th March 1999.

125 Anon, Conference proceedings, Kruss Surface science, Hull, 1999.

126 Magure, J. Yang, J., The effect of drop volume on contact angle. J food protection v54 (3) pp232-235, 1991.

127 Mason, S.G., Wetting and spreading – some effects of surface roughness. In: Wetting, Spreading and adhesion Padday, J. F. Academic press New York, 384, 1978.

128 Walkling, M. W., *Arena product data sheet,* Coates Lorrelleux UK. 1997.

129 Huang et al *Surface energetics and acid-base character of sized and unsized paper handsheets* J. adhesion Sci. technol. v9 (11) pp1403-1411, 1995.

130 Anon, *Ask Dr Math* [online} Available from: http://mathforum.org/dr.math/faq/formulas/faq.ellipsoid.html [Accessed on 28th June 2002]

131 Abdelsalam, M. E. Bartlett, P. N. Kelf, T. Baumberg, J., *Wetting of regularly structured gold surfaces* Langmuir 21,1753-1757, 2005.

132 Anon, *Platinum anilox rolls* [online].(date unknown) Available from: http://www.harperimage.com/Anilox_Directory/PlatinumInfo.htm {Accessed on 27th July 2005]

133 Weisstein, E.W., *Surface of Revolution.* MathWorld [online] March 2005. Available from: http://mathworld.wolfram.com/SurfaceofRevolution.html [Accessed on 4th June 2005]

134 Kinloch, A.J. Kodokian, G.K.A.& Watts, J.F., *The adhesion of thermoplastic fibre composites* Royal Soc. Phil. Trans. Lond., A338, 83-112, 1992.

Appendix

Appendix A3

Appendix Section A3-1

Contact angle data for anilox Harper 1 measured using the MAMS instrument and reagent grade water as the test liquid.

The drop volume reported for each measurement is calculated by the instrument, from the measured height and width of the drop. The drop volume shown in the table headings is the volume dispensed by the pipette.

40μl water drops						
	Polished band		**CO_2 band**		**YAG band**	
Repeat number	**Angle (deg)**	**Volume (μl)**	**Angle (deg)**	**Volume (μl)**	**Angle (deg)**	**Volume (μl)**
1	48.58	47.55	59.18	35.39	73.87	40.46
2	45.01	45.61	60.67	37.90	76.32	41.62
3	45.19	43.84	59.01	31.35	73.09	30.98
4	49.95	36.71	58.10	28.37	68.93	36.20
5	50.30	40.82	56.72	29.89	75.38	35.40
6	45.64	42.61	60.56	33.67	70.16	32.12
7	45.90	35.25	50.73	33.02	69.14	45.42
8	44.63	30.31	63.49	30.36	66.79	36.71
9	50.50	51.15	52.50	30.68	70.75	34.64
10	45.11	42.33	53.12	29.92	69.94	35.63
11	50.65	38.08	58.90	28.71	72.84	35.74
12	47.96	32.12	63.49	38.60	67.18	30.92
13	48.56	41.65	56.99	33.81	74.95	40.95
14	52.15	32.88	60.84	41.11	72.41	35.99
15	49.85	36.75	62.76	35.19	67.08	38.28
Mean	**48.0**	**39.8**	**58.5**	**33.2**	**71.3**	**36.7**
Standard Deviation	2.5	6.0	3.9	3.8	3.1	4.1

Appendix Section A3-1 Continued

Contact angle data for anilox Harper 1 measured using the MAMS instrument and reagent grade water as the test liquid.

The drop volume reported for each measurement is calculated by the instrument, from the measured height and width of the drop. The drop volume shown in the table headings is the volume dispensed by the pipette.

20μl water drops						
	Polished band		**CO_2 band**		**YAG band**	
Repeat number	**Angle (deg)**	**Volume (μl)**	**Angle (deg)**	**Volume (μl)**	**Angle (deg)**	**Volume (μl)**
1	55.48	18.68	63.80	14.73	77.14	17.12
2	54.35	15.37	62.11	15.41	74.56	15.82
3	49.55	15.02	65.44	13.84	77.80	17.82
4	52.15	16.42	64.25	17.40	77.96	15.04
5	51.80	14.83	62.53	15.19	75.27	16.10
6	49.95	16.63	64.71	16.98	80.10	13.15
7	54.69	17.00	61.89	17.52	75.62	12.93
8	56.91	19.69	65.99	17.29	79.70	12.63
9	54.45	17.91	64.38	13.07	83.15	14.06
10	53.99	18.75	64.85	15.92	81.07	15.07
11	55.87	20.33	63.15	12.56	79.18	18.78
12	51.96	12.48	60.89	14.92	77.37	14.24
13	51.39	17.13	67.93	12.77	80.68	12.31
14	56.17	17.76	65.90	13.56	81.65	17.04
15	49.59	15.60	62.40	19.44	75.23	15.83
16	52.87	19.49	69.35	13.62	77.42	16.06
17	53.64	13.21	65.51	11.73	76.02	13.84
18	53.21	14.13	68.04	10.94	74.22	14.18
19	57.14	13.31	62.89	16.24	75.96	15.94
20	52.04	10.30	67.19	14.85	80.07	11.92
Mean	**53.4**	**16.2**	**64.7**	**14.9**	**78.0**	**15.0**
Standard Deviation	2.4	2.3	2.3	2.2	2.6	1.8

Appendix Section A3-1 Continued

Contact angle data for anilox Harper 1 measured using the MAMS instrument and reagent grade water as the test liquid.

The drop volume reported for each measurement is calculated by the instrument, from the measured height and width of the drop. The drop volume shown in the table headings is the volume dispensed by the pipette.

5µl water drops						
	Polished band		**CO_2 band**		**YAG band**	
Repeat number	**Angle (deg)**	**Volume (µl)**	**Angle (deg)**	**Volume (µl)**	**Angle (deg)**	**Volume (µl)**
1	57.98	3.94	62.84	5.05	83.63	5.30
2	56.05	5.25	66.70	4.03	74.12	4.63
3	56.67	6.02	61.11	3.73	77.32	3.51
4	55.64	4.78	60.65	4.46	74.52	3.47
5	55.13	6.34	64.98	4.94	75.89	4.14
6	54.01	3.69	62.50	4.83	79.27	3.63
7	52.84	6.31	62.12	4.56	76.49	3.59
8	53.61	4.94	68.89	5.66	79.52	3.94
9	60.36	5.52	61.21	5.01	74.40	4.81
10	52.74	6.36	63.27	5.14	76.22	5.16
11	54.47	6.26	68.12	4.46	74.12	4.63
12	57.18	8.37	63.07	3.91	74.83	5.11
13	59.45	4.39	62.92	5.56	71.83	5.27
14	55.40	3.93	64.27	4.93	76.73	3.61
15	58.45	5.07	65.21	4.83	75.72	7.04
16	56.49	4.59	63.61	5.62	72.92	6.51
17	58.27	4.65	61.10	4.84	72.73	6.38
18	54.24	3.24	64.07	4.81	74.06	4.57
19	57.50	4.53	63.43	4.09	82.93	4.32
20	55.55	4.02	62.50	8.15	78.23	3.94
Mean	**56.1**	**5.1**	**63.6**	**4.9**	**76.3**	**4.7**
Standard Deviation	2.2	1.2	2.3	0.6	3.2	1.1

Appendix Section A3-2

Contact angle data for anilox Harper 1 measured using the MAMS instrument and diiodomethane as the test liquid.

The drop volume reported for each measurement is calculated by the instrument, from the measured height and width of the drop. The drop volume shown in the table headings is the volume dispensed by the pipette.

5μl diiodomethane drops						
	Polished band		**CO_2 band**		**YAG band**	
Repeat number	**Angle (deg)**	**Volume (μl)**	**Angle (deg)**	**Volume (μl)**	**Angle (deg)**	**Volume (μl)**
1	18.45	5.16	22.55	4.27	12.77	3.30
2	24.33	3.6	17.18	4.94	14.87	4.43
3	19.51	3.44	21.55	4.67	13.42	2.99
4	18.7	6.85	15.96	3.89	19.32	4.32
5	19.46	4.33	14.53	5.63	10.84	3.22
6	16.86	2.46	21.28	5.23	15.46	3.08
7	19.58	4.02	16.90	2.92	13.78	2.25
8	18.45	4.77	20.16	4.39	16.39	4.05
9	22.24	4.62	20.34	3.33	21.17	3.06
10	17.22	4.04	20.58	4.52	16.26	3.71
11	21.4	3.94	21.50	3.79	15.46	3.08
12	18.26	5.17	18.08	4.28	12.70	4.58
13	21.25	4.76	17.46	4.24	11.22	4.28
14	17.07	6.19	19.75	3.30	19.39	5.36
15	17.04	5.25	21.06	4.20	13.99	3.77
16	22.98	5.3	19.55	5.39	10.56	3.39
17	19.13	4.57	19.29	4.44	16.32	2.76
18	18.68	5.57	16.65	3.54	11.43	4.12
19	19.6	5.27	19.60	3.63	14.31	2.97
20	19.06	5.3	19.80	3.43	12.22	3.78
Mean	**19.5**	**4.7**	**19.2**	**4.2**	**14.6**	**3.6**
Standard Deviation	2.1	1.0	2.2	0.7	3.0	0.8

Appendix Section A3-3

Contact angle measurements using the FTA instrument with water and diiodomethane as the test liquids.

The drop volume reported for each measurement is calculated by the instrument, using the ADSA technique. The drop volume shown in the table headings is the volume dispensed by the syringe.

5µl water drops						
run number	polished band		CO_2 band		YAG band	
	contact angle (degrees)	drop volume (µl)	contact angle (degrees)	drop volume (µl)	contact angle (degrees)	drop volume (µl)
1	77.6	4.6	85.2	4.6	95.9	4.9
2	72.3	4.9	81.6	5.1	101.0	4.9
3	74.7	4.7	84.3	5.0	100.0	5.2
4	74.1	5.2	83.6	5.2	97.3	4.7
5	78.6	5.0	86.4	5.2	99.8	4.9
6	73.8	5.3	83.6	4.2	101.6	5.0
7	71.3	4.8	84.1	4.9	97.2	4.9
8	73.9	4.9	82.2	5.8	102.3	5.2
9	72.0	4.9	87.1	5.2	98.9	4.8
10	76.0	5.0	85.3	5.0	99.9	5.0
11	75.7	4.3	82.9	4.8	100.6	4.6
12	72.6	4.8	84.6	5.2	96.2	4.9
13	74.1	5.2	83.7	4.7	95.6	5.1
14	77.0	5.2	86.9	5.3	97.6	4.7
15	76.2	4.8	81.6	5.0	102.8	4.9
16	76.9	4.6	88.7	5.1	100.9	5.0
17	73.8	5.0	87.4	4.9	99.8	4.8
18	74.4	5.3	82.9	5.1	99.5	5.1
19	76.5	5.2	81.2	5.3	100.3	5.2
20	73.7	4.8	84.3	4.7	102.6	4.6
Mean	**74.8**	**4.9**	**84.4**	**5.0**	**99.5**	**4.9**
Standard deviation	2.0	0.3	2.1	0.3	2.2	0.2

Appendix Section A3-3 Continued

Contact angle measurements using the FTA instrument with water and diiodomethane as the test liquids.

The drop volume reported for each measurement is calculated by the instrument, using the ADSA technique. The drop volume shown in the table headings is the volume dispensed by the syringe.

7μl diiodomethane drops						
run number	polished band		CO_2 band		YAG band	
	contact angle (degrees)	drop volume (μl)	contact angle (degrees)	drop volume (μl)	contact angle (degrees)	drop volume (μl)
1	41.2	7.2	44.8	6.9	42.9	6.4
2	40.3	6.8	42.0	6.3	41.0	6.0
3	39.7	6.8	45.3	6.8	44.2	6.0
4	43.9	6.9	45.2	6.5	43.2	6.2
5	42.7	6.3	47.2	7.1	42.5	6.7
6	41.2	6.7	42.9	6.7	43.8	6.2
7	44.3	6.8	43.3	6.6	46.4	6.1
8	43.0	6.6	47.7	6.8	44.8	6.6
9	41.6	6.3	45.5	6.3	42.0	6.3
10	40.1	6.9	46.0	6.9	43.1	6.1
Mean	**41.8**	**6.7**	**45.0**	**6.7**	**43.4**	**6.3**
Standard deviation	1.6	0.3	1.8	0.3	1.5	0.2

Appendix Section A3-4

Contact angle measurements using the FTA instrument with formamide as the test liquid.

The drop volume reported for each measurement is calculated by the instrument, using the ADSA technique. The drop volume shown in the table headings is the volume dispensed by the syringe.

5μl formamide drops						
run number	polished band		CO_2 band		YAG band	
	contact angle (degrees)	drop volume (μl)	contact angle (degrees)	drop volume (μl)	contact angle (degrees)	drop volume (μl)
1	42.8	4.2	60.8	4.8	62.7	4.7
2	44.1	4.8	62.3	4.5	63.7	4.6
3	43.1	4.6	63.4	4.4	65.1	4.7
4	43.8	4.7	59.8	4.5	64.7	5.1
5	45.4	4.7	60.2	4.4	64.2	4.6
6	44.1	4.7	61.5	4.4	60.1	4.7
7	41.5	4.6	59.7	4.5	62.9	4.6
8	42.3	4.6	58.8	4.8	64.4	4.9
9	42.6	4.9	57.0	4.8	65.0	4.5
10	43.1	4.6	59.4	4.6	63.8	4.5
Mean	**43.3**	**4.6**	**60.3**	**4.6**	**63.7**	**4.7**
Standard deviation	1.1	0.2	1.8	0.2	1.5	0.2

Appendix Section A3-5

Contact angle measurements using the FTA instrument using commercially available Cyan inks as the test liquids.

The drop volume reported for each measurement is calculated by the instrument, using the ADSA technique. The drop volume shown in the table headings is the volume dispensed by the syringe.

Water-based ink process cyan Sun Chemical						
run number	polished band		CO_2 band		YAG band	
	contact angle (degrees)	drop volume (µl)	contact angle (degrees)	drop volume (µl)	contact angle (degrees)	drop volume (µl)
1	52	2.9	63	6.3	73	3.5
2	52	6.1	63	3.3	75	3.4
3	54	7.2	65	3.8	73	8.1
4	52	5.7	65	5.3	73	10.9
5	56	7.3	64	5.6	72	4.3
6	52	5.3	67	6.5	72	7.6
Mean	**53.0**	**5.8**	**64.5**	**5.1**	**73.0**	**6.3**
Standard deviation	1.7	1.6	1.5	1.3	1.1	3.0

UV ink Process cyan "Arena" Coates lorrelleux						
run number	polished band		CO_2 band		YAG band	
	contact angle (degrees)	drop volume (µl)	contact angle (degrees)	drop volume (µl)	contact angle (degrees)	drop volume (µl)
1	30	2.7	49	5.0	36	2.8
2	33	3.8	44	3.8	41	3.0
3	28	3.6	46	5.4	44	2.0
4	35	2.0	41	4.5	44	3.4
5	56*	7.2*	47	4.2	43	3.8
Mean	**32**	**3.0**	**45**	**4.6**	**42**	**3.0**
Standard deviation	3	0.8	3	0.6	3	0.7

* indicated not included in average figures

Appendix Section A3-6

Contact angle measurements on Harper 1 post cleaning, using the FTA instrument with water and diiodomethane as the test liquids.

The drop volume reported for each measurement is calculated by the instrument, using the ADSA technique. The drop volume shown in the table headings is the volume dispensed by the syringe.

5µl water drops						
run number	polished band		CO_2 band		YAG band	
	contact angle (degrees)	drop volume (µl)	contact angle (degrees)	drop volume (µl)	contact angle (degrees)	drop volume (µl)
1	71.5	5.0	86.8	3.8	75.6	8.6
2	76.0	4.6	86.6	3.3	80.0	8.2
3	72.1	3.9	87.7	3.7	79.5	7.8
4	71.0	4.7	80.5	5.4	79.3	7.4
5	69.2	4.8	87.3	3.8	76.8	7.1
6	75.1	4.1	80.9	3.9	78.8	8.9
7	75.9	4.5	83.4	4.0	76.1	8.5
8	71.2	4.1	84.7	4.4	80.5	7.7
9	76.1	4.9	86.4	4.4	76.3	6.5
10	70.5	4.1	85.6	4.6	78.6	7.5
11	69.2	4.2	84.4	4.3		
12	69.5	4.5	81.5	5.0		
13	74.6	4.4	82.5	4.1		
14	68.4	4.1	79.7	4.4		
15	74.8	4.9	81.0	3.9		
Mean	**72.3**	**4.4**	**83.9**	**4.2**	**78.1**	**7.8**
Standard deviation	2.8	0.4	2.8	0.5	1.8	0.7

5µl diiodomethane drops						
run number	polished band		CO_2 band		YAG band	
	contact angle (degrees)	drop volume (µl)	contact angle (degrees)	drop volume (µl)	contact angle (degrees)	drop volume (µl)
1	43.5	4.6	42.8	4.4	40.2	4.2
2	41.7	4.5	41.4	5.0	43.0	4.4
3	40.4	4.9	46.5	4.5	43.4	4.0
4	42.0	5.1	42.0	4.4	45.9	4.6
5	42.7	4.3	41.4	4.5	44.6	4.8
Mean	**42.1**	**4.7**	**42.8**	**4.5**	**43.4**	**4.4**
Standard deviation	1.2	0.3	2.1	0.2	2.2	0.3

Appendix A4

Appendix Section A4-1

Contact angle data for anilox Pira 1 measured using the MAMS instrument

The drop volume reported is again a calculated volume from the measured height and width of the drop. The drop volume shown in the table header is the volume dispensed by the pipette.

5μl water drops								
	Polished band		**Band 1**		**Band 2**		**Band 3**	
Repeat number	**Angle (deg)**	**Volume (μl)**	**Angle (deg)**	**Volume (μl)**	**Angle (deg)**	**Volume (μl)**	**Angle (deg)**	**Volume (μl)**
1	50.7	6.5	50.9	5.6	51.7	3.1	52.8	4.8
2	45.9	5.4	49.5	7.1	50.7	3.3	54.5	6.1
3	45.9	6.3	52.6	5.4	52.0	4.3	54.6	4.5
4	49.6	6.7	55.9	5.5	56.7	6.1	52.2	5.7
5	48.3	5.5	54.9	5.7	56.1	3.6	50.3	5.5
6	48.5	6.2	50.5	5.9	55.6	5.3	50.5	5.9
7	51.8	4.8	49.6	5.9	53.3	4.7	55.3	6.2
8	44.9	6.4	49.0	5.8	51.3	5.6	48.0	5.5
9	47.5	5.6	55.5	3.4	48.3	4.4	52.7	5.5
10	53.3	5.5	53.3	7.4	50.1	7.4	53.0	7.5
11	48.1	4.8	53.2	6.9	54.5	3.8		
12	50.6	5.0	48.8	7.8	53.7	6.6		
13	44.5	5.6	48.4	5.3	55.9	6.5		
14	47.9	3.5	53.6	4.6	52.1	6.1		
15	54.8	4.3	54.1	5.0	53.6	5.2		
16	54.2	4.6	49.1	6.0	50.9	5.2		
17	50.7	4.2	55.6	4.9	48.8	6.3		
18	49.1	5.5	50.3	4.8	50.4	5.8		
19	55.3	4.1	55.4	5.6	51.7	5.8		
20	51.9	3.9	51.1	5.5	55.4	6.3		
Mean	**49.7**	**5.2**	**52.1**	**5.7**	**52.6**	**5.3**	**52.4**	**5.7**
Standard Deviation	3.3	0.9	2.6	1.0	2.5	1.2	2.3	0.8

Appendix Section A4-1 continued

Contact angle data for anilox Pira 1 measured using the MAMS instrument continued

The drop volume reported is again a calculated volume from the measured height and width of the drop. The drop volume shown in the table header is the volume dispensed by the pipette.

5μl diiodomethane drops								
	Polished band		Band 1		Band 2		Band 3	
Repeat number	**Angle (deg)**	**Volume (μl)**	**Angle (deg)**	**Volume (μl)**	**Angle (deg)**	**Volume (μl)**	**Angle (deg)**	**Volume (μl)**
1	12.8	4.7	14.7	3.5	16.3	4.4	10.4	4.1
2	13.4	5.8	12.4	4.6	17.7	3.4	12.6	2.9
3	13.9	4.0	20.1	4.8	15.3	3.3	13.4	5.3
4	11.7	4.5	15.0	5.7	17.9	3.6	13.0	5.5
5	12.8	7.3	17.0	5.8	16.2	4.3	12.6	5.8
6	15.7	4.3	17.6	6.2	13.3	4.9	11.8	4.8
7	12.7	4.2	16.4	5.9	15.4	4.5	12.3	4.6
8	12.1	4.0	12.2	6.7	15.7	4.6	10.7	5.6
9	14.0	4.0	13.8	4.8	17.3	4.0	13.0	4.9
10	12.9	4.5	19.3	4.4	13.9	5.0	12.3	5.5
11	16.7	5.0	12.7	4.7	12.7	4.7		
12	14.0	7.1	19.4	4.4	15.6	3.7		
13	14.3	6.0	18.9	4.7	16.7	4.5		
14	15.3	5.0	17.0	5.9	16.6	6.5		
15	15.3	4.2	18.0	5.4	12.7	5.9		
16	12.8	4.4	20.4	5.8	18.7	4.7		
17	13.5	4.0	16.3	6.0	12.4	5.4		
18	14.4	5.2	19.7	5.7	13.5	5.2		
19	11.1	4.1	17.6	5.2	14.9	6.2		
20	14.4	4.9	17.5	3.5	15.6	5.7		
Mean	**13.7**	**4.9**	**16.8**	**5.2**	**15.4**	**4.7**	**12.2**	**4.9**
Standard Deviation	1.4	1.0	2.7	0.8	1.9	0.9	1.0	0.9

Appendix Section A4-2

Optical density measurements made on the prints from anilox Pira 1

25 Meters per Minute					
Light pressure		Medium pressure		High pressure	
Band 1	Band 2	Band 1	Band 2	Band 1	Band 2
0.64	0.58	0.68	0.77	0.64	0.58
0.65	0.69	0.77	0.81	0.65	0.69
0.61	0.67	0.70	0.75	0.61	0.67
0.67	0.70	0.64	0.80	0.67	0.70
0.54	0.63	0.67	0.83	0.54	0.63
0.63	0.69	0.73	0.78	0.63	0.69
0.70	0.72	0.61	0.77	0.70	0.72
0.60	0.75	0.64	0.78	0.60	0.75
0.63	0.69	0.68	0.82	0.63	0.69
0.62	0.66	0.65	0.78	0.62	0.66
0.62	0.65	0.70	0.72	0.62	0.65
0.58	0.62	0.71	0.73	0.58	0.62
0.66	0.62	0.70	0.73	0.66	0.62
0.60	0.66	0.69	0.81	0.60	0.66
0.57	0.64	0.69	0.80	0.57	0.64
0.61	0.68	0.70	0.75	0.61	0.68
0.58	0.65	0.68	0.80	0.58	0.65
0.55	0.69	0.64	0.77	0.55	0.69
0.59	0.69	0.66	0.81	0.59	0.69
0.56	0.61	0.71	0.79	0.56	0.61
0.67	0.67	0.79	0.71	0.82	0.77
0.66	0.66	0.78	0.74	0.82	0.82
0.64	0.65	0.83	0.74	0.81	0.84
0.62	0.75	0.72	0.76	0.73	0.79
0.61	0.71	0.72	0.77	0.74	0.80
0.59	0.64	0.74	0.74	0.70	0.81
0.61	0.72	0.77	0.73	0.70	0.78
0.60	0.73	0.79	0.74	0.72	0.81
0.65	0.70	0.78	0.76	0.69	0.77
0.69	0.69	0.76	0.80	0.74	0.81
0.64	0.69	0.73	0.82	0.77	0.75
0.62	0.65	0.71	0.79	0.82	0.79
0.68	0.68	0.75	0.83	0.79	0.81
0.58	0.68	0.65	0.76	0.67	0.80
0.59	0.71	0.66	0.78	0.71	0.85
0.64	0.72	0.69	0.78	0.75	0.86
0.56	0.69	0.67	0.79	0.69	0.78
0.57	0.72	0.62	0.82	0.72	0.84
0.66	0.73	0.66	0.84	0.72	0.82
0.61	0.66	0.74	0.78	0.68	0.84
0.62	**0.68**	**0.71**	**0.78**	**0.68**	**0.74**
0.04	0.04	0.05	0.03	0.08	0.08

Appendix Section A4-2 continued

Optical density measurements made on the prints from anilox Pira 1 continued

50 Meters per Minute					
Light pressure		Medium pressure		High pressure	
Band 1	Band 2	Band 1	Band 2	Band 1	Band 2
0.72	0.65	0.71	0.69	0.67	0.7
0.71	0.64	0.69	0.69	0.65	0.68
0.69	0.60	0.68	0.65	0.62	0.7
0.64	0.64	0.65	0.68	0.58	0.71
0.62	0.66	0.66	0.69	0.62	0.75
0.63	0.69	0.62	0.67	0.63	0.71
0.61	0.70	0.56	0.66	0.61	0.67
0.61	0.68	0.63	0.68	0.61	0.68
0.58	0.64	0.59	0.72	0.68	0.67
0.62	0.68	0.63	0.70	0.64	0.68
0.62	0.67	0.64	0.75	0.67	0.7
0.63	0.67	0.64	0.69	0.68	0.68
0.65	0.70	0.62	0.71	0.60	0.7
0.60	0.70	0.64	0.74	0.67	0.75
0.59	0.75	0.62	0.72	0.68	0.71
0.63	0.70	0.62	0.72	0.62	0.76
0.60	0.75	0.62	0.70	0.61	0.71
0.59	0.73	0.58	0.71	0.62	0.76
0.60	0.71	0.60	0.67	0.62	0.74
0.61	0.72	0.58	0.71	0.62	0.74
0.69	0.70	0.60	0.68	0.58	0.74
0.67	0.67	0.61	0.72	0.64	0.75
0.66	0.78	0.66	0.77	0.60	0.78
0.74	0.71	0.60	0.72	0.68	0.72
0.61	0.69	0.65	0.70	0.65	0.72
0.67	0.74	0.67	0.70	0.63	0.72
0.61	0.66	0.63	0.69	0.67	0.75
0.62	0.65	0.70	0.70	0.72	0.74
0.66	0.66	0.68	0.71	0.72	0.7
0.62	0.70	0.74	0.72	0.70	0.69
0.69	0.69	0.72	0.74	0.78	0.71
0.66	0.74	0.75	0.75	0.70	0.73
0.71	0.71	0.72	0.72	0.71	0.68
0.67	0.69	0.62	0.67	0.67	0.76
0.64	0.68	0.65	0.68	0.63	0.74
0.64	0.69	0.68	0.69	0.65	0.74
0.60	0.63	0.64	0.67	0.64	0.73
0.61	0.67	0.65	0.70	0.62	0.75
0.66	0.69	0.60	0.69	0.62	0.73
0.66	0.66	0.72	0.67	0.63	0.79
0.69	0.75	0.67	0.71	0.68	0.77
0.64	0.78	0.73	0.77	0.67	0.74
0.67	0.74	0.75	0.76	0.64	0.82
0.64	0.70	0.67	0.67	0.64	0.72
0.67	0.72	0.68	0.67	0.63	0.79
0.65	0.74	0.70	0.70	0.69	0.73
0.66	0.69	0.67	0.69	0.61	0.73
0.62	0.69	0.66	0.66	0.63	0.75
0.63	0.69	0.66	0.66	0.63	0.7
0.63	0.72	0.76	0.62	0.66	0.73
0.64	**0.69**	**0.66**	**0.70**	**0.65**	**0.73**
0.04	0.04	0.05	0.03	0.04	0.03

Appendix Section A4-2 continued

Optical density measurements made on the prints from anilox Pira 1 continued

75 Meters per Minute						
Light pressure			Medium pressure			High pressure
Band 1	Band 2		Band 1	Band 2		Band 1	Band 2
0.55	0.49		0.58	0.55		0.66	0.64
0.57	0.47		0.58	0.56		0.61	0.69
0.45	0.49		0.55	0.53		0.7	0.68
0.5	0.5		0.56	0.53		0.63	0.67
0.45	0.49		0.51	0.57		0.6	0.73
0.43	0.49		0.5	0.57		0.64	0.72
0.45	0.52		0.52	0.6		0.58	0.69
0.44	0.5		0.53	0.61		0.63	0.72
0.44	0.48		0.49	0.56		0.6	0.66
0.45	0.5		0.57	0.58		0.62	0.7
0.52	0.48		0.56	0.55		0.71	0.68
0.45	0.48		0.6	0.58		0.64	0.69
0.51	0.55		0.55	0.6		0.63	0.65
0.45	0.55		0.55	0.56		0.67	0.69
0.44	0.52		0.55	0.61		0.65	0.65
0.42	0.52		0.51	0.61		0.62	0.7
0.42	0.52		0.48	0.61		0.63	0.74
0.44	0.55		0.52	0.65		0.61	0.73
0.45	0.6		0.49	0.64		0.64	0.71
0.43	0.51		0.52	0.6		0.65	0.65
0.42	0.53		0.63	0.61		0.72	0.64
0.43	0.54		0.57	0.66		0.69	0.65
0.42	0.6		0.6	0.62		0.68	0.67
0.47	0.54		0.6	0.65		0.62	0.65
0.47	0.54		0.54	0.66		0.62	0.64
0.47	0.51		0.57	0.65		0.63	0.66
0.47	0.57		0.59	0.63		0.71	0.7
0.45	0.55		0.53	0.69		0.69	0.7
0.46	0.56		0.55	0.68		0.66	0.71
0.47	0.56		0.59	0.6		0.68	0.67
0.45	0.6		0.61	0.57		0.67	0.76
0.48	0.59		0.61	0.59		0.64	0.68
0.44	0.6		0.59	0.6		0.67	0.69
0.51	0.53		0.54	0.62		0.61	0.69
0.48	0.56		0.54	0.65		0.64	0.68
0.5	0.58		0.54	0.64		0.62	0.68
0.5	0.57		0.56	0.61		0.62	0.66
0.56	0.55		0.56	0.61		0.6	0.71
0.47	0.55		0.56	0.66		0.68	0.66
0.56	0.52		0.59	0.61		0.64	0.68
0.47	**0.53**		**0.55**	**0.61**		**0.65**	**0.68**
0.04	0.04		0.04	0.04		0.03	

Appendix Section A4-2 continued

Optical density measurements made on the prints from anilox Pira 1 continued

100 Meters per Minute					
Light pressure		Medium pressure		High pressure	
Band 1	Band 2	Band 1	Band 2	Band 1	Band 2
0.48	0.54	0.53	0.53	0.6	0.62
0.48	0.52	0.53	0.53	0.61	0.63
0.47	0.49	0.54	0.54	0.58	0.58
0.45	0.52	0.51	0.54	0.61	0.59
0.43	0.49	0.49	0.57	0.59	0.59
0.44	0.48	0.48	0.57	0.58	0.62
0.45	0.5	0.5	0.58	0.56	0.59
0.45	0.54	0.5	0.63	0.53	0.62
0.43	0.54	0.49	0.61	0.55	0.61
0.46	0.5	0.5	0.62	0.53	0.66
0.41	0.43	0.54	0.59	0.49	0.6
0.4	0.45	0.55	0.54	0.52	0.62
0.4	0.45	0.54	0.53	0.57	0.53
0.44	0.44	0.49	0.56	0.49	0.6
0.41	0.44	0.51	0.54	0.49	0.57
0.44	0.45	0.5	0.56	0.53	0.62
0.47	0.45	0.46	0.57	0.51	0.6
0.45	0.49	0.49	0.53	0.49	0.6
0.48	0.45	0.47	0.55	0.48	0.59
0.45	0.46	0.55	0.55	0.49	0.57
0.48	0.51	0.54	0.52	0.54	0.57
0.48	0.48	0.5	0.54	0.52	0.55
0.49	0.46	0.49	0.51	0.54	0.58
0.46	0.48	0.49	0.52	0.52	0.55
0.46	0.49	0.53	0.54	0.51	0.54
0.44	0.52	0.46	0.53	0.5	0.58
0.44	0.47	0.44	0.55	0.51	0.63
0.42	0.51	0.48	0.53	0.51	0.53
0.42	0.48	0.48	0.51	0.49	0.54
0.44	0.5	0.52	0.57	0.5	0.56
0.44	0.5	0.57	0.59	0.58	0.58
0.46	0.5	0.56	0.56	0.53	0.63
0.46	0.55	0.55	0.57	0.54	0.61
0.4	0.48	0.5	0.52	0.59	0.58
0.42	0.47	0.49	0.53	0.57	0.56
0.42	0.46	0.5	0.51	0.58	0.64
0.4	0.47	0.48	0.5	0.59	0.5
0.42	0.48	0.49	0.55	0.59	0.52
0.41	0.43	0.48	0.52	0.65	0.5
0.45	0.52	0.55	0.6	0.55	0.54
0.44	**0.48**	**0.51**	**0.55**	**0.54**	**0.58**
0.03	0.03	0.03	0.03	0.04	0.04

Appendix Section A4-3

Results of film thickness measurements determined by optical microscopy on sections of print from anilox Pira 1. Measurements are reported in microns.

1736A Pira 1 band 1 75 metres per minute low pressure

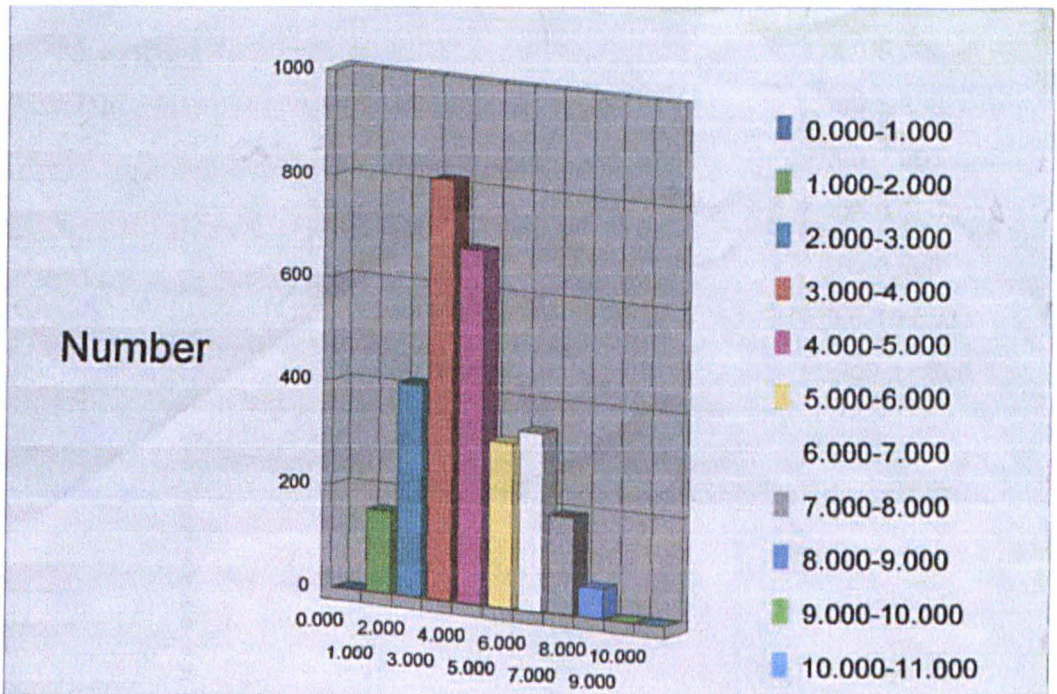

Bin	Lower Limit	Upper Limit	Contents	%
1	0	1	0	0.000
2	1	2	157	5.295
3	2	3	408	13.761
4	3	4	810	27.319
5	4	5	682	23.002
6	5	6	318	10.725
7	6	7	344	11.602
8	7	8	189	6.374
9	8	9	57	1.922
10	9	10	0	0.000
11	10	11	0	0.000

Count	178
Sum	769.7030
Mean	4.3242
Std Dev	18.2373
Std Err	4.2705
2s Range	72.9494
Min	1.0020
Max	8.6840
Median	0.0000
Mode	0.0000
Skewness	-0.4092
Kurtosis	-3.1239

1736(A)

1736B Pira 1 band 1 75 metres per minute medium pressure

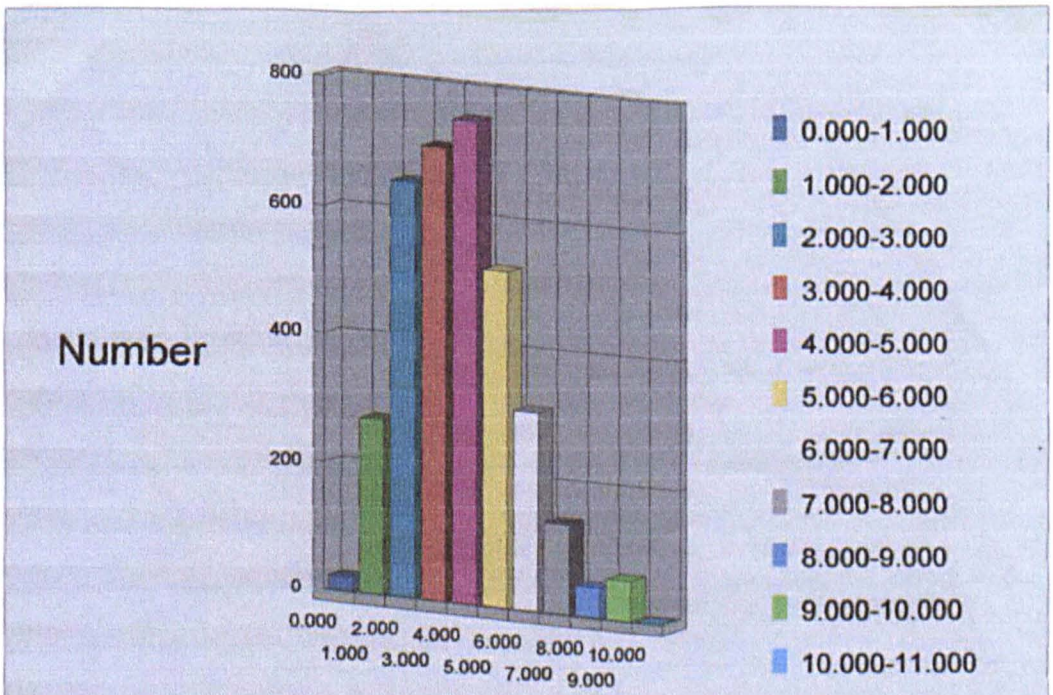

Feret0

Bin	Lower Limit	Upper Limit	Contents	%
1	0	1	23	0.659
2	1	2	272	7.794
3	2	3	650	18.625
4	3	4	708	20.287
5	4	5	753	21.576
6	5	6	524	15.014
7	6	7	309	8.854
8	7	8	141	4.040
9	8	9	47	1.347
10	9	10	63	1.805
11	10	11	0	0.000

Count	205
Sum	828.3200
Mean	4.0406
Std Dev	18.2260
Std Err	4.2692
2s Range	72.9039
Min	0.3340
Max	9.8530
Median	0.0000
Mode	0.0000
Skewness	-0.3549
Kurtosis	-3.1062

1736(B)

1736C Pira 1 band 1 50 metres per minute high pressure

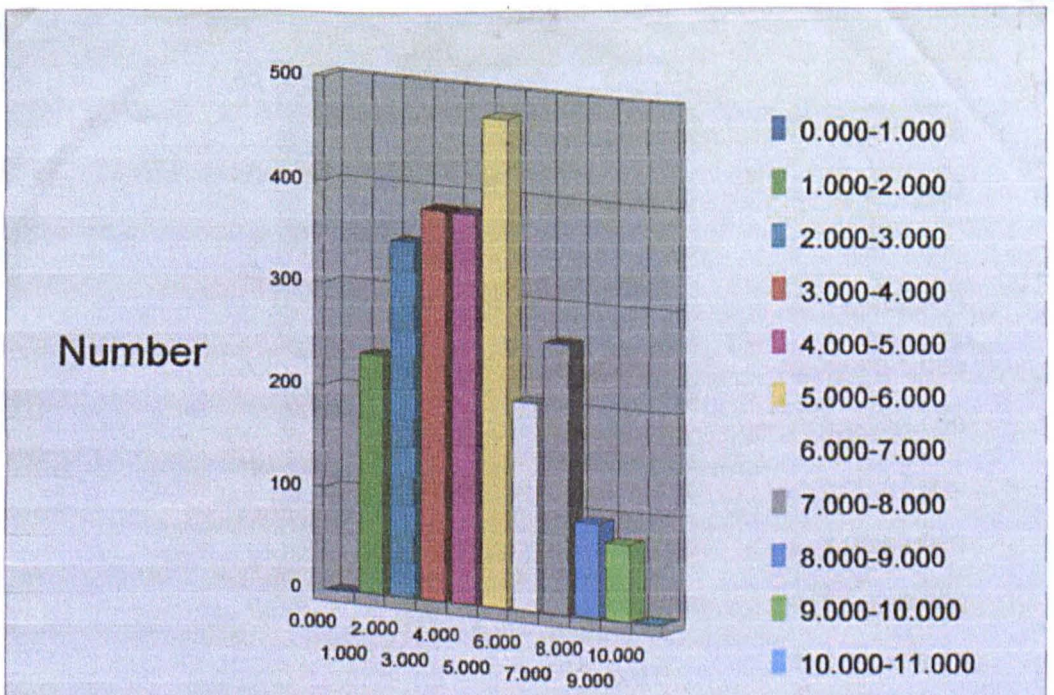

Bin	Lower Limit	Upper Limit	Contents	%
1	0	1	0	0.000
2	1	2	233	9.510
3	2	3	347	14.163
4	3	4	381	15.551
5	4	5	381	15.551
6	5	6	476	19.429
7	6	7	202	8.245
8	7	8	263	10.735
9	8	9	92	3.755
10	9	10	75	3.061
11	10	11	0	0.000

Count	161
Sum	715.0940
Mean	4.4416
Std Dev	19.4962
Std Err	4.4154
2s Range	77.9848
Min	1.0020
Max	9.3520
Median	0.0000
Mode	0.0000
Skewness	-0.3547
Kurtosis	-3.1249

1736C

1736D Pira 1 band 1 50 metres per minute medium pressure

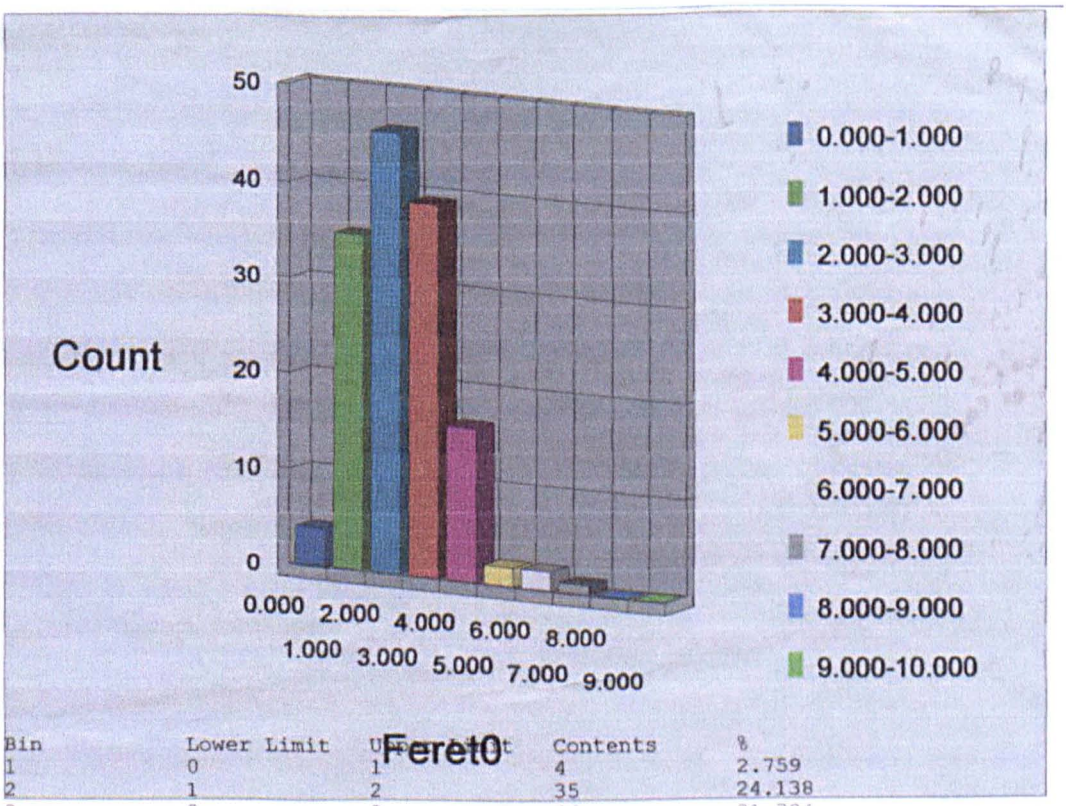

Bin	Lower Limit	Upper Limit	Contents	%
1	0	1	4	2.759
2	1	2	35	24.138
3	2	3	46	31.724
4	3	4	39	26.897
5	4	5	16	11.034
6	5	6	2	1.379
7	6	7	2	1.379
8	7	8	1	0.690
9	8	9	0	0.000
10	9	10	0	0.000

Count	145
Sum	402.6370
Mean	2.7768
Std Dev	1.2057
Std Err	1.0980
2s Range	4.8227
Min	0.6680
Max	7.3480
Median	0.0000
Mode	0.0000
Skewness	0.8602
Kurtosis	-127.1020

1736D

1736E Pira 1 band 1 50 metres per minute low pressure

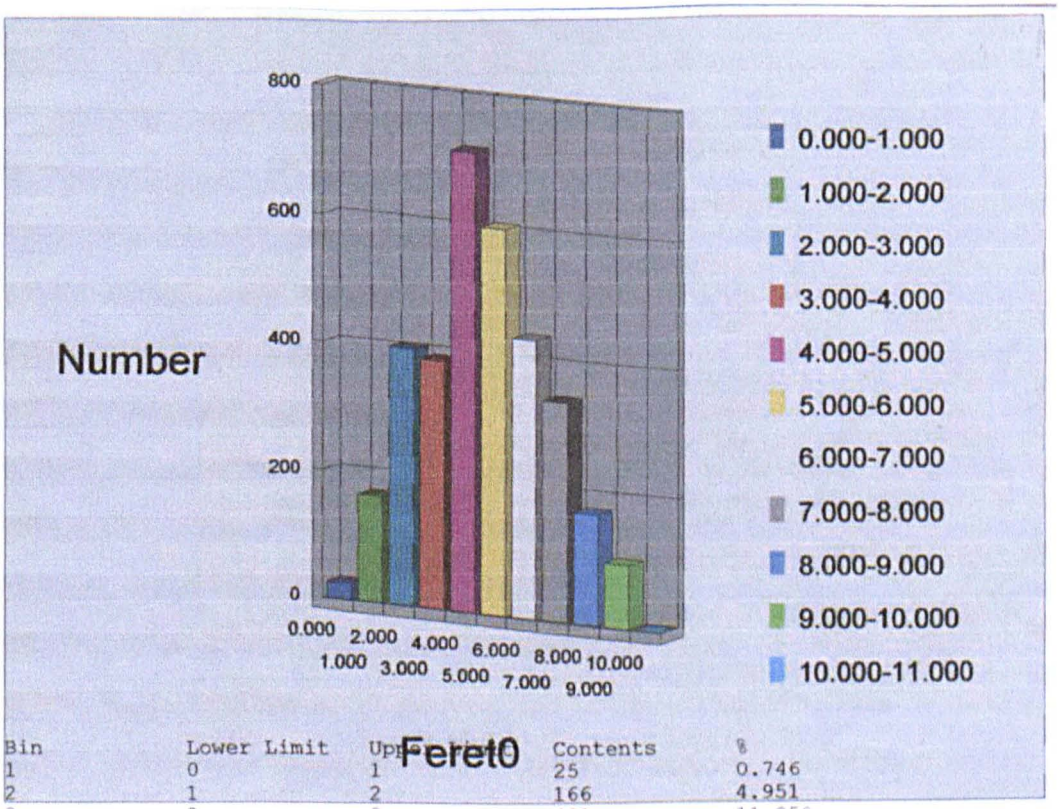

Bin	Lower Limit	Upper Limit	Contents	%
1	0	1	25	0.746
2	1	2	166	4.951
3	2	3	401	11.959
4	3	4	387	11.542
5	4	5	718	21.414
6	5	6	604	18.014
7	6	7	435	12.973
8	7	8	343	10.230
9	8	9	174	5.189
10	9	10	100	2.982
11	10	11	0	0.000

Count	174
Sum	798.5940
Mean	4.5896
Std Dev	23.2008
Std Err	4.8167
2s Range	92.8030
Min	0.3340
Max	9.8530
Median	0.0000
Mode	0.0000
Skewness	-0.3128
Kurtosis	-3.0931

1736E

1736F Pira 1 band 1 25 metres per minute medium pressure

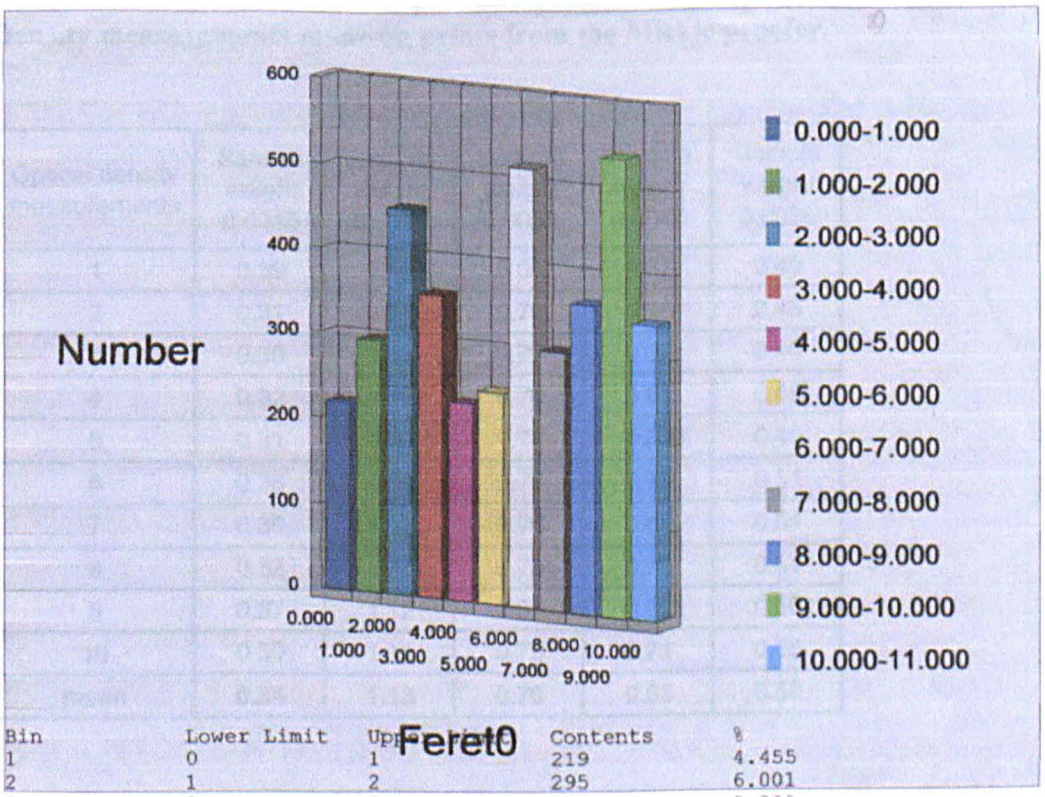

Bin	Lower Limit	Upper Limit	Contents	%
1	0	1	219	4.455
2	1	2	295	6.001
3	2	3	454	9.235
4	3	4	356	7.242
5	4	5	231	4.699
6	5	6	248	5.045
7	6	7	517	10.517
8	7	8	303	6.164
9	8	9	363	7.384
10	9	10	539	10.964
11	10	11	345	7.018

Count	234
Sum	1680.8550
Mean	7.1831
Std Dev	39.2956
Std Err	6.2686
2s Range	157.1823
Min	0.3340
Max	17.5350
Median	0.0000
Mode	0.0000
Skewness	-0.2482
Kurtosis	-3.0990

1736F

Appendix Section A4-4

Density measurements made on prints from the Mickle proofer.

Optical density measurements	Sample weight 0.0015	Sample weight 0.0110	Sample weight 0.0052	Sample weight 0.0045	Sample weight 0.0026
1	0.39	1.12	0.08	0.67	0.49
2	0.31	1.14	0.76	0.63	0.46
3	0.30	1.11	0.72	0.37	0.45
4	0.32	1.15	0.76	0.67	0.49
5	0.31	1.21	0.78	0.68	0.49
6	0.38	1.09	0.78	0.73	0.51
7	0.30	1.13	0.76	0.68	0.51
8	0.32	1.14	0.78	0.70	0.51
9	0.37	1.12	0.83	0.67	0.56
10	0.39	1.11	0.78	0.71	0.55
mean	**0.34**	**1.13**	**0.70**	**0.65**	**0.50**

Appendix A5

Appendix Section A5-1

Repeat of contact angle data for anilox Harper 1, measured using the MAMS instrument and reagent grade water and diiodomethane as the test liquids.

The drop volume reported for each measurement is calculated by the instrument, from the measured height and width of the drop. The drop volume shown in the table headings is the volume dispensed by the pipette.

5µl water drops						
	Polished band		**CO_2 band**		**YAG band**	
Repeat number	**Angle (deg)**	**Volume (µl)**	**Angle (deg)**	**Volume (µl)**	**Angle (deg)**	**Volume (µl)**
1	52.44	4.10	65.86	3.84	76.82	5.07
2	59.65	5.44	66.13	3.55	74.30	4.15
3	51.64	4.11	64.08	4.83	77.67	5.60
4	55.00	4.63	64.10	4.76	70.17	5.74
5	59.89	3.26	63.63	4.73	70.46	5.62
6	59.89	3.26	64.42	5.45	74.90	4.45
7	55.20	3.70	60.13	4.27	77.61	5.71
8	58.00	7.19	61.00	4.90	83.28	4.39
9	56.46	6.67	62.81	4.35	71.68	3.57
10	51.98	7.42	60.77	4.18	71.17	5.05
11	58.77	6.75	62.90	6.56	70.23	5.70
12	50.34	6.35	66.03	5.35	83.89	4.97
13	58.89	4.94	65.38	5.46	76.04	3.63
14	51.40	6.25	63.49	5.27	74.52	4.14
15	55.28	5.18	62.59	4.91	70.41	5.02
16					79.14	4.37
17					74.52	4.14
18					77.91	4.93
19					77.83	4.26
20					76.48	5.16
Mean	**55.7**	**5.3**	**63.6**	**4.8**	**75.5**	**4.8**
Standard Deviation	3.4	1.4	1.9	0.7	4.1	0.7

Appendix Section A5-2

Contact angle data for anilox Harper 2 measured using the MAMS instrument using water and diiodomethane as the test liquids.

The drop volume reported for each measurement is calculated by the instrument, from the measured height and width of the drop. The drop volume shown in the table headings is the volume dispensed by the pipette.

5μl water drops						
	Polished band		CO_2 band		YAG band	
Repeat number	Angle (deg)	Volume (μl)	Angle (deg)	Volume (μl)	Angle (deg)	Volume (μl)
1	59.70	4.46	72.97	4.85	84.49	5.50
2	56.60	6.33	78.29	5.87	83.84	4.27
3	60.25	4.38	78.19	2.76	83.49	4.34
4	57.06	5.96	77.09	5.56	80.46	5.51
5	60.27	6.66	72.37	6.07	81.76	3.91
6	58.64	4.03	74.75	6.42	87.69	4.84
7	60.74	6.78	76.43	9.45	80.65	5.36
8	59.73	6.77	78.17	9.16	83.50	4.86
9	61.47	4.81	74.63	7.35	83.48	8.74
10	58.67	4.67	74.24	7.42	85.11	4.67
11	59.87	3.67	73.85	6.70	81.57	4.44
12	61.21	3.86	72.99	4.28	81.33	6.86
13	60.75	4.58	78.73	3.65	84.15	4.06
14	55.09	3.31	69.92	9.09	81.25	5.38
15	58.27	4.41	76.20	7.64	79.56	7.74
16	61.93	5.00	70.07	4.19	81.44	4.44
17	57.41	4.41	71.90	4.03	83.68	5.15
18	59.24	4.73	73.94	6.03	85.48	5.84
19	59.41	2.99	75.73	4.98	87.23	6.87
20	56.73	4.21	71.93	4.00	83.89	4.63

Appendix Section A5-2 continued

Contact angle data for anilox Harper 2 measured using the MAMS instrument using water and diiodomethane as the test liquids.

The drop volume reported for each measurement is calculated by the instrument, from the measured height and width of the drop. The drop volume shown in the table headings is the volume dispensed by the pipette

5μl water drops						
	Polished band		**CO_2 band**		**YAG band**	
Repeat number	**Angle (deg)**	**Volume (μl)**	**Angle (deg)**	**Volume (μl)**	**Angle (deg)**	**Volume (μl)**
21	59.08	3.60	72.68	4.90	88.30	4.98
22	59.79	5.35	71.08	4.94	89.64	4.51
23	61.72	4.30	76.58	4.72	85.90	4.90
24	54.33	4.27	76.68	4.59	87.57	4.42
25	59.30	4.24	76.67	4.81	86.36	5.37
26	61.98	6.61	69.08	5.19	84.60	5.27
27	55.61	4.82	75.72	4.34	90.31	4.98
28	65.95	4.98	72.58	5.49	84.07	4.24
29	62.62	5.56	76.65	5.18	83.08	5.64
30	59.55	4.81	75.07	4.96	95.30	5.93
31	61.29	6.18	71.94	4.89	93.88	4.84
32	63.30	4.91	70.79	4.31	88.22	4.60
33	60.48	4.21	75.27	5.10	87.16	4.57
34	61.14	5.15	72.01	5.17	87.95	4.94
35	58.23	5.10	78.44	4.09	87.39	3.62
36	61.33	4.58	72.25	5.25	90.32	5.50
37	58.71	4.74	78.94	4.29	94.43	5.05
38	61.67	6.54	76.48	4.08	95.93	4.83
39	60.30	5.14	78.72	4.76	90.60	4.90
40	59.18	5.08	75.99	4.15	92.46	4.83
Mean	**59.7**	**4.9**	**74.7**	**5.4**	**86.2**	**5.1**
Standard Deviation	2.3	1.0	2.8	1.5	4.3	1.0

Appendix Section A5-3

Contact angle measurements using the FTA instrument with water and diiodomethane as the test liquids.

The drop volume reported for each measurement is calculated by the instrument, using the ADSA technique.

water drops						
	Polished band		**CO_2 band**		**YAG band**	
Repeat number	**Angle (deg)**	**Volume (µl)**	**Angle (deg)**	**Volume (µl)**	**Angle (deg)**	**Volume (µl)**
1	76.2	8.8	86.7	8.7	106.6	9.4
2	71.7	9.0	89.3	9.2	103.3	8.2
3	72.2	8.6	88.5	9.0	104.2	9.5
4	74.4	8.6	92.4	9.4	107.3	9.2
5	70.5	8.6	90.1	9.7	103.6	8.2
6	73.8	8.7	90.7	9.3	106.2	9.2
7	73.2	8.9	88.6	9.2	101.9	9.4
8	73.8	9.2	86.5	9.3	103.1	9.5
9	73.4	9.0	95.6	9.5	104.6	9.5
10	69.5	8.7	88.4	8.1	103.8	9.4
11	79.5	8.5	95.8	9.6	102.4	9.7
12	77.3	8.5	93.2	9.7	101.3	10.1
13	70.9	8.1	92.0	9.5	108.3	8.0
14	74.3	8.6	87.5	9.5	101.6	9.0
15	72.1	8.5	93.0	8.2	105.8	7.1
16	73.8	9.1	94.5	9.7	107.4	8.0
17	77.3	8.5	94.0	9.6	107.7	8.9
18	73.7	6.1	92.1	9.5	103.8	7.7
19	77.7	8.4	87.9	9.3	108.1	9.0
20	76.1	8.1	88.9	9.6	108.9	8.7
Mean	**74.1**	**8.5**	**90.8**	**9.3**	**105.0**	**8.9**
Standard Deviation	2.6	0.6	2.9	0.5	2.4	0.8

Appendix Section A5-3 Continued

Contact angle measurements using the FTA instrument with water and diiodomethane as the test liquids.

The drop volume reported for each measurement is calculated by the instrument, using the ADSA technique.

diiodamethane drops						
	Polished band		**CO_2 band**		**YAG band**	
Repeat number	**Angle (deg)**	**Volume (µl)**	**Angle (deg)**	**Volume (µl)**	**Angle (deg)**	**Volume (µl)**
1	44.7	1.9	45.5	2.0	44.8	1.6
2	43.1	1.8	42.3	1.8	44.7	1.8
3	44.2	1.9	45.9	1.9	40.1	1.8
4	44.7	1.8	43.6	1.8	47.1	1.8
5	42.3	1.8	40.5	1.5	45.2	1.8
6	46.8	1.9	44.6	1.7	43.9	1.8
7	44.3	1.8	42.1	1.8	39.2	1.9
8	41.5	1.8	44.0	1.7	42.7	1.4
9	43.6	1.8	40.1	1.8	42.1	1.8
10	42.6	1.7	42.2	1.6	43.1	1.9
Mean	**43.8**	**1.8**	**43.1**	**1.8**	**43.3**	**1.8**
Standard Deviation	1.5	0.1	2.0	0.1	2.4	0.2

Appendix Section A5-4

Advancing and receding contact angle measurements using the FTA instrument with water as the test liquid.

	Polished band	CO_2 band	YAG band
Repeat number	Angle (deg)	Angle (deg)	Angle (deg)
1	92	99	110
2	94	100	104
3		98	
4		101	
5		100	
Mean	**93.0**	**99.5**	**107.0**
Standard Deviation	1.4	1.1	4.2

Appendix Section A5-5

Contact angle measurements using the FTA instrument with formamide as the test liquid.

The drop volume reported for each measurement is calculated by the instrument, using the ADSA technique.

Formamide drops						
	Polished band		CO_2 band		YAG band	
Repeat number	Angle (deg)	Volume (μl)	Angle (deg)	Volume (μl)	Angle (deg)	Volume (μl)
1	44.0	6.0	60.0	5.1	65.5	6.7
2	40.9	6.2	59.3	6.8	64.5	5.7
3	39.6	6.3	59.7	6.3	63.8	6.6
4	47.3	6.2	61.6	7.5	64.0	6.9
5	42.1	4.4	62.0	6.4	66.3	7.1
6	43.8	5.4	62.8	7.2	63.6	6.7
7	39.9	7.2	61.9	7.0	60.9	5.9
8	43.1	6.9	60.8	7.9	65.3	5.0
9	40.8	7.0	60.7	6.5	66.7	6.7
10	46.6	6.1	61.8	7.5	68.8	6.7
Mean	**42.8**	**6.2**	**61.1**	**6.8**	**64.9**	**6.4**
Standard Deviation	2.7	0.8	1.1	0.8	2.1	0.7

Appendix Section A5-6

Density measurements made on the prints from the RK mini web press using anilox Harper 2 and Arena process cyan (UV ink from Coates Lorilleux).

Measurement position		Sample number									
		A1 CO2	A2 CO2	A3 CO2	A4 CO2	A5 CO2	A6 CO2	A7 CO2	A8 C02	A9 C02	A10 CO2
EDGE		0.52	0.49	0.53	0.54	0.57	0.44	0.43	0.57	0.51	0.56
		0.54	0.51	0.56	0.54	0.48	0.50	0.45	0.53	0.55	0.53
		0.55	0.53	0.59	0.56	0.50	0.49	0.45	0.46	0.50	0.56
		0.55	0.54	0.52	0.56	0.51	0.52	0.44	0.52	0.50	0.54
		0.51	0.56	0.51	0.55	0.54	0.50	0.42	0.54	0.53	0.55
	mean	**0.53**	**0.53**	**0.54**	**0.55**	**0.52**	**0.49**	**0.44**	**0.52**	**0.52**	**0.55**
	std dev	**0.02**	**0.03**	**0.03**	**0.01**	**0.04**	**0.03**	**0.01**	**0.04**	**0.02**	**0.01**
MID 1		0.46	0.43	0.49	0.45	0.40	0.39	0.38	0.39	0.45	0.50
		0.44	0.47	0.49	0.48	0.43	0.43	0.38	0.43	0.42	0.48
		0.45	0.46	0.51	0.43	0.47	0.42	0.33	0.45	0.39	0.50
		0.50	0.51	0.49	0.47	0.45	0.41	0.37	0.42	0.42	0.46
		0.49	0.47	0.49	0.44	0.47	0.41	0.33	0.42	0.37	0.44
	mean	**0.47**	**0.47**	**0.49**	**0.45**	**0.44**	**0.41**	**0.36**	**0.42**	**0.41**	**0.48**
	Std dev	**0.03**	**0.03**	**0.01**	**0.02**	**0.03**	**0.01**	**0.03**	**0.02**	**0.03**	**0.03**
CENTRE		0.40	0.41	0.43	0.39	0.33	0.30	0.30	0.33	0.34	0.46
		0.44	0.39	0.40	0.36	0.34	0.31	0.29	0.31	0.33	0.41
		0.41	0.44	0.45	0.35	0.35	0.33	0.31	0.30	0.32	0.42
		0.42	0.41	0.43	0.37	0.34	0.35	0.29	0.30	0.30	0.40
		0.45	0.42	0.39	0.35	0.34	0.32	0.34	0.31	0.33	0.44
	mean	**0.42**	**0.41**	**0.42**	**0.36**	**0.34**	**0.32**	**0.31**	**0.31**	**0.32**	**0.43**
	std dev	**0.02**	**0.02**	**0.02**	**0.02**	**0.01**	**0.02**	**0.02**	**0.01**	**0.02**	**0.02**
MID 2		0.42	0.42	0.40	0.32	0.30	0.32	0.33	0.30	0.32	0.42
		0.41	0.40	0.41	0.33	0.33	0.33	0.29	0.31	0.32	0.46
		0.44	0.42	0.41	0.34	0.31	0.35	0.28	0.29	0.32	0.44
		0.43	0.39	0.44	0.34	0.33	0.34	0.28	0.29	0.30	0.43
		0.40	0.39	0.44	0.34	0.32	0.33	0.29	0.31	0.30	0.40
	mean	**0.42**	**0.40**	**0.42**	**0.33**	**0.32**	**0.33**	**0.29**	**0.30**	**0.31**	**0.43**
	std dev	**0.02**	**0.02**	**0.02**	**0.01**	**0.01**	**0.01**	**0.02**	**0.01**	**0.01**	**0.02**
JOIN		0.42	0.39	0.43	0.33	0.32	0.31	0.26	0.27	0.29	0.43
		0.40	0.40	0.45	0.34	0.32	0.32	0.30	0.31	0.30	0.40
		0.42	0.39	0.44	0.36	0.35	0.34	0.39	0.31	0.38	0.46
		0.46	0.43	0.42	0.38	0.34	0.34	0.27	0.32	0.35	0.43
		0.44	0.43	0.42	0.34	0.33	0.29	0.31	0.32	0.36	0.42
	mean	**0.43**	**0.41**	**0.43**	**0.35**	**0.33**	**0.32**	**0.31**	**0.31**	**0.34**	**0.43**
	std dev	**0.02**	**0.02**	**0.01**	**0.02**	**0.01**	**0.02**	**0.05**	**0.02**	**0.04**	**0.02**
Combined mean		**0.40**	**0.39**	**0.41**	**0.36**	**0.35**	**0.33**	**0.30**	**0.33**	**0.34**	**0.41**
Combined standard deviation		**0.15**	**0.15**	**0.15**	**0.15**	**0.15**	**0.14**	**0.12**	**0.15**	**0.14**	**0.15**

Appendix Section A5-6 continued

Density measurements made on the prints from the RK mini web press using anilox Harper 2 and Arena process cyan (UV ink from Coates Lorilleux).

Measurement position		Sample number									
		A1 YAG	A2 YAG	A3 YAG	A4 YAG	A5 YAG	A6 YAG	A7 YAG	A8 YAG	A9 YAG	A10 YAG
EDGE		0.65	0.61	0.59	0.54	0.53	0.51	0.53	0.53	0.61	0.59
		0.60	0.63	0.59	0.57	0.51	0.51	0.54	0.53	0.61	0.62
		0.63	0.62	0.61	0.51	0.57	0.50	0.49	0.57	0.59	0.64
		0.68	0.60	0.59	0.53	0.54	0.49	0.49	0.56	0.55	0.61
		0.63	0.60	0.61	0.58	0.52	0.52	0.49	0.51	0.57	0.59
	mean	0.64	0.61	0.60	0.55	0.53	0.51	0.51	0.54	0.59	0.61
	std dev	0.03	0.01	0.01	0.03	0.02	0.01	0.02	0.02	0.03	0.02
MID 1		0.57	0.52	0.54	0.50	0.45	0.44	0.47	0.41	0.50	0.54
		0.59	0.55	0.53	0.47	0.46	0.43	0.45	0.46	0.58	0.51
		0.55	0.54	0.51	0.46	0.51	0.44	0.45	0.42	0.51	0.56
		0.54	0.54	0.55	0.49	0.45	0.40	0.42	0.42	0.50	0.55
		0.55	0.57	0.58	0.47	0.50	0.43	0.40	0.40	0.49	0.60
	mean	0.56	0.54	0.54	0.48	0.47	0.43	0.44	0.42	0.52	0.55
	Std dev	0.02	0.02	0.03	0.02	0.03	0.02	0.03	0.02	0.04	0.03
CENTRE		0.44	0.50	0.46	0.42	0.42	0.39	0.39	0.41	0.46	0.50
		0.44	0.46	0.49	0.44	0.46	0.38	0.37	0.38	0.47	0.51
		0.49	0.54	0.50	0.46	0.43	0.42	0.37	0.37	0.41	0.56
		0.52	0.49	0.53	0.41	0.40	0.39	0.39	0.37	0.45	0.50
		0.50	0.51	0.49	0.42	0.39	0.39	0.38	0.36	0.45	0.48
	mean	0.48	0.50	0.49	0.43	0.42	0.39	0.38	0.38	0.45	0.51
	std dev	0.04	0.03	0.03	0.02	0.03	0.02	0.01	0.02	0.02	0.03
MID 2		0.45	0.49	0.48	0.44	0.43	0.37	0.37	0.38	0.44	0.47
		0.48	0.48	0.47	0.41	0.40	0.35	0.36	0.34	0.44	0.45
		0.49	0.50	0.48	0.41	0.39	0.36	0.34	0.40	0.46	0.46
		0.46	0.46	0.48	0.40	0.38	0.36	0.33	0.37	0.44	0.48
		0.44	0.47	0.48	0.41	0.41	0.36	0.36	0.34	0.40	0.47
	mean	0.46	0.48	0.48	0.41	0.40	0.36	0.35	0.37	0.44	0.47
	std dev	0.02	0.02	0.00	0.02	0.02	0.01	0.02	0.03	0.02	0.01
JOIN		0.47	0.47	0.47	0.41	0.38	0.35	0.31	0.33	0.39	0.48
		0.45	0.47	0.45	0.38	0.40	0.33	0.37	0.34	0.39	0.46
		0.44	0.48	0.44	0.39	0.37	0.34	0.29	0.33	0.39	0.49
		0.47	0.49	0.43	0.39	0.37	0.35	0.31	0.37	0.38	0.45
		0.48	0.45	0.44	0.40	0.39	0.37	0.30	0.33	0.39	0.50
	mean	0.46	0.47	0.45	0.39	0.38	0.35	0.32	0.34	0.39	0.48
	std dev	0.02	0.01	0.02	0.01	0.01	0.01	0.03	0.02	0.00	0.02
Combined mean		0.46	0.46	0.45	0.40	0.39	0.36	0.36	0.36	0.42	0.46
Combined standard deviation		0.18	0.17	0.17	0.15	0.15	0.14	0.14	0.15	0.16	0.17

Appendix Section A5-6 continued

Density measurements made on the prints from the RK mini web press using anilox Harper 2 and Arena process cyan (UV ink from Coates Lorilleux).

Measurement position		Sample number									
		B1 CO2	B2 CO2	B3 CO2	B4 CO2	B5 CO2	B6 CO2	B7 CO2	B8 CO2	B9 CO2	B10 CO2
EDGE		0.45	0.47	0.44	0.49	0.46	0.47	0.50	0.48	0.43	0.46
		0.46	0.52	0.45	0.49	0.44	0.47	0.46	0.48	0.46	0.48
		0.51	0.47	0.46	0.46	0.44	0.49	0.48	0.47	0.46	0.43
		0.46	0.44	0.49	0.50	0.46	0.45	0.49	0.49	0.46	0.47
		0.49	0.48	0.52	0.47	0.46	0.48	0.47	0.49	0.48	0.49
	mean	**0.47**	**0.48**	**0.47**	**0.48**	**0.45**	**0.47**	**0.48**	**0.48**	**0.46**	**0.47**
	std dev	**0.03**	**0.03**	**0.03**	**0.02**	**0.01**	**0.01**	**0.02**	**0.01**	**0.02**	**0.02**
MID 1		0.44	0.41	0.38	0.40	0.42	0.42	0.41	0.44	0.42	0.41
		0.40	0.40	0.39	0.42	0.43	0.43	0.46	0.42	0.42	0.39
		0.41	0.45	0.43	0.46	0.43	0.42	0.44	0.44	0.44	0.43
		0.43	0.41	0.44	0.44	0.43	0.42	0.42	0.46	0.42	0.44
		0.44	0.42	0.42	0.42	0.45	0.43	0.46	0.47	0.42	0.41
	mean	**0.42**	**0.42**	**0.41**	**0.43**	**0.43**	**0.42**	**0.44**	**0.45**	**0.42**	**0.42**
	Std dev	**0.02**	**0.02**	**0.03**	**0.02**	**0.01**	**0.01**	**0.02**	**0.02**	**0.01**	**0.02**
CENTRE		0.35	0.33	0.32	0.33	0.32	0.33	0.34	0.35	0.30	0.34
		0.34	0.36	0.35	0.35	0.33	0.35	0.32	0.34	0.31	0.33
		0.37	0.38	0.33	0.36	0.33	0.33	0.37	0.36	0.34	0.35
		0.36	0.38	0.39	0.38	0.36	0.38	0.40	0.37	0.35	0.36
		0.33	0.38	0.36	0.37	0.40	0.41	0.37	0.37	0.35	0.36
	mean	**0.35**	**0.37**	**0.35**	**0.36**	**0.35**	**0.36**	**0.36**	**0.36**	**0.33**	**0.35**
	std dev	**0.02**	**0.02**	**0.03**	**0.02**	**0.03**	**0.03**	**0.03**	**0.01**	**0.02**	**0.01**
MID 2		0.32	0.34	0.32	0.34	0.36	0.32	0.32	0.31	0.31	0.35
		0.33	0.34	0.34	0.34	0.34	0.33	0.31	0.31	0.31	0.32
		0.34	0.36	0.30	0.32	0.35	0.33	0.35	0.34	0.29	0.40
		0.33	0.35	0.36	0.35	0.37	0.35	0.35	0.33	0.36	0.35
		0.32	0.37	0.32	0.33	0.34	0.39	0.33	0.32	0.32	0.39
	mean	**0.33**	**0.35**	**0.33**	**0.34**	**0.35**	**0.34**	**0.33**	**0.32**	**0.32**	**0.36**
	std dev	**0.01**	**0.01**	**0.02**	**0.01**	**0.01**	**0.03**	**0.02**	**0.01**	**0.03**	**0.03**
JOIN		0.29	0.29	0.33	0.30	0.31	0.31	0.31	0.30	0.34	0.33
		0.29	0.33	0.33	0.29	0.37	0.32	0.33	0.31	0.29	0.34
		0.29	0.35	0.36	0.32	0.35	0.34	0.33	0.30	0.35	0.35
		0.34	0.34	0.34	0.34	0.34	0.38	0.34	0.31	0.35	0.39
		0.33	0.37	0.36	0.33	0.36	0.36	0.33	0.31	0.31	0.36
	mean	**0.31**	**0.34**	**0.34**	**0.32**	**0.35**	**0.34**	**0.33**	**0.31**	**0.33**	**0.35**
	std dev	**0.02**	**0.03**	**0.02**	**0.02**	**0.02**	**0.03**	**0.01**	**0.01**	**0.03**	**0.02**
Combined mean		**0.34**	**0.35**	**0.34**	**0.34**	**0.34**	**0.35**	**0.35**	**0.34**	**0.33**	**0.35**
Combined standard deviation		**0.13**	**0.13**	**0.13**	**0.14**	**0.13**	**0.13**	**0.14**	**0.14**	**0.13**	**0.13**

Appendix Section A5-6 continued

Density measurements made on the prints from the RK mini web press using anilox Harper 2 and Arena process cyan (UV ink from Coates Lorilleux).

Measurement position		Sample number									
		B1 YAG	B2 YAG	B3 YAG	B4 YAG	B5 YAG	B6 YAG	B7 YAG	B8 YAG	B9 YAG	B10 YAG
EDGE		0.49	0.52	0.47	0.47	0.50	0.48	0.49	0.48	0.51	0.50
		0.49	0.47	0.49	0.51	0.47	0.50	0.48	0.49	0.46	0.52
		0.46	0.46	0.50	0.54	0.48	0.50	0.47	0.50	0.49	0.51
		0.45	0.51	0.47	0.49	0.47	0.50	0.50	0.49	0.48	0.54
		0.49	0.50	0.51	0.51	0.53	0.53	0.50	0.52	0.47	0.56
	mean	0.48	0.49	0.49	0.50	0.49	0.50	0.49	0.50	0.48	0.53
	std dev	0.02	0.03	0.02	0.03	0.03	0.02	0.01	0.02	0.02	0.02
MID 1		0.41	0.41	0.43	0.44	0.47	0.43	0.42	0.39	0.39	0.44
		0.44	0.42	0.43	0.44	0.47	0.41	0.48	0.45	0.40	0.45
		0.47	0.40	0.45	0.43	0.49	0.41	0.46	0.43	0.42	0.46
		0.40	0.42	0.40	0.48	0.47	0.43	0.43	0.42	0.43	0.45
		0.39	0.46	0.45	0.48	0.49	0.47	0.48	0.43	0.41	0.46
	mean	0.42	0.42	0.43	0.45	0.48	0.43	0.45	0.42	0.41	0.45
	Std dev	0.03	0.02	0.02	0.02	0.01	0.02	0.03	0.02	0.02	0.01
CENTRE		0.38	0.38	0.38	0.40	0.39	0.41	0.39	0.38	0.38	0.38
		0.38	0.38	0.38	0.41	0.39	0.41	0.38	0.36	0.35	0.43
		0.42	0.40	0.38	0.40	0.46	0.42	0.37	0.42	0.41	0.41
		0.45	0.38	0.42	0.45	0.42	0.40	0.41	0.40	0.37	0.43
		0.42	0.40	0.42	0.38	0.42	0.39	0.42	0.40	0.41	0.41
	mean	0.41	0.39	0.40	0.41	0.42	0.41	0.39	0.39	0.38	0.41
	std dev	0.03	0.01	0.02	0.03	0.03	0.01	0.02	0.02	0.03	0.02
MID 2		0.38	0.38	0.38	0.33	0.41	0.37	0.36	0.39	0.36	0.39
		0.37	0.43	0.40	0.37	0.38	0.39	0.39	0.37	0.40	0.37
		0.43	0.36	0.39	0.34	0.39	0.40	0.37	0.37	0.41	0.37
		0.39	0.40	0.39	0.45	0.35	0.38	0.43	0.38	0.36	0.42
		0.41	0.42	0.42	0.41	0.41	0.42	0.37	0.40	0.42	0.38
	mean	0.40	0.40	0.40	0.38	0.39	0.39	0.38	0.38	0.39	0.39
	std dev	0.02	0.03	0.02	0.05	0.02	0.02	0.03	0.01	0.03	0.02
JOIN		0.36	0.38	0.34	0.35	0.36	0.37	0.32	0.36	0.34	0.32
		0.36	0.36	0.38	0.36	0.36	0.34	0.36	0.34	0.38	0.36
		0.36	0.37	0.38	0.34	0.35	0.35	0.36	0.33	0.35	0.36
		0.38	0.37	0.35	0.35	0.39	0.36	0.38	0.35	0.36	0.37
		0.38	0.37	0.39	0.38	0.41	0.36	0.41	0.39	0.38	0.39
	mean	0.37	0.37	0.37	0.36	0.37	0.36	0.37	0.35	0.36	0.36
	std dev	0.01	0.01	0.02	0.02	0.03	0.01	0.03	0.02	0.02	0.03
Combined mean		0.37	0.37	0.37	0.38	0.38	0.37	0.37	0.36	0.36	0.38
Combined standard deviation		0.13	0.14	0.14	0.14	0.14	0.14	0.14	0.14	0.13	0.15

Appendix Section A5-7

Contact angle measurements on uncoated paper using the FTA instrument with water, diiodomethane and formamide as the test liquids.

	Water drops		Diiodamethane drops		Formamide drops	
Repeat number	Angle (deg)	Volume (μl)	Angle (deg)	Volume (μl)	Angle (deg)	Volume (μl)
1	106.6	8.5	48.9	2.9	98.3	7.9
2	107.2	8.8	44.8	3.0	98.0	8.3
3	102.8	8.6	47.2	2.4	97.2	8.4
4	102.3	8.3	44.6	2.5	98.0	8.3
5	110.0	8.9	48.4	2.7	92.1	8.0
6	105.1	9.1	50.6	2.6	95.0	7.9
7	109.4	9.3	54.0	2.9	89.2	7.8
8	108.5	8.6	51.2	2.9	97.3	8.1
9	100.7	7.9	55.3	2.8	97.7	8.1
10	107.5	8.5	49.4	2.6	98.4	8.2
11	107.1	8.7	52.4	2.9		
12	105.0	8.4	49.9	2.6		
13	108.1	8.5	55.4	2.9		
14	108.5	8.7	47.3	3.0		
15	105.9	8.3	46.2	2.6		
16	103.7	8.2	49.4	2.7		
17	105.0	8.1	49.6	2.5		
18	102.6	7.7	45.1	2.6		
19	104.6	8.8	46.6	2.5		
20	108.6	9.4	49.3	2.6		
Mean	**42.8**	**6.2**	**61.1**	**6.8**	**64.9**	**6.4**
Standard Deviation	2.7	0.8	1.1	0.8	2.1	0.7

Appendix Section A5-8

Contact angle measurements on anilox Harper 2 after cleaning had taken place. Measurements were made using the FTA instrument with water and diiodomethane as the test liquids.

post clean contact angles

5μl water drops						
run number	polished band		CO_2 band		YAG band	
	contact angle (degrees)	drop volume (μl)	contact angle (degrees)	drop volume (μl)	contact angle (degrees)	drop volume (μl)
1	72.8	4.9	92.5	4.3	80.4	4.9
2	73.0	4.7	94.2	5.0	85.1	4.8
3	75.3	4.7	90.7	4.6	79.3	5.1
4	71.1	4.5	92.9	4.7	84.6	4.9
5	70.4	4.6	95.0	4.8	80.1	4.3
6	71.9	4.2	92.1	4.6	83.7	4.5
7	74.9	4.8	92.7	4.4	78.2	4.6
8	75.6	5.1	91.8	4.5	82.6	4.5
9	74.0	4.2	95.8	4.9	85.5	4.5
10	72.6	4.4	94.1	4.7	84.0	4.6
Mean	**73.2**	**4.6**	**93.2**	**4.7**	**82.4**	**4.7**
Standard deviation	1.8	0.3	1.6	0.2	2.6	0.2

5μl diiodomethane drops						
run number	polished band		CO_2 band		YAG band	
	contact angle (degrees)	drop volume (μl)	contact angle (degrees)	drop volume (μl)	contact angle (degrees)	drop volume (μl)
1	40.0	4.7	42.5	4.5	43.1	4.7
2	41.2	4.5	44.3	4.5	42.1	4.7
3	43.8	4.6	45.3	4.9	40.8	4.5
4	41.9	4.3	42.8	4.4	41.4	4.3
5	43.4	4.5	44.2	4.4	43.7	4.8
Mean	**42.1**	**4.5**	**43.8**	**4.5**	**42.2**	**4.6**
Standard deviation	1.6	0.1	1.2	0.2	1.2	0.2

Appendix A6

Appendix Section A6-1

Cell profiles of the CO_2 and YAG cells on anilox Harper 1, Measured using the Veeco interferometer.

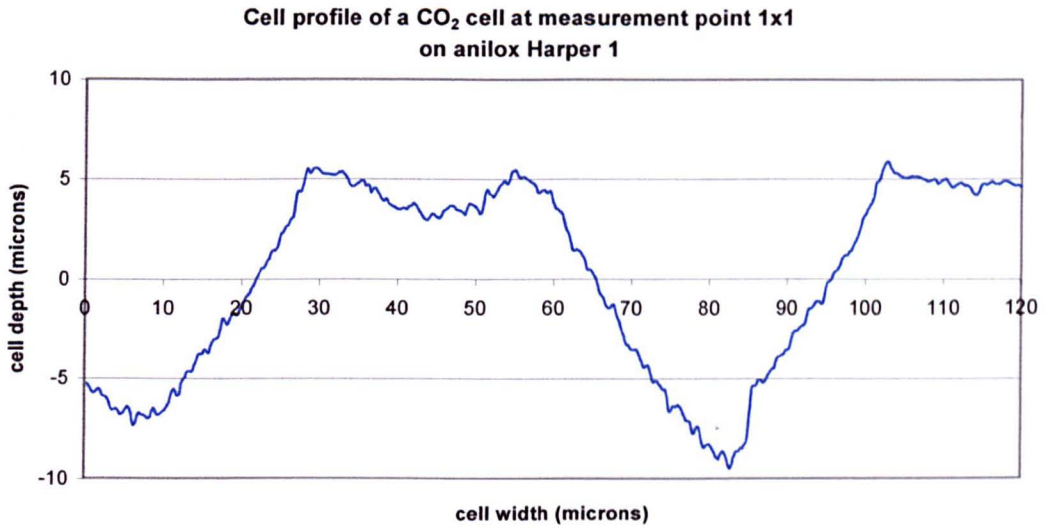

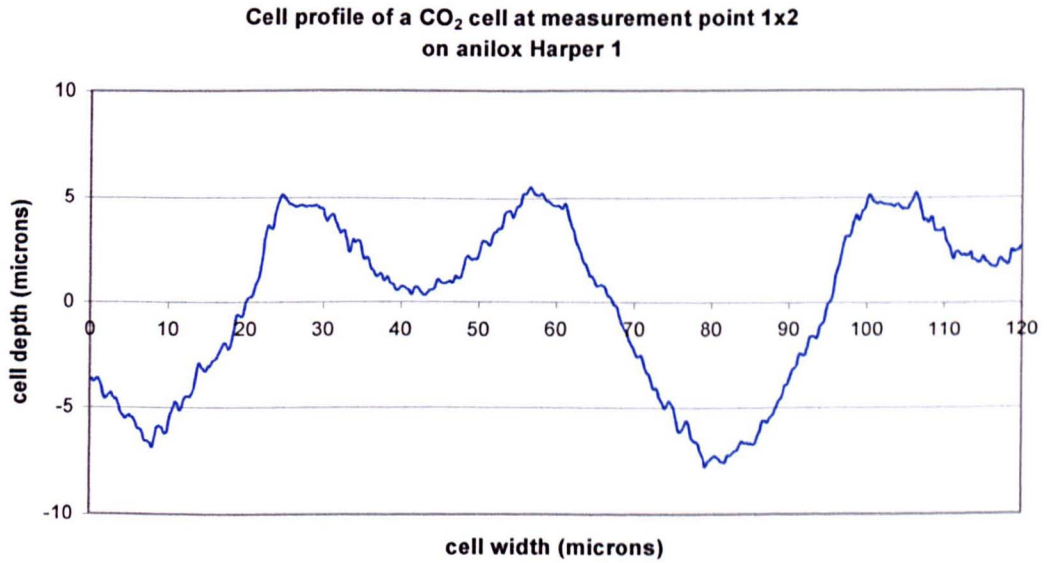

Appendix Section A6-1 continued

Cell profiles of the CO_2 and YAG cells on anilox Harper 1, Measured using the Veeco interferometer.

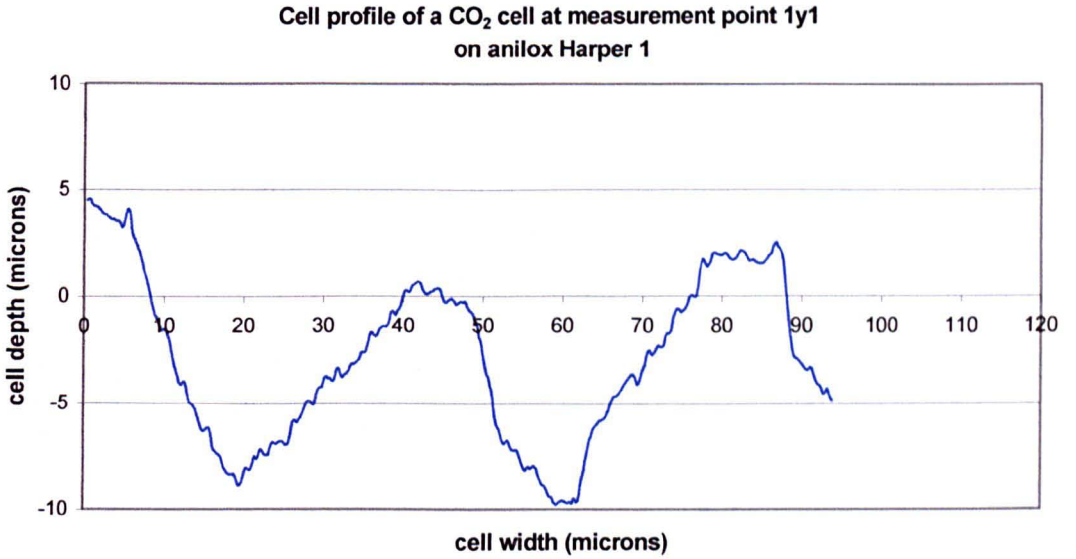

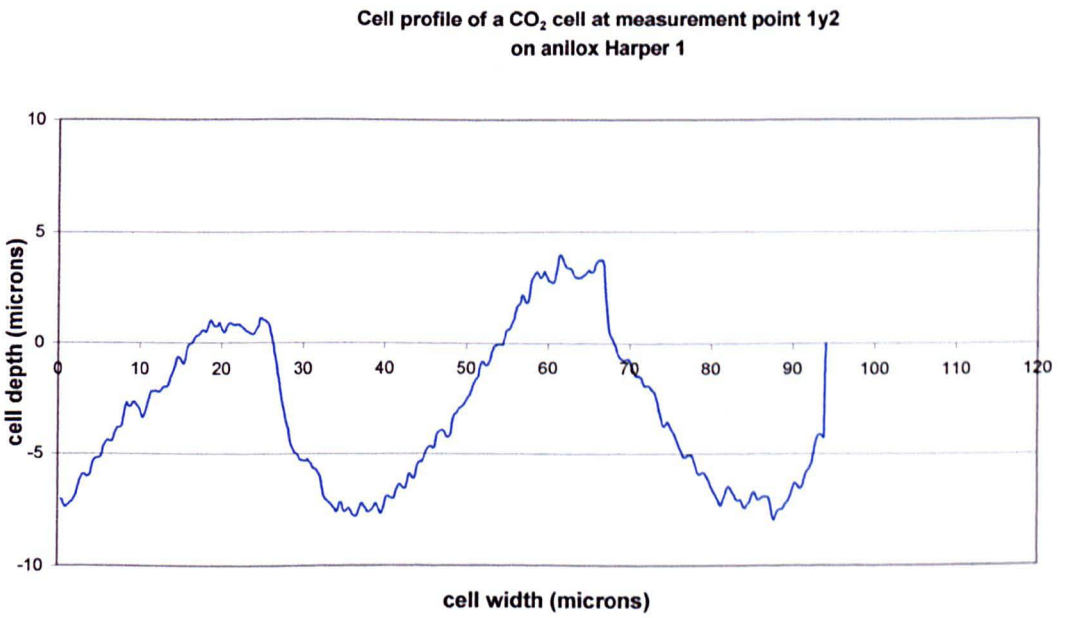

Appendix Section A6-1 continued

Cell profiles of the CO_2 and YAG cells on anilox Harper 1, Measured using the Veeco interferometer.

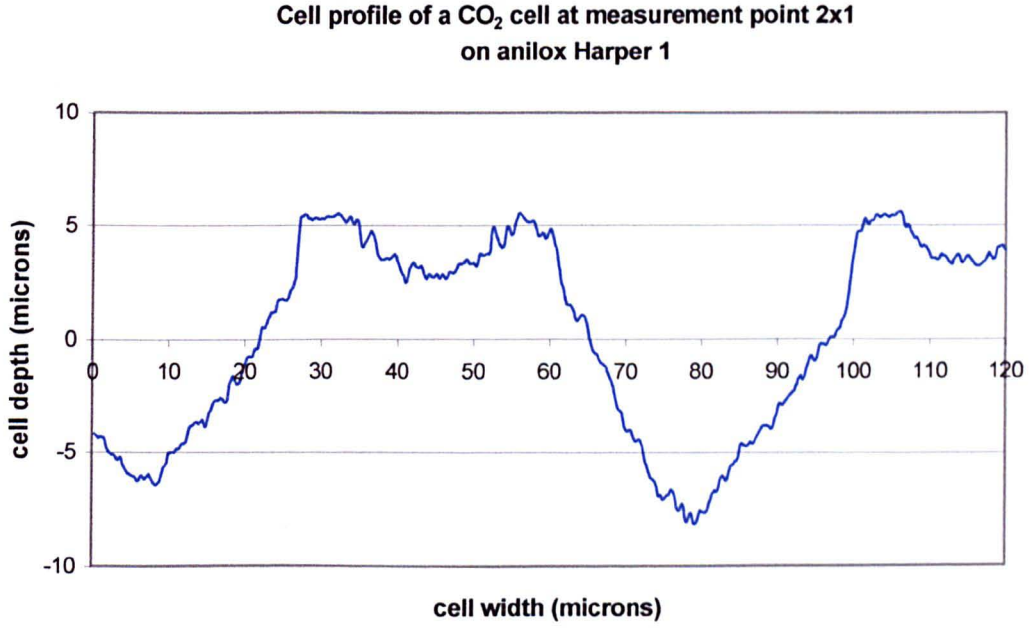

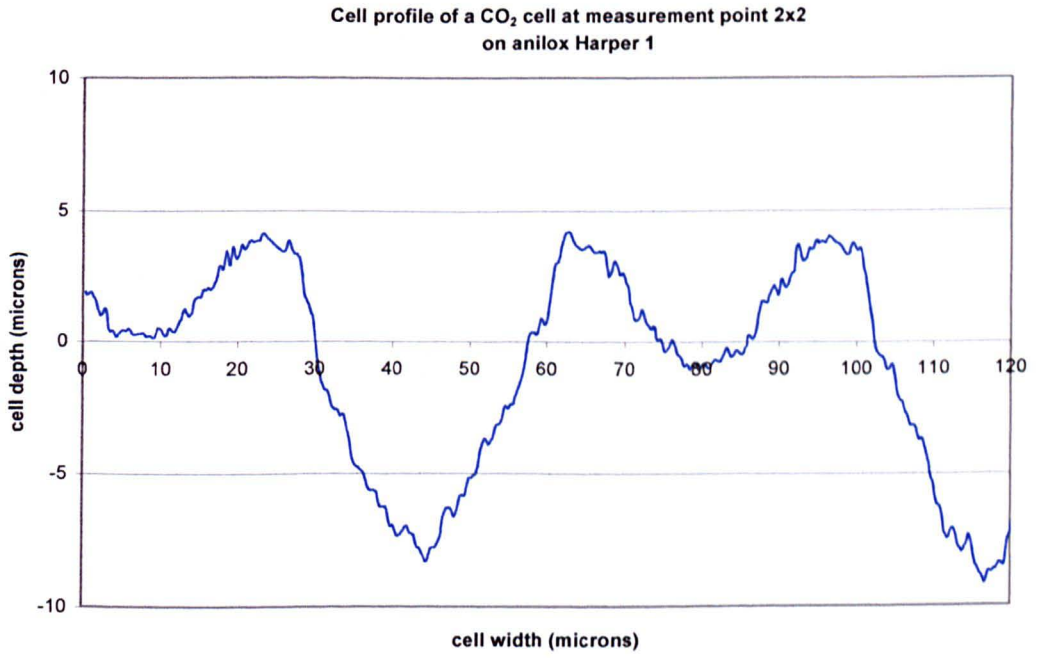

Appendix Section A6-1 continued

Cell profiles of the CO_2 and YAG cells on anilox Harper 1, Measured using the Veeco interferometer.

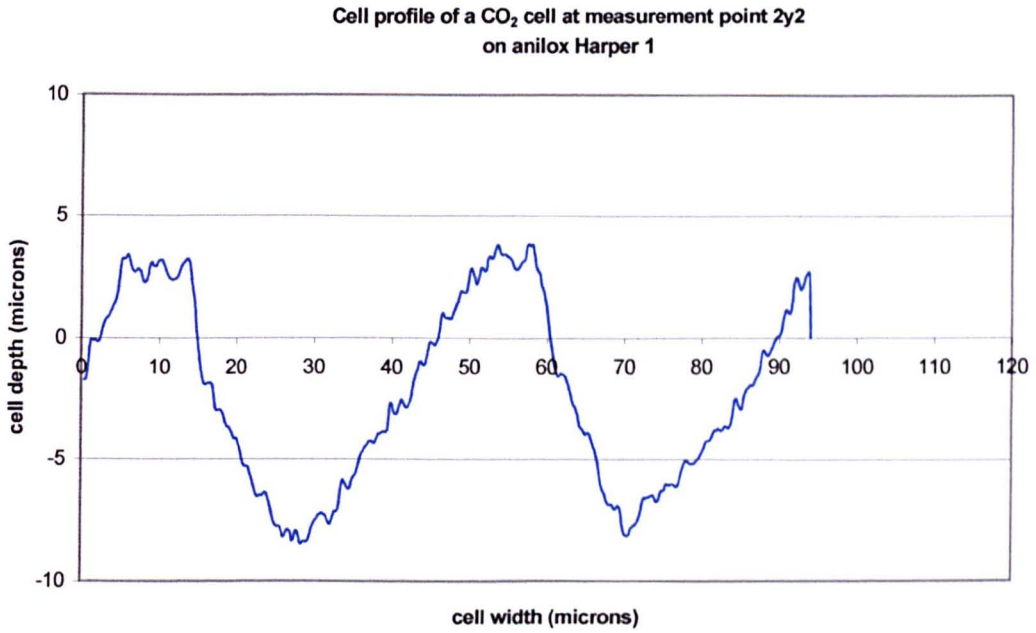

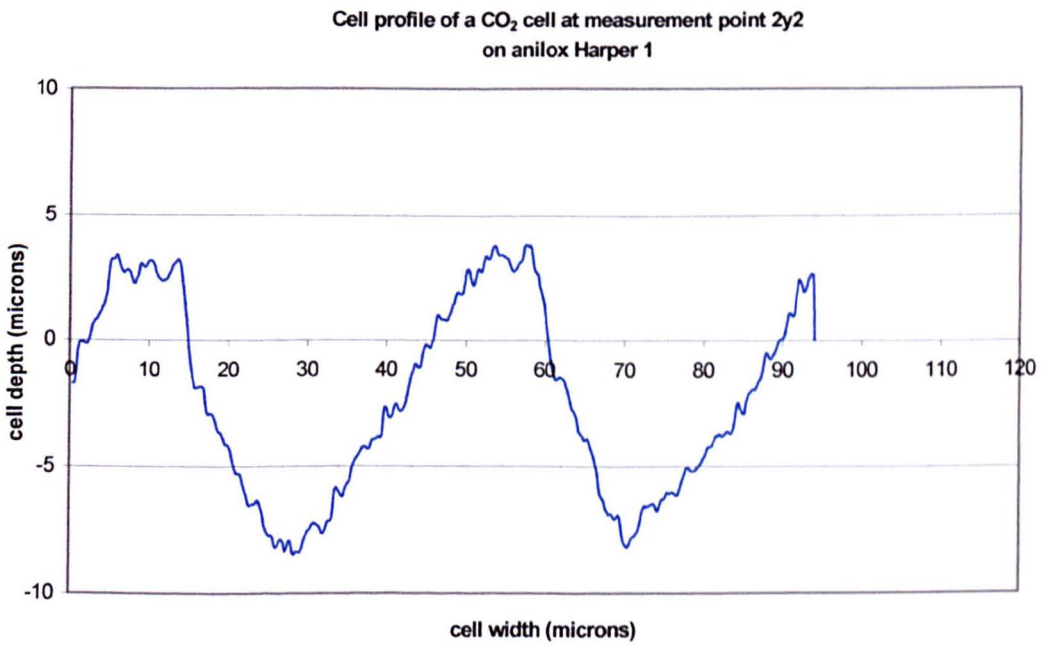

Appendix Section A6-1 continued

Cell profiles of the CO_2 and YAG cells on anilox Harper 1, Measured using the Veeco interferometer.

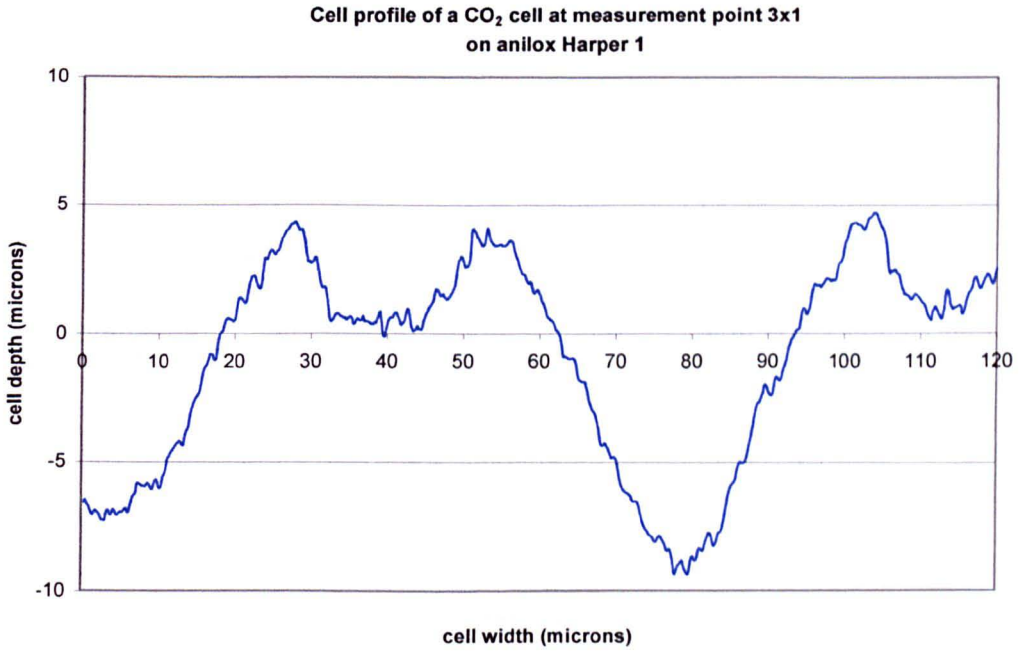

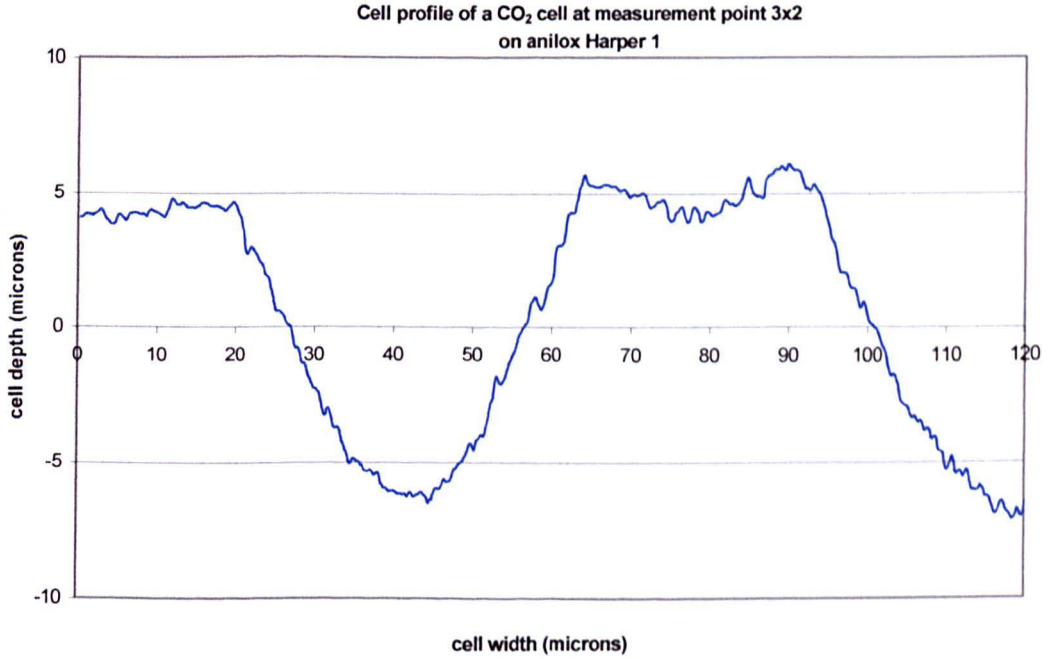

Appendix Section A6-1 continued

Cell profiles of the CO_2 and YAG cells on anilox Harper 1, Measured using the Veeco interferometer.

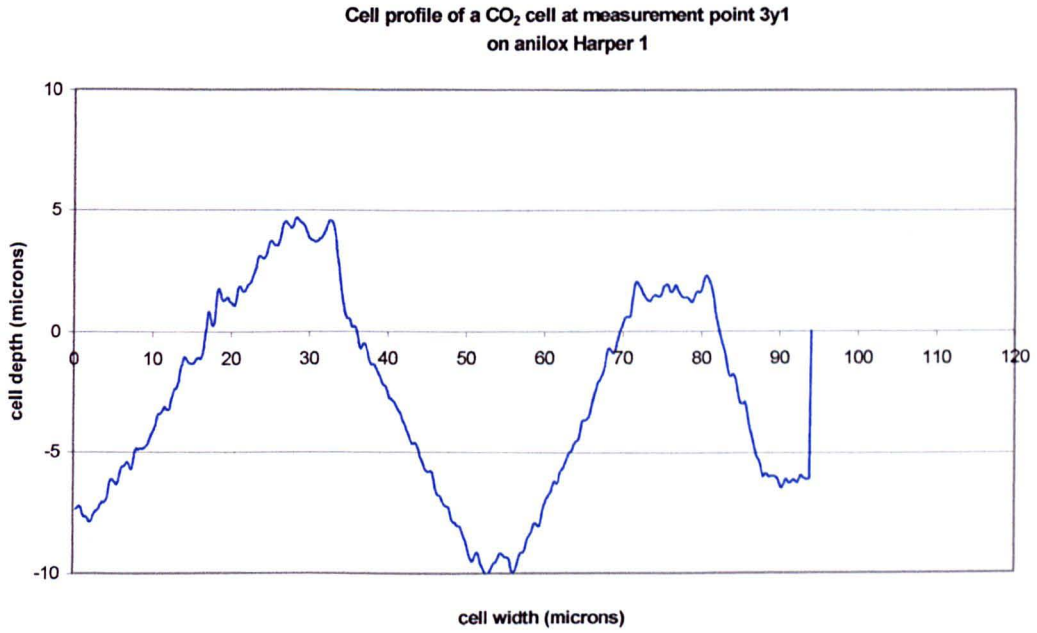

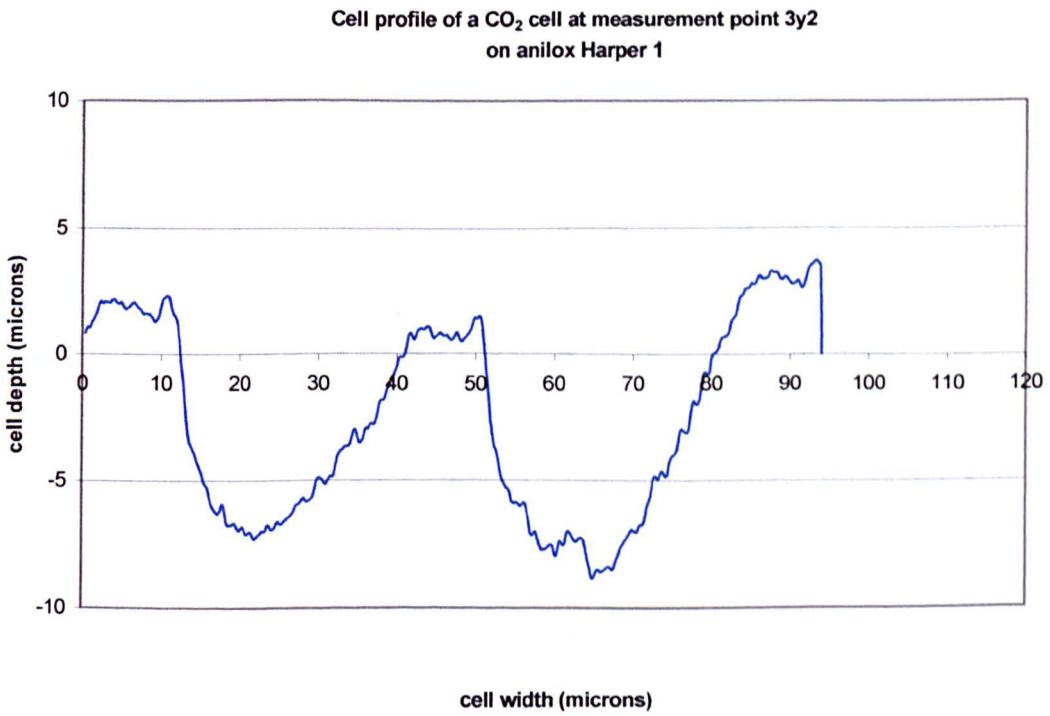

Appendix Section A6-1 continued

Cell profiles of the CO_2 and YAG cells on anilox Harper 1, Measured using the Veeco interferometer.

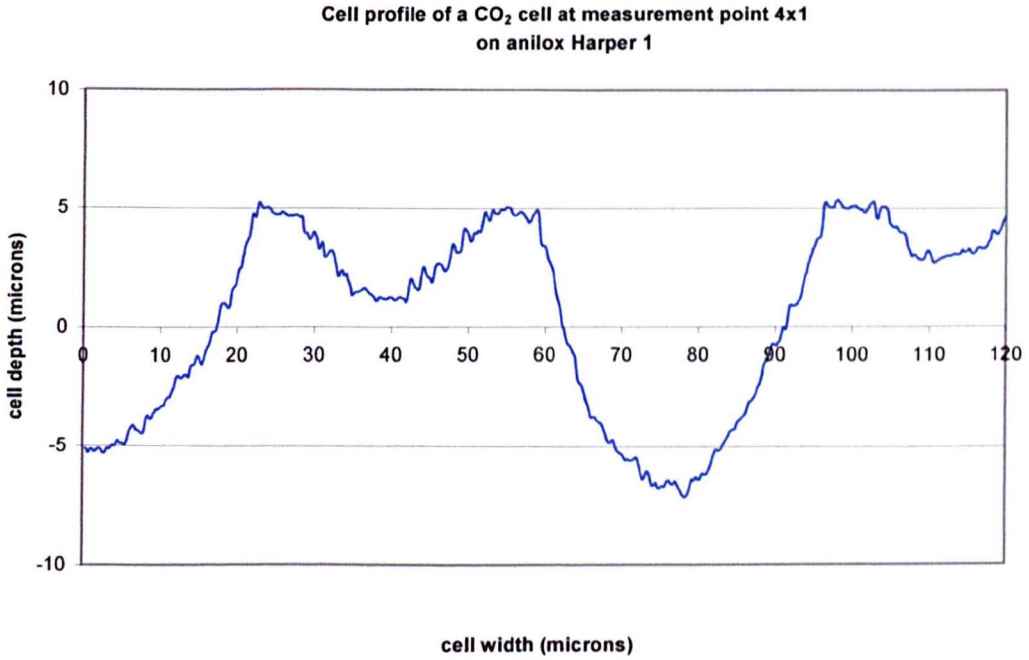

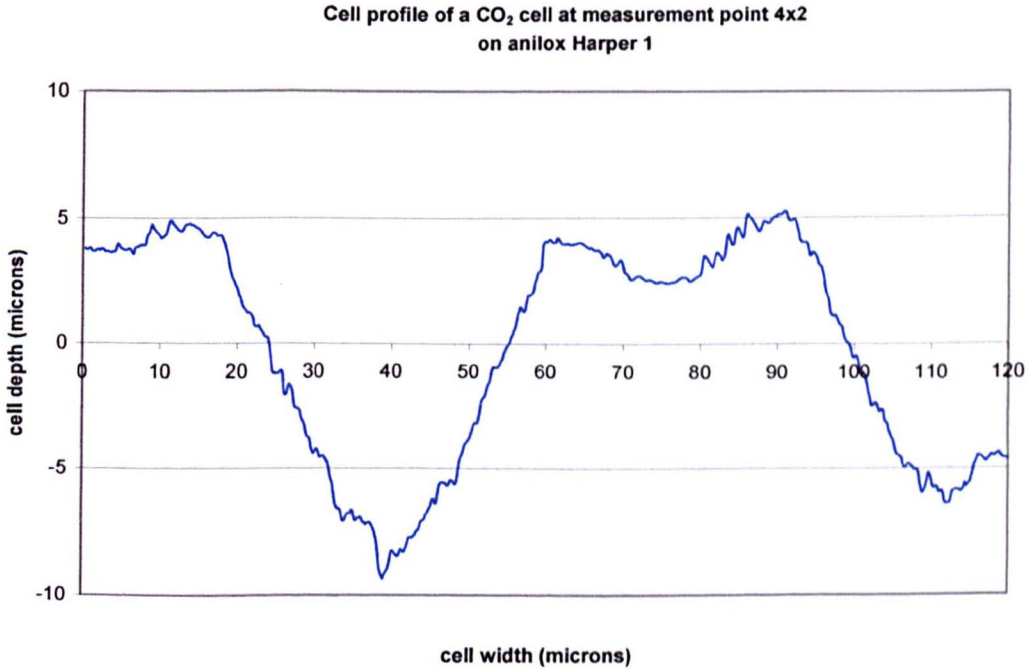

Appendix Section A6-1 continued

Cell profiles of the CO_2 and YAG cells on anilox Harper 1, Measured using the Veeco interferometer.

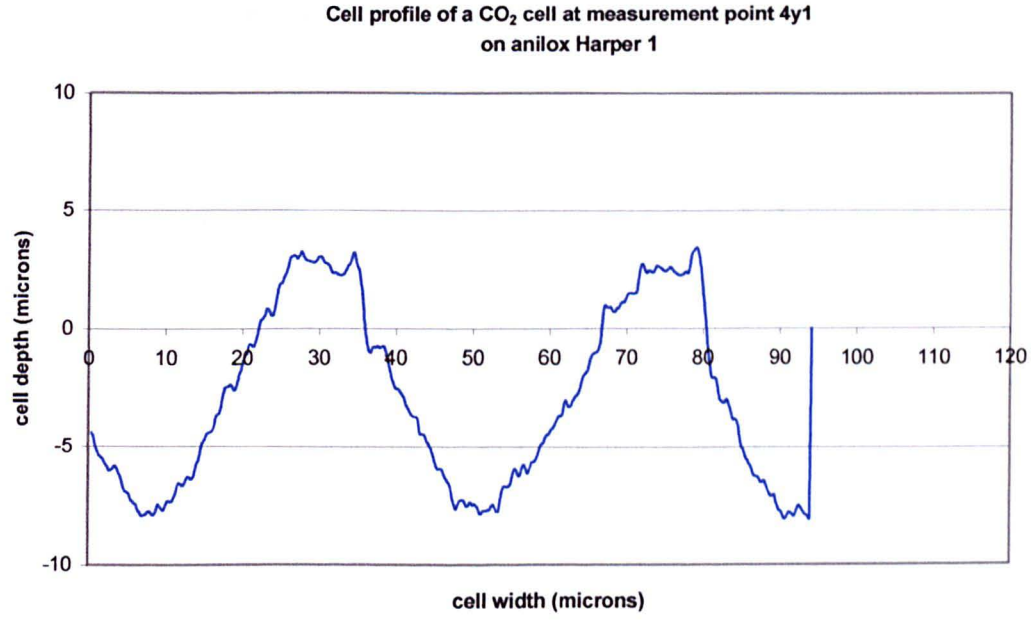

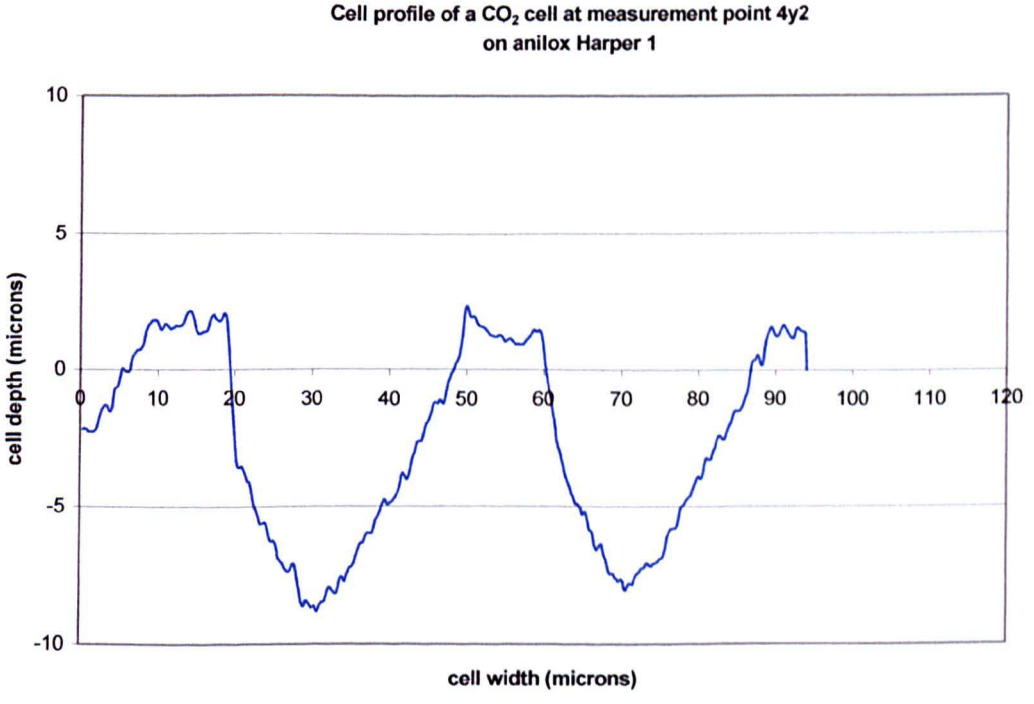

Appendix Section A6-1 continued

Cell profiles of the CO_2 and YAG cells on anilox Harper 1, Measured using the Veeco interferometer.

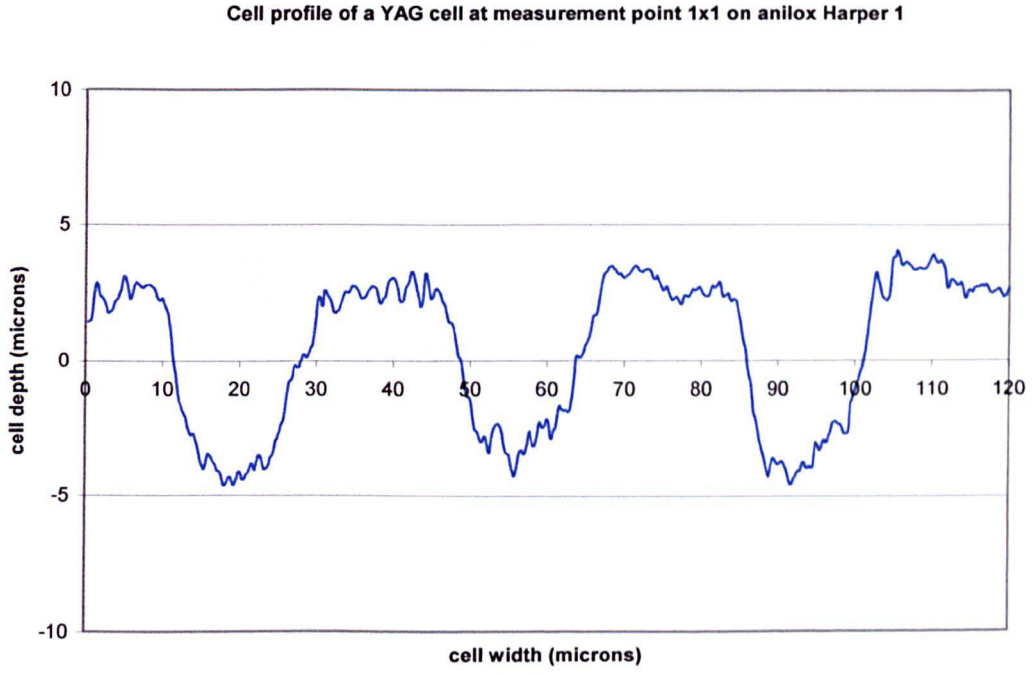

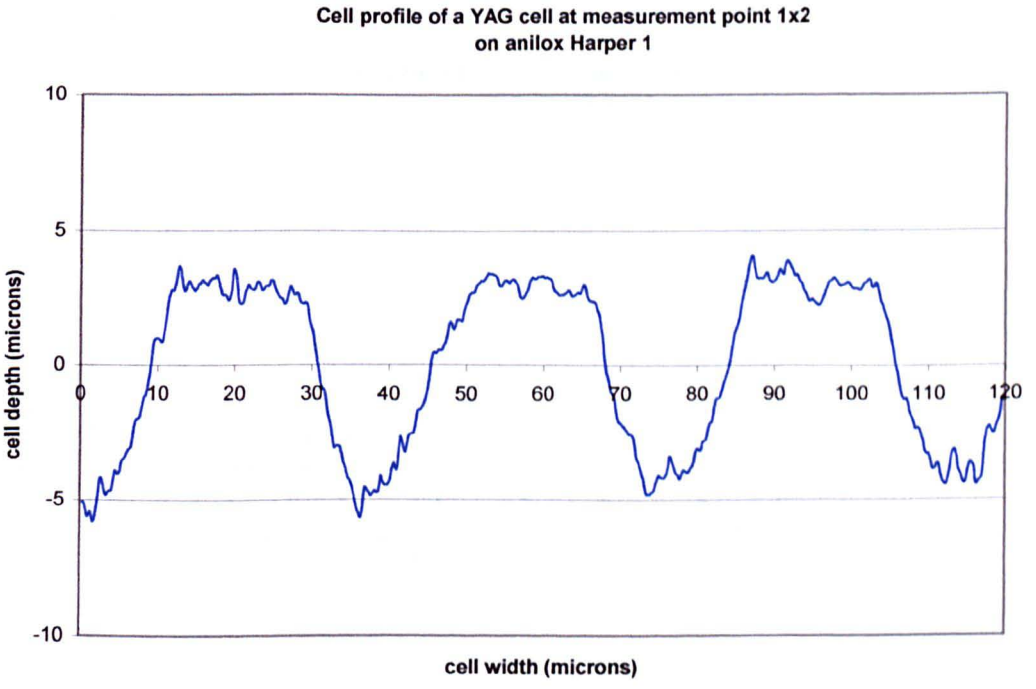

Appendix Section A6-1 continued

Cell profiles of the CO_2 and YAG cells on anilox Harper 1, Measured using the Veeco interferometer.

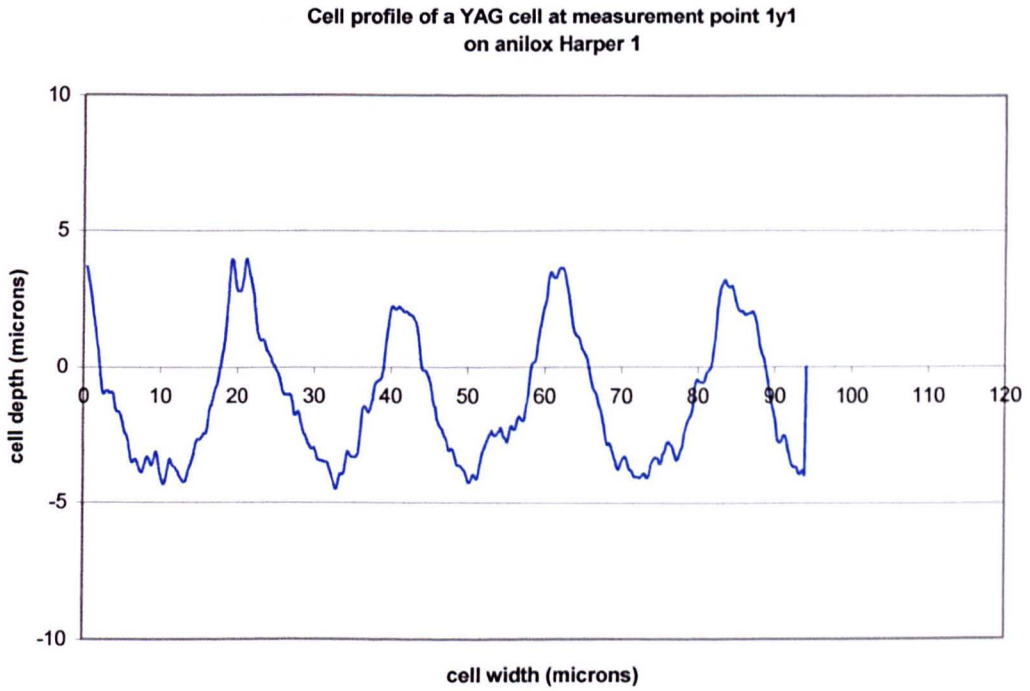

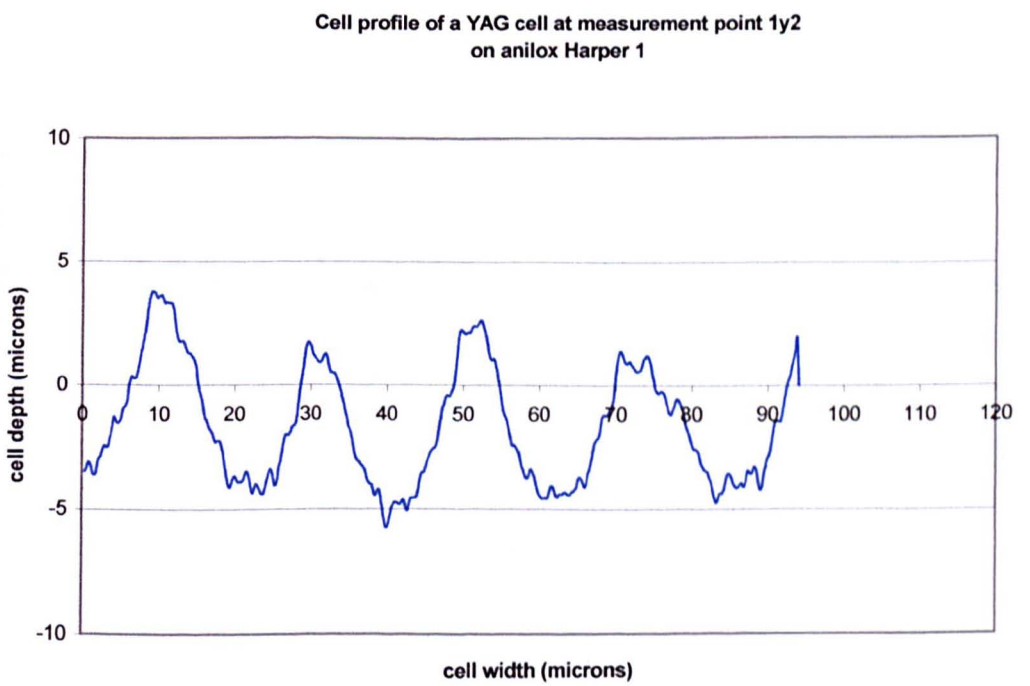

Appendix Section A6-1 continued

Cell profiles of the CO_2 and YAG cells on anilox Harper 1, Measured using the Veeco interferometer.

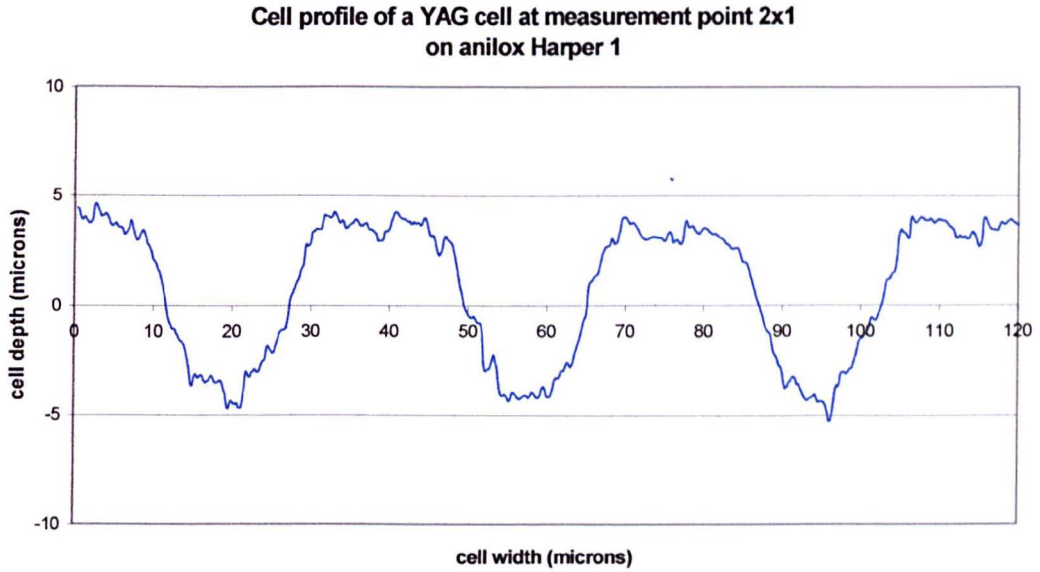

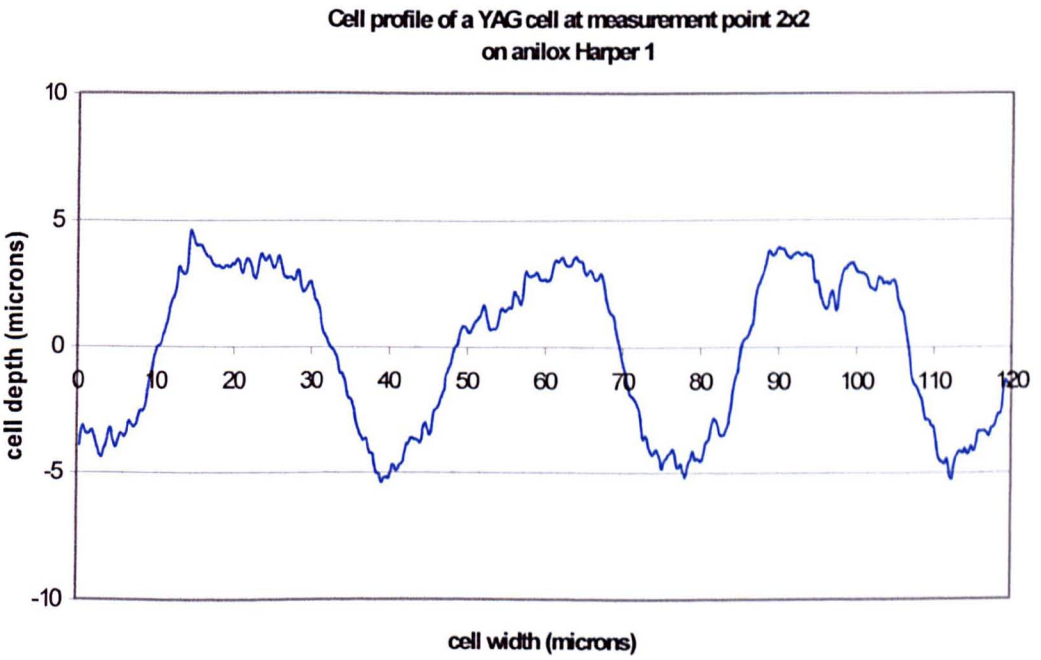

Appendix Section A6-1 continued

Cell profiles of the CO_2 and YAG cells on anilox Harper 1, Measured using the Veeco interferometer.

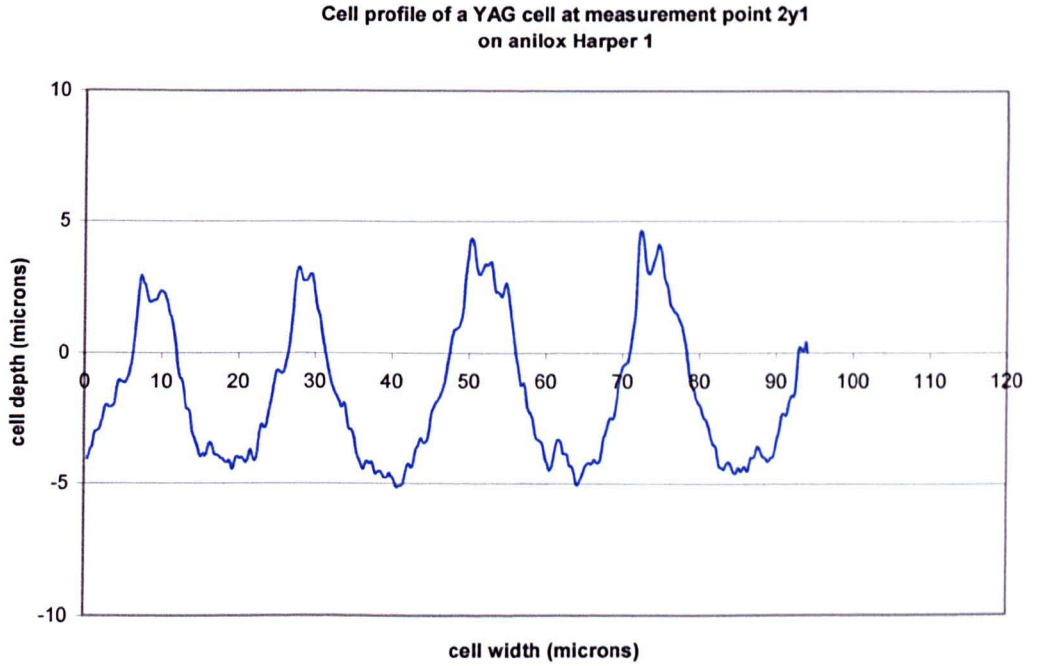

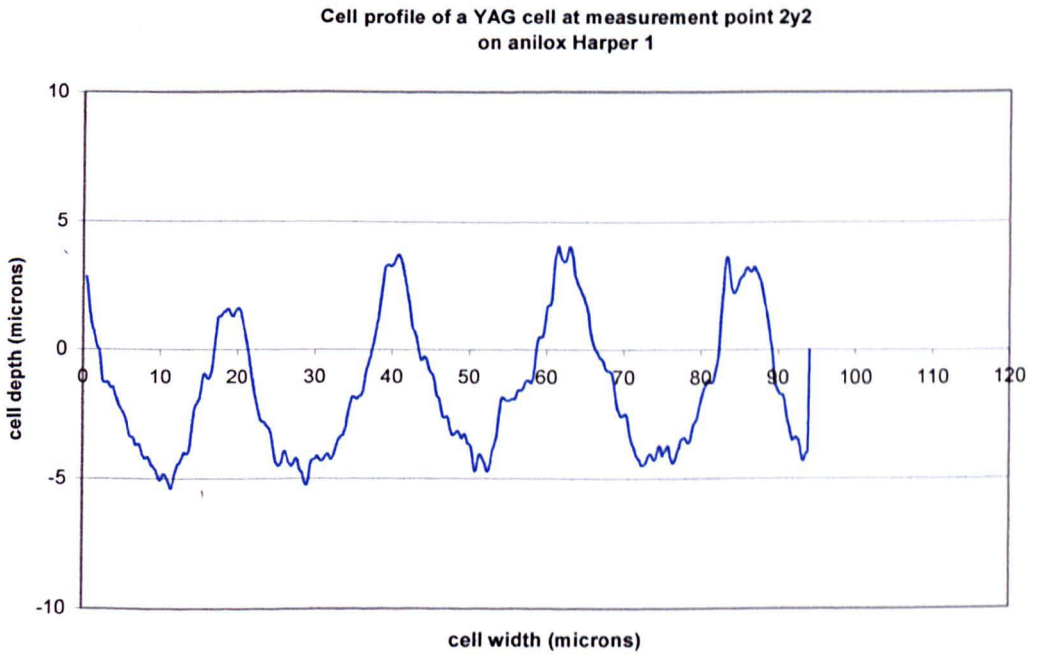

Appendix Section A6-1 continued

Cell profiles of the CO_2 and YAG cells on anilox Harper 1, Measured using the Veeco interferometer.

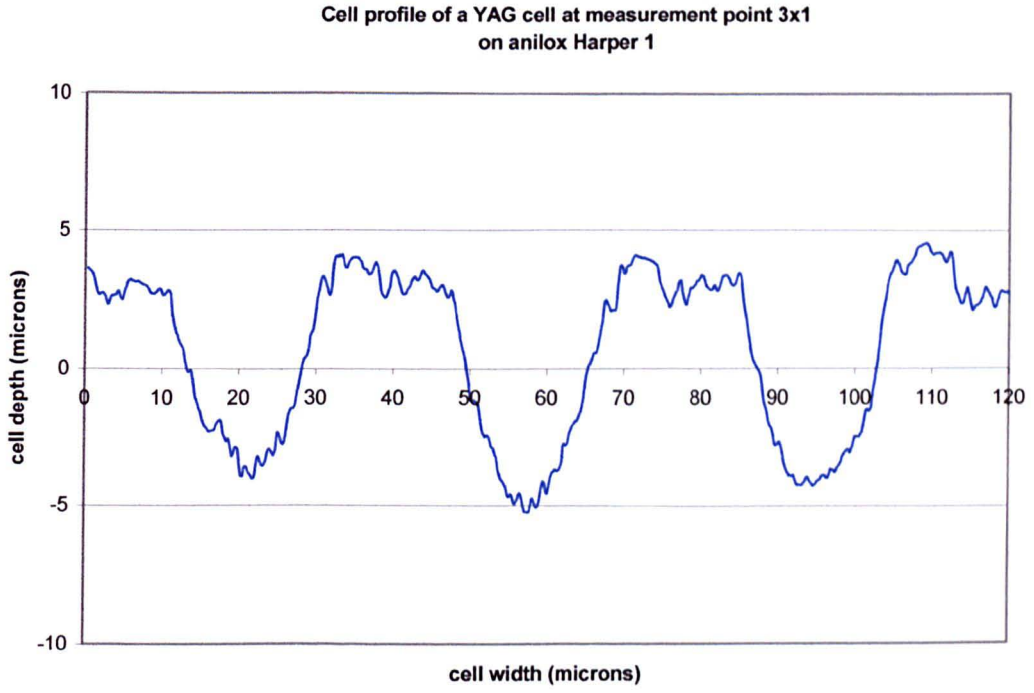

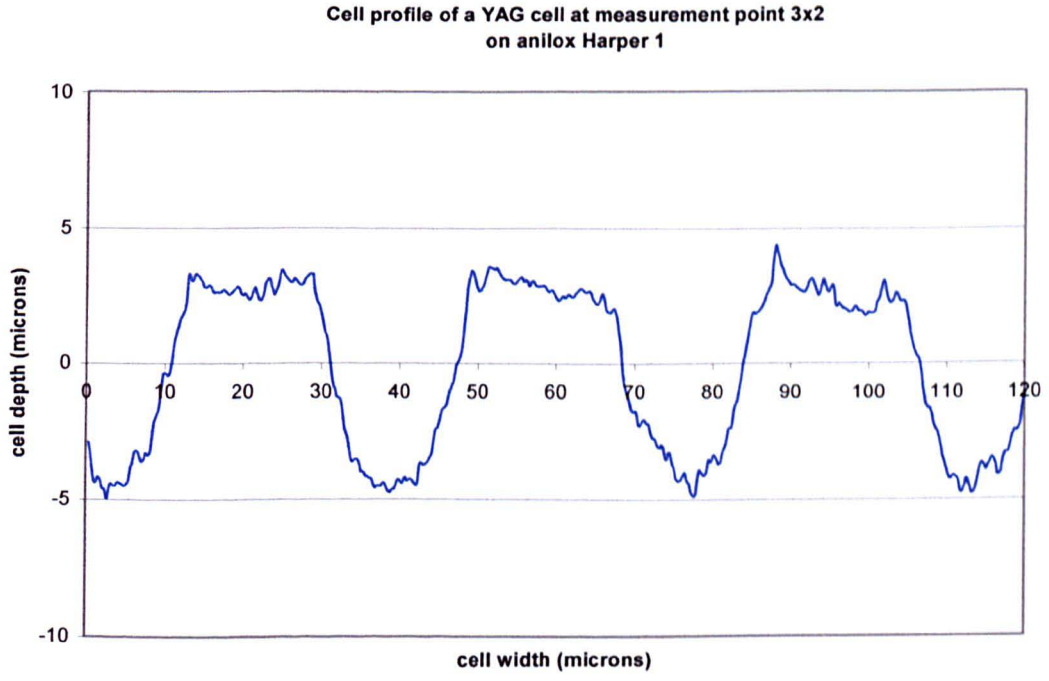

Appendix Section A6-1 continued

Cell profiles of the CO_2 and YAG cells on anilox Harper 1, Measured using the Veeco interferometer.

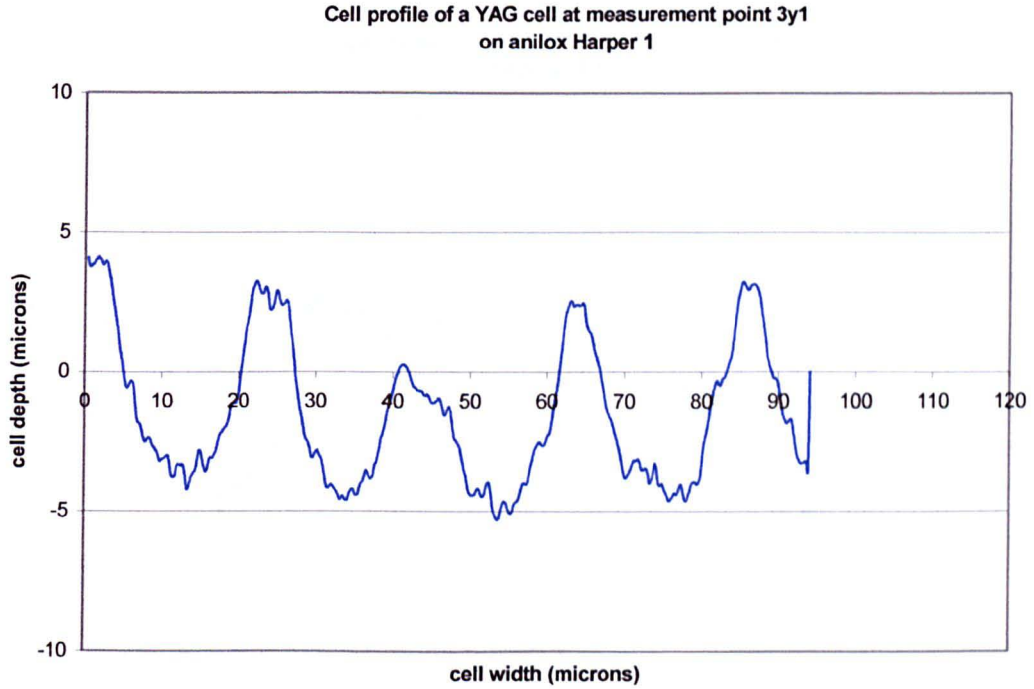

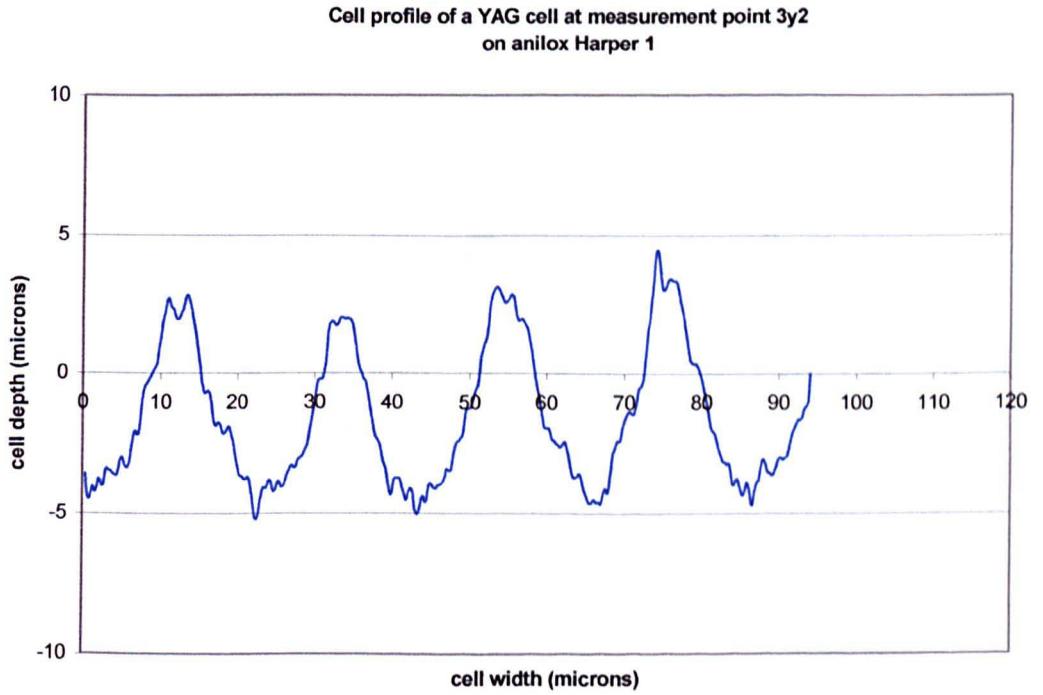

Appendix Section A6-1 continued

Cell profiles of the CO_2 and YAG cells on anilox Harper 1, Measured using the Veeco interferometer.

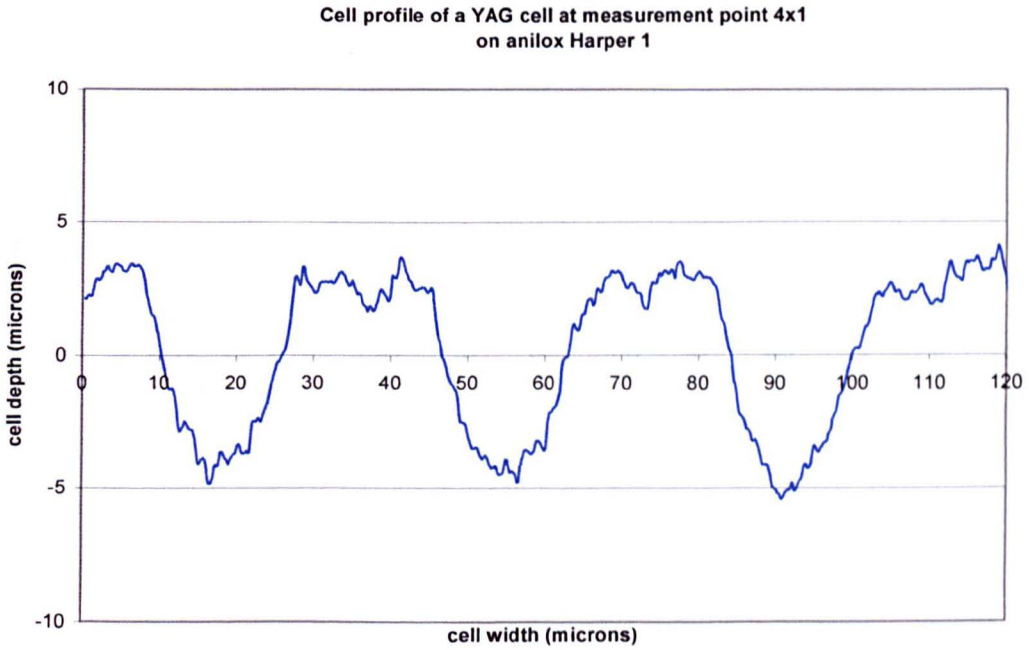

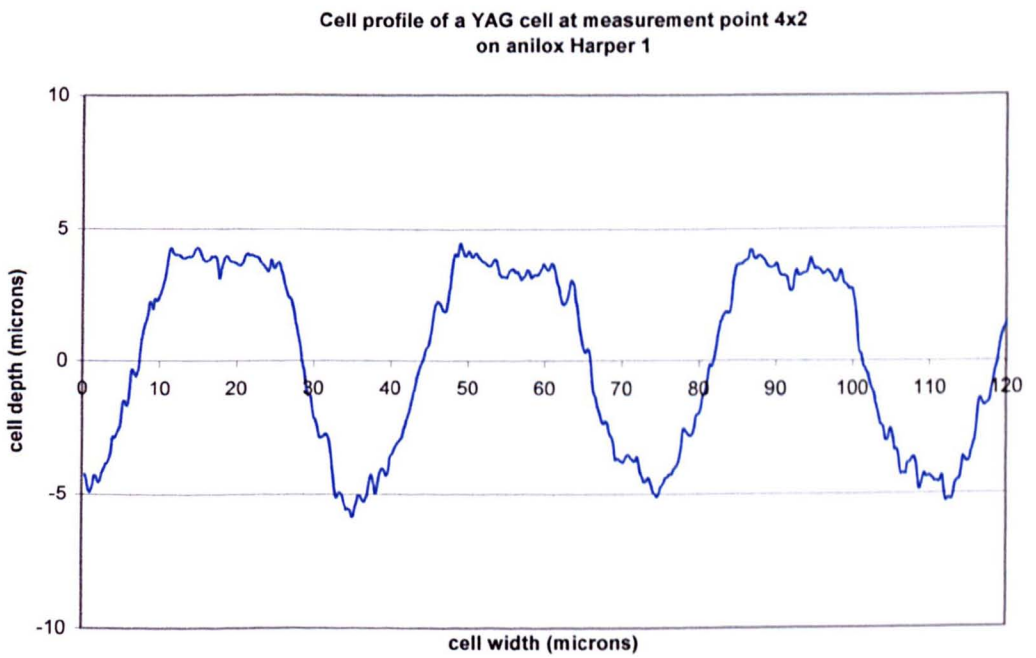

Appendix Section A6-1 continued

Cell profiles of the CO_2 and YAG cells on anilox Harper 1, Measured using the Veeco interferometer.

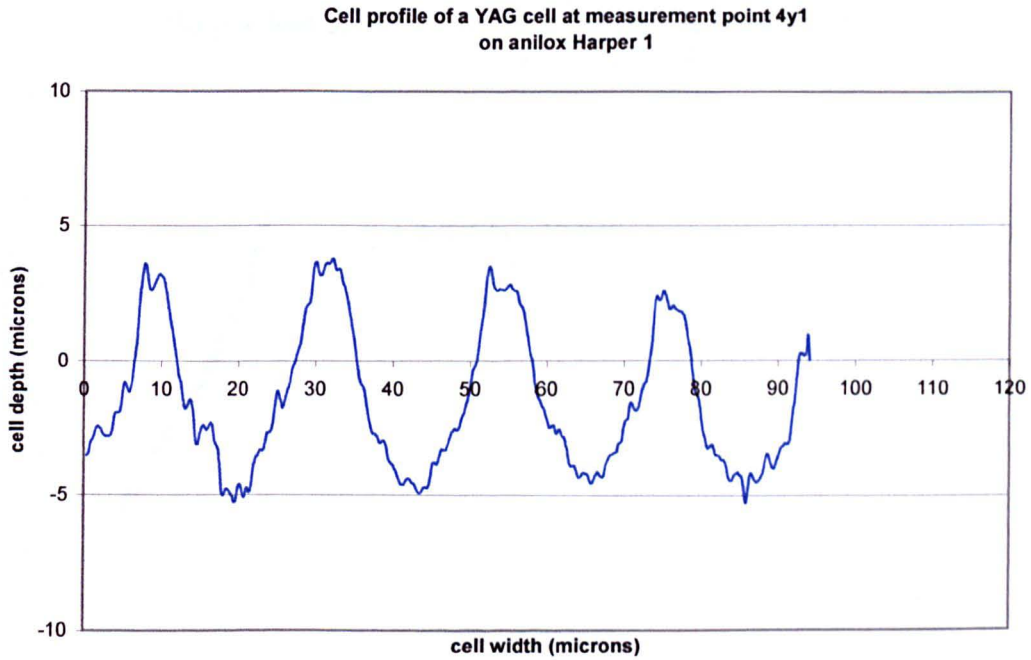

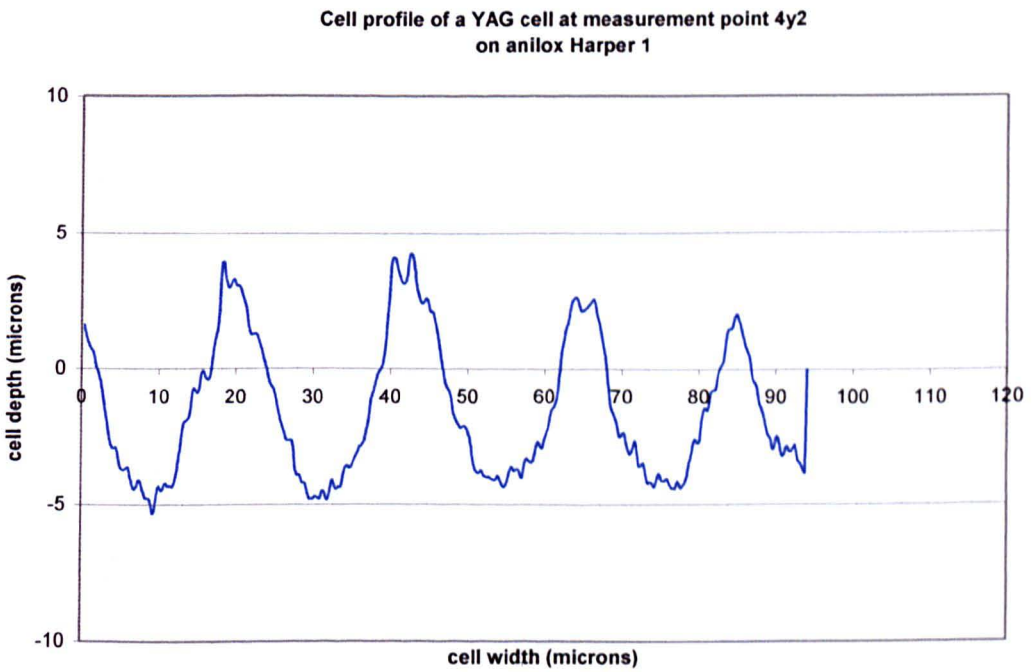

Appendix Section A6-2

Gradient measurements made from the cell profiles of the CO_2 and YAG cells on anilox Harper 1, Measured using the Veeco interferometer.

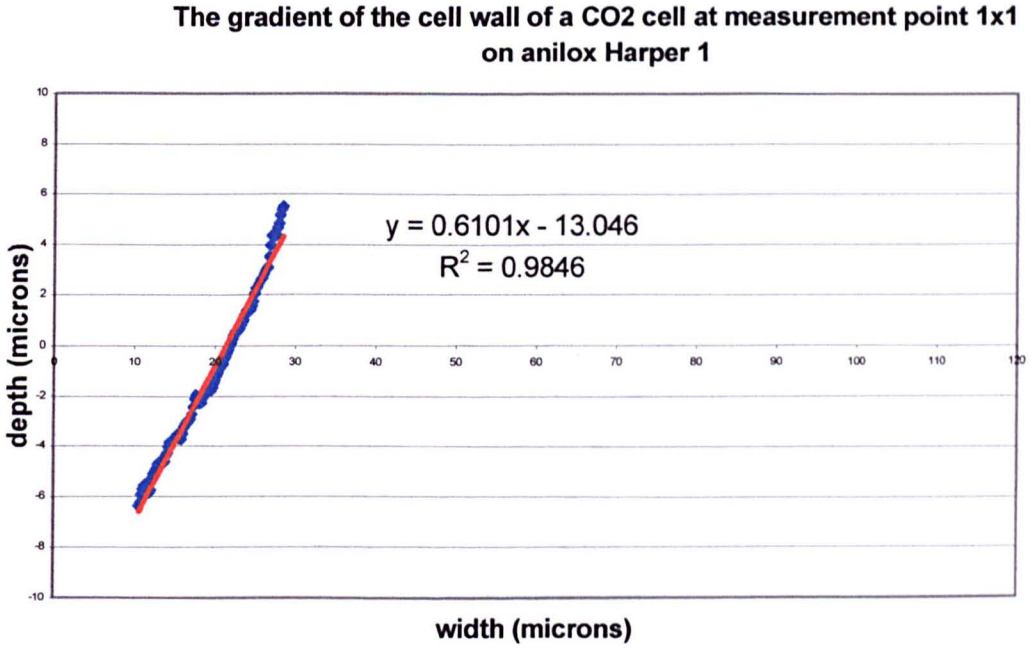

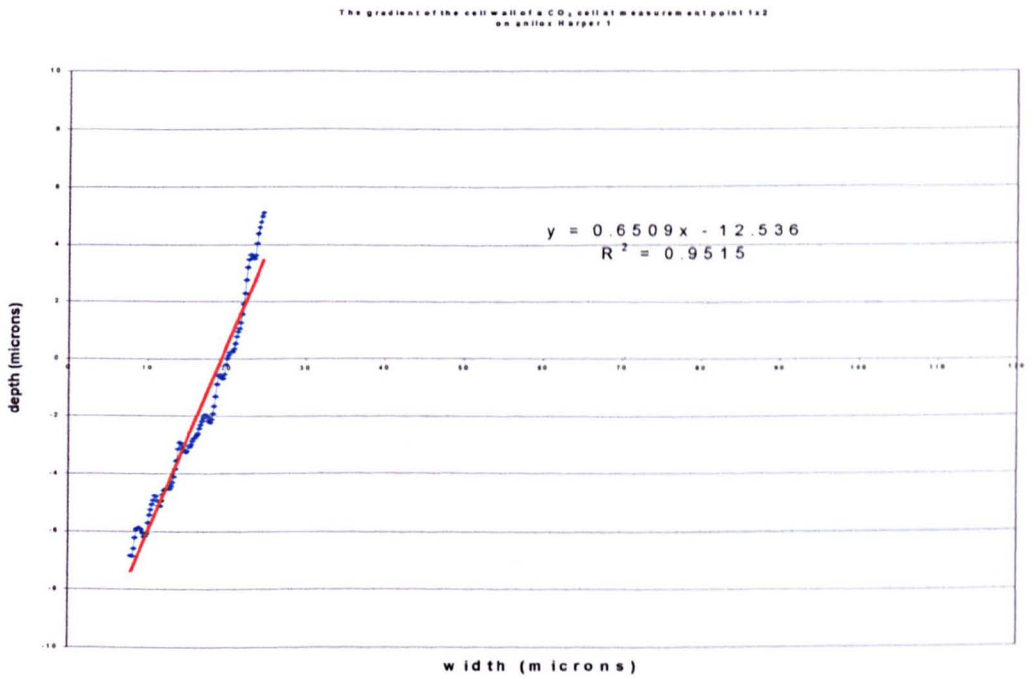

Appendix Section A6-2 continued

Gradient measurements made from the cell profiles of the CO_2 and YAG cells on anilox Harper 1, Measured using the Veeco interferometer.

The gradient of the cell wall of a CO_2 cell at measurement point 1y1 on anilox Harper 1

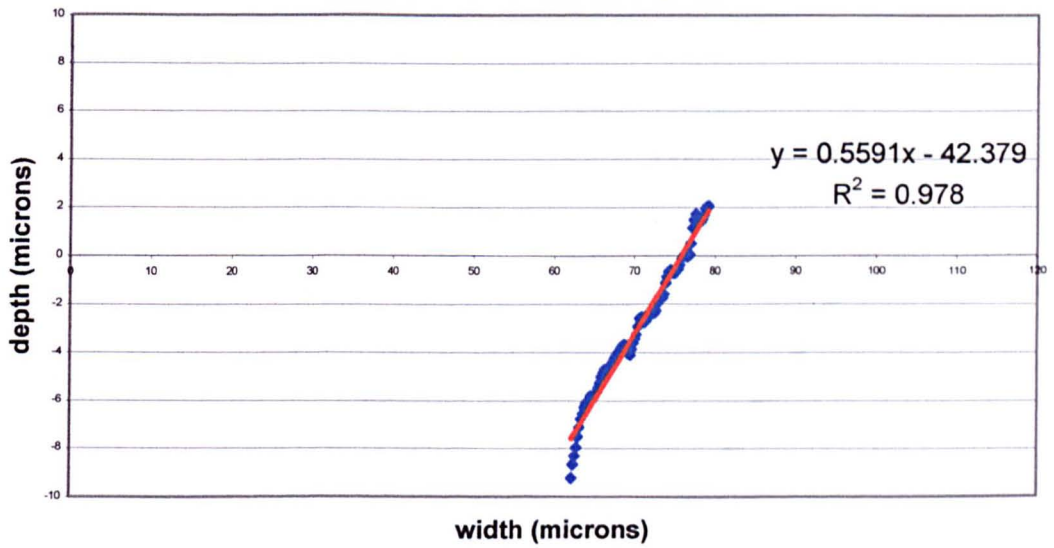

The gradient of the cell wall of a CO_2 cell at measurement point 1y2 on anilox Harper 1

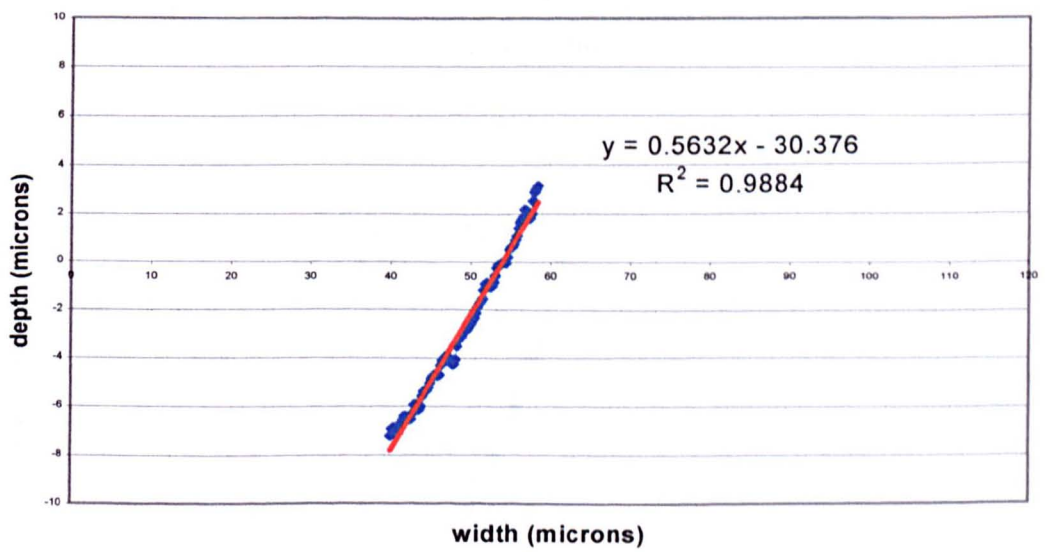

Appendix Section A6-2 continued

Gradient measurements made from the cell profiles of the CO_2 and YAG cells on anilox Harper 1, Measured using the Veeco interferometer.

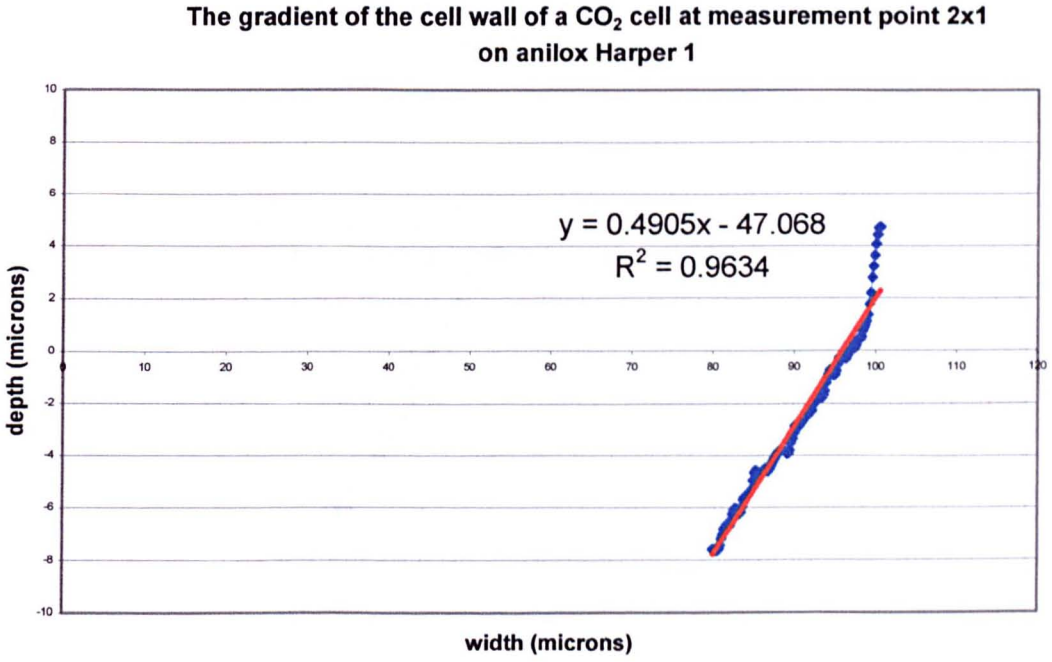

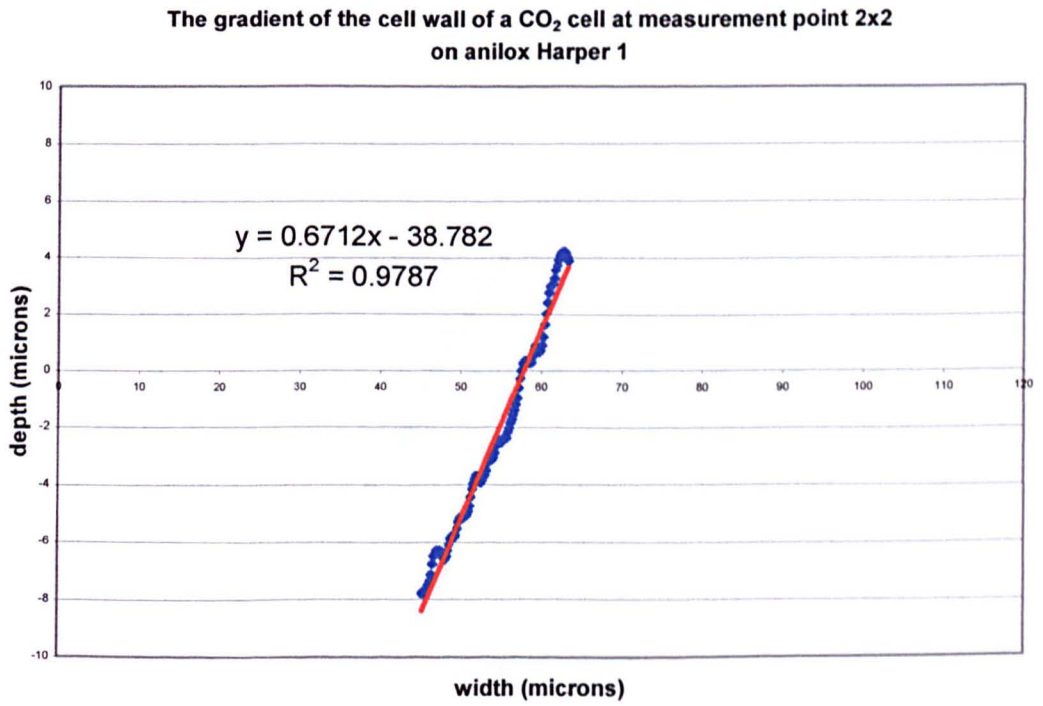

Appendix Section A6-2 continued

Gradient measurements made from the cell profiles of the CO_2 and YAG cells on anilox Harper 1, Measured using the Veeco interferometer.

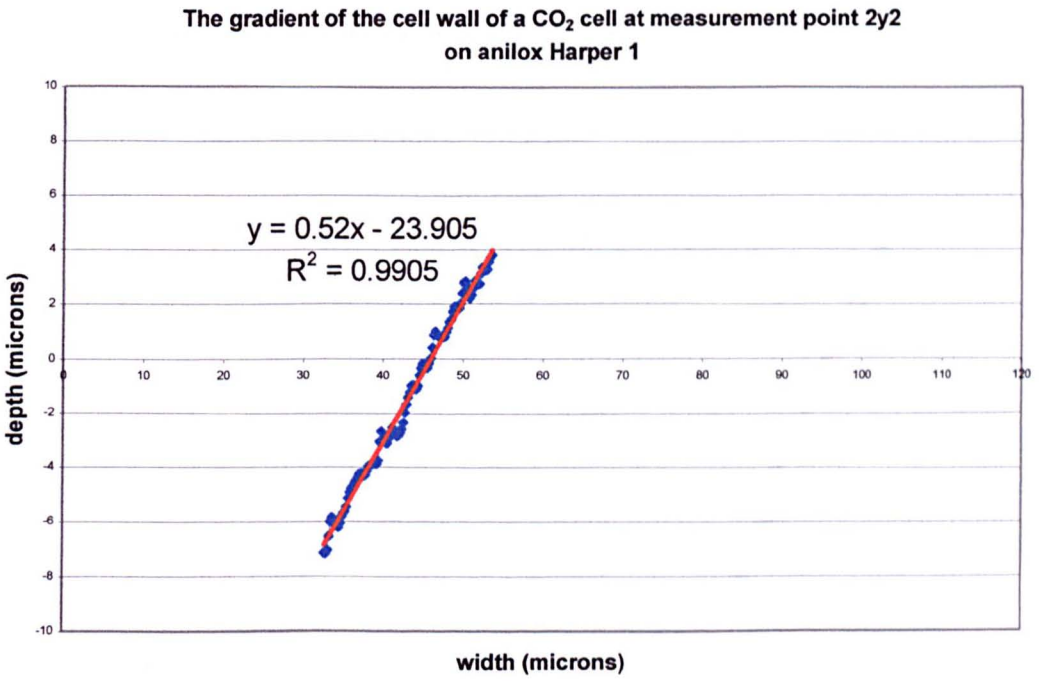

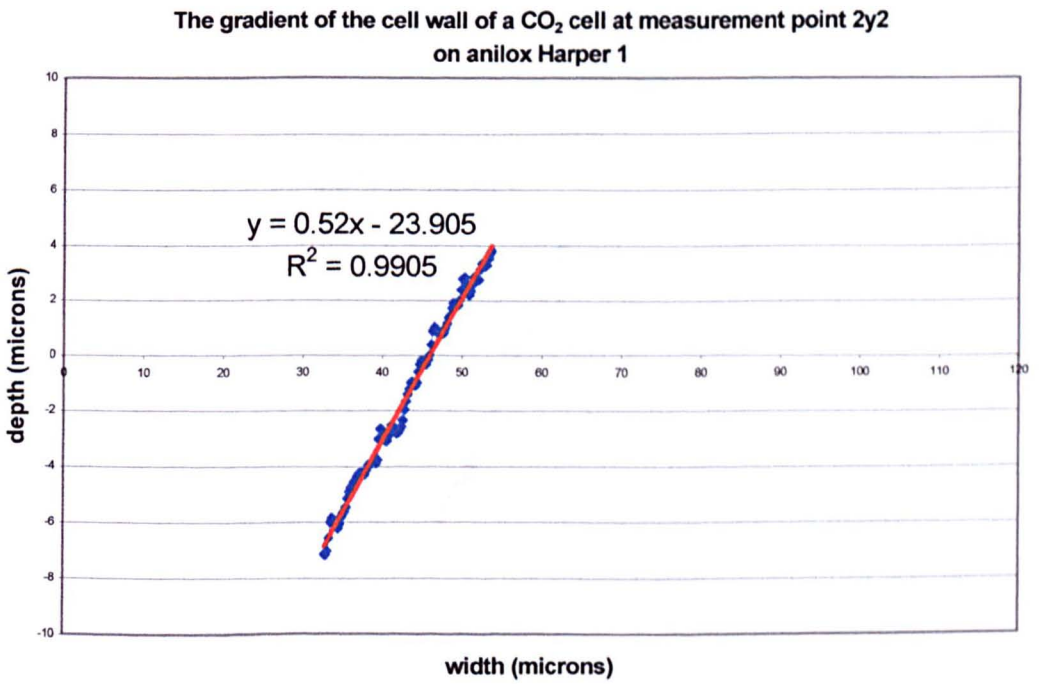

Appendix Section A6-2 continued

Gradient measurements made from the cell profiles of the CO_2 and YAG cells on anilox Harper 1, Measured using the Veeco interferometer.

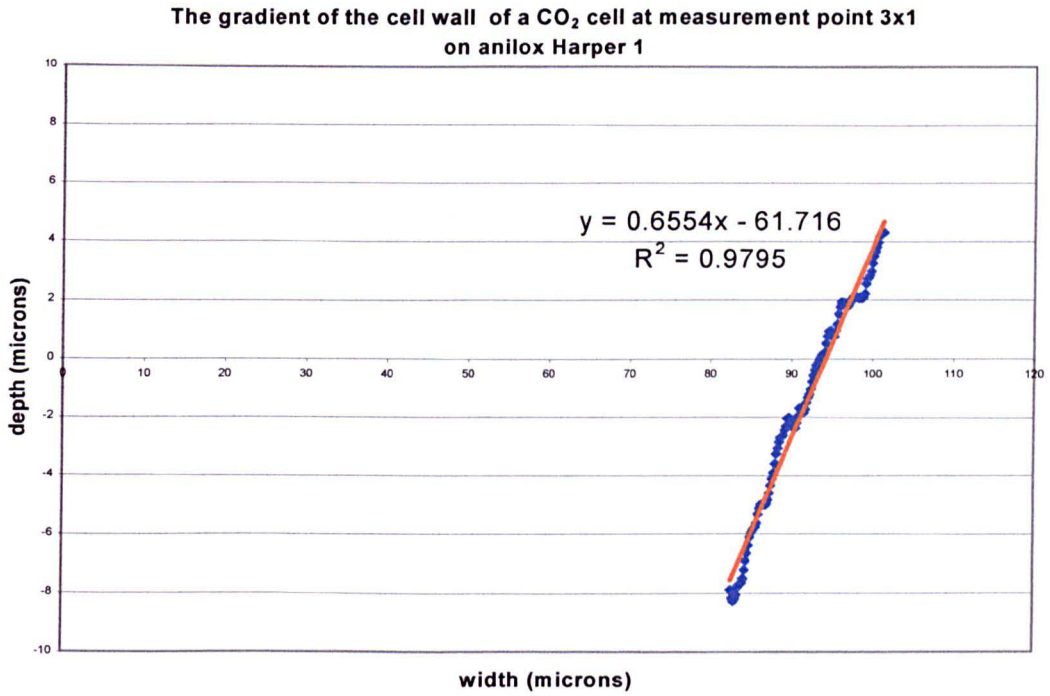

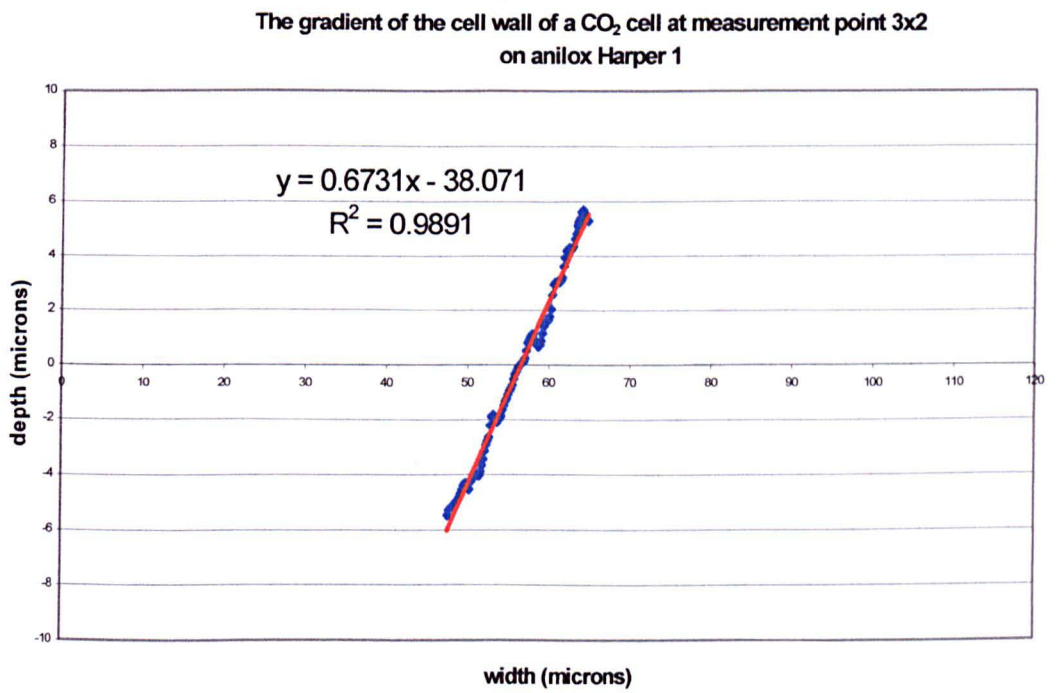

Appendix Section A6-2 continued

Gradients measurements made from the cell profiles of the CO_2 and YAG cells on anilox Harper 1, Measured using the Veeco interferometer.

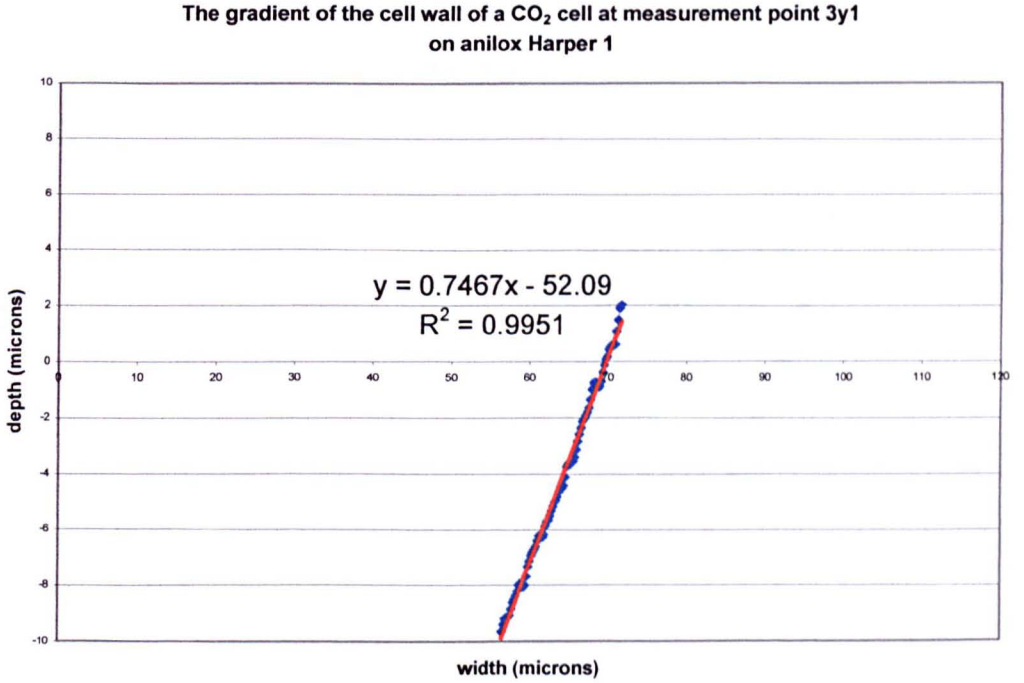

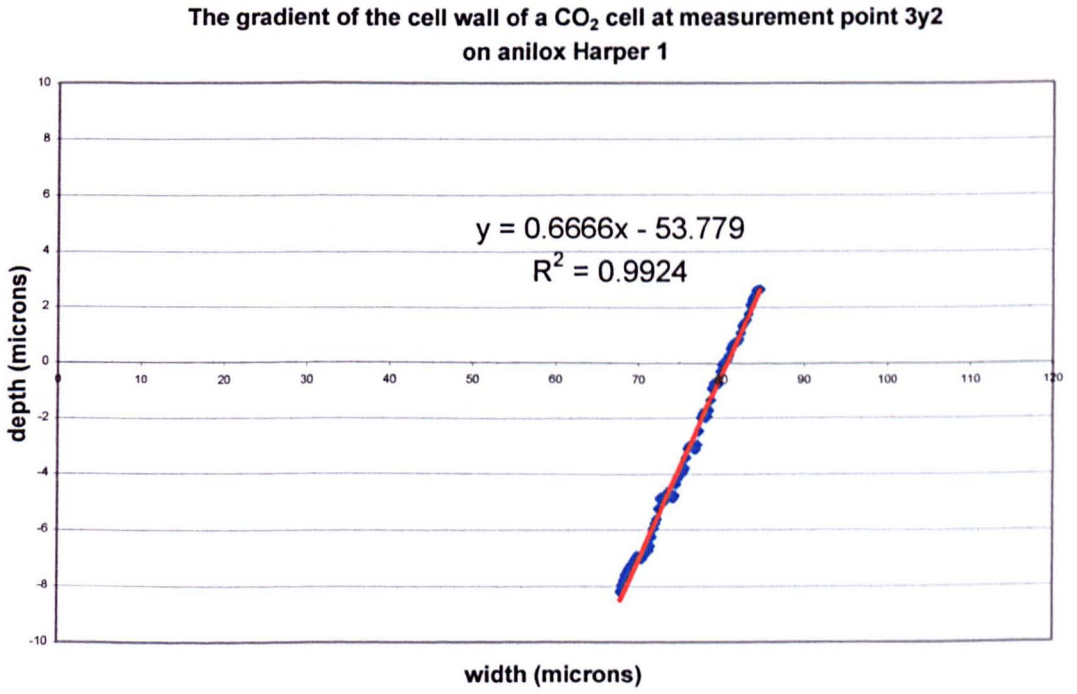

Appendix Section A6-2 continued

Gradients measurements made from the cell profiles of the CO_2 and YAG cells on anilox Harper 1, Measured using the Veeco interferometer.

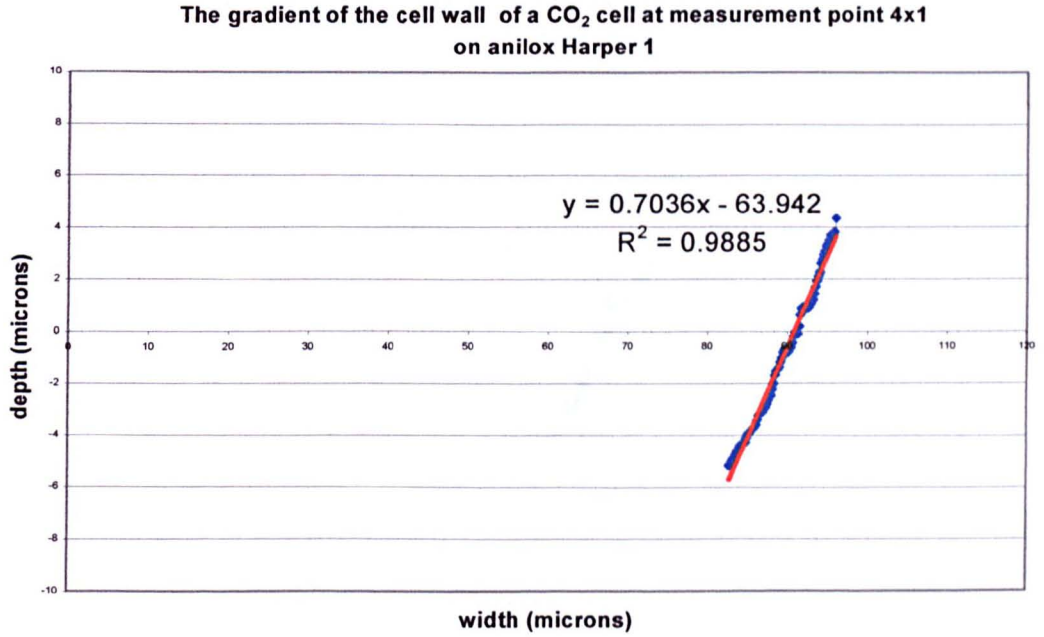

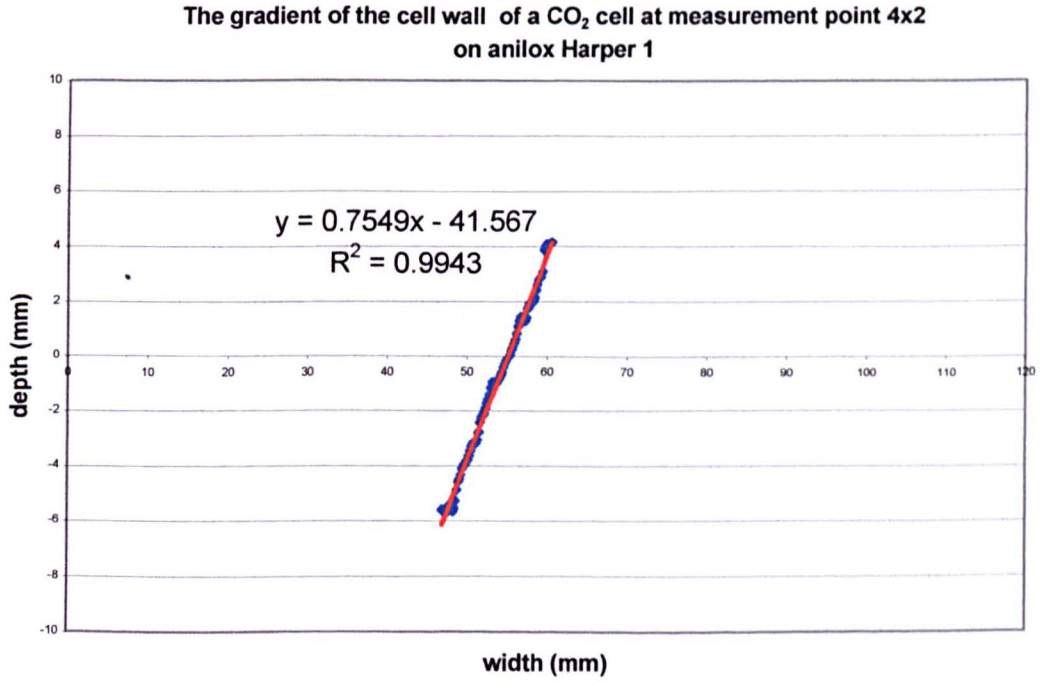

Appendix Section A6-2 continued

Gradient measurements made from the cell profiles of the CO_2 and YAG cells on anilox Harper 1, Measured using the Veeco interferometer.

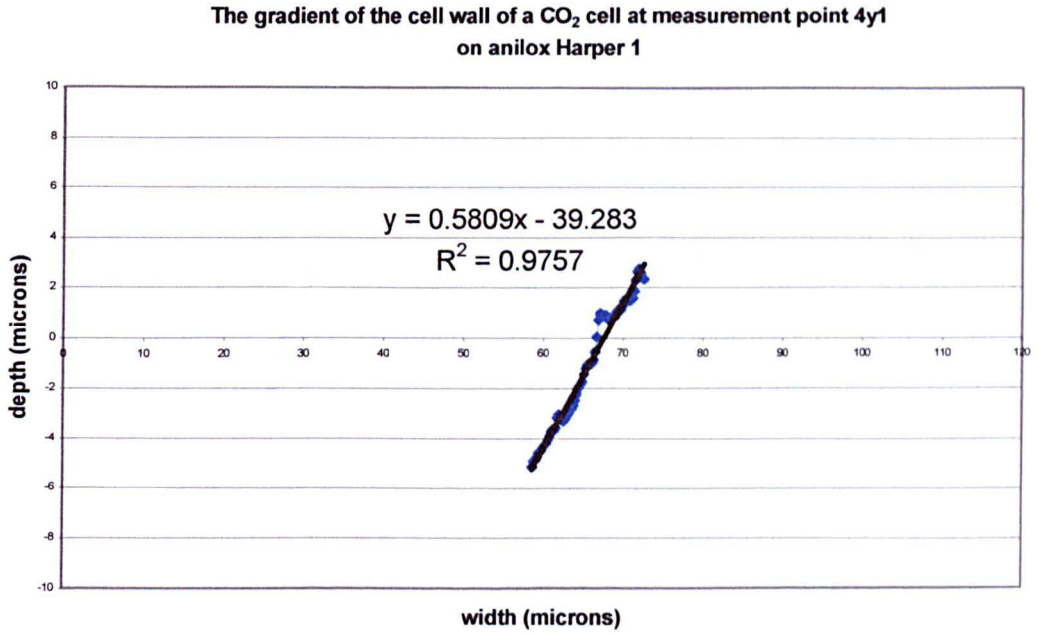

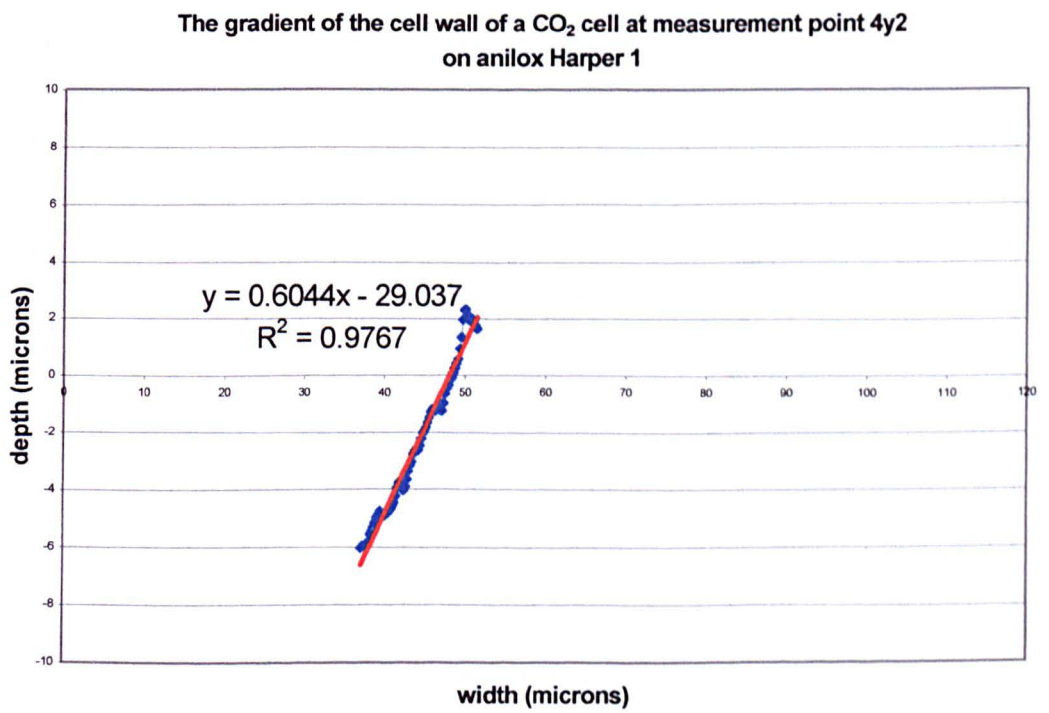

Appendix Section A6-2 continued

Gradients measurements made from the cell profiles of the CO_2 and YAG cells on anilox Harper 1, Measured using the Veeco interferometer.

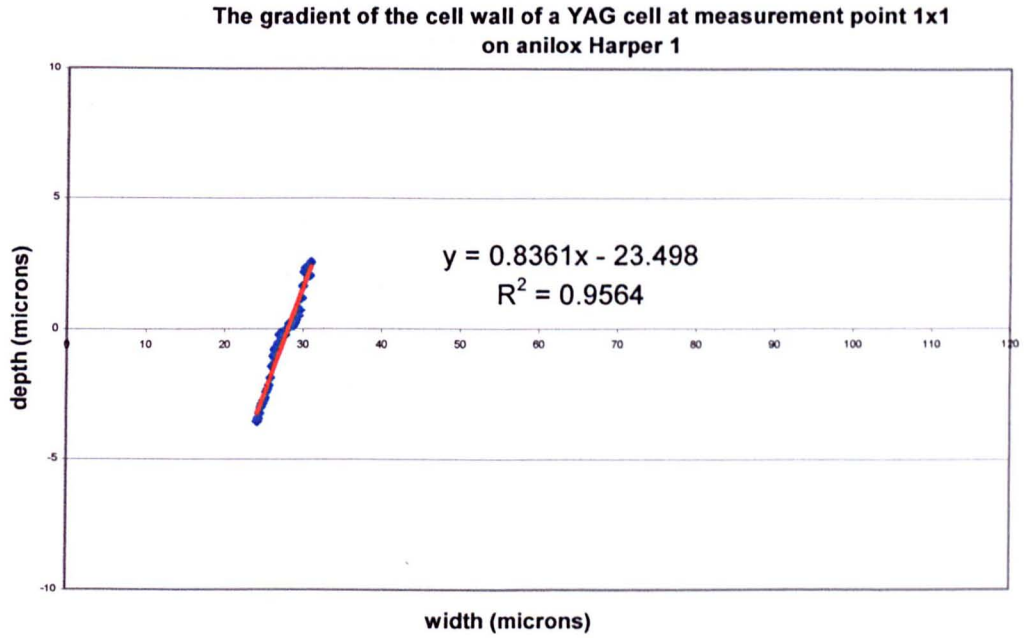

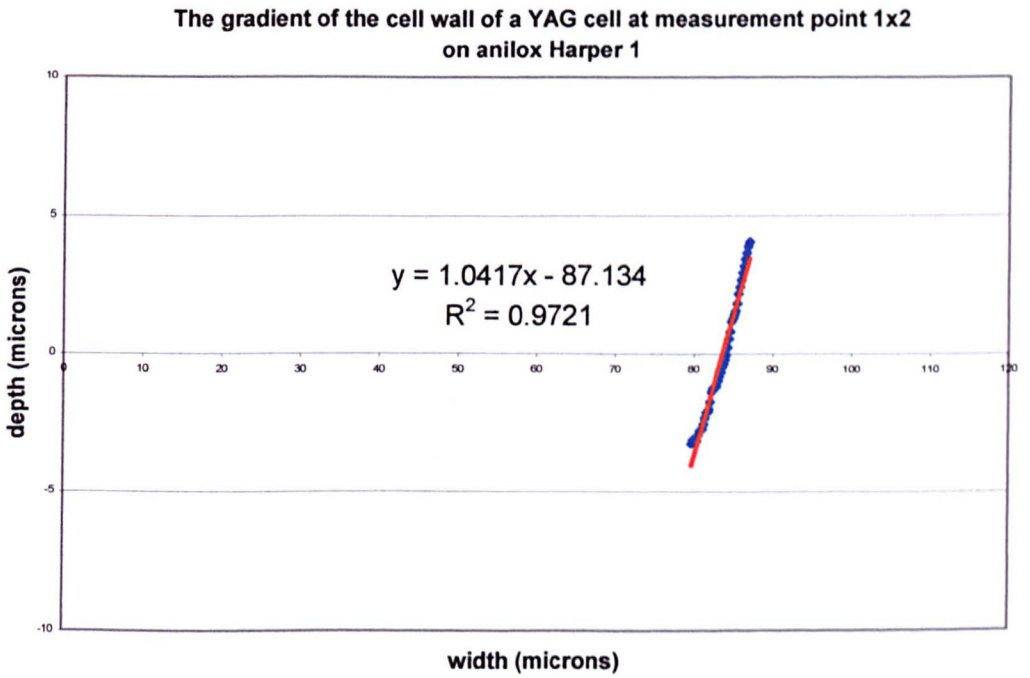

Appendix Section A6-2 continued

Gradients measurements made from the cell profiles of the CO_2 and YAG cells on anilox Harper 1, Measured using the Veeco interferometer.

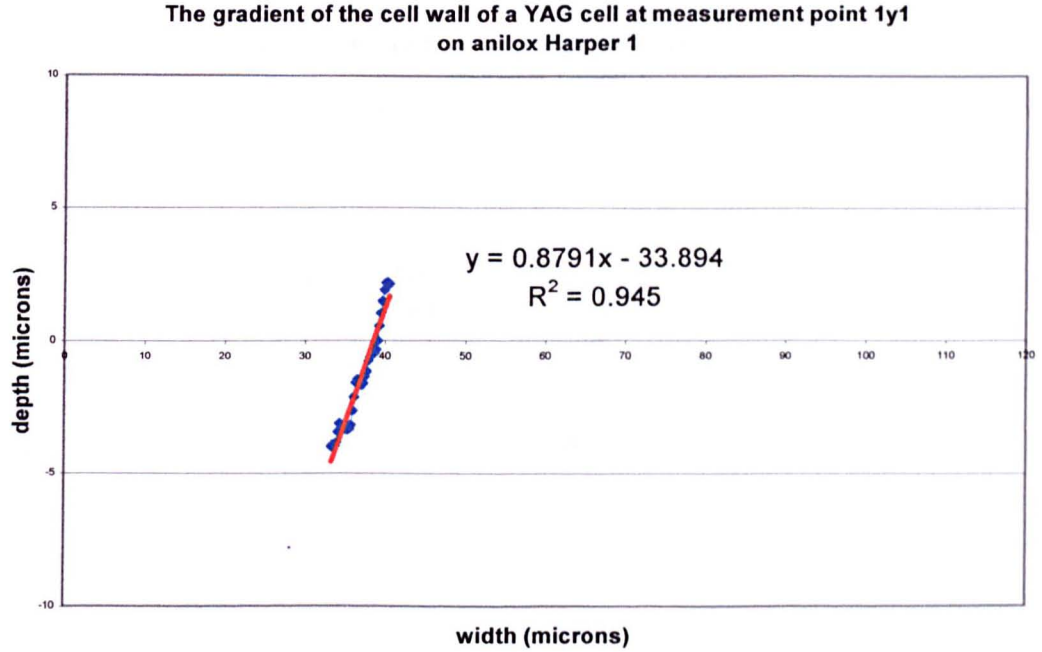

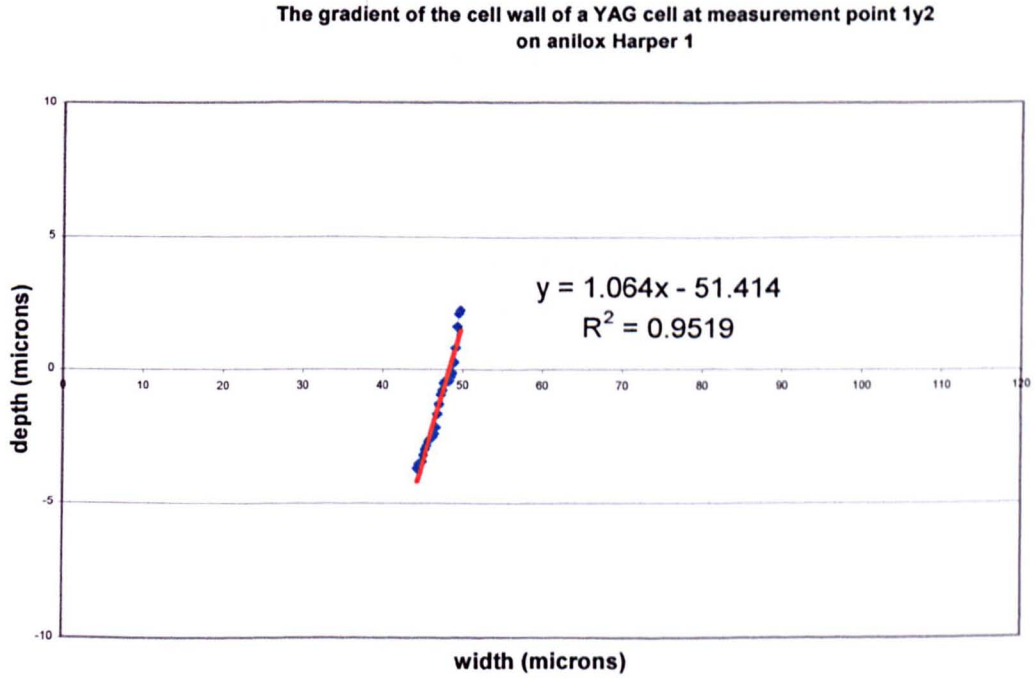

Appendix Section A6-2 continued

Gradients measurements made from the cell profiles of the CO_2 and YAG cells on anilox Harper 1, Measured using the Veeco interferometer.

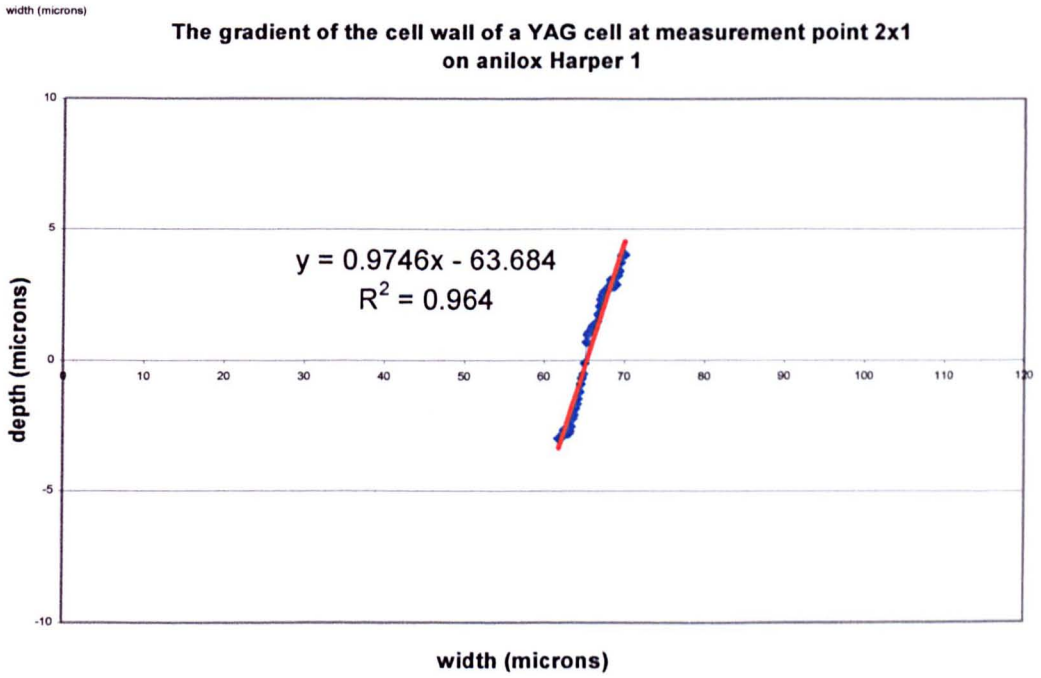

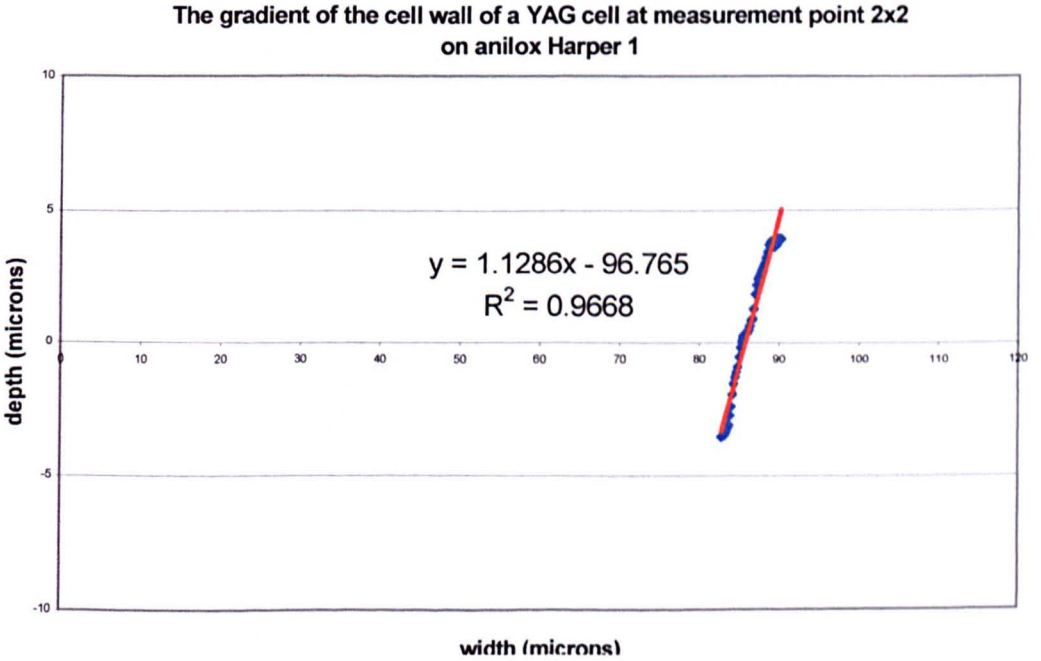

Appendix Section A6-2 continued

Gradients measurements made from the cell profiles of the CO_2 and YAG cells on anilox Harper 1, Measured using the Veeco interferometer.

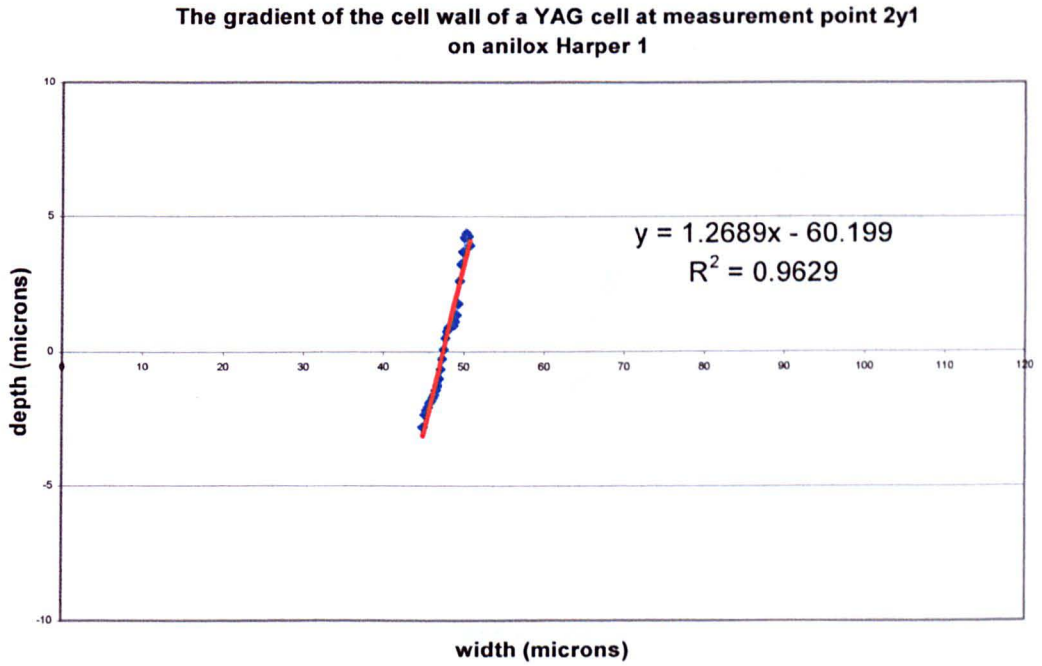

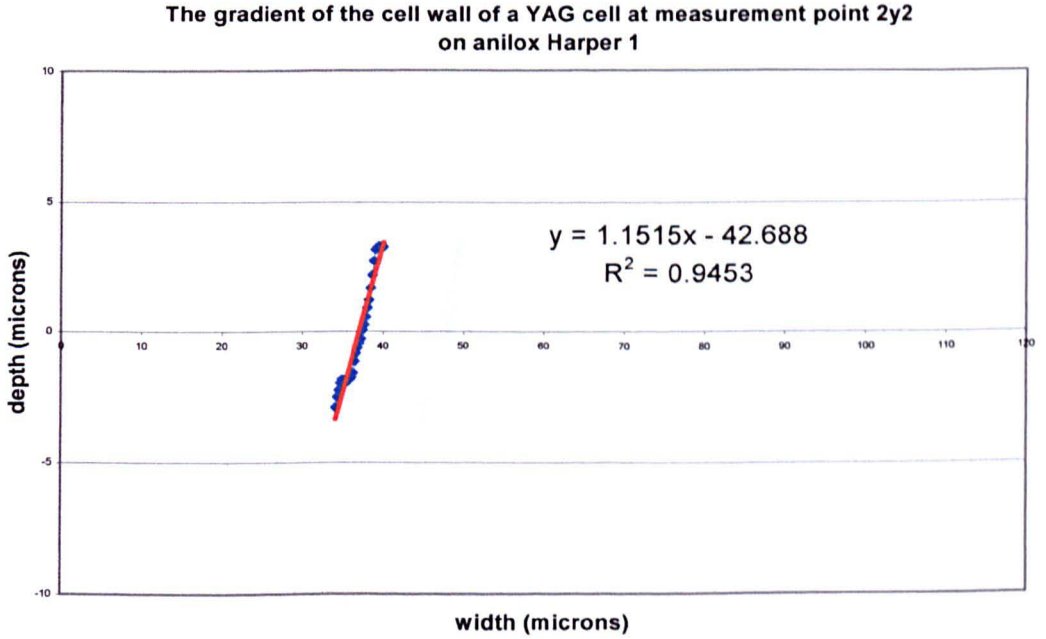

Appendix Section A6-2 continued

Gradients measurements made from the cell profiles of the CO_2 and YAG cells on anilox Harper 1, Measured using the Veeco interferometer.

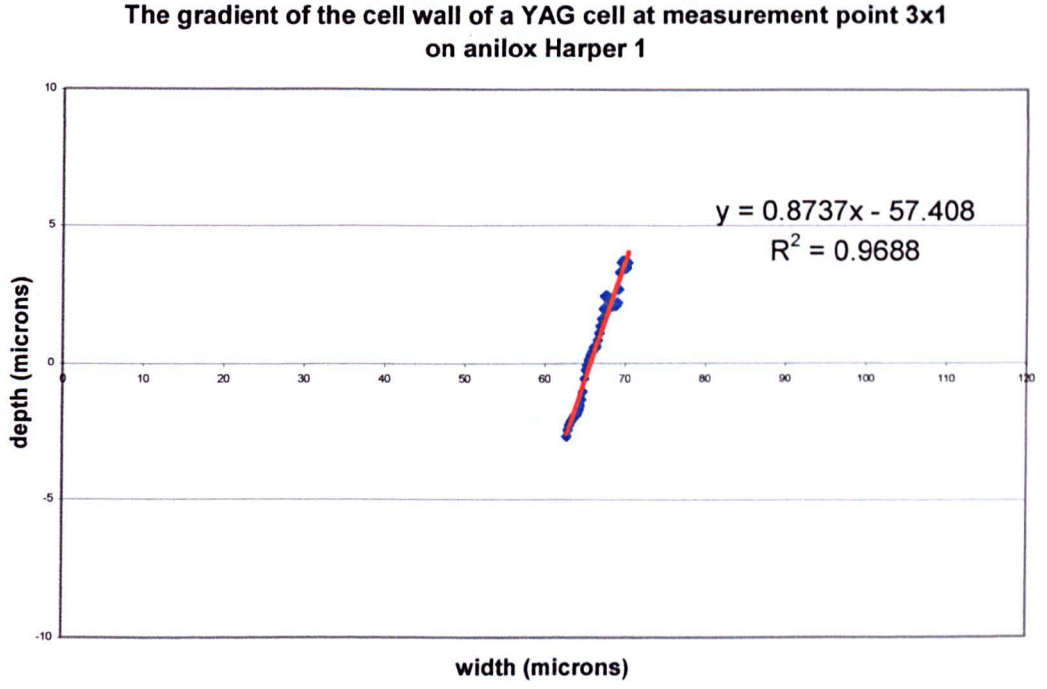

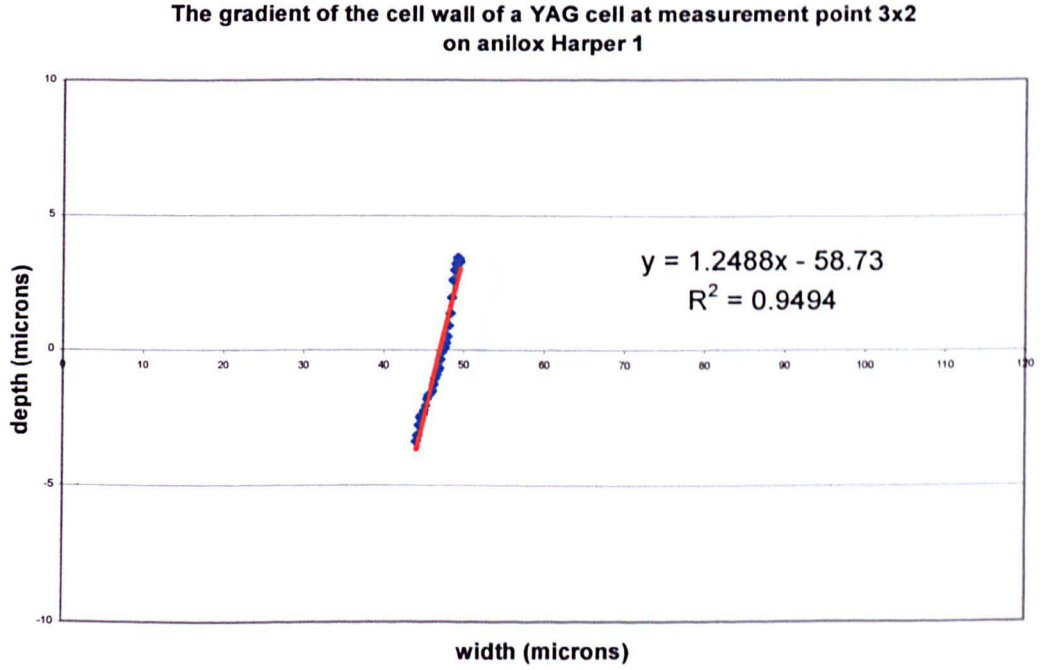

Appendix Section A6-2 continued

Gradients measurements made from the cell profiles of the CO_2 and YAG cells on anilox Harper 1, Measured using the Veeco interferometer.

The gradient of the cell wall of a YAG cell at measurement point 3y1 on anilox Harper 1

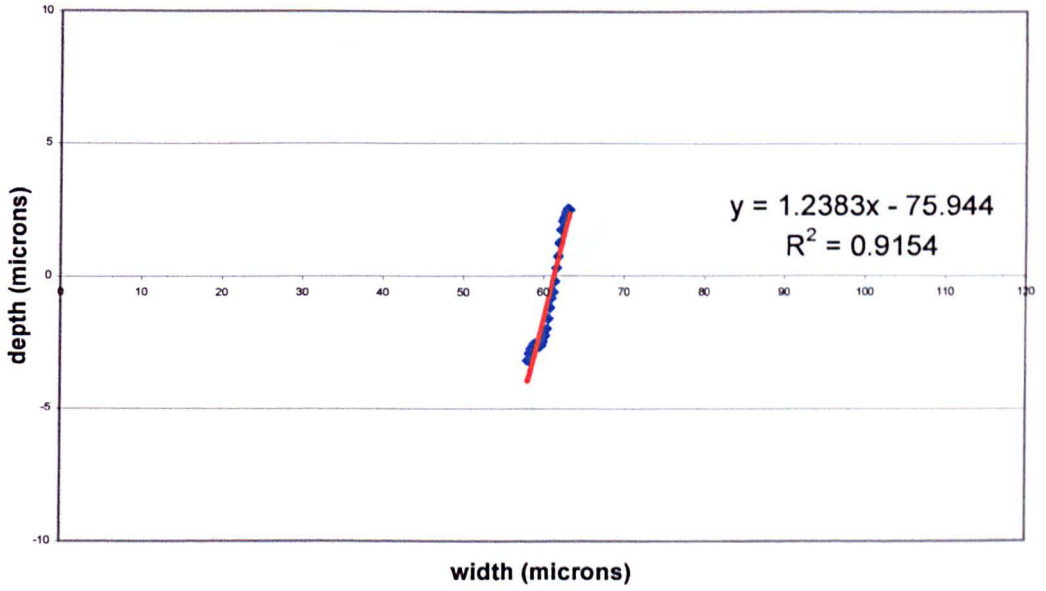

The gradient of the cell wall of a YAG cell at measurement point 3y2 on anilox Harper 1

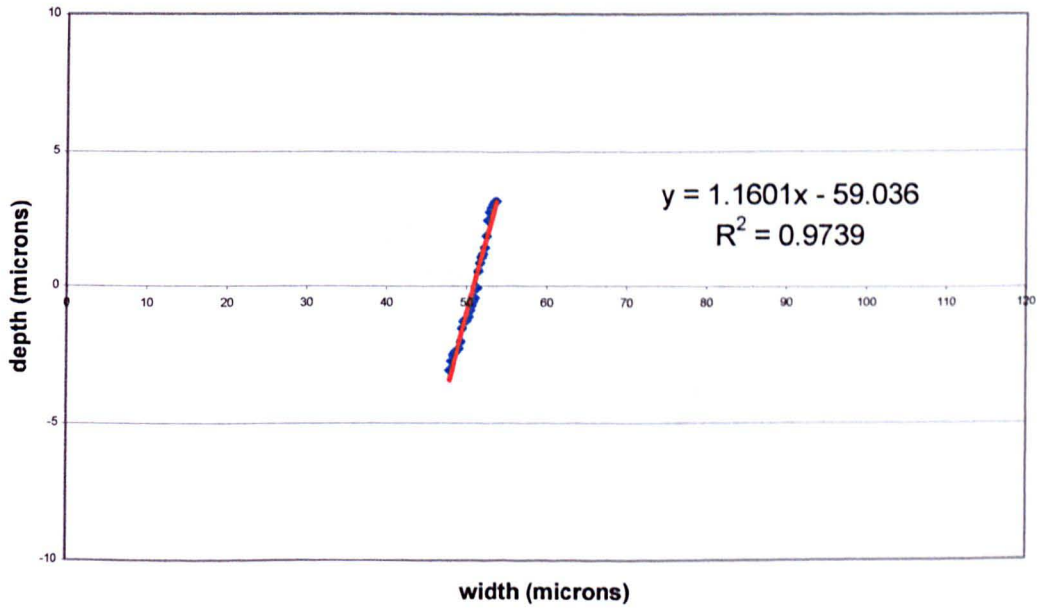

Appendix Section A6-2 continued

Gradients measurements made from the cell profiles of the CO_2 and YAG cells on anilox Harper 1, Measured using the Veeco interferometer.

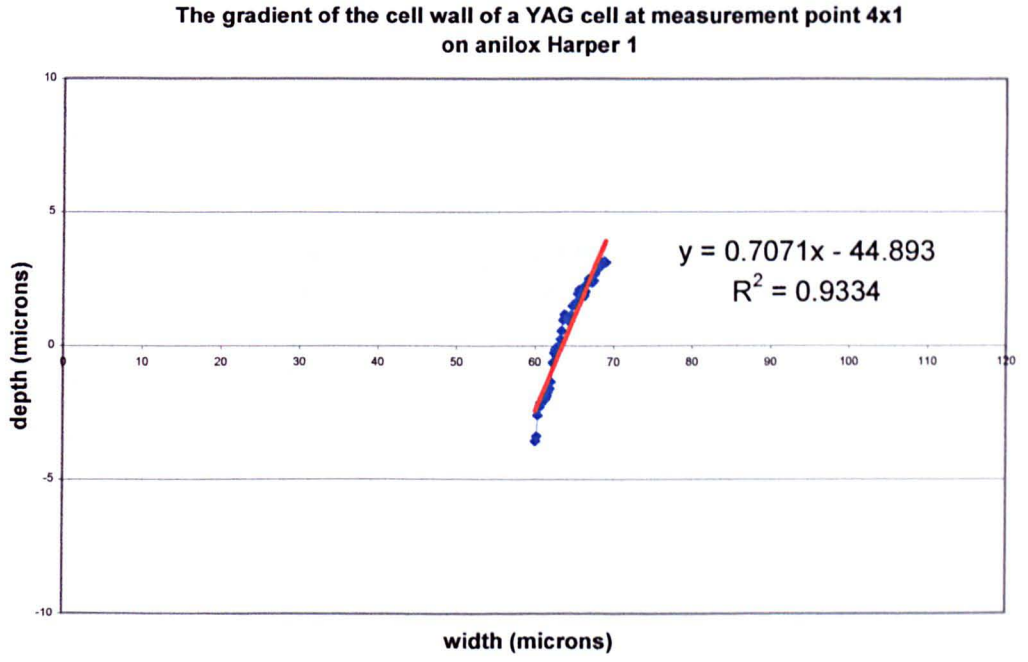

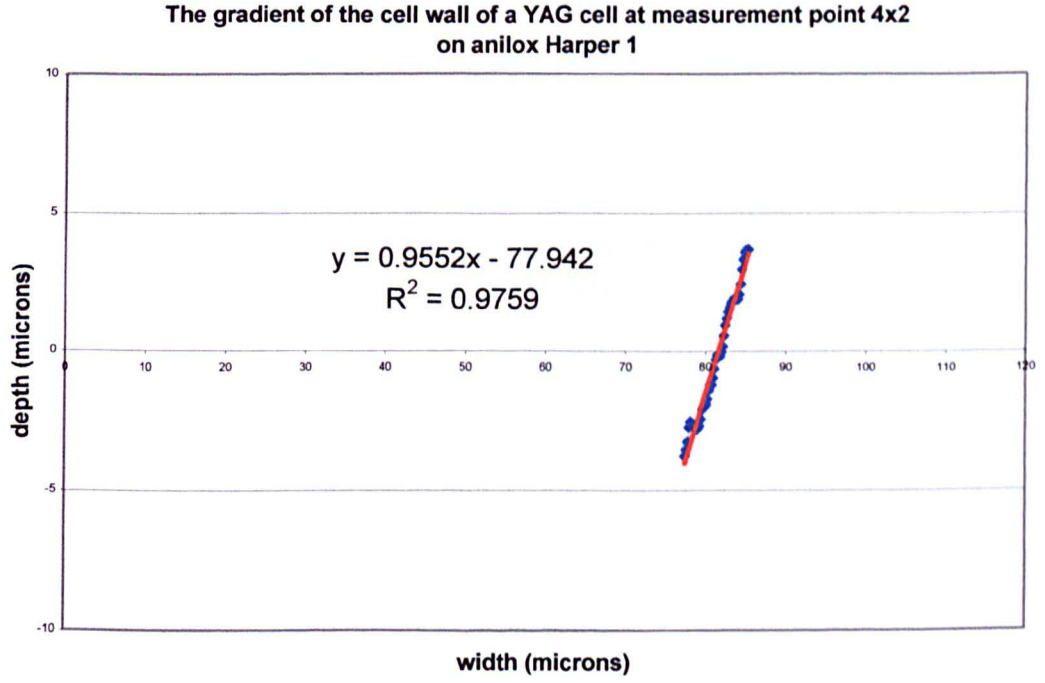

Appendix Section A6-2 continued

Gradients measurements made from the cell profiles of the CO_2 and YAG cells on anilox Harper 1, Measured using the Veeco interferometer.

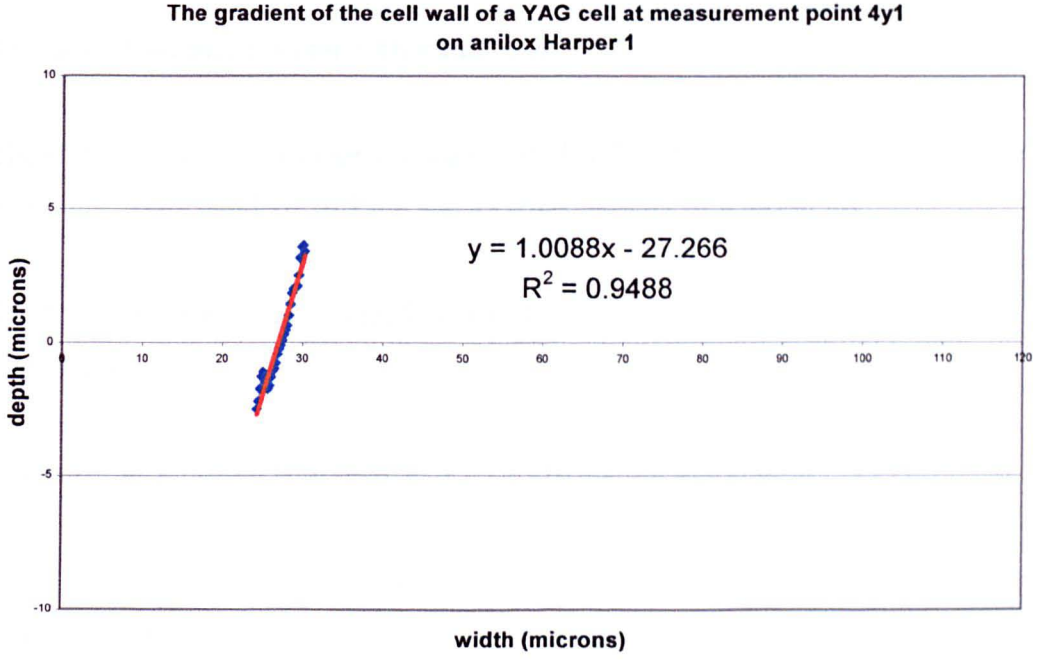

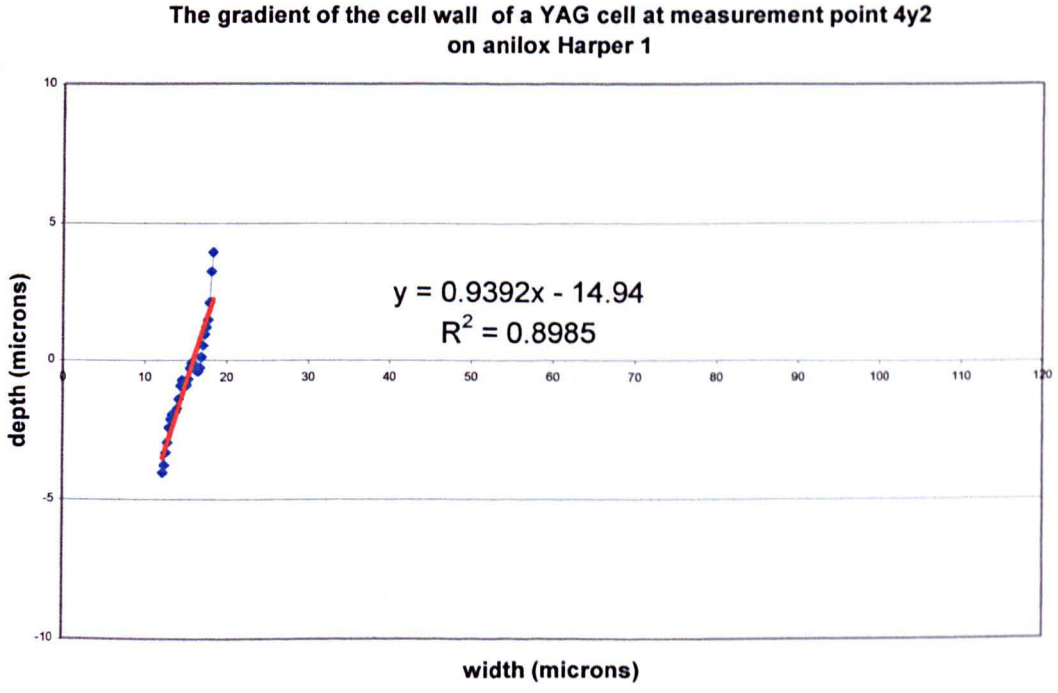

Appendix Section A6-3

Calculations for the ellipsoid model used to obtain the r values for use with the Wenzel equation.

A6-3a Calculating r on the CO_2 band of Harper 1

The CO_2 engraving on Harper 1 has a reported cell opening of 38.0 μm, a wall width of 4.0 μm, a cell depth of 10.7 μm and a caring capacity of 4.08 cm^3/m^2.

The CO2 engraving approximated to an oblate ellipsoid with radii a = 10.7 μm and b = 19.0 μm.

For an oblate ellipsoid with radii: a, b, b (a < b) and surface area: S [130]

$S = 2\pi\, b(b+a \operatorname{arcsinh}[be/a]/[be/a])$,

where $e = \sqrt{(b^2-a^2)}/b$

e = 0.83

be/a = 1.47

arcsinh [be/a] = 1.18

S = 2842.85

S/2 = 1421.42 μm^2 The estimate of the surface area of a cell on the CO_2 engraving using the ellipsoid model.

The cell wall was assumed to be circular, and the diameter of the land area of the cell was assumed to be the cell opening plus the width of the cell wall. This made the radius of the cell (38 + 4) / 2 or 21μm. This gives the flat land area the cell of 1385.44 μm^2 for a CO_2 cell

The actual land area is equal to the surface area calculated from the hemi-ellipsoid plus the land area from the wall.

Calculations for the ellipsoid model used to obtain the r values for use with the Wenzel equation.

The land area of the wall is equal to the area of the call plus the wall minus the area of the cell. The area of the cell is $\pi*19^2$ or 1134.11 μm^2

The land area from the wall of the CO_2 cell = 1385.44 – 1134.11 = 251.33 μm^2

The actual area of one cell and its land for the model then becomes

actual area CO_2 = 1421.42 + 251.33 = 1672.75

When the calculated surface area for the hemi-ellipsoid model plus the wall area is divided by the flat land area, Wenzel's r factor is obtained.

For the CO_2 band on Harper 1 r = 1672.75 / 1385.44 = 1.2

A6-3b Calculating r on the YAG band of Harper 1.

The YAG engraving has a reported cell opening of 19.1 μm, a wall width of 2.1 μm, a cell depth of 10.6 μm and a caring capacity of 3.63cm^3/m^2.

The YAG band was approximated by a prolate ellipsoid with radii a = 10.6 μm and b = 9.55 μm

The following equations were used to calculate the surface area of the ellipsoid. This value was then halved to get the surface area of the hemi-ellipsoid.

For a prolate ellipsoid with radii: a, b, b (a > b) and surface area: S [130]

$S = 2\pi b(b+a \arcsin[e]/e)$,

where $e = \sqrt{(a^2-b^2)}/a$

e = 0.43

Appendix Section A6-3 continued

Calculations for the ellipsoid model used to obtain the r values for use with the Wenzel equation.

arcsine[e] = 0.45

S = 1250.66

S/2= 625.33 μm^2 The estimate of the surface area of a cell on the YAG engraving using the ellipsoid model.

The cell wall was assumed to be circular, and the diameter of the land area of the cell was assumed to be the cell opening plus the width of the cell wall (half at each side of the cell. The other half assumed to belong to the neighbouring cells). The diameter is therefore 19.1 + 2.1 or 21.2. (The radius therefore being half this, 10.6) The area of a circle is given by πr^2 This gives the flat land area the cell of 352.99 μm^2.

The actual land area is equal to the surface area calculated from the hemi-ellipsoid plus the land area from the wall.

This land area is equal to the area of the call plus half the wall minus the area of the cell. The area of the cell is $\pi * (19.1/2)^2 = 286.52\ \mu m^2$

The land area from the wall of the YAG cell = 352.99 –286.52 = 66. 47 μm^2

The actual area of one cell and its land for the model then becomes

actual area YAG = 625.33 + 66.47 = 691.90 μm^2.

When the calculated surface area is divided by the flat land area for the hemi-ellipsoid model plus the wall area Wenzel's r factor is obtained.

For the YAG band on Harper 1 r = 691.80/ 352.99 = 2.0

Appendix Section A6-3 continued

Calculations for the ellipsoid model used to obtain the r-values for use with the Wenzel equation.

A6-3c Calculating r on the bands of Harper 2.

The CO_2 and YAG bands on anilox Harper 2 were both approximated by ellipsoids in the same way as described for the YAG cells of Harper 1.

The CO_2 band has cells with an opening of 22.0 μm a depth of 7.8 μm and a land of 3.0 μm. This approximates to an oblate ellipsoid with radii of 7.8, 11.0 and 11.0. The surface area of the ellipsoid was 1146.49 μm^2 the surface area of the cell was therefore 573.25 μm^2

The wall area was calculated to be 110.74 μm^2 giving a total area of 683.99 μm^2 the apparent area corresponding to the cell and half the wall was 490.87 μm^2

This gave an r-value of 683.99 / 490.87 r = 1.4 for the CO_2 band on Harper 2.

The YAG band has cells with an opening of 19.4 μm a depth of 7.5 μm and a land of 2.1μm. This approximates to an oblate ellipsoid with radii of 7.5, 9.7 and 9.7. The surface area of the ellipsoid was 956.48 μm^2 the surface area of the cell was therefore 478.24 μm^2

The wall area was calculated to be 67.46 μm^2 giving a total area of 545.70 μm^2 the apparent area corresponding to the cell and half the wall was 363.05 μm^2

This gave an r-value of 545.70 / 363.05 r = 1.5 for the YAG band on Harper 2.

Appendix Section A6-4

Calculation of the cell volumes predicted by the hemi-ellipsoid model on anilox Harper 1.

The volume of the hemi-ellipsoid was calculated using the formula [130]

$$V = (4/3\pi a*b*c)/2$$

Where a b and c are the axis of the ellipsoid (for both cells c = b) and were expressed in centimetres. The resulting volumes were then divided by the surface area of the cell opening (including half the wall) in metres to give values comparable to the EVT volume.

Calculated volumes for the CO_2 band. volume = 16180.04μm^3 or $1.61x10^{-8}$ cm^3

Therefore volume of cell = $1.61x10^{-8}$ / 2 or $8.1*10^{-9}$

Cell opening area (from A6-1a) = 1385.44μm^2 or $1.39x10^{-9}$ m^2

Volume in cm^3 / area in m^2 is $8.1*10^{-9}$/ $1.39*10^{-9}$ = **5.8 cm^3/m^2**

Calculated volumes for the YAG band. volume = 4049.50μm^3 or $4.05*10^{-9}$ cm^3

Therefore volume of cell = $4.05x10^{-9}$ / 2 or $2.02*10^{-9}$

Cell opening area (from A6-1b) = 352.99 μm^2 or $3.53*10^{-10}$ m^2

Volume in cm^3 / area in m^2 is $2.02*10^{-9}$/ $3.53*10^{-10}$ = **5.7 cm^3/m^2**

Appendix Section A6-5

The surface area of the parabolas modelled to fit the cells on anilox rolls Harper 1 and 2.

The surface area S of a parabola rotated around the y axis is given by the equation [133]

$$S = 2\pi \int_a^b g(y)\sqrt{1+[g'(y)]^2}\, dy$$

The equation of the parabola is of the form $y = ax^2 + b$
The integral in the form of x as a function of y is

$S = \int 2\pi [1+(dx/dy)^2]^{½}$ dy between limits p and q

$dx/dy = ½ a^{-½} (y-b)^{-½}$ so the integral becomes

$S = \int 2\pi [-a^{-½} (y-b)^{-½}] [1+ ¼ a^{-1} (y-b)^{-1}]^{½}$ dy

$S = \int 2\pi [-a^{-½} (y-b)^{-½}] [(4a\{y-b)+1)/\{4a(y-b))]^{½}$ dy

Cancelling out the $(y-b)^{½}$ terms leaves

$S = \int 2\pi a^{-½} / 2a^{½} (4a(y-b)+1)^{½}$ dy

$S = \pi / a \int (4a(y-b)+1)^{½}$ dy

$S = \pi / a [(1/4a) (2/3) (4a(y-b)+1)^{3/2}]$ between limits p and q

$S = \pi / 6a^2 \{[4a(y-b)+1]^{3/2}\}$ between limits p and q

This is general formula. Limits p and q relate to the cell depth and terms a and b are given by the parabola equations for each cell

For CO_2 cells of Harper 1 the limits of y are p = 0 and q = -10.7 a = 0.0296 and b = -10.7

$S = \pi / 6(0.0296)^2 [(4(0.0296)(0 + 10.7)+1)^{3/2} - (4(0.0296)(-10.7+10.7) +1)^{3/2}]$

$S = 1442.05\ \mu m^2$ This is the surface area of the parabola approximating the CO_2 cells on anilox Harper 1

The surface area of the parabolas modelled to fit the cells on anilox rolls Harper 1 and 2.

For YAG cells of Harper 1 the limits of y are p = 0 and q = -10.6, a = 0.117 and b = -10.6

$S = \pi / 6(0.117)^2 [(4(0.117)(0 + 10.6)+1)^{3/2} - (4(0.117)(-10.6+10.6)+1)^{3/2}]$

$S = 518.40\ \mu m^2$ This is the surface area of the parabola approximating the YAG cells on anilox Harper 1

For CO_2 cells of Harper 2 the limits of y are p = 0 and q = -7.8, a = 0.0645 and b = -7.8

$S = \pi / 6(0.0645)^2 [(4(0.0645)(0 + 7.8)+1)^{3/2} - (4(0.0645)(-7.8+7.8)+1)^{3/2}]$

$S = 532.18\ \mu m^2$ This is the surface area of the parabola approximating the CO_2 cells on anilox Harper 2

For YAG cells of Harper 2 the limits of y are p = 0 and q = -7.5, a = 0.0797 and b = -7.5

$S = \pi / 6(0.0797)^2 [(4(0.0797)(0 + 7.5)+1)^{3/2} - (4(0.0797)(-7.5+7.5)+1)^{3/2}]$

$S = 432.29\ \mu m^2$ This is the surface area of the parabola approximating the CO_2 cells on anilox Harper 2

Appendix Section A6-6

Calculation of Wenzel r-values from the parabola surface areas.

A6-7a Calculations of r-values on Harper 1.

The surface area calculations from the parabola models of the cells on Harper 1 detailed in Section A6-5 were used to calculate Wenzel's r values by the same method detailed in Section A6-3.

As shown in Section A6-3a, the land area from the wall of the CO_2 cell = 251.33 μm^2

Section A6-6 gives the area of the parabola that approximates the CO_2 band on Harper 1 as 1442.05 μm^2.

The actual area of one cell and its land for the parabola model then becomes
actual area CO_2 = 1442.05 + 251.33 = 1693.38 μm^2

When the calculated surface area for the parabola model plus the wall area is divided by the flat land area, Wenzel's r factor is obtained. The flat land area was shown to be 1385.44 μm^2 in Section A6-3a.

For the CO_2 band on Harper 1 r = 1693.38 / 1385.44 = 1.2

As shown in Section A6-3b, the land area from the wall of the YAG cell = 66.47 μm^2.

Section A6-6 gives the area of the parabola that approximates the YAG band on Harper 1 as 518.40 μm^2.

The actual area of one cell and its land for the parabola model then becomes
actual area YAG = 518.40 + 66.47 = 584.87 μm^2.

When the calculated surface area for the parabola model plus the wall area is divided by the flat land area, Wenzel's r factor is obtained. The flat land area was shown to be 352.99 μm^2 in Section A6-3b

For the YAG band on Harper 1 r = 584.87 / 352.99 = 1.7

Appendix Section A6-6 continued

Calculation of Wenzel r-values from the parabola surface areas.

6-7b Calculations of r-values on Harper 2.

As shown in Section A6-3c, the land area from the wall of the CO_2 cell = 110.74 μm^2

Section A6-6 gives the area of the parabola that approximates the CO_2 band on Harper 2 as 532.18 μm^2

The actual area of one cell and its land for the parabola model then becomes
actual area CO_2 = 532.18 + 110.74 = 642.92 μm^2

When the calculated surface area for the parabola model plus the wall area is divided by the flat land area, Wenzel's r factor is obtained. The flat land area was shown to be 490.87 μm^2 in Section A6-3

For the CO_2 band on Harper 2 r = 642.92 / 490.87 = 1.3

As shown in Section A6-3c, the land area from the wall of the YAG cell = 67.46 μm^2.

Section A6-6 gives the area of the parabola that approximates the YAG band on Harper 2 as 432.29 μm^2.

The actual area of one cell and its land for the parabola model then becomes
actual area YAG = 432.29 + 67.46 = 499.75 μm^2.

When the calculated surface area for the parabola model plus the wall area is divided by the flat land area, Wenzel's r factor is obtained. The flat land area was shown to be 363.05 μm^2 in Section A6-3c

For the YAG band on Harper 2 r = 499.75 / 363.05 = 1.4

Appendix Section A6-7

Using the parabola model to calculate the depth to which a CO_2 cell is unwet according to the Cassie and Baxter model.

This example shows the calculation for the CO_2 cell on anilox Harper 1. the parabola which approximates the cell dimensions is shown below (all other calculations were done in the same way using different parabola equations).

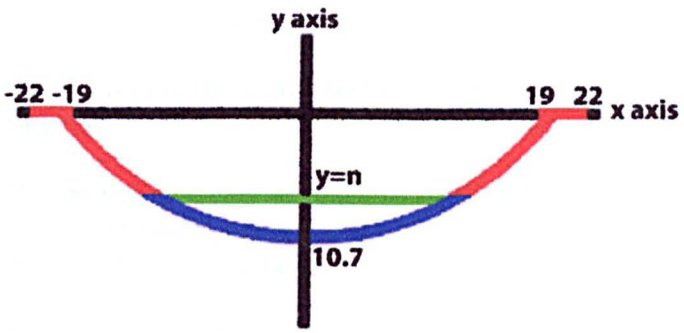

The green line is the area of air/water interface. The area interface corresponds to the area of the circle with its diameter at y=n
The red line shows the area of the cell and land in contact with the water .
The blue line shows the unwet area.

The surface area was calculated as shown in Section A6-5 using the general formula

$$S = \pi / 6a^2 \{[4a(y-b)+1]^{3/2}\}$$ **between limits p and q**

This time the surface area of the unwet area was calculated by using the limits of y = n and y = -10.7. this was then subtracted from the total area (cell plus land) to get the total wet area

The x value at n was calculated from the equation of the parabola and used to calculate the area of air/liquid interface.

The ratio between the air/liquid interface and solid/liquid interface was calculated.

An Excel spreadsheet was set up to carry out these calculations so that n could be easily varied until the ratio predicted by the Cassie and Baxter equation was found.

The value of n that produced this ratio was then used to find the depth of the cell which remained unwet.

In the case of the CO_2 cell on anilox Harper 1 a value of n of –9.4 produced an unwet parabola of area of 139.74μm^2 this was subtracted from the total cell and land area of 1693.38μm^2 to give 1553.64μm^2

Appendix Section A6-7 continued

Using the parabola model to calculate the depth to which a CO_2 cell is unwet according to the Cassie and Baxter model.

The total surface area of the interfaces was calculated by summing the area of the wet parabola section and the air/liquid interface. In this case the n values of –9.43 gave a corresponding x value of 6.55 which produced an area of 134.79 μm^2 this was added to the wet portion of the parabola, already known to be 1553.64 μm^2 to give a total of 1688.43 μm^2.

The fraction of the total interface area that is solid/liquid interface was given by 1553.64 / 1688.43 = 0.92 or 92 % (and therefore the air/liquid interface is 8%.

The spreadsheet was designed so that the terms from the equations of parabolas used to approximate engraved cells on the other bands studied could be entered and the results generated by the same method as described above.

The equations and values of n selected and corresponding unwet heights are shown below

Harper 1 YAG band $y = 0.1170x^2 - 10.6$ n = -5.93, unwet height = 4.67μm

Harper 2 CO_2 band $y = 0.0645x^2 - 7.8$ n = -5.73, unwet height = 2.07μm

Harper 2 YAG band $y = 0.0797x^2 - 7.5$ n = -4.06, unwet height = 2.44μm

Appendix Section A6-8

Mathematical modelling of the cells on anilox Pira 1.

The cell count is known to be 149 cells per cm or 14900 cells per m. 1 cell (including its land area) therefore has a width of $6.7*10^{-5}$ m and an area of $4.5*10^{-9}$ m^2.

Without the use of an optical measurement device it is impossible to provide an accurate figure for the width of the land area between the cells. A figure for the percentage area occupied by the cells of a 45° engraving of 53% was given by the DFTA [47] this is close to estimates made from sample photographs of 45° engravings made by taking measurements using adobe illustrator.

53% of $4.5*10^{-9}$ m^2 is $2.4*10^{-9}$ m^2 this is the area of the cell opening

The shape of cell can be approximated to a square based pyramid, with a surrounding land area as shown below. The opening is therefore square and can be found by taking the root of the area. $4.9*10^{-5}$ m or 49 microns

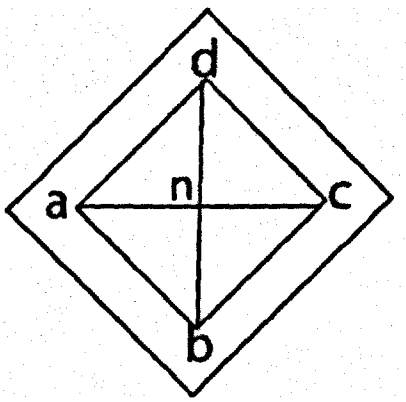

Top view of one cell

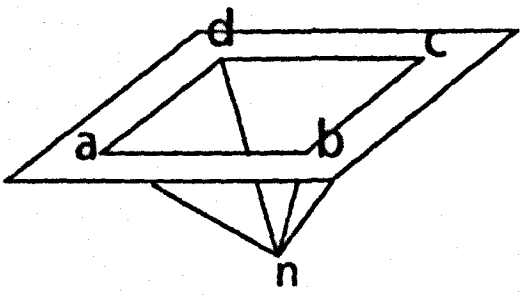

Side view of one cell

The error in this measurement is uncertain as it is dependent on the accuracy of the value 53% to describe the percentage of the roll area taken up by cells. there is also a large error involved in approximating the cell to a square based pyramid.

Cell opening 49 microns

The volume of the cell can be calculated from the values provided by Pira International for the reported volume in cm^3/m^2. This is multiplied by the area taken up by one cell (with wall) to get the volume of one cell.

For band one 3.3 cm^3/m^2 * $4.5*10^{-9}m^2$ = $1.5*10^{-8}cm^3$ or $1.5*10^{-14}$ m^3
For band two 3.8 cm^3/m^2 * $4.5*10^{-9}m^2$ = $1.7*10^{-8}$ cm^3 or $1.7*10^{-14}m^3$
For band three 4.4 cm^3/m^2 * $4.5*10^{-9}m^2$ = $1.9*10^{-8}$ cm^3 or $1.9*10^{-14}m^3$

Appendix Section A6-8 continued

Mathematical modelling of the cells on anilox Pira 1.

The depth of the cell corresponds to the height of the pyramid. The pyramid height was then found by rearranging the formula for the volume of a square based pyramid

$V = a^2 h/3$ to give

$h = 3V/a^2$, where a is the width of the pyramid (and in this case the cell opening), h is the height and V is the volume

For band one $h = 3*1.5*10^{-14}/2.4*10^{-9}$
$h = 19$ microns
For band two $h = 3*1.7*10^{-14}m^3/2.4*10^{-9}$
$h = 21$ microns
For band three $h = 3*1.9*10^{-14}m^3/2.4*10^{-9}$
$h = 24$ microns

Appendix Section A6-9

Calculating the surface area of the pyramid approximation to the cells on anilox Pira 1 for the estimation of Wenzel's r-value.

The surface area of the pyramid model of the cell can be found by adding together the area of the four triangles making up the cell walls and the land area surrounding the cell.

The height of the triangular face is found from the right angle triangle m n o. the length no is the cell depth which has already been determined as 19 microns for band one, 21 microns for band two, and 24 microns for band three. The length *mo* is half the cell opening i.e. 49/2 microns. The length *mn* can be found by using the Pythagoras theorem

The values for the length *mn* were

Band one $mn = \sqrt{(19^2 + (49/2)^2)} = 31$ microns or $3.1*10^{-5}$ m
Band two $mn = \sqrt{(21^2 + (49/2)^2)} = 32$ microns or $3.2*10^{-5}$ m
Band three $mn = \sqrt{(24^2 + (49/2)^2)} = 34$ microns or $3.4*10^{-5}$ m

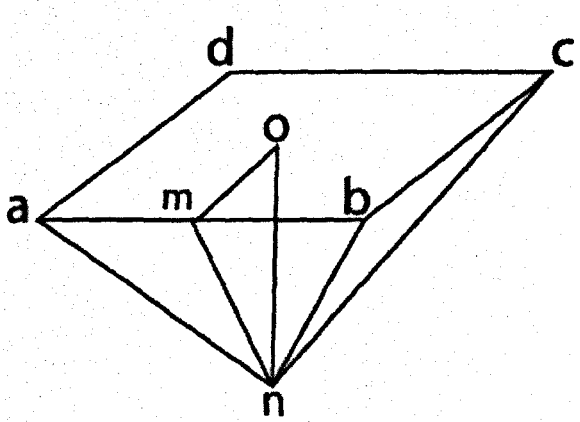

The area of the four triangular faces is found from four lots of half the base (1/2*ab*) multiplied by the height (*no*) or 2*ab**h.

For band one $2*4.9*10^{-5}*3.1*10^{-5} = 3.0*10^{-9}m^2$
For band two $2*4.9*10^{-5}*3.2*10^{-5} = 3.1*10^{-9}m^2$
For band three $2*4.9*10^{-5}*3.4*10^{-5} = 3.3*10^{-9}m^2$

These figures must then be added to the land area. Using the assumption that the cell occupies 53% of the total area, which is $4.5*10^{-9}$. The remaining 47% or $2.1*10^{-9}$ m^2 is the land area.

For band one $2.1*10^{-9} + 3.0*10^{-9} = 5.1*10^{-9}m^3$
For band two $2.1*10^{-9} + 3.1*10^{-9} = 5.2*10^{-9}m^3$
For band three $2.1*10^{-9} + 3.3*10^{-9} = 5.4*10^{-9}m^3$

Appendix Section A6-9 continued

Calculating the surface area of the pyramid approximation to the cells on anilox Pira 1 for the estimation of Wenzel's r-value.

To get the Wenzel r-values the area of a flat sample was assumed to be $4.5*10^{-9}$

The values estimated for the true area of the cell are divided by the area of the flat sample to get r

For band one $5.1*10^{-9}/ 4.5*10^{-9} = 1.13$
For band two $5.2*10^{-9}/ 4.5*10^{-9} = 1.15$
For band three $5.4*10^{-9}/ 4.5*10^{-9} = 1.20$

Appendix Section A6-10

Finding the slope of the pyramid approximation to the cells on anilox Pira 1 for use with the Shuttleworth and Bailey equation.

The height and half the base of the pyramid form a right-angled triangle *nmo*. The angle at the base of this pyramid, angle *onm*, when added to the angle corresponding to the slope of the pyramid, equals 90°. The angle at the base of the pyramid can be calculated using simple trigonometry.

$\tan\theta$ = opp/adj

For band one $\tan\theta = (49/2) / 19$ $\theta = 52°$ therefore the gradient = 38°
For band two $\tan\theta = (49/2) / 21$ $\theta = 49°$ therefore the gradient = 41°
For band three $\tan\theta = (49/2) / 24$ $\theta = 46°$ therefore the gradient = 44°

Appendix Section A6-11

Cell profiles of the CO_2 and YAG cells on anilox Harper, Measured using the Veeco roll-scope interferometer.

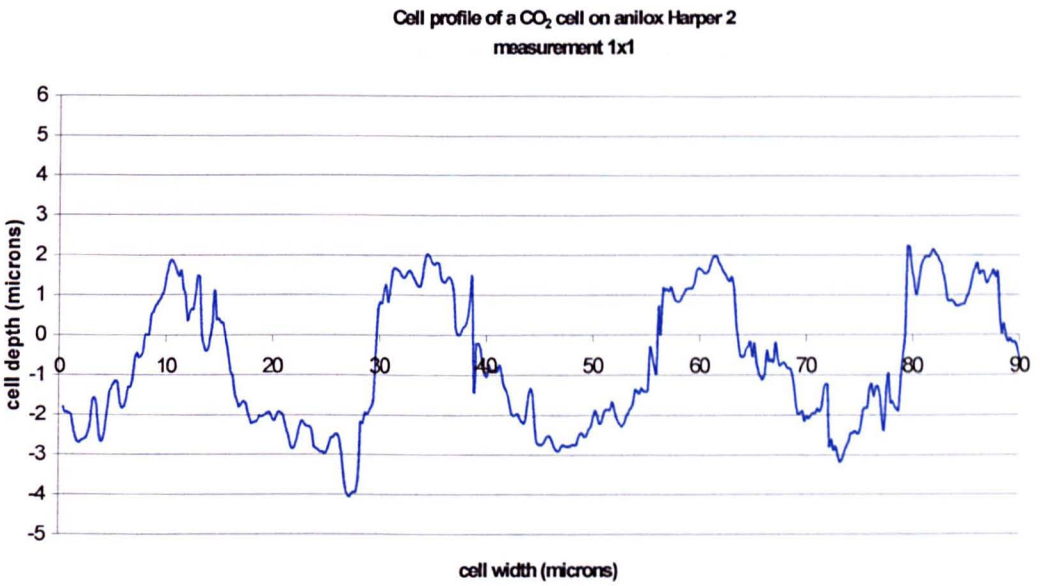

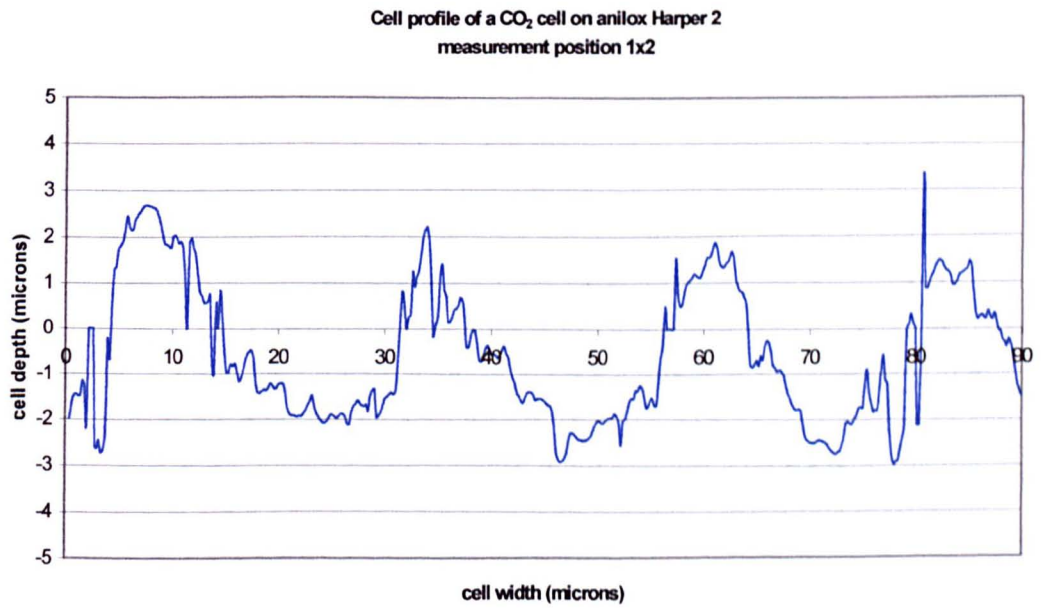

Appendix Section A6-11 continued

Cell profiles of the CO_2 and YAG cells on anilox Harper, Measured using the Veeco roll-scope interferometer.

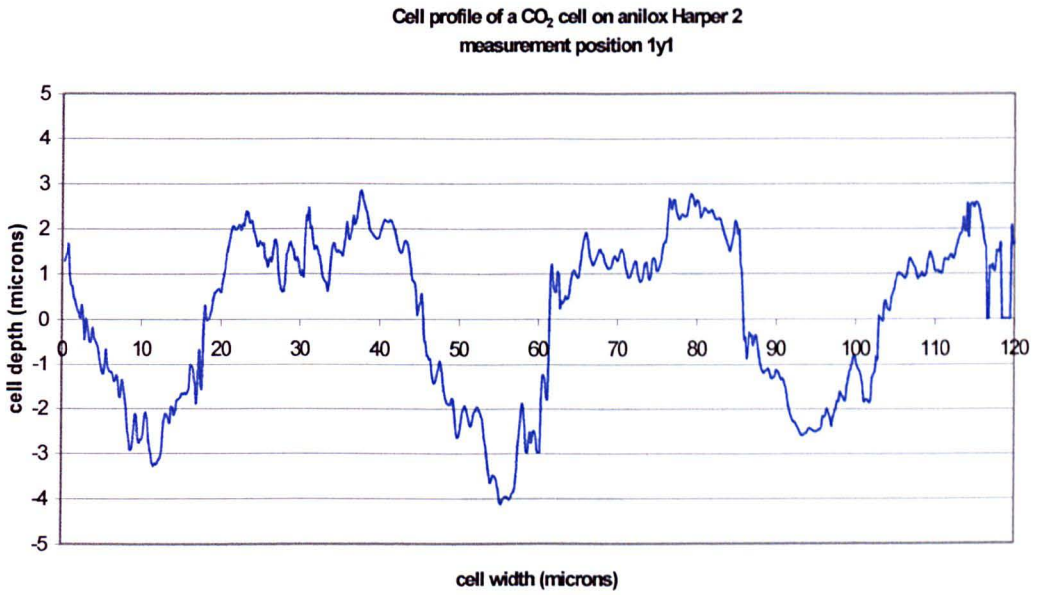

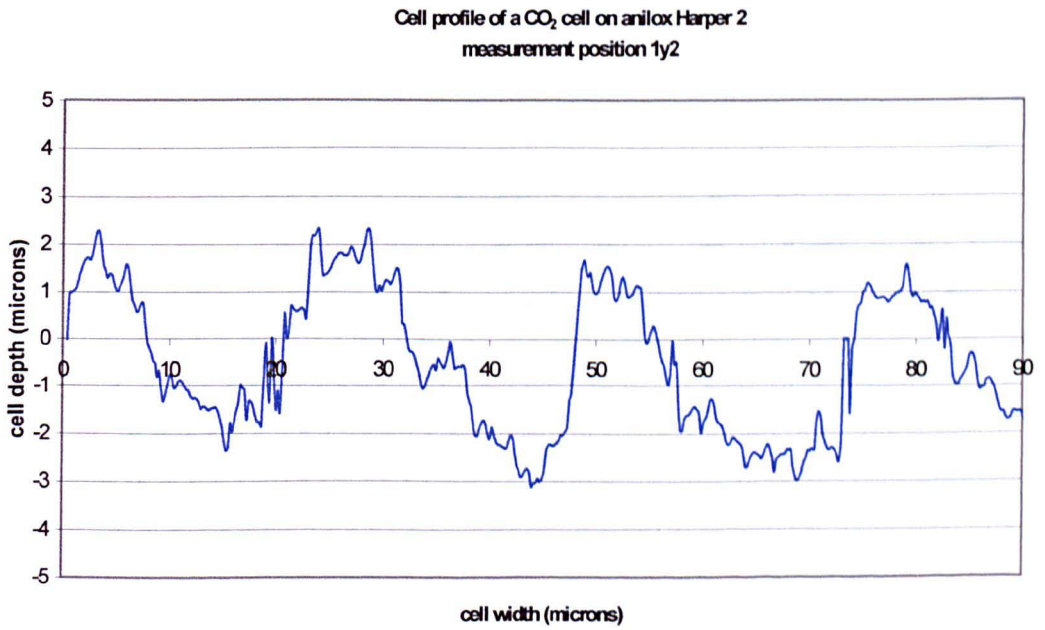

Appendix Section A6-11 continued

Cell profiles of the CO_2 and YAG cells on anilox Harper, Measured using the Veeco roll-scope interferometer.

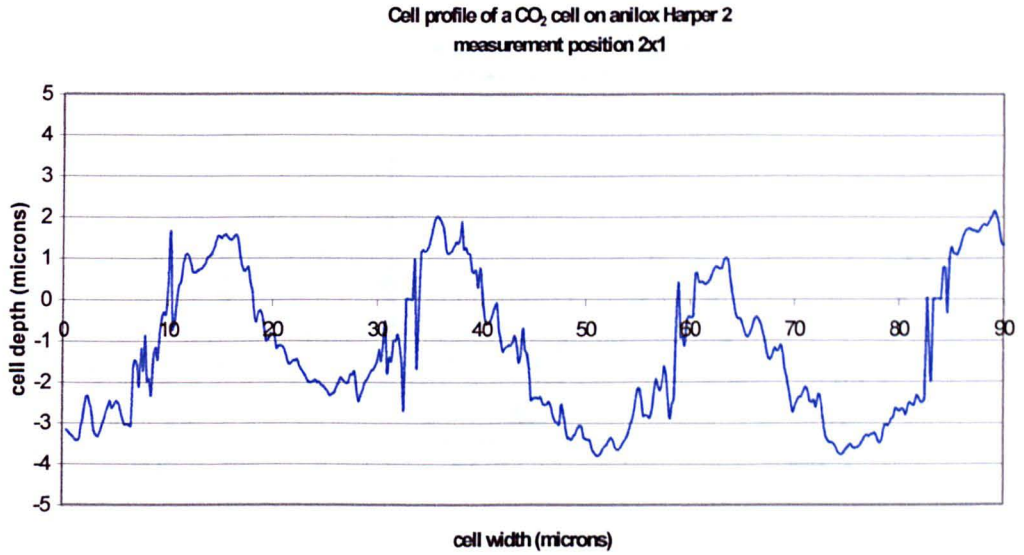

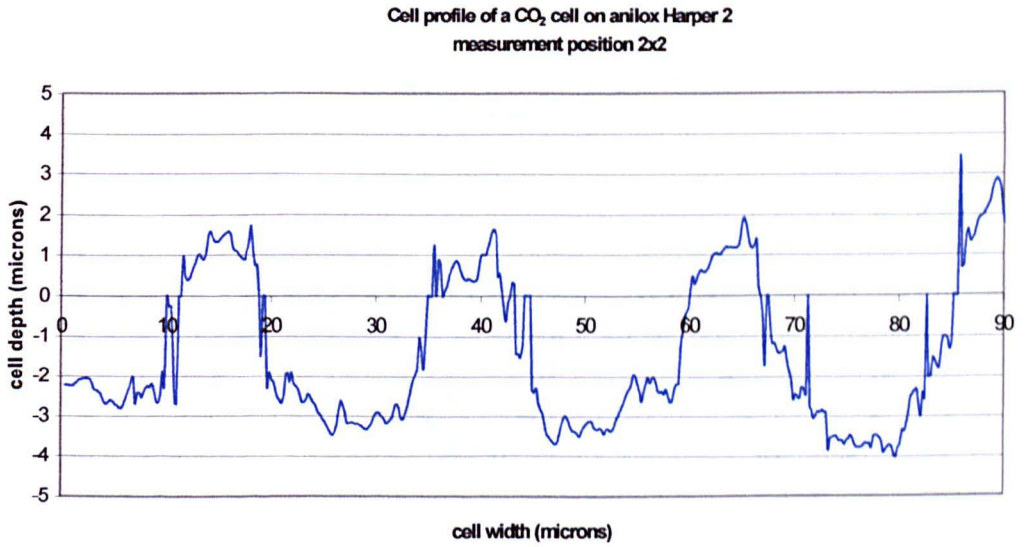

Appendix Section A6-11 continued

Cell profiles of the CO_2 and YAG cells on anilox Harper, Measured using the Veeco roll-scope interferometer.

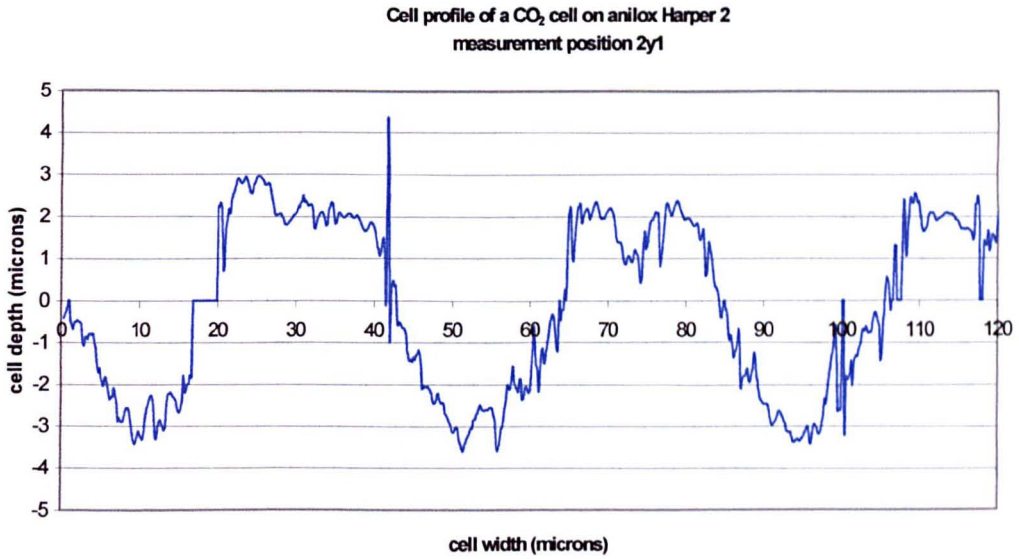

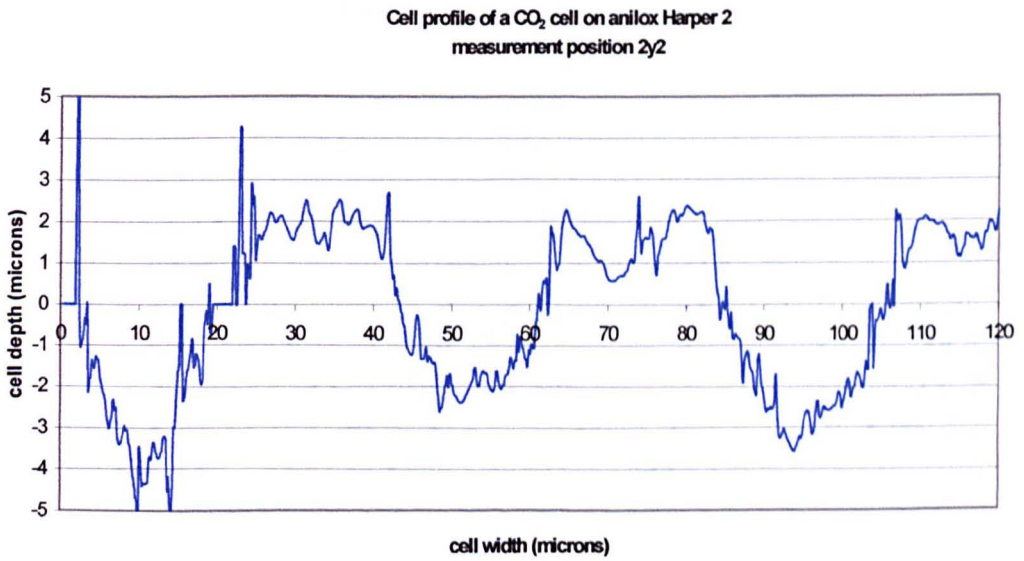

Appendix Section A6-11 continued

Cell profiles of the CO_2 and YAG cells on anilox Harper, Measured using the Veeco roll-scope interferometer.

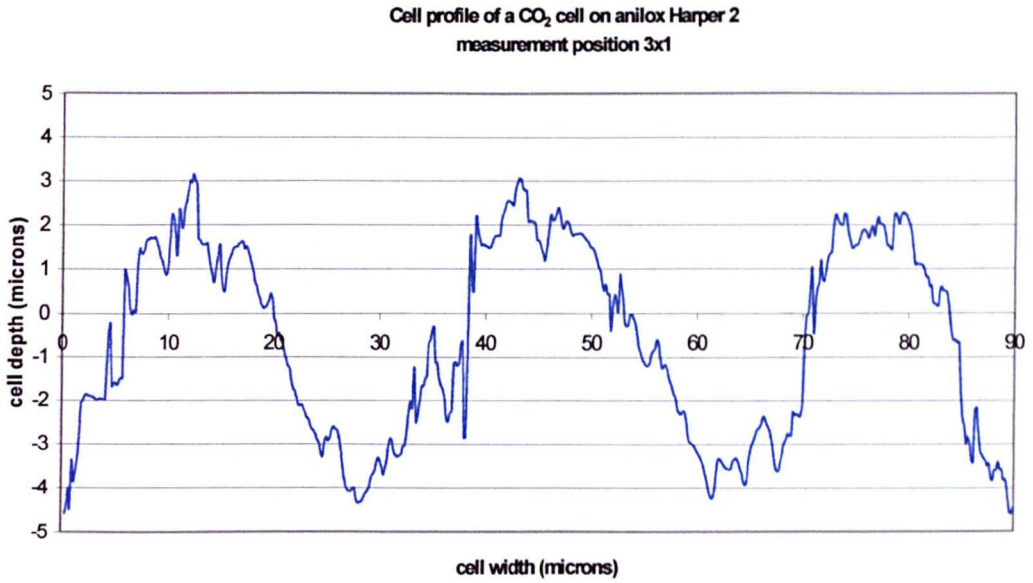

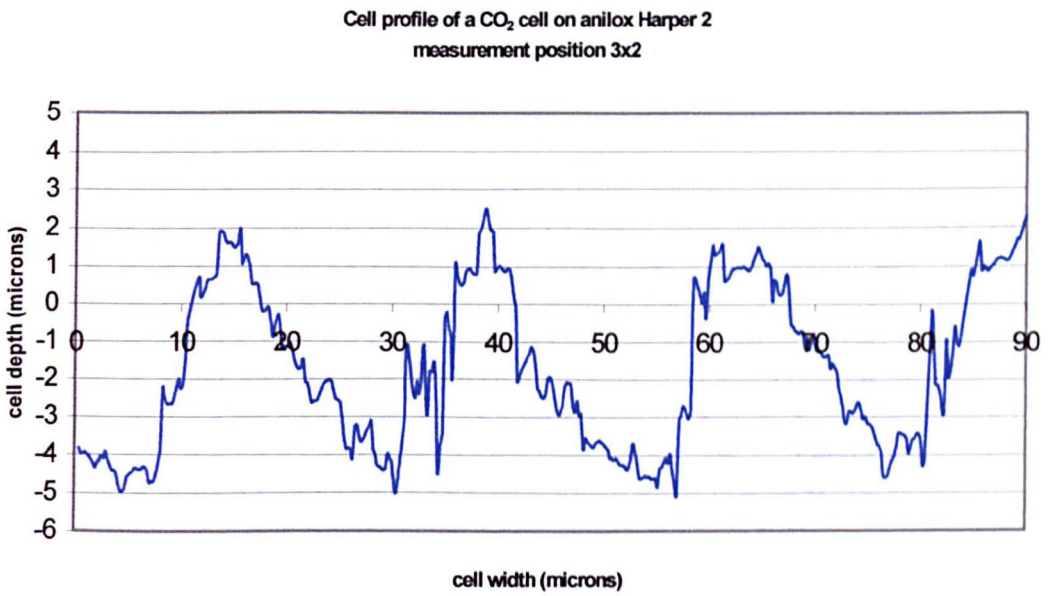

Appendix Section A6-11 continued

Cell profiles of the CO_2 and YAG cells on anilox Harper, Measured using the Veeco roll-scope interferometer.

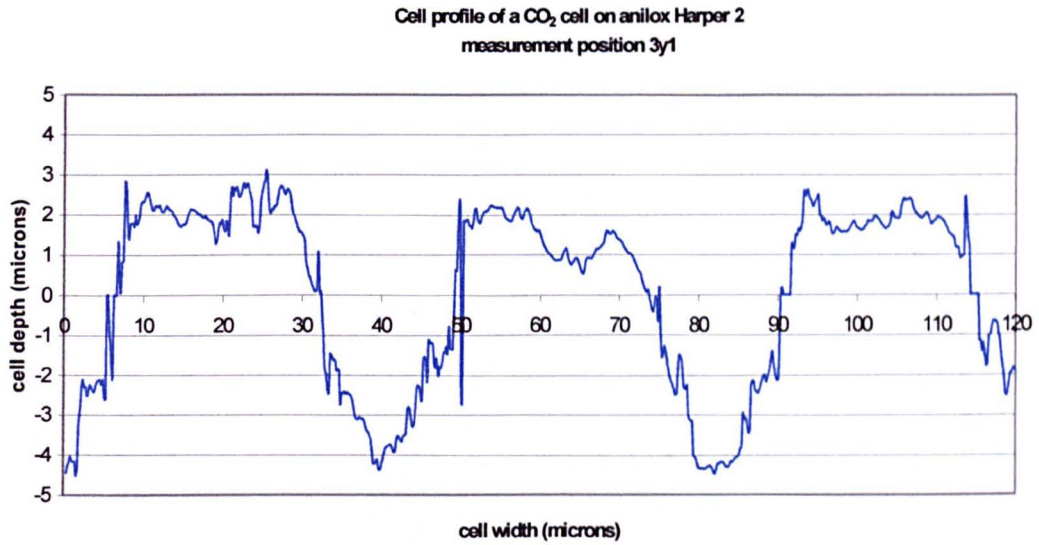

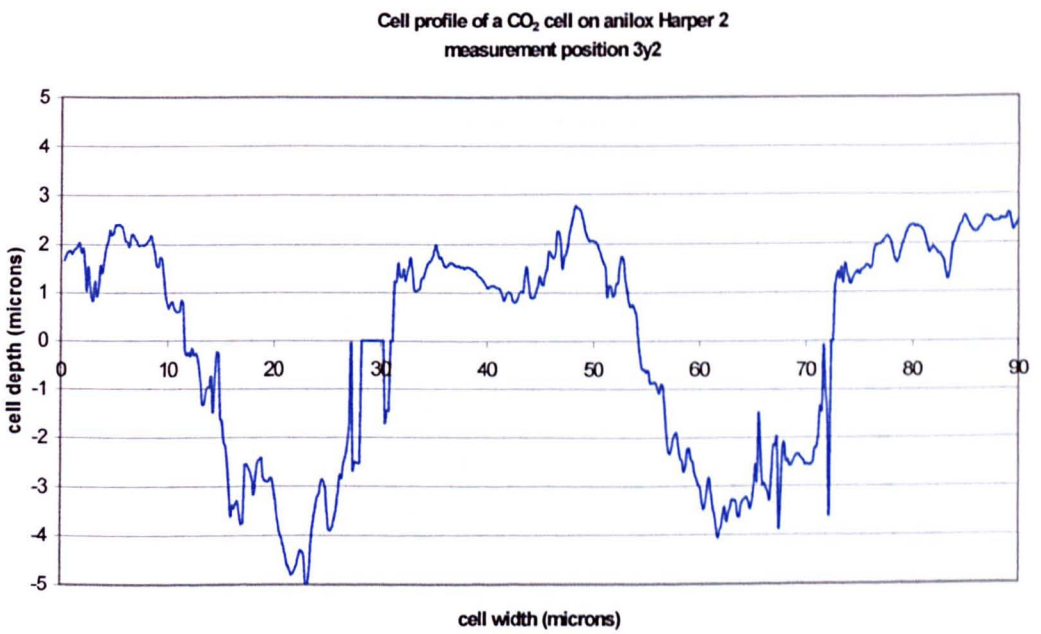

Appendix Section A6-11 continued

Cell profiles of the CO_2 and YAG cells on anilox Harper, Measured using the Veeco roll-scope interferometer.

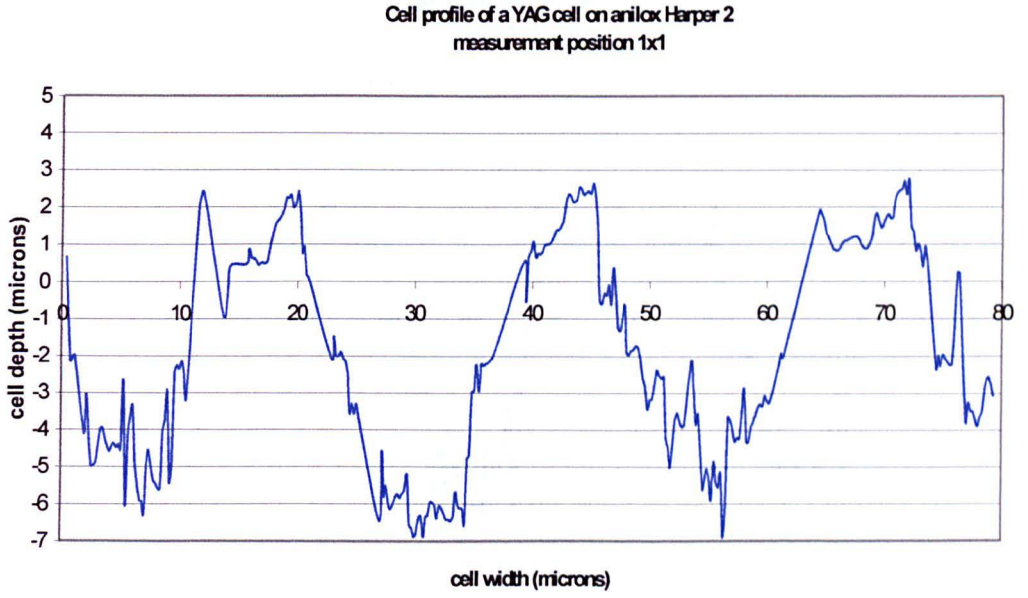

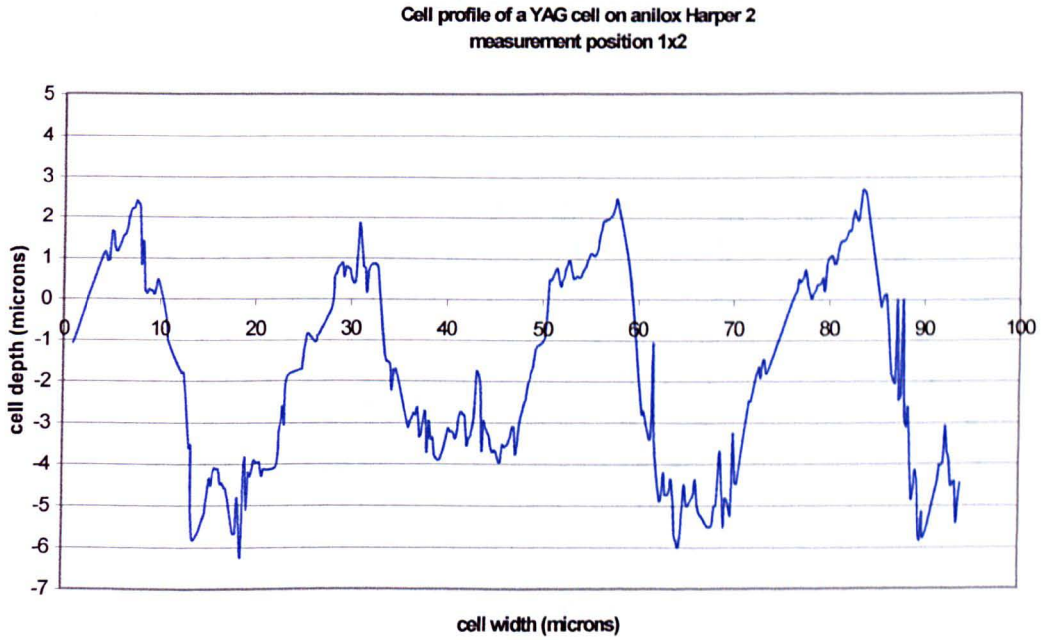

Appendix Section A6-11 continued

Cell profiles of the CO_2 and YAG cells on anilox Harper, Measured using the Veeco roll-scope interferometer.

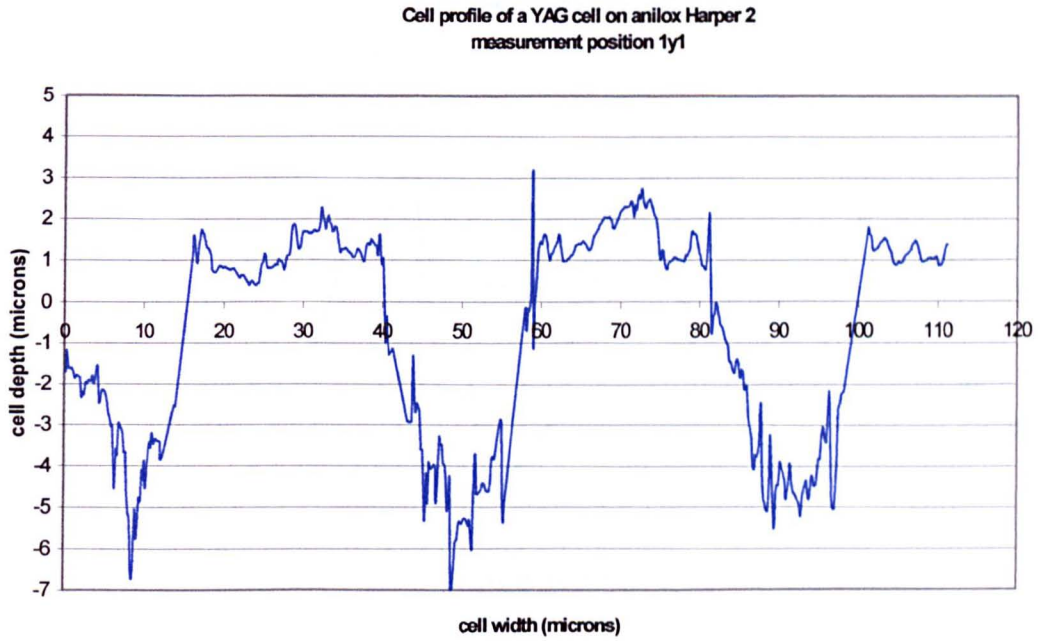

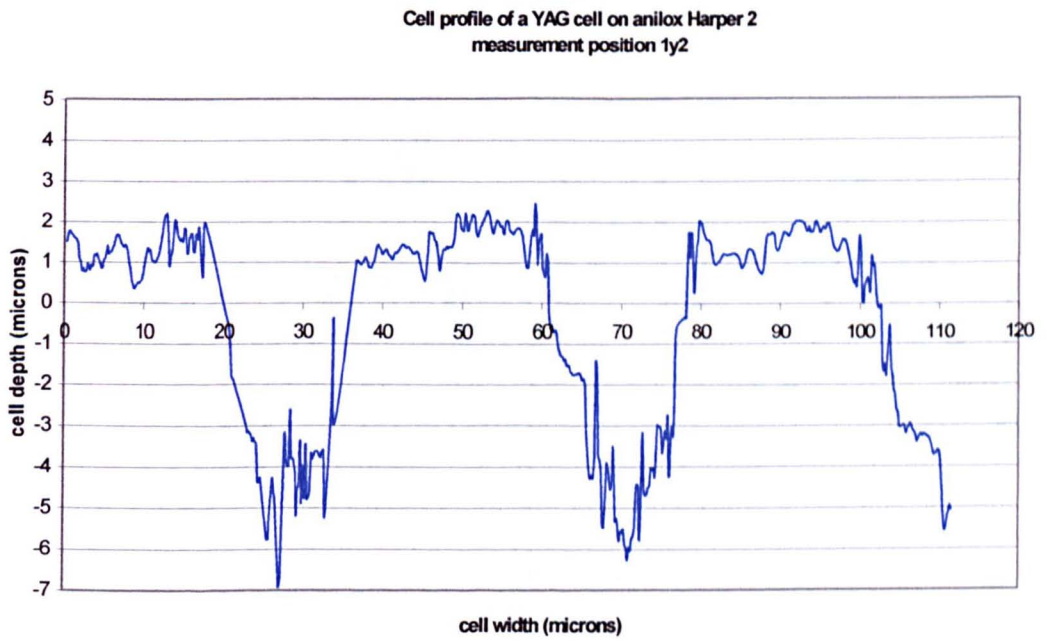

Appendix Section A6-11 continued

Cell profiles of the CO_2 and YAG cells on anilox Harper, Measured using the Veeco roll-scope interferometer.

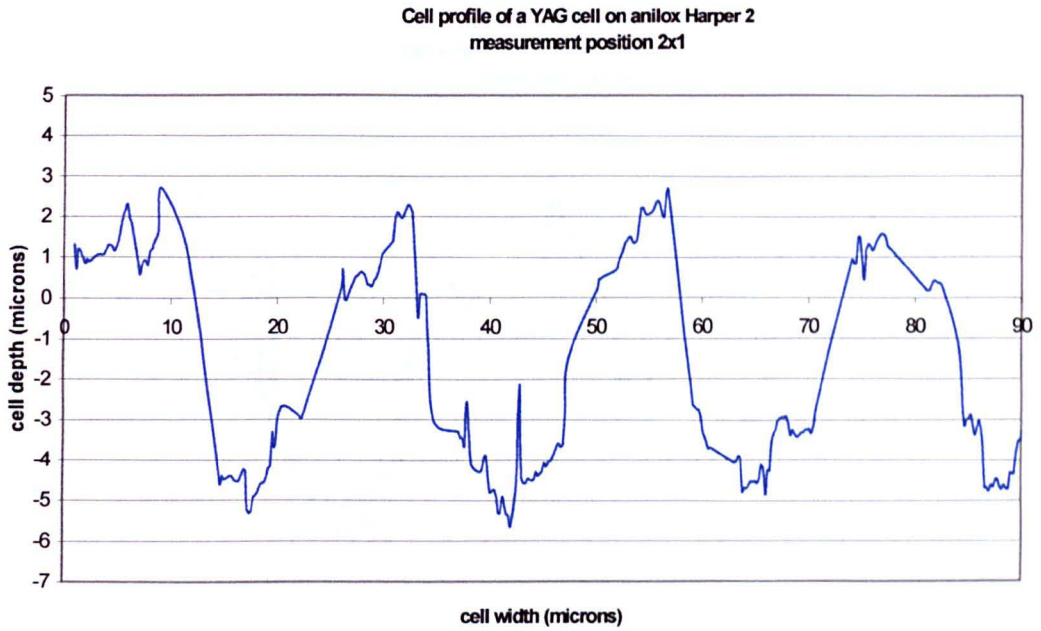

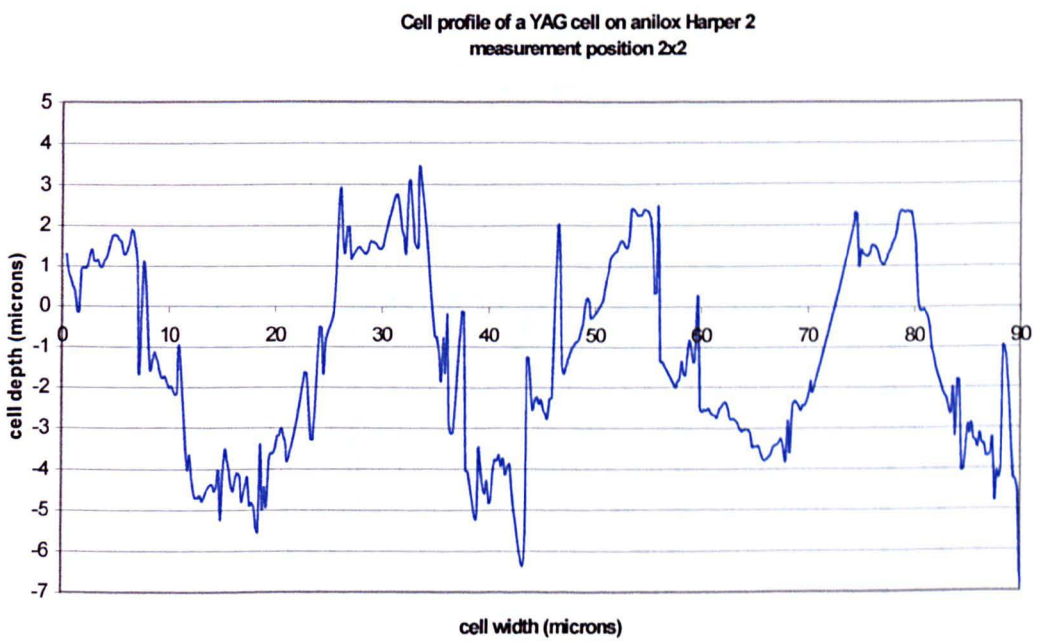

Appendix Section A6-11 continued

Cell profiles of the CO_2 and YAG cells on anilox Harper, Measured using the Veeco roll-scope interferometer.

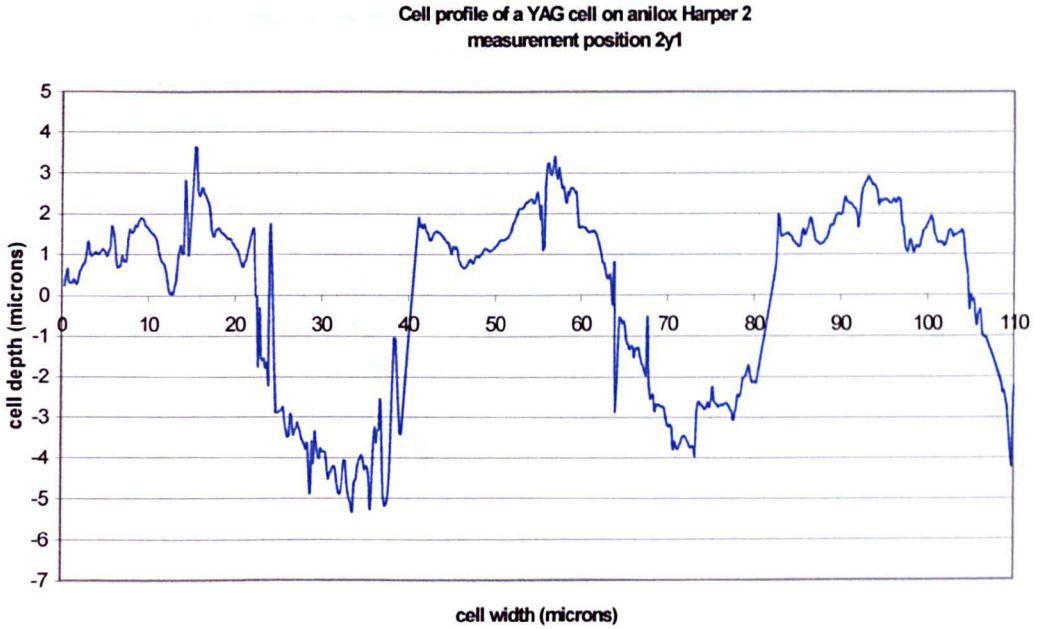

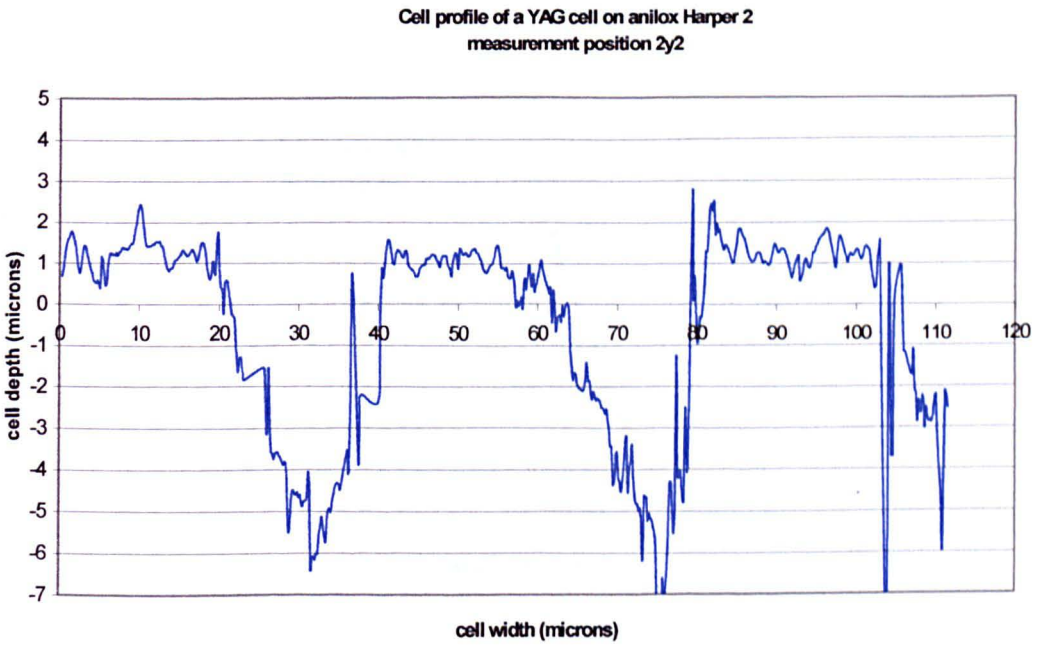

Appendix Section A6-12

Gradient measurements made from the cell profiles of the CO_2 and YAG cells on anilox Harper 2, Measured using the Veeco roll-scope interferometer.

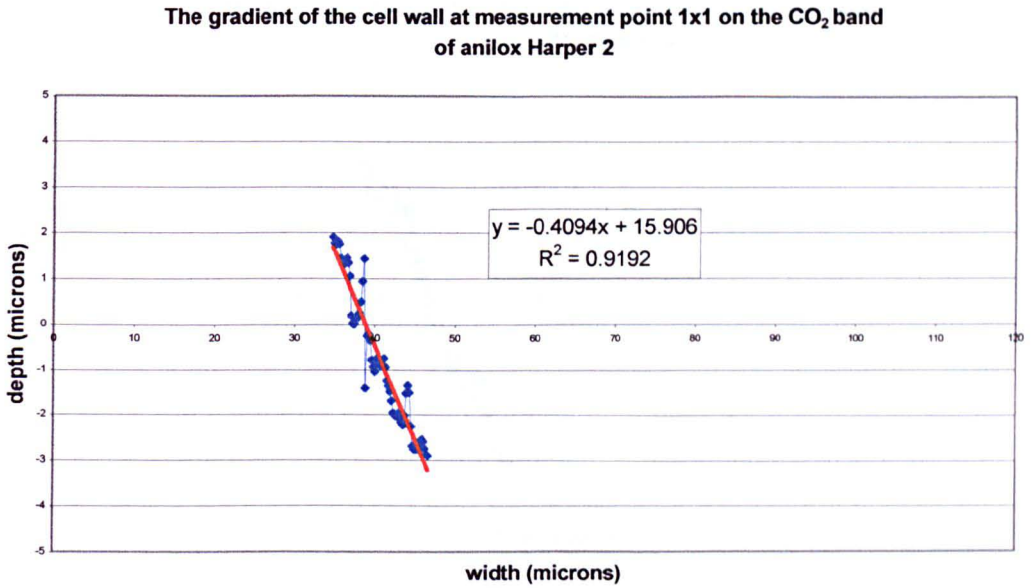

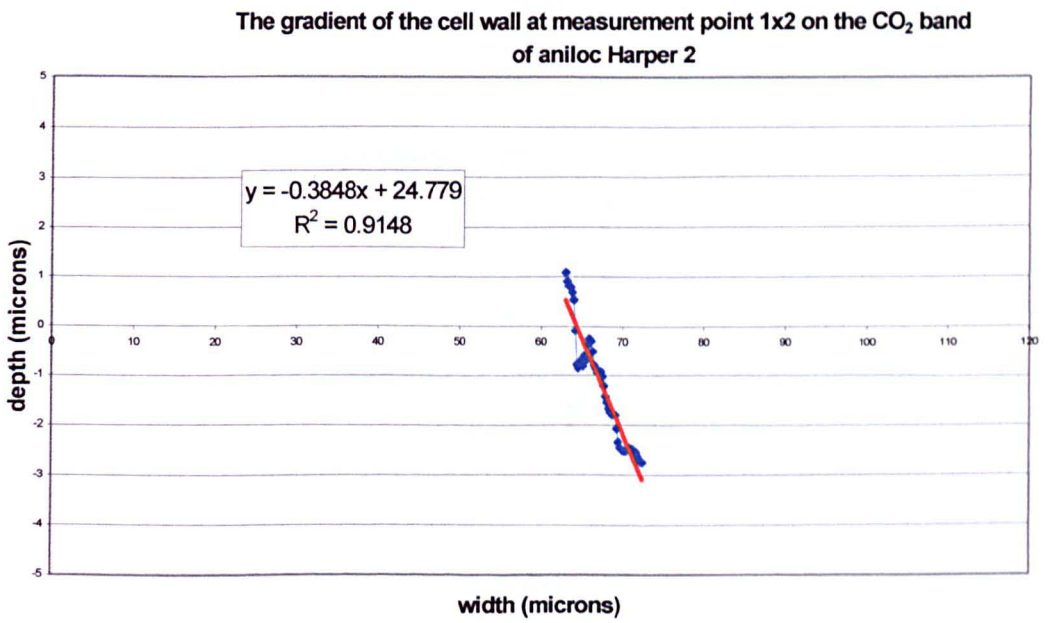

Appendix Section A6-12 continued

Gradient measurements made from the cell profiles of the CO_2 and YAG cells on anilox Harper 2, Measured using the Veeco roll-scope interferometer.

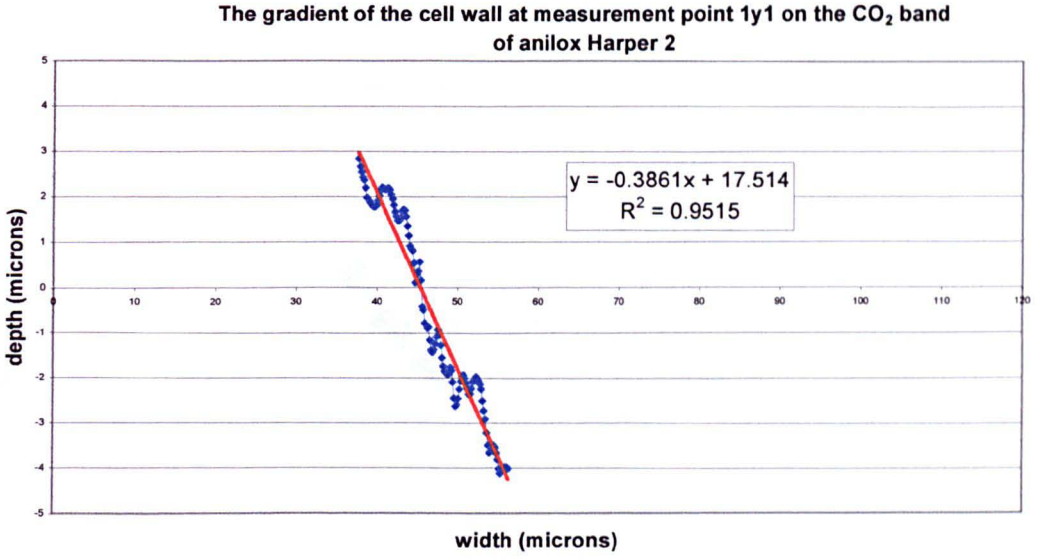

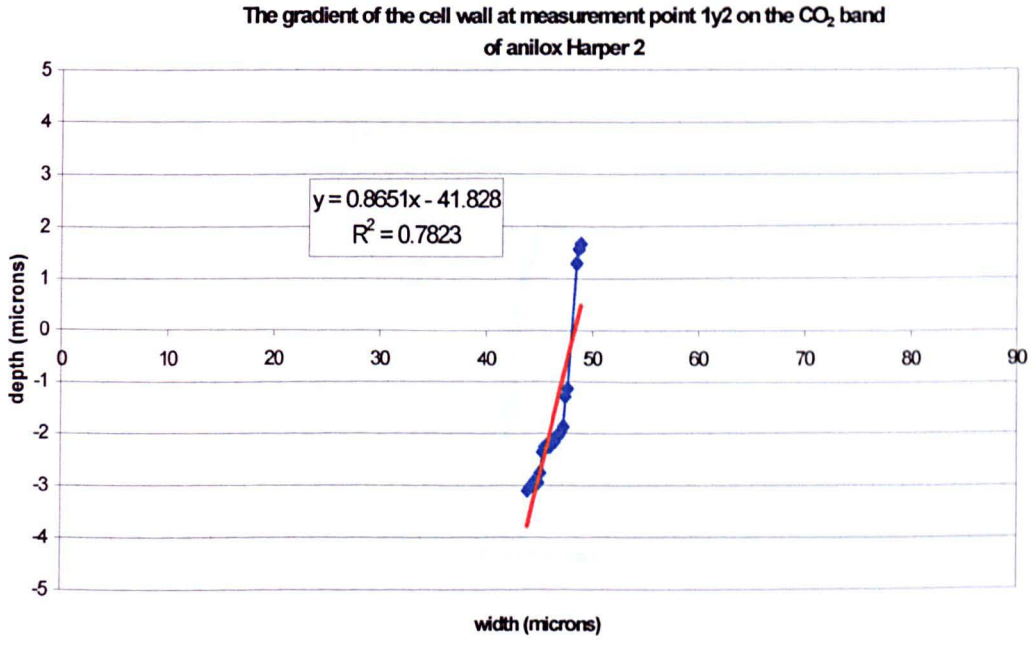

Appendix Section A6-12 continued

Gradient measurements made from the cell profiles of the CO_2 and YAG cells on anilox Harper 2, Measured using the Veeco roll-scope interferometer.

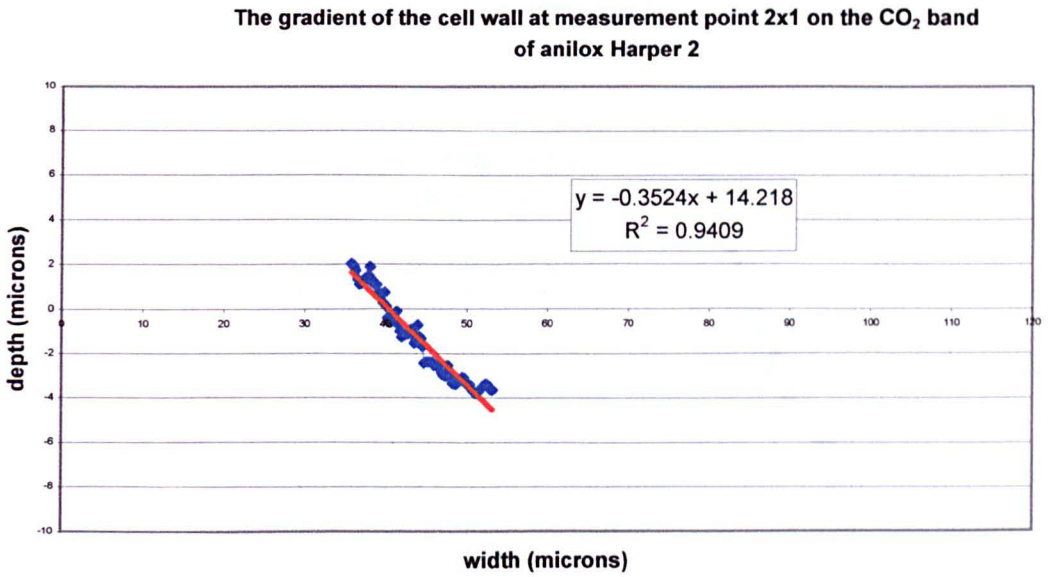

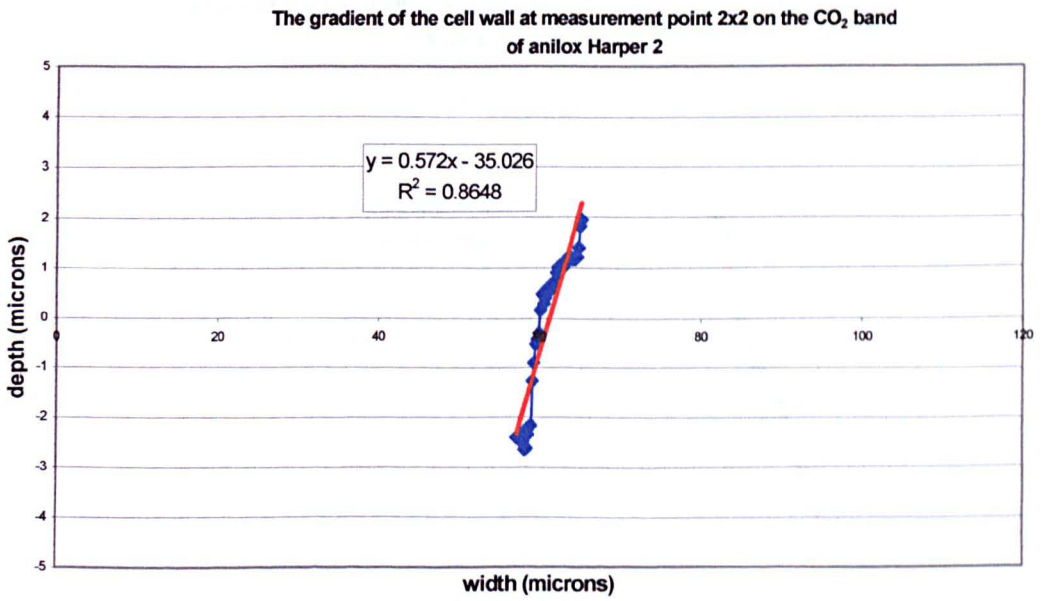

Appendix Section A6-12 continued

Gradient measurements made from the cell profiles of the CO_2 and YAG cells on anilox Harper 2, Measured using the Veeco roll-scope interferometer.

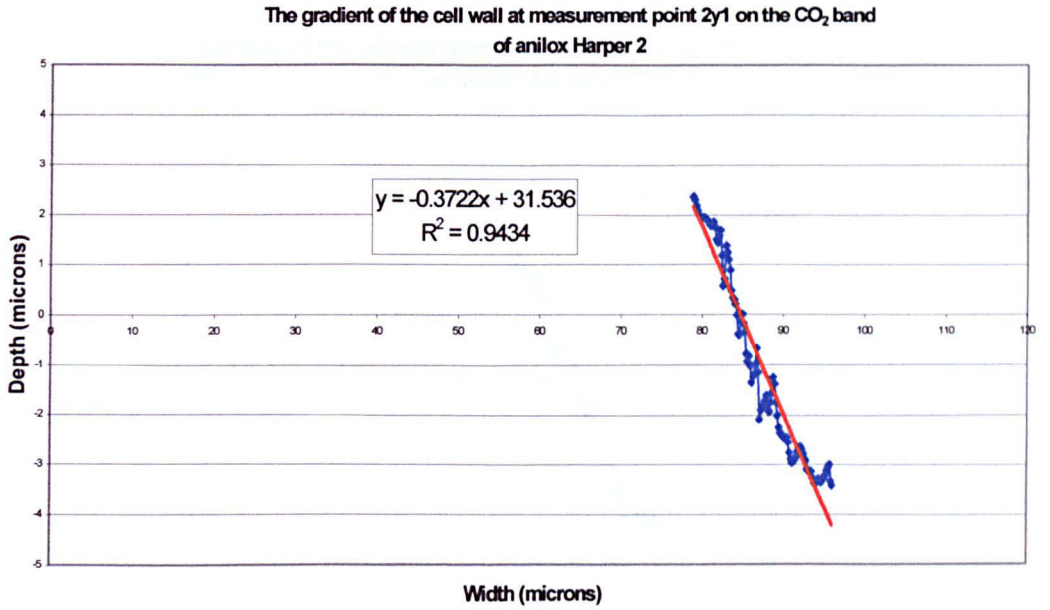

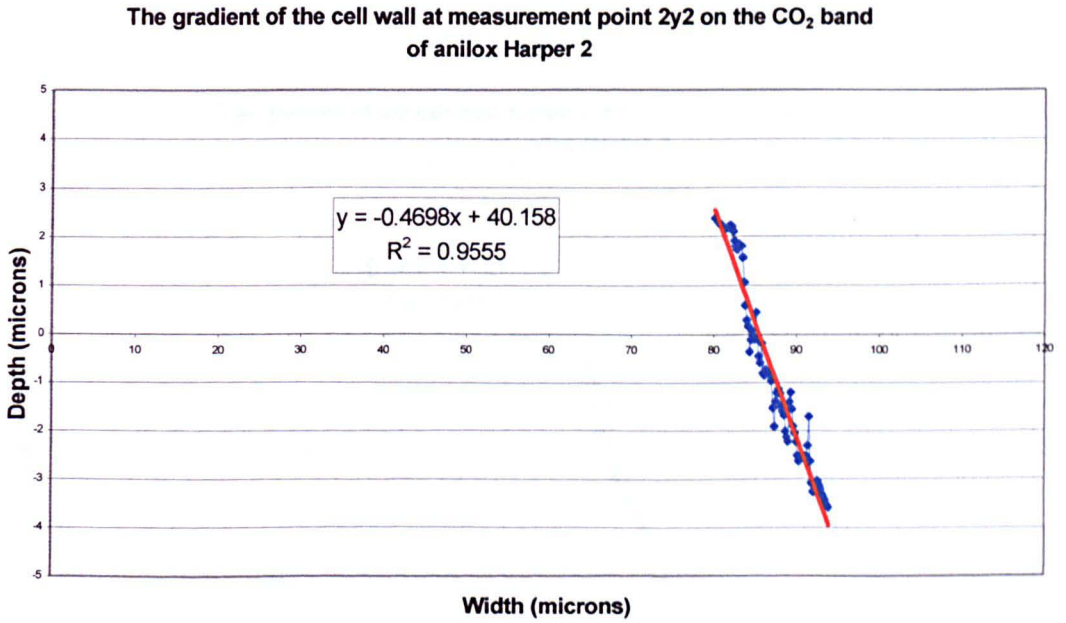

Appendix Section A6-12 continued

Gradient measurements made from the cell profiles of the CO_2 and YAG cells on anilox Harper 2, Measured using the Veeco roll-scope interferometer.

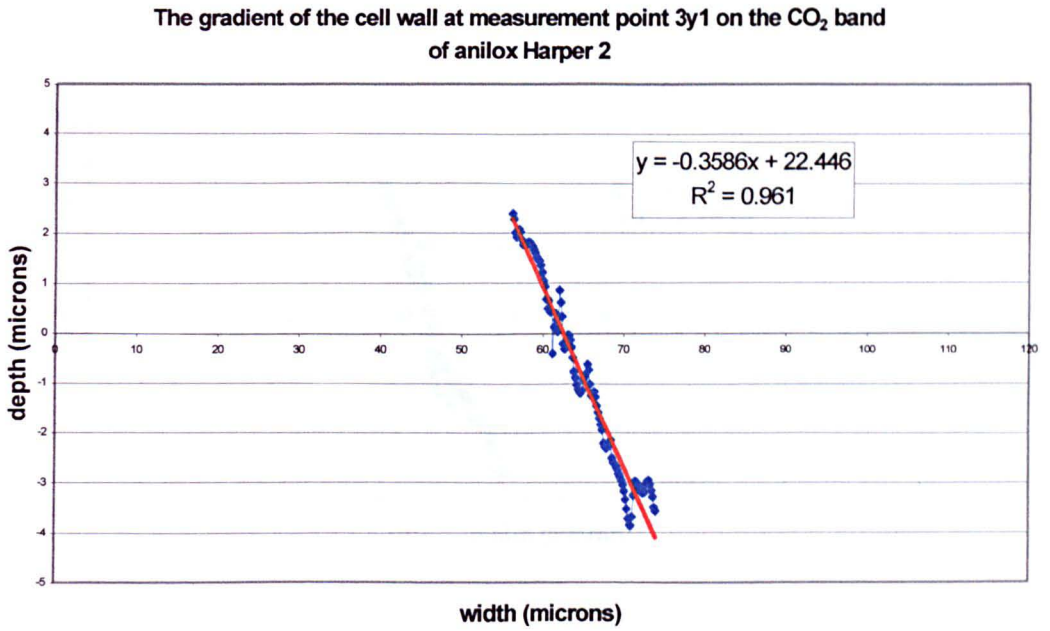

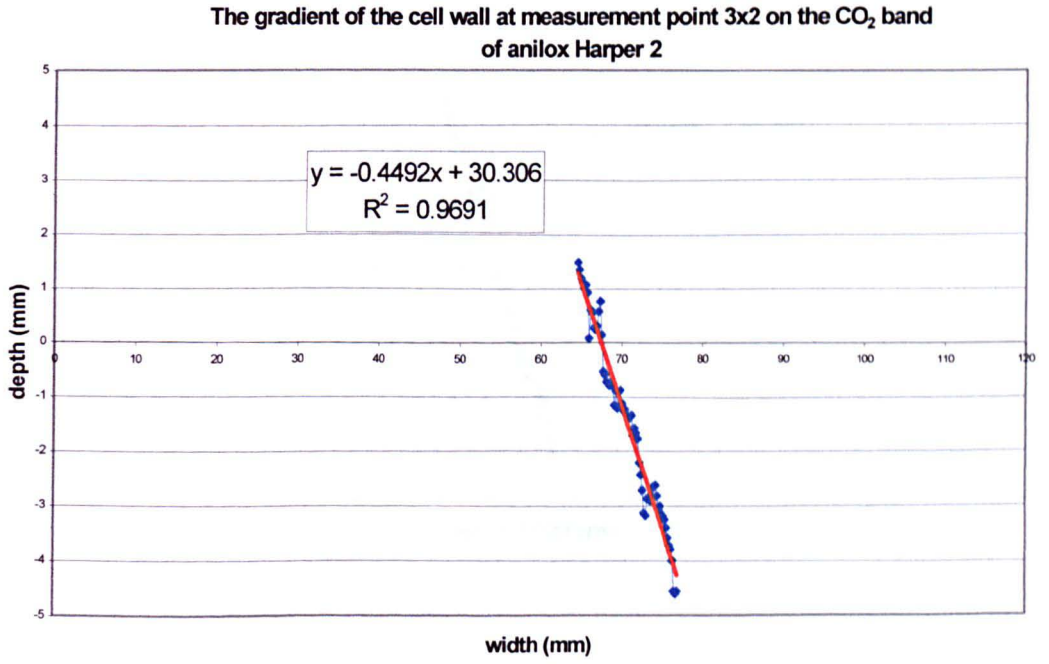

Appendix Section A6-12 continued

Gradient measurements made from the cell profiles of the CO_2 and YAG cells on anilox Harper 2, Measured using the Veeco roll-scope interferometer.

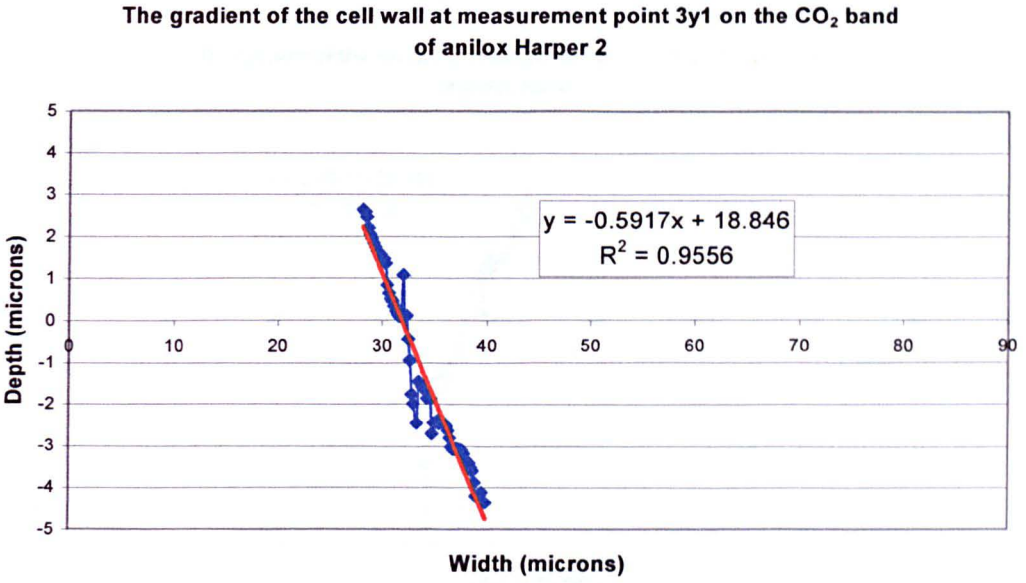

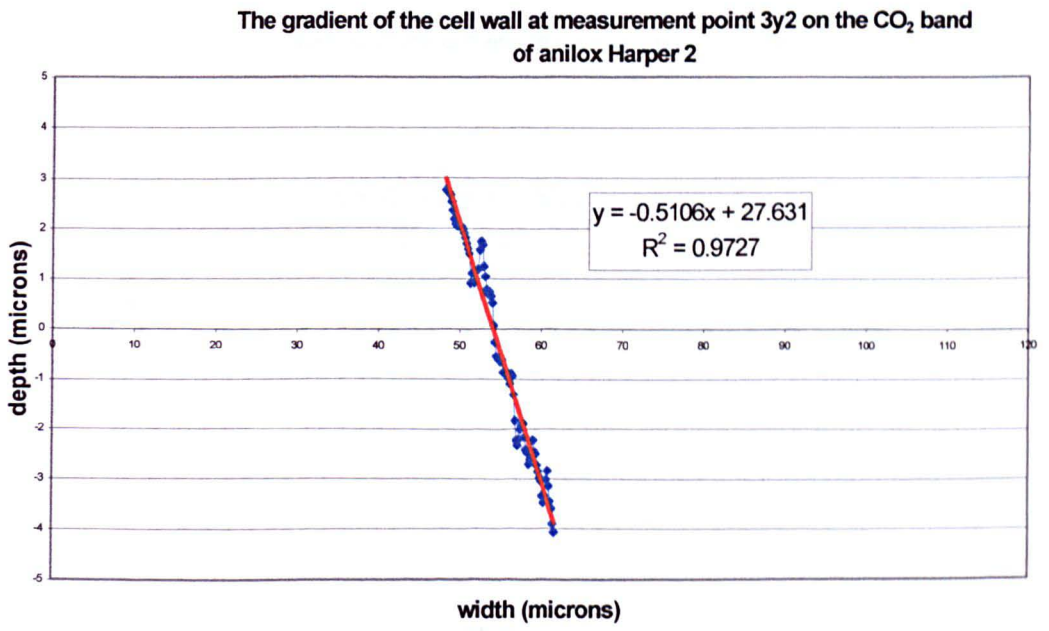

Appendix Section A6-12 continued

Gradient measurements made from the cell profiles of the CO_2 and YAG cells on anilox Harper 2, Measured using the Veeco roll-scope interferometer.

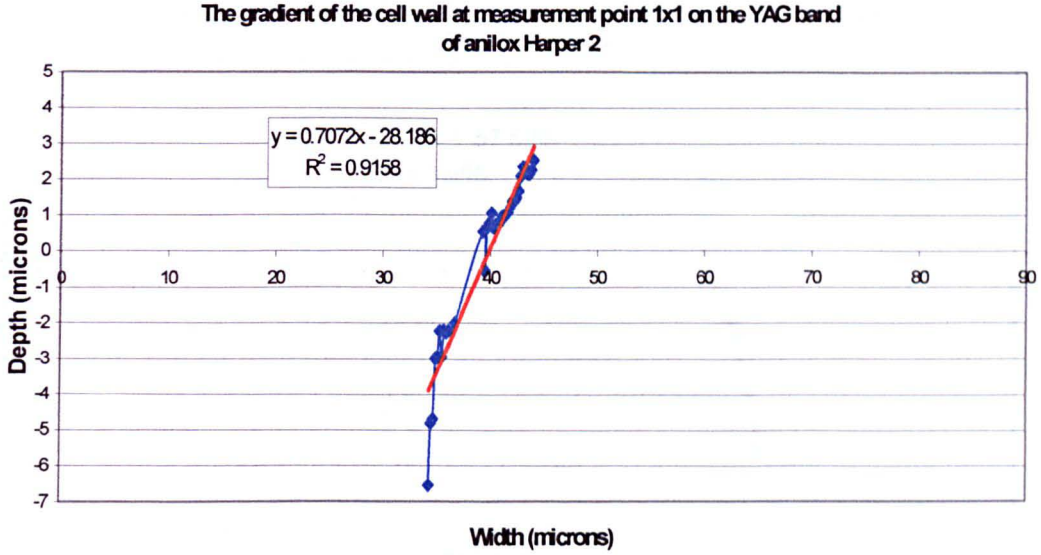

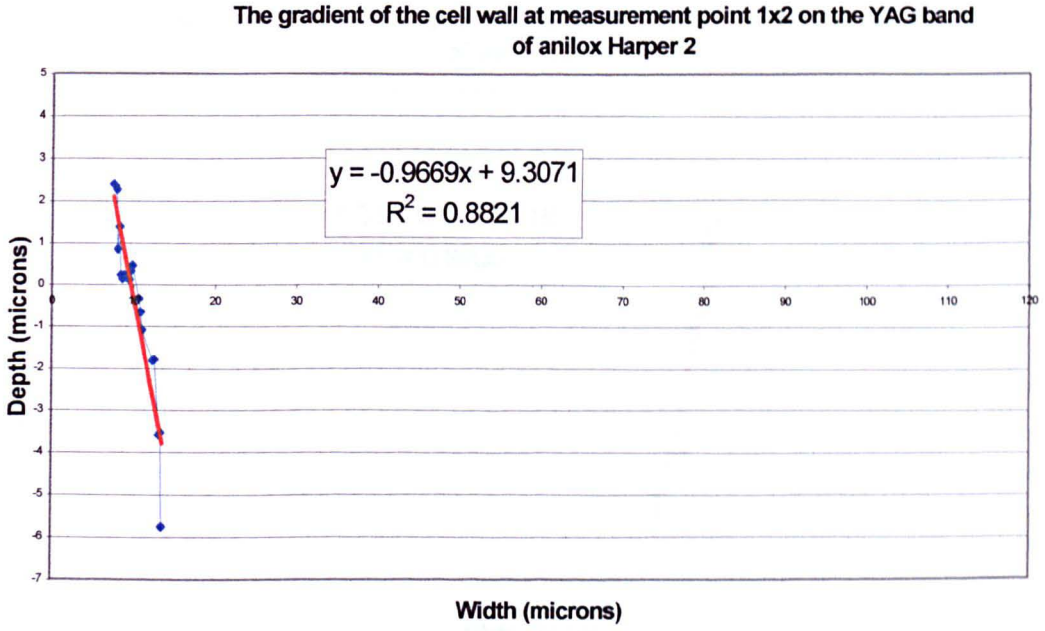

Appendix Section A6-12 continued

Gradient measurements made from the cell profiles of the CO_2 and YAG cells on anilox Harper 2, Measured using the Veeco roll-scope interferometer.

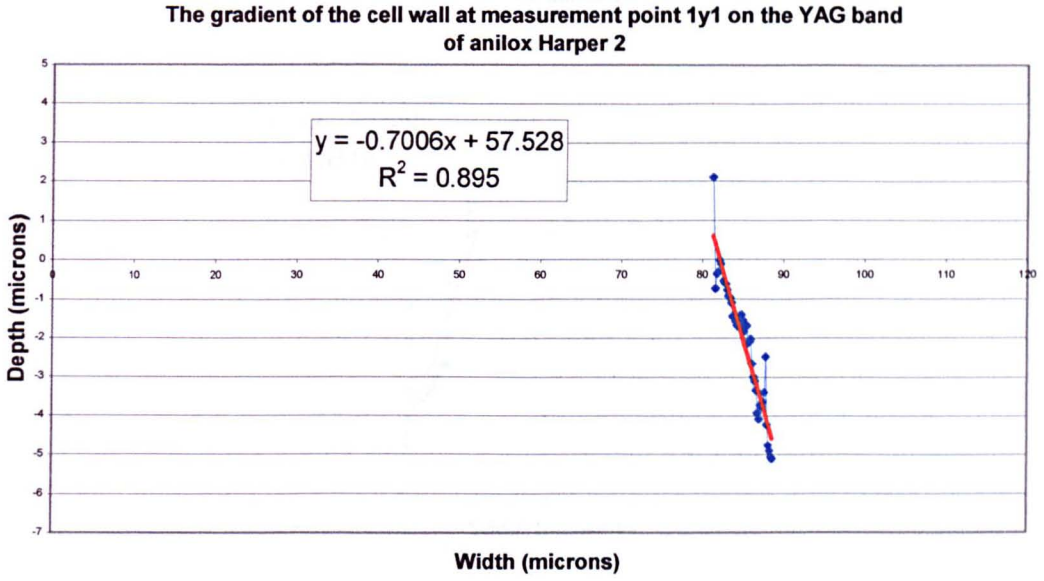

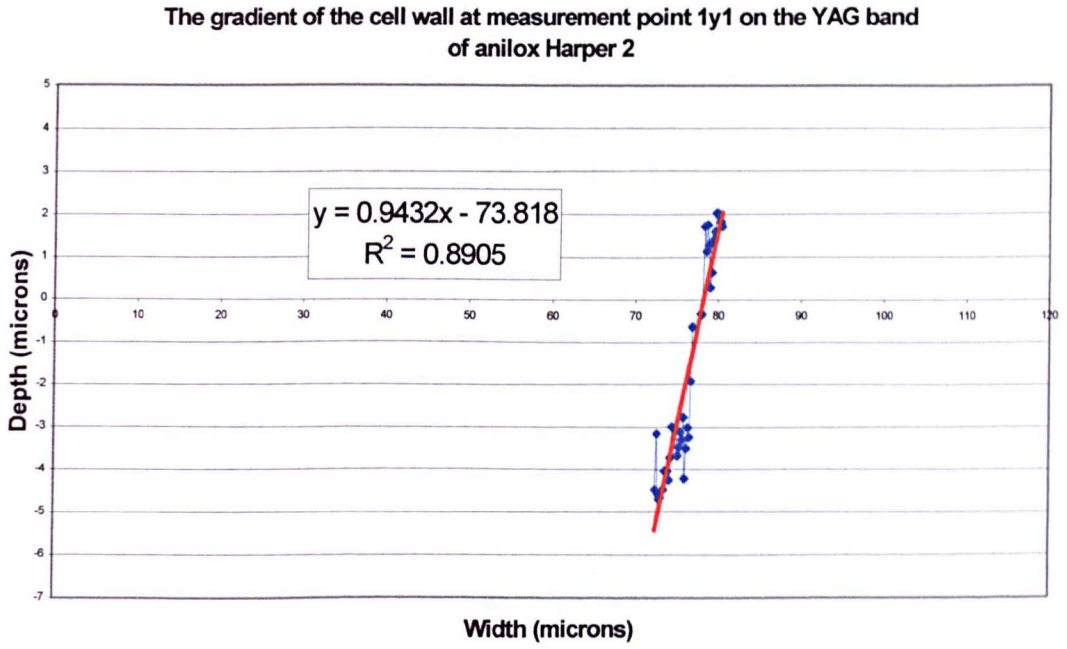

Appendix Section A6-12 continued

Gradient measurements made from the cell profiles of the CO_2 and YAG cells on anilox Harper 2, Measured using the Veeco roll-scope interferometer.

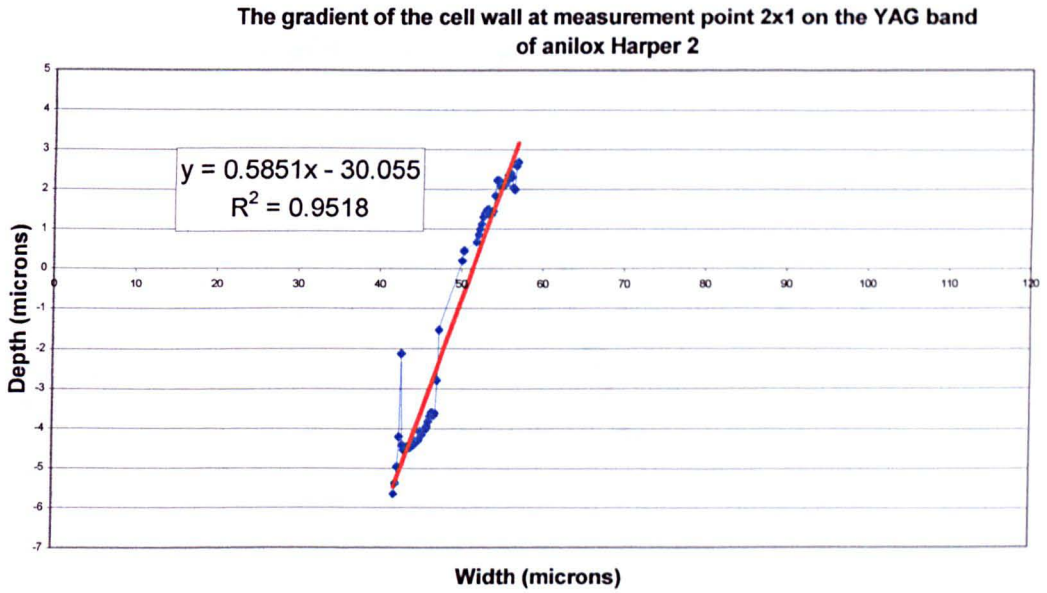

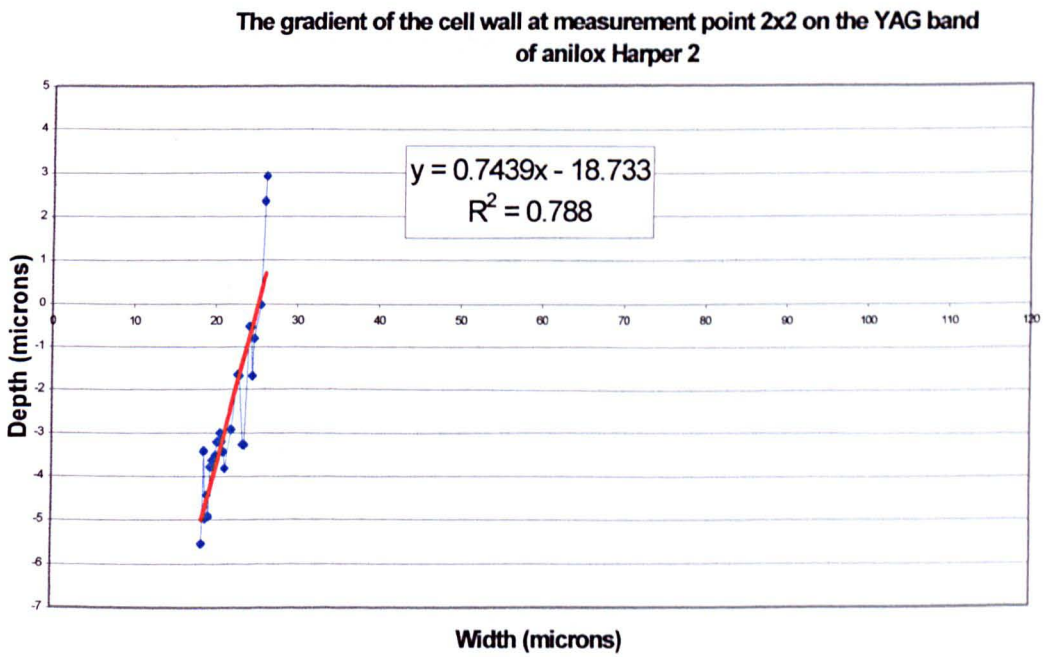

Appendix Section A6-12 continued

Gradient measurements made from the cell profiles of the CO_2 and YAG cells on anilox Harper 2, Measured using the Veeco roll-scope interferometer.

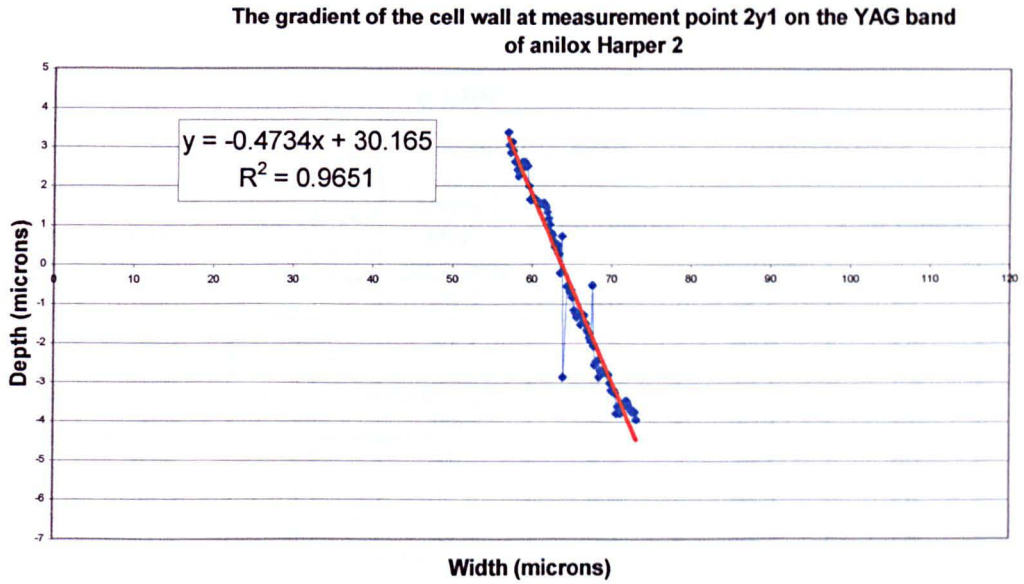

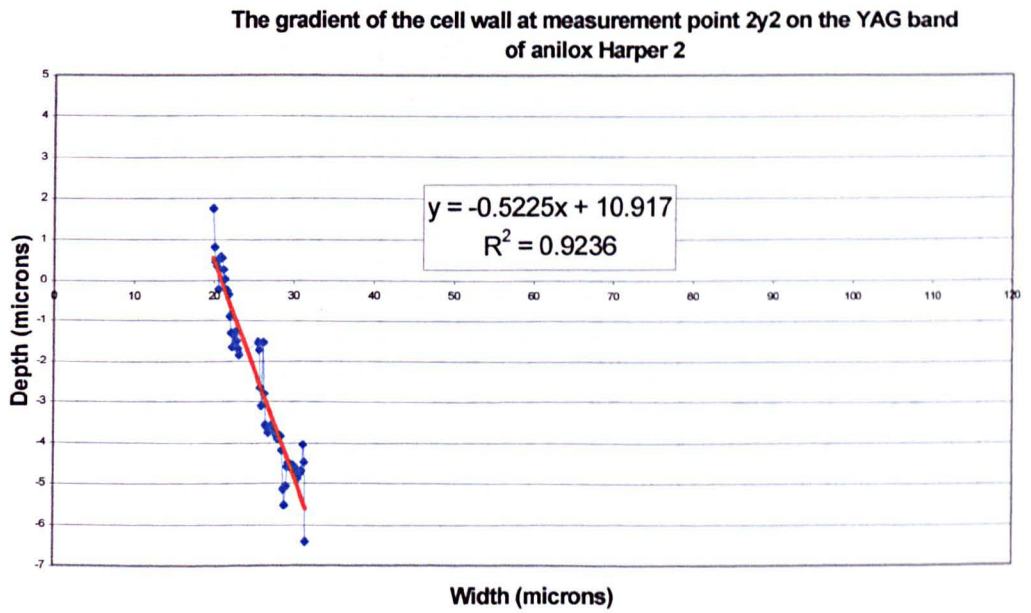

Appendix A7

Appendix Section A7-1

Contact angle data for anilox Harper 3 measured using the FTA instrument and water, diiodomethane and formamide as the test liquids

water						
	platinum band		normal CO_2 band		polished band	
run number	contact angle (degrees)	drop volume (microlitres)	contact angle (degrees)	drop volume (microlitres)	contact angle (degrees)	drop volume (microlitres)
1	86.0	8.7	88.6	9.0	82.2	1.7
2	86.6	9.5	91.1	8.8	85.6	1.6
3	85.8	8.7	89.4	9.0	79.1	1.3
4	86.8	9.1	86.9	9.3	80.9	1.7
5	83.4	9.2	89.7	9.1	79.7	1.6
6	88.6	9.1	89.8	9.9	84.6	1.6
7	87.0	8.7	89.5	9.1	84.3	1.6
8	86.4	8.9	87.6	8.8	82.7	1.3
9	87.1	9.1	85.7	9.4	81.4	1.4
10	86.9	9.5	88.9	9.2	82.3	1.3
11	87.4	9.2	91.1	8.7		
12	88.2	8.7	89.5	8.7		
13	85.9	9.6	87.9	8.8		
14	85.6	9.3	90.3	9.3		
15	84.7	8.9	89.1	9.0		
16	84.7	8.7	87.6	8.8		
17	83.1	8.5	87.5	8.7		
18	84.3	8.7	86.1	8.0		
19	82.5	8.1	86.8	8.7		
20	87.5	8.5	87.0	8.6		
mean	**85.9**	**8.9**	**88.5**	**8.9**	**82.3**	**1.5**
Standard deviation	**1.7**	**0.4**	**1.6**	**0.4**	**2.1**	**0.2**

Appendix Section A7-1 continued

Contact angle data for anilox Harper 3 measured using the FTA instrument and water, diiodomethane and formamide as the test liquids

diiodomethane						
	platinum band		normal CO_2 band		polished band	
run number	contact angle (degrees)	drop volume (microlitres)	contact angle (degrees)	drop volume (microlitres)	contact angle (degrees)	drop volume (microlitres)
1	41.5	1.8	45.9	1.8	46.6	0.4
2	42.6	1.6	46.3	1.7	49.9	0.4
3	41.4	1.5	46.5	1.7	48.0	0.4
4	43.1	1.7	47.4	1.7	49.7	0.3
5	44.3	1.8	46.7	1.1	44.3	0.3
6	43.8	1.8	46.9	1.7	47.8	0.3
7	44.7	1.6	44.3	1.5	47.1	0.3
8	44.6	1.7	45.5	1.8	49.2	0.3
9	44.7	1.7	46.0	1.8	46.3	0.6
10	44.1	1.8	47.7	1.7	47.1	0.3
mean	43.5	1.7	46.3	1.7	47.6	0.4
Standard deviation	1.3	0.1	1.0	0.2	1.7	0.1

Formamide						
	platinum band		normal CO_2 band		polished band	
run number	contact angle (degrees)	drop volume (microlitres)	contact angle (degrees)	drop volume (microlitres)	contact angle (degrees)	drop volume (microlitres)
1	65.7	4.8	60.4	4.2	77.4	1.1
2	62.8	4.7	62.9	4.2	79.2	1.0
3	62.6	4.5	66.4	4.6	85.3	1.0
4	62.0	4.3	63.6	4.4	77.3	1.1
5	62.3	4.3	62.7	5.1	79.2	1.0
6	59.8	2.8	64.2	4.1	76.6	1.0
7	62.7	4.0	64.0	4.9	78.9	1.1
8	63.3	3.6	62.9	3.9	78.5	1..1
9	67.5	4.6	61.7	4.4	79.2	1.1
10	66.8	3.9	62.4	4.7	80.0	1.1
mean	63.6	4.2	63.1	4.5	79.2	1.1
Standard deviation	2.4	0.6	1.6	0.4	2.4	0.1

Appendix Section B-1

Report by Victoria Verona (nee Maxfield) BSc. MSc. London College of Printing

INVESTIGATION INTO THE EFFECT OF SURFACE ENERGY AND SURFACE ROUGHNESS ON THE WETTABILITY OF AN ANILOX ROLL

BACKGROUND

The function of the anilox roll is to take up and then release a precisely controlled volume of ink onto the printing plate. Ink is doctored from the surface of the roll and held inside engraved cells. To quantify the amount of ink that will be transferred, it is necessary to calculate the extent to which the cell will empty on contact with the plate. Although research has been carried out on the effect of the wettability and roughness of the plate, [1, 2] the effect of the anilox has largely been ignored. The extent to which the anilox wets is worthy of consideration. If the anilox cannot be sufficiently wetted, beads of ink form inside the cells, leading to incomplete filling. If however the anilox surface is completely wetted, a large amount of work has to be done to remove the ink from the surface of the roll and the ink would have a tendency to remain in the cell, held by surface tension forces.

Wettability can be quantified by introducing the concept of surface energy. Surface energy is defined as "the reversible work done in creating unit area of fresh, flat, free

surface." [1] Surface energy is a term only applicable to solid surfaces but is analogous to the surface tension of a liquid surface. Surface energy is most commonly quoted with the units mNm^{-1}, $dynescm^{-1}$ or mJm^{-2}. These have the advantage of being numerically equivalent. The most common way of observing wettability and surface energy is to measure the contact angles formed by a polar and non-polar liquid at rest on the test surface. If the surface tensions of these liquids are known it is possible to calculate polar and non-polar components of surface energy by using equation 1. [4]

$$2(G_S^d\, G_L^d)^{0.5} + 2(G_S^p\, G_L^p)^{0.5} = G_S^L(1 + \cos\theta) \quad \text{equation 1}$$

G_S^d = The dispersive component of the surface energy of the solid

G_L^d = The dispersive component of the surface energy of the liquid (known)

G_S^p = The polar component of the surface energy of the solid

G_L^p = The polar component of the surface energy of the liquid (known)

G_S^L = The surface energy of the liquid (equivalent to the surface tension) (known)

θ = The observed contact angle (measured)

The polar component of the surface free energy of diiodomethane, the non-polar solvent, can be regarded as zero, which eliminates the term $+2(G_S^p\, G_L^p)^{0.5}$ from the equation and allows the calculation of G_S^d the non polar surface energy. This value is then put into the equation to calculate the polar component of the surface energy. The total surface energy of the solid surface is the sum of the polar and non-polar surface energies.

Wetting characteristics are heavily influenced by surface roughness of the sample. [3] It is normal to consider a smooth flat sample. However, measurement of the wetting characteristics of a flat unengraved ceramic sample would not be representative of the surface that the ink comes into contact with. The process of engraving produces a roughened surface. The effect of surface roughness on the contact angles depends on the angles themselves. If the true contact angle is less than 90°, surface roughness lowers the observed contact angle. However if the true contact angle is greater than 90° the observed contact angle is increased by surface roughness. [5]

EXPERIMENTAL WORK

n this investigation, tests were carried out on a banded ceramic anilox provided by the Harper Corporation of America. The first test band was unengraved, polished ceramic. The second test band was engraved by a CO_2 laser and the third by a YAG laser. The cells were designed to have equivalent cell depths and comparable cell volumes. To make engravings comparable in this way it is necessary for them to have very different line screens. Table 1 shows the specifications of the engravings

Table 1. Specification of the banded Harper anilox

Anilox band	Line screen (lines per inch)	Line screen (lines per cm)	Cell volume (BCM)	Cell volume (cm^3/m^2)	Cell depth (microns)	Cell opening (microns)	Cell wall (microns)
Polished	N/A	N/A	N/A	N/A	N/A	N/A	N/A
CO2	600	236	2.63	4.08	10.70	38.00	4.00
YAG	1200	472	2.34	3.63	10.60	19.04	2.11

Additional work was carried out on a banded anilox of unknown ceramic origin, owned by Pira International. This banded roll was engraved with a CO_2 laser at a line screen of 149 lines per cm (or 380 lines per inch). Each band has different cell volume and cell depth. The absolute volumes of these bands were not known but estimations made by an ink spreading method gave volumes of $3.25cm^3m^{-2}$ for band 1 and $3.75cm^3m^{-2}$ for band 2.

Contact angle measurements were made using the Micro Absorbency Measurement System (MAMS) at Pira International. Every measurement was taken with the roll position adjusted to be horizontal and the droplet positioned on the zenith of the roll. Experimentation with drop volume showed that a droplet of 5 μl was sufficiently small to minimise droplet distortion caused by the curvature of the roll. Whilst some distortion of the droplet was observed this remained constant for all measurements with a given liquid on a given roll. The contact angle data obtained for the Harper roll is shown in Table 2.

Table 2. Contact angle data for the banded Harper anilox made by 5 µl droplets of water and diiodomethane

Water

Polished Band	Angle (deg)	Radius (mm)	Width (mm)	Volume (µl)
1	57.98	1.86	3.18	3.94
2	56.05	2.09	3.53	5.25
3	56.67	2.23	3.73	6.02
4	55.64	2.10	3.47	4.78
5	55.13	2.34	3.84	6.34
6	54.01	2.00	3.24	3.69
7	52.84	2.43	3.89	6.31
8	53.61	2.20	3.57	4.94
9	60.36	2.03	3.52	5.52
10	52.74	2.46	3.92	6.36
11	54.47	2.36	3.85	6.26
12	57.18	2.47	4.14	8.37
13	59.45	1.92	3.29	4.39
14	55.40	1.99	3.27	3.93
15	58.45	2.03	3.47	5.07
16	56.49	1.92	3.41	4.59
17	58.27	1.97	3.37	4.65
18	54.24	1.91	3.09	3.24
19	57.50	2.00	3.37	4.53
20	55.55	1.99	3.29	4.02
Mean	**56.10**			
St. Dev	**2.14**			

Diiodomethane

Polished Band	Angle (deg)	Radius (mm)	Width (mm)	Volume (µl)
1	18.45	8.47	5.41	5.16
2	24.33	5.11	4.33	3.60
3	19.51	6.65	4.60	3.44
4	18.70	8.95	5.89	6.85
5	19.46	7.11	4.95	4.33
6	16.86	7.14	4.32	2.46
7	19.58	7.05	4.85	4.02
8	18.45	7.93	5.22	4.77
9	22.24	6.17	4.84	4.62
10	17.22	7.99	5.02	4.04
11	21.40	6.17	4.66	3.94
12	18.26	8.24	5.38	5.17
13	21.25	6.63	4.97	4.76
14	17.07	9.41	5.82	6.19
15	17.04	8.90	5.51	5.25
16	22.98	6.03	4.97	5.30
17	19.13	8.41	5.25	4.57
18	18.68	8.05	5.44	5.57
19	19.60	7.67	5.30	5.27
20	19.06	7.99	5.37	5.30
Mean	**19.46**			
St. Dev	**2.04**			

Water

CO_2 Band	Angle (deg)	Radius (mm)	Width (mm)	Volume (µl)
1	62.84	1.86	3.32	5.05
2	66.70	1.64	3.01	4.03
3	61.11	1.75	3.06	3.73
4	60.65	1.85	3.25	4.46
5	64.98	1.80	3.26	4.94
6	62.50	1.86	3.30	4.83
7	62.12	1.87	3.27	4.56
8	68.89	1.77	3.31	5.66
9	61.21	1.94	3.39	5.01
10	63.27	1.86	3.34	5.14
11	68.12	1.65	3.07	4.46
12	63.07	1.71	3.06	3.91
13	62.92	1.94	3.45	5.56
14	64.27	1.84	3.30	4.93
15	65.21	1.72	3.21	4.83
16	63.61	1.94	3.46	5.62
17	61.10	1.91	3.34	4.84
18	64.07	1.86	3.33	4.81
19	63.43	1.74	3.11	4.09
20	62.50	2.22	3.94	8.15
Mean	**63.63**			
St. Dev	**2.25**			

Diiodomethane

CO_2 Band	Angle (deg)	Radius (mm)	Width (mm)	Volume (µl)
1	22.55	6.13	4.74	4.27
2	17.18	9.06	5.45	4.94
3	21.55	6.69	4.96	4.67
4	15.96	9.05	5.14	3.89
5	14.53	11.65	6.01	5.63
6	21.28	6.95	5.16	5.23
7	16.90	7.83	4.61	2.92
8	20.16	7.13	4.97	4.39
9	20.34	6.45	4.52	3.33
10	20.58	6.92	4.97	4.52
11	21.50	6.27	4.63	3.79
12	18.08	8.15	5.12	4.28
13	17.46	8.28	5.13	4.24
14	19.75	6.46	4.52	3.30
15	21.06	6.58	4.81	4.20
16	19.55	7.75	5.34	5.39
17	19.29	9.29	5.34	4.44
18	16.65	8.28	4.91	3.54
19	19.60	6.95	4.71	3.63
20	19.80	6.54	4.58	3.43
Mean	**19.19**			
St. Dev	**2.14**			

Table 2 contintued

Water					Diiodomethane				
YAG Band	Angle (deg)	Radius (mm)	Width (mm)	Volume (µl)	YAG Band	Angle (deg)	Radius (mm)	Width (mm)	Volume (µl)
1	83.63	1.45	2.88	5.30	1	12.77	12.00	5.31	3.30
2	74.12	1.54	2.97	4.63	2	14.87	10.83	5.56	4.43
3	77.32	1.35	2.64	3.51	3	13.42	10.87	5.05	2.99
4	74.52	1.40	2.69	3.47	4	19.32	7.62	5.04	4.32
5	75.89	1.53	2.91	4.14	5	10.84	14.80	5.57	3.22
6	79.27	1.34	2.63	3.63	6	15.46	9.12	4.86	3.08
7	76.49	1.38	2.68	3.59	7	13.78	9.38	4.53	2.25
8	79.52	1.37	2.70	3.94	8	16.39	9.08	5.20	4.05
9	74.40	1.54	2.97	4.81	9	21.17	5.91	4.33	3.06
10	76.22	1.56	3.03	5.16	10	16.26	9.07	5.08	3.71
11	74.12	1.54	2.97	4.63	11	15.46	9.12	4.86	3.08
12	74.83	1.67	3.15	5.11	12	12.70	13.50	5.93	4.58
13	71.83	1.59	3.08	5.27	13	11.22	15.53	6.04	4.28
14	76.73	1.37	2.67	3.61	14	19.39	8.14	5.41	5.36
15	75.72	1.62	3.21	7.04	15	13.99	11.12	5.38	3.77
16	72.92	1.73	3.33	6.51	16	10.56	15.59	5.71	3.39
17	72.73	1.74	3.33	6.38	17	16.32	8.19	4.60	2.76
18	74.06	1.59	3.03	4.57	18	11.43	14.97	5.93	4.12
19	82.93	1.29	2.58	4.32	19	14.31	9.78	4.90	2.97
20	78.23	1.37	2.75	3.94	20	12.22	12.51	5.55	3.78
Mean	**76.27**				Mean	**14.59**			
St. Dev	**3.16**				St. Dev	**2.96**			

The distribution of contact angle data is shown below for each test liquid.

Figure 1. Contact angles made by a 5 microlitre water droplet on a Harper banded anilox

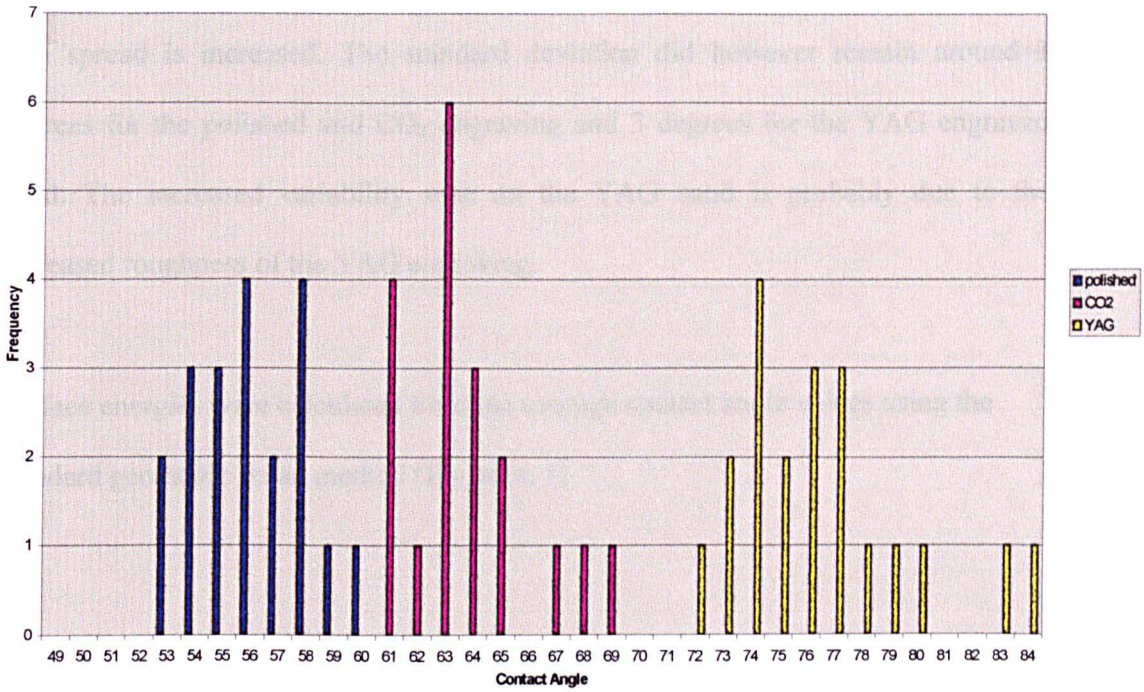

Figure 2. Contact angles made by a 5 microlitre drop of diiodomethane on a Harper banded anilox

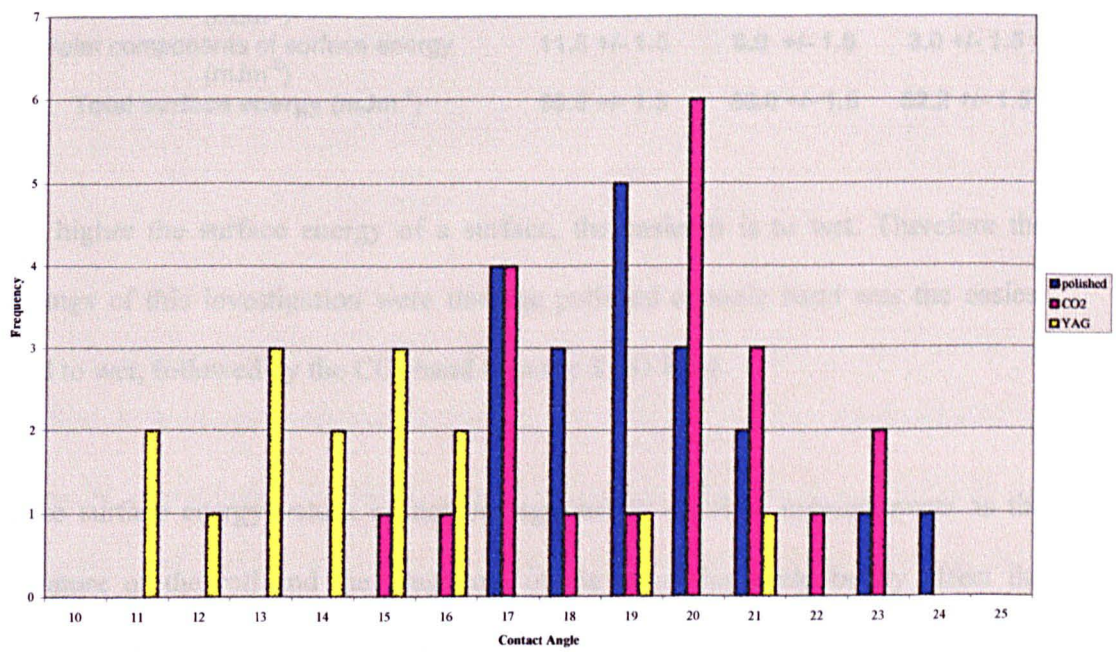

Under standard conditions, it is usual for the MAMS contact angle analysis to produce contact angle data that spreads over a 4-degree range.[6] The sample roughness and roll curvature however introduce new sources of variation and the data spread is increased. The standard deviation did however remain around 2 degrees for the polished and CO_2 engraving and 3 degrees for the YAG engraved band. The increased variability seen on the YAG band is probably due to the increased roughness of the YAG engraving.

Surface energies were calculated from the average contact angle values using the standard geometric mean method (Equation 1)

Table 3. Surface energies calculated for the Harper banded anilox

	Polished Band	CO_2 Band	YAG Band
Dispersive component of surface energy (mJm^{-2})	47.9 +/- 1.5	48.0 +/- 1.5	49.2+/- 1.5
Polar components of surface energy (mJm^{-2})	11.6 +/- 1.5	8.0 +/- 1.5	3.0 +/- 1.5
Total surface energy (mJm^{-2})	59.5 +/- 1.5	56.0 +/- 1.5	52.2 +/- 1.5

The higher the surface energy of a surface, the easier it is to wet. Therefore the findings of this investigation were that the polished ceramic band was the easiest band to wet, followed by the CO_2 band then the YAG band.

These surface energy values cannot be regarded as absolute measurements as the curvature of the roll and the roughness of the engraving undoubtedly affect the contact angle and therefore the surface energy. Because the roll curvature is constant for the three bands, comparisons between the bands can be made.

Figure 4 shows the variation in the component surface energies across the Harper banded anilox. The dispersive or non-polar component of the surface energy is reasonably constant across the bands. The drop in total surface energy seen from the polished band to the CO_2 to the YAG band is as a result of a drop in the polar component of surface energy across the bands.

Figure 4 Variation in surface energy across the Harper banded anilox

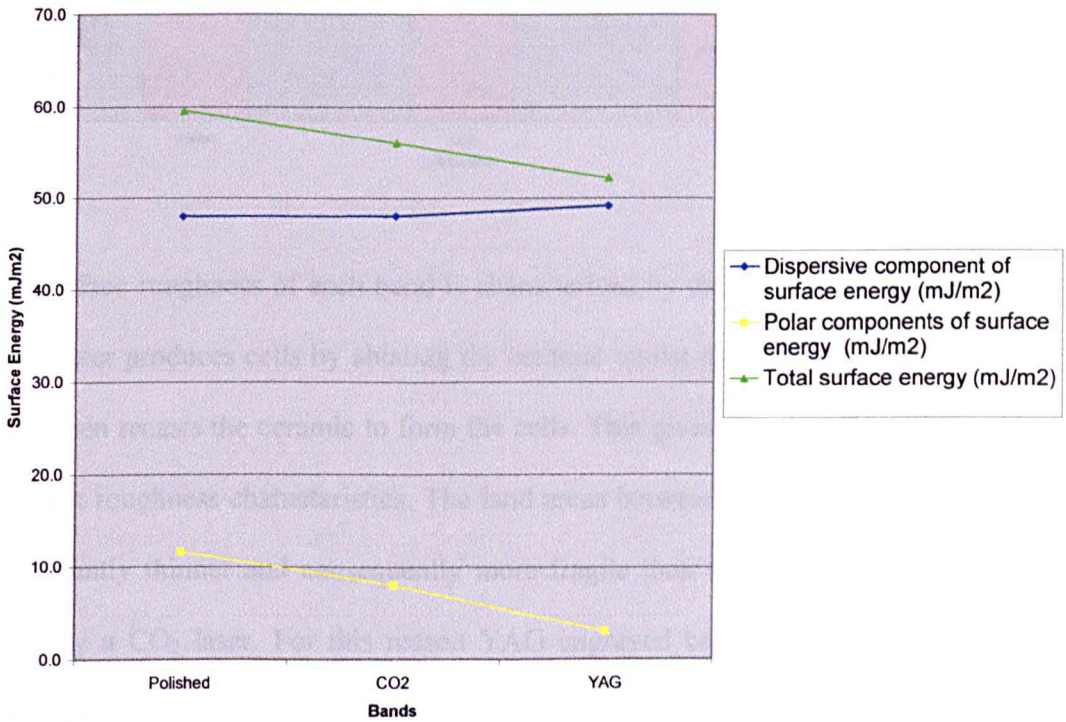

Figure 5 demonstrates the contributions to the total surface energy from non-polar (dispersive) interactions and polar interactions. All three bands are dominated by non-polar interactions. However, due to the chemical nature of printing inks the interactions between ink and roller are largely polar. Therefore the polar interactions, whilst making up a very small part of the total surface energy, are extremely important when considering wetting by printing inks. It is perhaps more useful to use contact angle data to predict and characterise wetting.

Figure 5. Comparison of the makeup of total surface energy across the Harper banded anilox

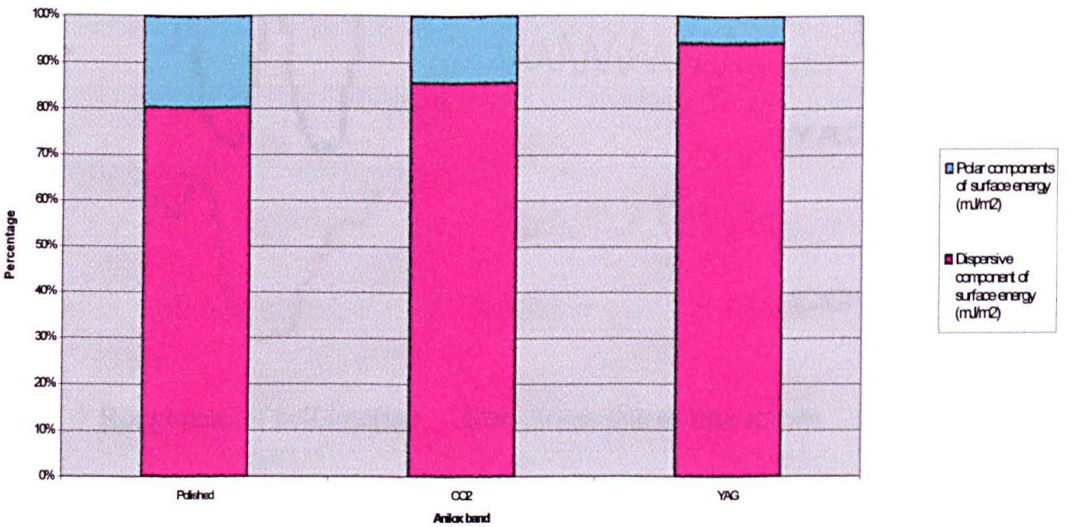

The surface roughness of each band is characterised by the laser power output. The YAG laser produces cells by ablating the ceramic whilst the lower power CO_2 laser melts then recasts the ceramic to form the cells. This gives rise to cell interiors with different roughness characteristics. The land areas between YAG engraved cells are significantly thinner and consequently more fragile than those areas between cells made by a CO_2 laser. For this reason YAG engraved cells are not polished after engraving as is usual with CO_2 engraved bands.

The YAG band under investigation has a much finer line screen than the CO_2 band. The test liquids therefore covered a much greater number of cells on the YAG band.

The roughness apparent to the test droplets is a combination of the roughness created by the laser used to engrave the ceramic and the roughness due to the number of cells. Figure 3 shows images taken from actual 2D surface scans of the engraved bands made by the Proscan 1000 optical sensor.

Figure 3. Roughness of the engraved bands

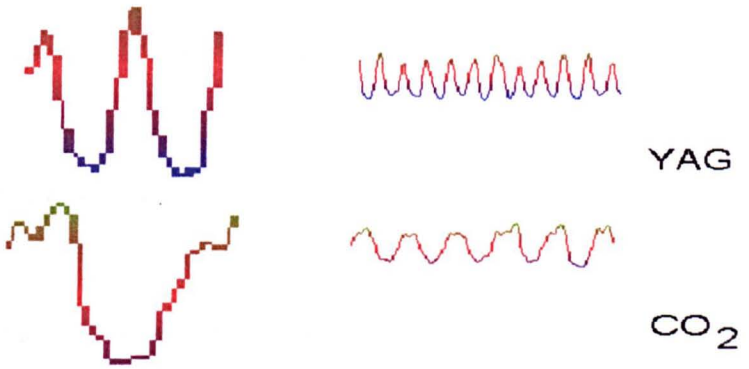

Roughness of cell interior Roughness due to line screen

As the test droplets are very large in comparison with the size of the cells it is possible that the apparent roughness due to line screen differences may mask the effect of cell interior roughness on wetting character.

As all the observed contact angles are below 90° the effect of surface roughness is to lower the true contact angle. [3] Considering line screen as the dominant roughness the order of roughness can be regarded as YAG band > CO_2 band > polished band, therefore the contact angle observed for the YAG band would be the most lowered from its true value, followed by the CO_2 band, then the polished band. As the magnitude of the observed contact angles for the polar liquid (the liquid that produced the difference in surface energies) is the same as the order of roughness, the effect of compensating for roughness would be to increase the differences in contact angle, and therefore in surface energies, between the bands.

A further study, using an anilox supplied by Pira, was carried out under the same conditions. Three bands were studied, two engraved bands done with a CO_2 laser with constant line screen but varying in volume, and a polished band. The line screen was 150 lines per cm (380 lines per inch). The radius of curvature of this roll was significantly greater than that of the Harper roll.

he contact angle data collected for the Pira roll is summarised below.

Table 4. Contact angles observed on three bands of the Pira anilox

Water

	Band 1	Band 2	Polished band
Average contact angle (degrees)	**52.06**	**52.63**	**49.68**
Standard deviation	2.62	2.50	3.22

Diiodomethane

	Band 1	Band 2	Polished band
Average contact angle (degrees)	**16.81**	**15.42**	**13.68**
Standard deviation	2.59	1.84	1.40

These contact angles were used to calculate surface energies for each band using the same method as for the previous calculations.

Table 5. Surface energies calculated for the Pira banded anilox

	Band 1	Band 2	Polished band
Dispersive component of surface Energy (mJm^{-2})	48.7 +/-1.5	49.0 +/- 1.5	49.4 +/- 1.5
Polar components of surface energy (mJm^{-2})	13.5 +/- 1.5	13.1 +/- 1.5	13.1 +/- 1.5
Total Surface Energy (mJm^{-2})	**62.2** +/- 1.5	**62.1** +/- 1.5	**62.5** +/- 1.5

The cell volume and depth were seen to have no significant effect on contact angle. The contact angles on the polished band of the Pira roll were seen to be different to those observed on the Harper roll.

Table 6. Comparison of data for polished bands

	Contact angle with water (degrees)	Contact angle with diiodomethane (degrees)	Polar surface energy (mJ/m^2)	Non-polar surface energy (mJ/m^2)	Total surface energy (mJ/m^2)
Harper	56.1	19.5	11.6	47.9	59.6
Pira	49.7	13.7	13.1	49.4	62.4

Whilst these differences in contact angles do not translate to large differences in surface energies, they are significant in terms of the degree of wetting that was observed to be taking place. The nature of the ceramic on the Pira roll is unknown. It is therefore difficult to determine whether this effect is purely as a result of the difference in curvature between the rolls. However, this seems the most probable explanation.

SUMMARY

The surface energy of test bands on the Harper anilox was seen to decrease from the polished band to the CO_2 band to the YAG band. This was observed to be due to a change in the amount of polar wetting taking place, as the non-polar wetting was constant across the bands (within the margin of error). The change in surface energy and wetting character could be explained by chemical change at the ceramic surface during the engraving process. Differences in surface roughness, i.e. differences in cell interior roughness and roughness due to different line screens, have an affect on the observed contact angles (and therefore the calculated surface energies). However, roughness lowers the apparent contact angle, and the contact angles were observed to increase between bands of increasing roughness, therefore the differences in surface roughness cannot account for the observed trend.

The effect of line screen on the surface roughness and the contact angle is an important variable. In order to study the effect of cell roughness and chemical change caused by the laser, the line screen must be fixed as a constant between the engraved bands.

Analysis of the Pira banded anilox showed that cell volume and depth did not affect the contact angles made by test liquids and hence had no affect on the surface energy or wettability of the roll. However, it is widely accepted that cell depth has an effect on the amount of ink released by a cell. There is an established optimum cell opening to depth ration of 3:1 for CO_2 engraved cells, [7] but the relationship between cell depth and ink release does not hold for YAG engraved cells. [8] The CO_2 engraved

cells are easier to wet, therefore more work has to be done to empty the cell. The YAG cells, being slightly harder to wet do not hold on to the ink as strongly allowing the cells to empty to a greater depth and thus reducing the constraint of the opening to depth ratio.

Wetting is the product of the interaction between the surface tension of the ink and the surface energy of the roll. The difference in the polar wetting character between the CO_2 and the YAG engraved bands is particularly significant for assessing the potential for ink transfer, especially for those inks having a strong polar component, such as water-based inks. If more is known about the surface characteristics of the anilox, inks can be tailored to improve transfer out of the anilox cell.

FURTHER WORK

In order to determine that the differences in wettability and surface energy are produced by the laser, it is necessary to carry out further tests on YAG and CO_2 engravings with identical line screens.

To investigate the effect of roll wettability on ink release, a number of flexo inks of different surface tensions, will be tested and the extent to which they wet the anilox bands will be recorded. A flexo proofer, with an anilox having the same engraving specification, will then be used to study the ink release from the anilox and the optimum degree of wetting of the anilox by the ink to produce maximum ink transfer will be determined.

Thanks to Mr Ron Harper, Mr Colin Farrant and Mr Dan Reilly of the Harper Corporation of America for their input into the project, and for the generous donation of the banded anilox.

Thanks also to Mr David Atkinson and Mr Andrew Dilley of Pira International for their advice and help, and for the use of the facilities at Pira.

This project is supported by the Educational Charity of the Worshipful Company of Stationers' and Newspaper Makers', to whom I am also very grateful.

REFERENCES

1. Lindholm G. **Ink Transfer in Flexo.** Flexo Feb. 1998 pp 40-45
2. Quinn et al. **Does the surface Energy of the Plate Affect Ink Transfer?** Converter & Cartotecnica v.10 #55 Jan-Feb 1997 pp 135-143
3. Packham, D. E. Handbook of Adhesion, Longman Scientific & Technical, Harlow UK (1992) **Roughness of Surfaces** pp 379-382
4. Sutherland, I. & Heath, R. J. **Contact Angle Measurement to Wettability, Surface Energy and Adhesion Properties of Polymers.** Progress in Rubber and Plastics Technology, Vol. 14 No. 3, (1998) Ch. 2. pp 153-173
5. Packham, D. E. Handbook of Adhesion, Longman Scientific & Technical, Harlow UK (1992) **Contact Angle** pp 82-86
6. Personal communications with Mr Phil Anglim (formerly of Pira International) and Mr Andrew Dilley of Pira International (December 1999)
7. Carrillo, C. M. **Optimise Your Anilox Rolls** Flexo vol. 20, no. 7, July 1995, pp 58, 60-62
8. Reilly, D. **YAG Laser Engraving Technology** FlexoTech Feb 1999, pp 50-51